



DISSERTATION

Optimization of the light extraction from heavy inorganic scintillators

ausgeführt zum Zwecke der Erlangung des akademischen Grades eines Doktors
der technischen Naturwissenschaften unter der Leitung von

Univ. Prof. Dr. Christian W. Fabjan

Atominstitut der Österreichischen Universitäten (E141)

eingereicht an der Technischen Universität Wien
Fakultät für Physik von

Dipl.-Ing. Matthias Kronberger

Matrikel Nr. 9525123

Seifentruhe 7, A-4400 Steyr

Diese Arbeit wurde unterstützt vom Österreichischen Bundesministerium für
Bildung, Wissenschaft und Kultur.

Genf, am 18. Mai 2008

Kurzfassung

Inorganische Szintillatoren sind ein integraler Bestandteil moderner bildgebender Instrumentation zur Abbildung von Morphologie und Metabolismus des menschlichen Körpers. Ihre Aufgabe besteht dabei darin, die zur Bildgebung verwendete energiereiche Röntgen- und Gammastrahlung in ein für die Auswertung nutzbares Signal zu konvertieren. Dies beruht auf der sehr hohen Effizienz von Szintillatoren hinsichtlich der Detektion energiereicher Strahlung, welche den Bau von kompakten Systemen mit hoher Ortsauflösung erlaubt.

Eine der wichtigsten Herausforderungen in der Entwicklung von SPECT und PET-Detektoren der nächsten Generation ist die Optimierung der Energieauflösung der Detektoren. Dieser Parameter wird unter anderem durch die statistischen Fluktuationen der Anzahl der Photonen, die bei der Absorption eines energiereichen Teilchens detektiert werden, und damit durch die effektive Lichtausbeute des Kristalls bestimmt. Die effektive Lichtausbeute hängt dabei nicht nur von der Anzahl an emittierten Photonen, sondern auch von der Form des Kristalls, der Transmission im Wellenlängenbereich des vom Szintillator emittierten Lichts, sowie dessen Brechungsindex ab. Speziell in Kristallen mit einer im Vergleich zur Austrittsfläche sehr großen Längsausdehnung geht eine signifikante Anzahl an Photonen für den Messvorgang verloren. Ein großer Anteil der Verluste ist dabei durch Totalreflexion an der dem Photodetektor zugewandten Grenzfläche bedingt.

Ziel der vorliegenden Arbeit ist es, mittels geeigneter struktureller Änderungen das Problem der Totalreflexion an der Austrittsfläche des Szintillators zu umgehen. Der Schwerpunkt liegt dabei auf den Ce^{3+} -gedopten Szintillatoren LuYAP:Ce und LYSO:Ce, die in den von der Crystal Clear Collaboration entwickelten PET-Systemen ClearPEM und ClearPETTM als Detektoren Anwendung finden.

Startpunkt der Arbeit sind Simulationen von LuYAP und LYSO-Kristallen mit Hilfe des Monte-Carlo Programms LITRANI. Mit Hilfe dieser Simulationen werden für Szintillatoren mit planarer Austrittsfläche die Verluste durch Totalreflexion bestimmt und das Potenzial der Kristalle hinsichtlich einer Erhöhung der Lichtausbeute ausgelotet. Zur Kalibrierung des Modells werden die simulierten Daten mit experimentell ermittelten Werten für mehrere Referenzsetups verglichen. Dieser Ansatz erlaubt zudem eine Bestimmung der absoluten Lichtausbeute der Szintillatoren.

Im weiteren Verlauf der Arbeit wird der Einfluss von nicht-planaren Austrittsflächen auf die Lichtausbeute evaluiert. Zwei Ansätze werden dabei näher untersucht: Ein makroskopischer Ansatz, bei dem die Austrittsfläche über trapezoidale Kerben mit einer Tiefe von einigen $100\text{ }\mu\text{m}$ manipuliert wird; und ein mikroskopischer Ansatz, bei dem die Totalreflexion an der Austrittsfläche über eine Nanostrukturierung der Fläche mittels photonischer Kristalle umgangen wird.

Das Potenzial des makroskopischen Ansatzes wird mit Hilfe von LITRANI-Simulationen untersucht und mittels Experimenten an speziell hergestellten Prototypen überprüft. Dabei wird gezeigt, dass die im Experiment beobachtete Änderung der Lichtausbeute geringer ist als durch Simulationen eines idealisierten Systems vorhergesagt. Die experimentellen Werte werden allerdings gut von einem realistischeren Modell reproduziert, bei welchem den unmittelbar an die Kerbe angrenzenden Bereichen des Kristalls eine starke Absorption und Diffusion zugeordnet wird.

Das Potential des mikroskopischen Ansatzes wird anhand von Simulationen mit einem Streumatrix-Algorithmus evaluiert. Mit Hilfe des Algorithmus wird der Einfluss verschiedener struktureller Parameter des photonischen Kristalls auf die Transmissionseigenschaften der Austrittsfläche charakterisiert. Ausgehend von diesen Daten und der mit LITRANI berechneten Winkelverteilung der auf die Austrittsfläche auftreffenden Photonen wird ein Modell entwickelt, welches eine näherungsweise Berechnung der Lichtausbeute eines nanostrukturierten Szintillators erlaubt. In weitere Folge wird kurz auf mögliche Techniken zur Herstellung derartiger Mikrostrukturierungen eingegangen und zwei derzeit in Produktion befindliche Prototypen werden vorgestellt. Zum Abschluss der Doktorarbeit werden wesentliche Ergebnisse noch einmal in kompakter Form zusammengefasst und mögliche Strategien zur praktischen Umsetzung diskutiert.

Abstract

Inorganic scintillators are widely used in modern medical imaging modalities as converter for the x-rays and γ -radiation that are used to obtain information about the interior of the body. Likewise, they are applied in high-energy physics to measure the energy of particles that are produced in particle physics experiments. Their use is motivated by the very good detection efficiency of these materials for hard radiation which allows the construction of relatively compact and finely pixelised systems with a high spatial resolution.

One key problem in the development of the next generation of particle detectors and medical imaging systems is the optimisation of the energy resolution of the detectors. This parameter is influenced by the statistical fluctuations of the light output of the scintillators, i.e. by the number of photons that are detected when a particle deposits its energy in the scintillator. The light output of the scintillator depends not only on the absolute number of generated photons but also on the geometrical shape of the material, its transmission properties at the wavelength of scintillation, and its refractive index. Especially in tiny detector crystals with small aspect ratio, a significant fraction of photons is lost before conversion into an electronic signal in the photo detector. This effect increases the statistical fluctuations of the light output and therefore, deteriorates the energy resolution.

The present work explores possible ways to overcome the problem of total internal reflection at the surface of the scintillator that couples to the photo detector, which is one of the principal reasons for signal losses in heavy inorganic scintillators with high refractive index. The emphasis is placed on the recently developed Ce^{3+} doped scintillators LuYAP:Ce and LYSO:Ce which are used in the dedicated PET imaging systems ClearPEM and ClearPETTM developed by the Crystal Clear Collaboration.

Starting point of the work are Monte-Carlo simulations of standard LuYAP and LYSO crystals used in ClearPEM and ClearPETTM with the light ray tracing program LITRANI. These simulations are used to assess the losses induced by total internal reflection and the potential in effective light yield gain. In order to calibrate the model, experiments in several reference setups are performed and the results compared with those from simulations of equivalent systems. This combination of experimental and simulated data is also used for a precise determination of the absolute light yield of the scintillators.

The results of the simulations are then used to study the effect of non-planar coupling faces on the light extraction. Two approaches are considered: A macroscopic one, in which trapezoidal grooves with a depth of several hundred μm are used to break up total internal reflection at the coupling face; and a microscopic one that uses the unique optical properties of photonic crystals to assess photons outside the extraction cone of a plain coupling face.

The potential of the macroscopic approach is assessed by means of LITRANI simulations and validated by experiments with prototype samples designed on basis of the simulation results. The experimental results show that the gain in light yield is less than predicted from simulations of an idealized system. However, they are found to be well described by a model where the crystal layers immediately beneath the groove surfaces are described by a heavily absorbing and diffusing material.

The microscopic approach is probed by means of simulations with a scattering-matrix algorithm. This algorithm is used to evaluate the impact of several structural parameters of the photonic crystal on the transmission properties of the exit surface. From these data, a model is developed which uses the results obtained with LITRANI to calculate the gain in light collection efficiency for a number of possible designs. Finally, possible fabrication techniques for photonic crystal structures on scintillators are briefly discussed. The thesis closes with a short summary of the results and a short outlook on possible future projects based on the presented approaches.

Acknowledgments

Working on this doctoral thesis always felt to me like exploring a vast, unknown land: you have no idea what's ahead of you, and there are countless challenges, false trails, traps, and other dangers that can make you lose track. Especially at the beginning, it was therefore very helpful to have people around me that pushed me into the right direction, showed me the secrets of the arts of experimental science or just cheered me up during one of the frequent down-phases one endures during such a project. Therefore, I feel obliged to thank all those who accompanied me during the last 2 1/2 years.

In the very first place, I am grateful towards my doctoral thesis adviser Univ. Prof. Christian Fabjan for giving me the opportunity to carry out my PhD at CERN, for his guidance and his constant support throughout my stay. He always had an open ear for my problems and would answer my question whenever necessary and even during his well-deserved holidays.

At least the same amount of gratefulness I owe to my supervisors Paul Lecoq and Etienne Auffray for giving me an understanding of inorganic scintillators and medical imaging, for their constant support, their ideas and their suggestions. In particular, I would like to thank Paul for formulating the topic of this thesis (which was indeed an interesting one) and choosing me to do it, and to Etienne for spending much of her spare-time to read - and correct - my thesis. Moreover, I would like to thank both of them for their patience and encouragement during the first difficult year of my thesis - something I really appreciated a lot.

I am also deeply indebted to Francois-Xavier Gentit, the creator of this wonderful Monte-Carlo code LITRANI which I have used throughout my thesis. Whenever there was a question on or a problem with LITRANI I could not solve by myself, he always tried to answer it as quick as possible and gave me support whenever I needed it.

Very special thanks also to our colleagues at the Institute des Nanotechnologies de Lyon, Xavier Letartre, Jean-Louis Leclercq and Christian Seassal, for their interest in the scintillator - PhC concept and their massive efforts to produce prototype samples for further measurements. Moreover, I am indebted to Xavier for cross-reading and commenting the draft version of the chapter about photonic crystals.

Many thanks also to my colleagues of the Crystal Clear Collaboration and especially, to my CERN colleagues Julia Trummer and Benjamin Frisch; Julia for helping me gaining ground in Geneva and introducing me to the Austrian CERN gang, Benjamin especially for his ability to help me solving my various technical problems just by standing behind me. Was pretty much fun to work together with you in a team!

Thanks a lot also to all other individuals I have been working with and that were working for me during my stay at CERN: the technicians Dominique, Alain, Antonio, Herve, Igor and Norbert from CMS ECal, that were always there for discussions and in general helped me a lot; Andre Braem for clean-room access and some discussions on reflector materials; Alessandro Thea from the CMS ECal group for sharing his LaTeX skills with me; my office mate Niels for enduring me, my habits & my exquisite taste in music; and all the numerous stagieres and summer students I have worked with during my stay at CERN.

I also very grateful to all individuals that helped me understanding the physics behind photonic crystals and their simulation, as there are: Aurelien David from LumiLED; Sergei Tikhodeev from the General Physics Institute of the Russian Academy of Sciences; and Aaron Danner, University of Illinois.

Certainly, my life at CERN did not only consist of working but also had a decent social component. Special thanks to everyone who belongs or belonged either to the 10:00 coffee round, the 12:00 and 13:00 lunch rounds, the 16:00 tea round, the Wednesday and Friday evening Charly's rounds or the Sunday dinner round. It was a pleasure to have met you and you made my time being a PhD student indeed a very nice one!! Additional special thanks to my English referees Susan and Molly who spent quite some time and energy to make my English looking nicer as it actually is.

Of course, many, many, many thanks to my parents for their massive support, their love and their patience during my whole life in general and during the past 2 1/2 years in particular; to my sister, my brother, and all those who are still my friends even though I left you all back in Austria, and anywhere else ... it's damn good to know that you're still there !!!

And finally, the by far biggest "Thank you !!!" goes to a minha musa, mein Sternenschein, my one and only ... Denise. Because of you I never felt alone, you were always there despite the distance between you and me ... You simply complete me. I love you !!

Contents

Kurzfassung	I
Abstract	III
Acknowledgments	V
1 Introduction	1
1.1 Scope of this thesis	1
1.2 Positron-Emission-Tomography - PET	2
1.2.1 Principle of a conventional PET detector	2
1.2.2 Principle of a PET scan	3
1.3 Calorimetry in high energy physics experiments	9
1.3.1 HEP experiments at CERN	11
1.4 The Crystal Clear Collaboration (CCC)	15
1.4.1 Small animal imaging: the ClearPET	15
1.4.2 Mammography: The ClearPEM	17
1.4.3 Multimodality: the ClearPEM Sonic	18
2 Scintillators	25
2.1 Inorganic scintillators	25
2.1.1 Luminescence process	26
2.1.2 Energy absorption	28
2.1.3 Generation of scintillation light	28
2.1.4 Light loss mechanisms	33
2.2 General characteristics of inorganic scintillators	36
2.2.1 Conversion efficiency and absolute light yield	36
2.2.2 Light collection efficiency and measured light output	37
2.2.3 Non-proportionality of energy response	38
2.2.4 Energy Resolution	39
2.2.5 Decay time	41
2.2.6 Afterglow	42
2.2.7 Time resolution	42
2.2.8 Refractive index and transmission	43
2.3 Requirements for scintillators in high energy physics and PET	46
2.3.1 High energy physics	46
2.3.2 PET	47
2.4 An ideal scintillator for PET imaging	48

2.5	The Ce-doped compounds L(Y)SO and Lu(Y)AP	49
2.5.1	LSO and LYSO	49
2.5.2	LuAP and LuYAP	51
3	Experimental techniques	57
3.1	Light output and energy resolution	57
3.1.1	Determination of the scintillator light yield	58
3.1.2	Experimental setup	59
3.1.3	Setup configurations	60
3.2	Transmission	62
3.3	Emission and excitation spectra	64
4	Light propagation in inorganic scintillators	69
4.1	Light output and light collection efficiency	69
4.2	LITRANI	71
4.3	Experimental determination of crystal parameters	76
4.3.1	Emission and excitation spectra	76
4.3.2	Transmission spectra	79
4.4	Simulation of light propagation in LuYAP and LYSO	82
4.4.1	Simulated setups	82
4.4.2	Optical properties of setup materials	83
4.4.3	Results of simulations	85
4.5	Measurements of LuYAP and LYSO samples	94
4.5.1	Light output measurements	94
4.5.2	Comparison with simulated data	94
4.6	The absolute light yield of LuYAP and LYSO	97
4.7	Conclusions	101
5	Scintillators with macromachined exit surfaces	107
5.1	Principle of method	108
5.2	Simulations of crystals with macromachined exit surfaces	109
5.2.1	Simulated setup	109
5.2.2	Results of simulations	109
5.3	Measurements of LuYAP and LYSO samples	118
5.3.1	Fabrication of samples	118
5.3.2	Results of measurements	120
5.3.3	Discussion	120
5.4	The 'absorbing layer' approach	122
5.4.1	Simulation	122
5.4.2	Discussion of results	124
5.5	Conclusions	126
6	Scintillators with nanostructured exit surfaces	129
6.1	Photonic crystals	129
6.1.1	The Bloch-Floquet theorem	130
6.1.2	Optical properties of photonic crystals	131
6.1.3	Photonic crystal slabs	133

6.1.4	Fabrication of PhCs	135
6.2	Photonic crystals and light extraction	136
6.3	Simulation of the nanopatterned exit surface	138
6.3.1	Simulation algorithm	138
6.3.2	Results of simulations	139
6.4	Determination of the extraction potential	142
6.5	Experimental realisation of a PhC-scintillator system	148
6.6	Conclusions	149
7	Summary and outlook	157
A	Bloch Theorem, band gaps, and Tikhodeev algorithm	161
A.1	The Bloch-Floquet theorem	161
A.2	Formation of the band gap	162
A.3	The Tikhodeev algorithm	164

Chapter 1

Introduction

1.1 Scope of this thesis

Inorganic scintillators are widely used in modern medical imaging modalities as converters for the X- and γ -radiation that is used to obtain information about the morphology and the metabolism of the body. Furthermore, they are applied in high-energy physics to measure the energy of particles that are produced in a collider experiment. This is a consequence of their high stopping power which allows the construction of relatively compact and fine-pixelised systems with a high spatial resolution and good detection efficiency.

One key problem in the development of the next generation of particle detectors and medical imaging systems is the optimisation of the energy resolution of the detectors to improve the signal-to-noise (S/N) ratio. In the case of high-energy physics, a better S/N allows for a better discrimination between the signals from rare particle events and the background; in medical imaging systems, an improved S/N leads to a better spatial resolution and reduces examination time and radiation exposure of the patient. The energy resolution of a scintillator is strongly dependent on the statistical fluctuations of the number of photons that are produced during the scintillation process and therefore depends on the light output of the crystals. This parameter is severely limited by the geometry of the scintillators that are used in the detectors; usually, the aspect ratio (i.e. the ratio between the cross section and the length) of the crystals is much smaller than one, and a significant fraction of photons is lost before conversion into an electronic signal by the photo detector. Therefore, finding ways to recover some of these photons holds strong potential to improve the light output and thus the efficiency of image reconstruction and event rejection.

The present work was performed at CERN in the framework of the Crystal Clear Collaboration (CCC). The aim was to study light extraction from heavy inorganic scintillators used in the detector heads of modern positron emission tomographs (PET) and to explore possible ways to overcome total internal reflection at the face connected to the photodetector. The potential of two possible approaches - a macroscopic one using pyramidal grooves machined into

the exit surface of the crystals and a nanoscopic one utilizing photonic crystal structures - is assessed in this work by means of Monte-Carlo simulations and tested by samples fabricated from the two materials $\text{Lu}_{1-x}\text{Y}_x\text{AlO}_3\text{:Ce}$ and $\text{Lu}_{2-x}\text{Y}_x\text{SiO}_5\text{:Ce}$.

This thesis is organized as follows: The present chapter outlines the fundamental aspects of positron emission tomography and calorimetry in high energy physics and provides a short presentation of the Crystal Clear Collaboration and its recent projects on medical imaging. The basic principles of the scintillation process and the main characteristics of scintillators are explained in chapter 2. This chapter also presents the materials that were employed in this study. Chapter 3 provides a description of the experimental techniques used to study the properties of scintillating materials. Chapter 4 is dedicated to the problem of light extraction and discusses the results from respective Monte Carlo simulations and experiments. In addition, it provides an overview of the simulation software employed to the Monte-Carlo simulations. Chapter 5 presents the macroscopic approach and the results of simulations and experiments are discussed. Chapter 6 explains the physics behind photonic crystals and evaluates their impact on the light collection efficiency of scintillators. The thesis is summarized in the last chapter which also provides a short outlook on future CCC activities.

1.2 Positron-Emission-Tomography - PET

Positron Emission tomography is a nuclear medical imaging technique which uses a tracer (i.e. a biologically active compound labelled with a positron emitter) to obtain a three-dimensional map of functional processes in the body. As such, it is widely used to detect malignant tumors and metastases in clinical oncology and in the diagnosis of neurological diseases, as Alzheimer or epilepsy. In addition, it is an important tool in medical and biological research for mapping the function of organs and to assess the metabolism of different body regions. Dedicated PET systems for experimental small animal studies are often used in pharmacology as tools to assess the effectivity of potential new drugs for the treatment of diseases and malignant tumors. In the following, a short outline of a PET detector is given and the principles of PET imaging are explained.

1.2.1 Principle of a conventional PET detector

A typical modern PET-scanner (Fig. 1.1) consists of two main entities: an arrangement of one or more planar detector rings and a movable table which is used to place the patient in the center of the field of view (FOV). Each detector ring usually consists of several detector modules which are segmented into a number of detector blocks. In a typical PET scanner, every detector block contains several scintillating crystals with a typical size of several mm in transaxial direction and a few cm in radial direction, which record the γ -photons arriving

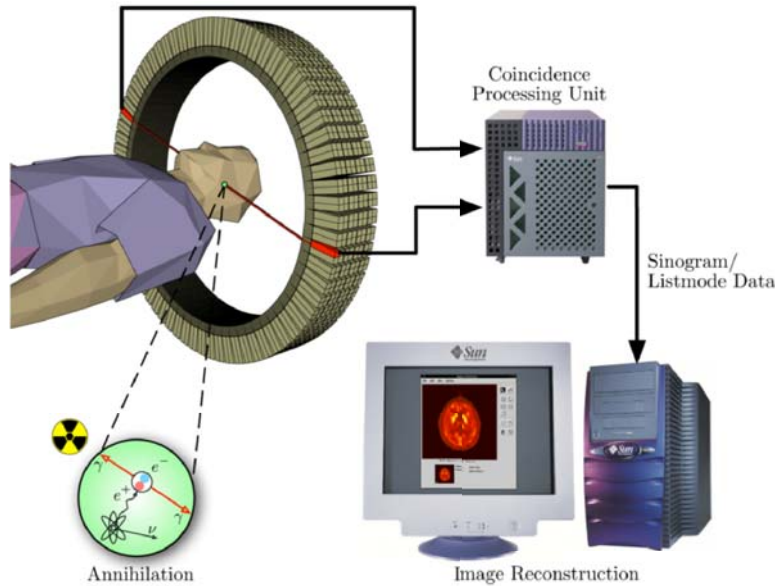


Figure 1.1: Principle of a PET scanner.

from the body. The scintillating crystals of each detector block are coupled to an array of photo detectors to convert the photons generated by the scintillation process into an electronic signal. As photo detectors, photomultiplier tubes (PMTs) or avalanche photodiodes (APDs) can be used. APDs have the advantage of a small size, which makes them appropriate detectors for compact PET systems. Their insensitivity to magnetic fields makes them also suited for operation in a magnetic environment, e.g. in multimodal systems (see Sect. 1.4.3).

After the signal has been converted, it is amplified, shaped, and converted into a digital signal by an analogue-to-digital converter (ADC) before it is sent to the data acquisition (DAQ) software. Finally, the events that are collected by the DAQ are used for image reconstruction.

1.2.2 Principle of a PET scan

Every PET scan starts with a radiopharmaceutical (tracer) marked with a positron emitter that is injected or inhaled by the patient.

Each time a positron emitter exhibits a β^+ -decay, a proton in the nucleus converts into a neutron, and a positron and a neutrino are ejected. While the neutrino will leave the body unharmed, the positron will travel only a short distance from the point of emission until it encounters an electron in the body tissue. The positron and electron then annihilate into two 511 keV γ -photons that are emitted in opposite directions. Since the positron typically has a kinetic energy greater than zero at the moment of annihilation, the propagation directions of the two photons are usually slightly acollinear (FWHM = 0.5 de-

degrees [1]) due to momentum conservation. Together with the non-zero mean free path-length of the positron, this acollinearity determines the spatial resolution that can be achieved at best with a PET scanner.

After the two γ -photons have left the body, they can produce a signal in the scintillators of the detector rings around the patient (Fig. 1.2). If both photons

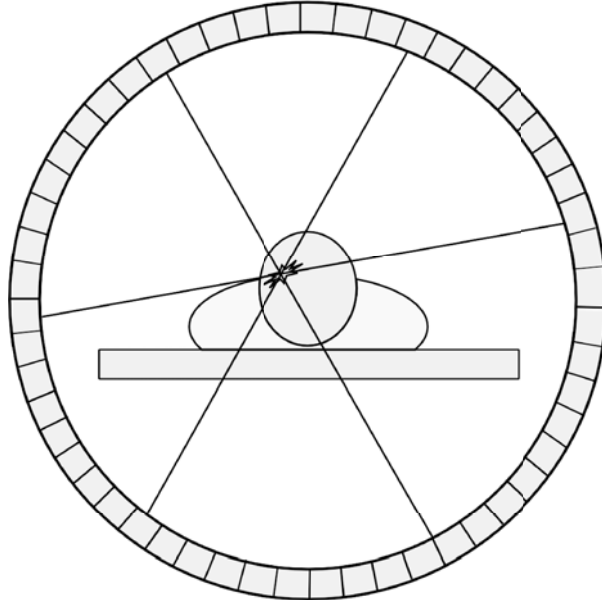


Figure 1.2: Principle of a PET scan.

are registered by the detector in coincidence, the origin of the photons - and therefore, the position where the interaction between electron and positron has taken place - can be traced back by connecting the two detector elements where the photons produced a signal. The resulting line or chord is called the line of response (LOR) and the event termed *coincidence event*. The orientation and the position of any LOR is characterised by its angle ϕ relative to the horizontal direction, and by the shortest distance $d_{c,LOR}$ between the LOR and the center of the detector ring. The sum of all LORs recorded during an examination is then used to generate a sinogram which in turn permits the reconstruction of the tracer distribution in the examined body region.

Radionuclides

Radionuclides used in PET imaging have very short half-lives typically in the range of a few minutes to 1 - 2 hours (Table 1.1). They are produced either in cyclotrons (^{11}C , ^{13}N , ^{15}O , and ^{18}F) or by means of radionuclide generators that contain a parent isotope (^{68}Ga , ^{82}Rb). The type of radionuclide which is used depends not only on the radiotracer but also on the performance of the PET scanner. Nuclides with a very short half-life (as e.g. ^{82}Rb or ^{15}O) require a detector system with very good timing resolution to deal with the high count

Table 1.1: Properties and selected fields of application of frequently used PET isotopes.

Radionuclide	$t_{\frac{1}{2}}$ [min]	Tracer	Field	Produced in
^{11}C	20.4	^{11}C -Cholin ^{11}C -Acetate	oncology cardiology	cyclotron
^{13}N	9.9	^{13}N -Ammonia ($^{13}\text{NH}_3$)	cardiology	cyclotron
^{15}O	2.05	^{15}O -Water $^{15}\text{O}_2$	perfusion oxygen uptake	cyclotron
^{18}F	109.7	^{18}F -FDG ^{18}F -DOPA	oncology neurology	cyclotron
^{68}Ga	67.7	^{68}Ga -DOTATOC	oncology	radionuclide generator
^{82}Rb	1.27	^{82}Rb -Chloride	cardiology	radionuclide generator

rates of several GBq. On the other hand, nuclides with a modest half-life of several tens of minutes (as e.g. ^{18}F) demand the use of PET scanners with high sensitivity as the dose rates during the examination will be relatively low.

Radiotracers used in PET imaging are selected by means of their ability to accumulate in the body regions of interest for the examination. In cancer diagnosis, common radiotracers are often derivatives of molecules that take part in the metabolism of the tumor cells. The most commonly used of them is the glucose analogue ^{18}F -FDG (^{18}F -Fluoro-Deoxy-Glucose). This tracer is also used in the examination of heart and brain diseases.

Image noise

As the dimensions of the PET scanner are small, it can be assumed that two γ -photons produced during the annihilation process reach the detector almost simultaneously. To account for small differences in the detection time, a *coincidence time window* is defined within which both photons have to be detected to be counted as an event.

However, not all events are true coincidences in the sense that the photons originate from the same point and their directions remain unchanged until they arrive at the detector. In fact, there are four types of coincidences that can be distinguished (Fig. 1.3):

- *true coincidences*: both photons originate from the same positron, no interaction between photons and body tissue takes place and no additional detection from a random photon occurs during the time window.
- *scattered coincidences*: same as true coincidence, but one or both photons undergo inelastic or elastic scattering in the tissue.

- *accidental or random coincidences*: two unrelated photons hit the detector within the coincidence time window.
- *multiple coincidences*: three or more photons detected during the coincidence time window; these events are rejected immediately after detection and therefore do not have any influence on the image quality.

In the following paragraphs, the term *false coincidence* is used for any of the three latter coincidence types.

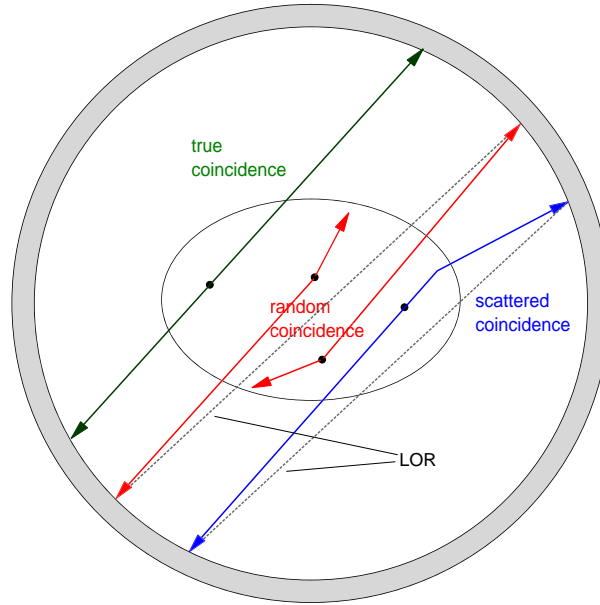


Figure 1.3: Coincidence types.

The quality of the image delivered by a PET scanner depends strongly on the validity of the events collected during the scan. Only in the case of a true coincidence does the LOR contain the point where the positron actually annihilated. Any type of false coincidence introduces background noise in the reconstructed image. This background noise affects the signal-to-noise ratio of the image and leads to a reduction of image resolution and contrast.

A photon that undergoes Compton scattering will transfer some of its energy to its scattering partner, and therefore will produce less photons in the scintillator. Due to the changed trajectory of the photon, the LOR will not contain the interaction point but will be displaced by a certain amount. As the transferred energy rises with the scattering angle, the Compton background of the image can be reduced by applying an energy threshold below which a detected photon is not taken into account. However, the limited energy resolution of the scintillators usually prevents a discrimination of photons that underwent small angle Compton scattering.

Random coincidences pose even more problems than scattered coincidences. As the spectrum of random coincidences contains many unscattered photons, they cannot be distinguished *a priori* from true coincidences by setting a simple energy threshold. A significant reduction of this type of false coincidence can however be achieved by using a detector with a good timing resolution: In a detector with a coincidence time window of width Δt and a single count rate S , the random coincidence rate R_r will be

$$R_r = \Delta t \cdot S^2. \quad (1.1)$$

whereas the true event rate R_t is given by

$$R_t = k \cdot S \quad (1.2)$$

k is a constant factor that depends on the detector system. From eqs. 1.1 and 1.2, the ratio of true to random coincidences follows to be

$$\frac{R_t}{R_r} = \frac{k}{\Delta t \cdot S} \quad (1.3)$$

It is apparent from eq. 1.3 that the random background can be reduced if the timing resolution of the detector is improved such that a smaller coincidence time window can be used. Another possibility to reduce the background of random coincidences is an efficient shielding of the detector against photons from body regions outside the FOV. Moreover, as the single count rate S is a function of the injected dose, the ratio of true to random coincidences R_t/R_r can be improved by using an optimised injected dose value. A detector with very good timing resolution (1 ns or less) can also be used for time-of-flight (TOF) measurements which narrow down the origin of the detected photons. This, in turn, improves the scatter rejection and enhances the signal-to-noise ratio of the resulting image.

Parallax error and depth of interaction

When a coincidence takes place at the margin of the FOV, the position 'seen' by the detector is different from the actual position. Consequently, a parallax error is introduced in the LOR (Fig. 1.4). This parallax error results from the inclination of the crystals relative to the LOR: A photon that does not travel parallel to the crystal axis can traverse the crystal without significant energy loss and deposit its energy in a neighboring one. If this effect is not taken into account, the LOR is shifted slightly towards the center relative to the real LOR, resulting in a displacement of the source in the reconstructed image.

Various techniques have been developed to compensate for the parallax error. One possibility is the implementation of thin bands made of lead or tungstate (septa) in front of the crystals, which however decrease the sensitivity of the system. An alternative method is the determination of the depth of interaction (DOI) point in the crystal. This can be done in two ways: by reading out a single crystal on both ends and using the difference in signal position to determine

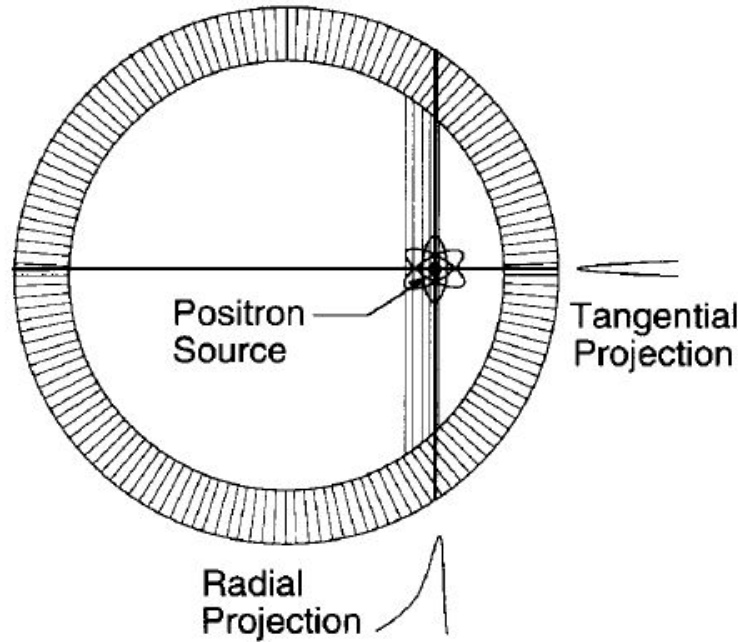


Figure 1.4: Origin of the parallax error in a PET scanner [2].

the interaction point (light sharing method); or by using a phosphor-sandwich (Phoswich) detector. A Phoswich detector consists of two back-to-back scintillators, where each of the crystals has different scintillation properties, e.g. in terms of emission wavelengths and decay times. By analysing the signal coming from the Phoswich detector, it can be determined in which crystal the interaction has taken place. Current efforts to avoid the parallax error include the usage of detectors with even higher segmentation [3] and detector designs with axially oriented crystals [4].

Dead time

An important aspect of a PET system is the dead time of the detector, i.e. the time span during which an incoming photon cannot be detected as the system is busy with a previous coincidence effect. Several sub-entities of the system, including the detector and the read-out electronics, contribute to the dead time. The scintillators contribute to the dead time by the lifetime of the fluorescent light, which is up to several 100 nanoseconds. However, if the detector is finely pixelized and each scintillator individually coupled to a photo detector, this influence is relatively small and extremely high event rates can be achieved. As an example, a scintillation detector with a dead time of 300 ns and a single readout channel loses 3% of the events at a rate of 10^5 events per second; if, however, this detector is replaced by a 8×8 matrix of individually read out scintillators, the event rate per read out channel is reduced by a factor of 64 and the losses due to the dead time of the scintillation detector become negligible.

Data correction

After the event data have been collected by the DAQ, it is necessary to apply several corrections in order to produce quantitative, un-biased images. Apart from corrections for random and scattered coincidences and the detector dead time, the correction for the attenuation of the photons in the body is of special importance. Usually, this information is gained by a separate x-ray transmission scan of the body. In combined PET-CT systems, information on photon attenuation is automatically delivered during the examination by the CT scan.

Spatial resolution

The spatial resolution of a PET detector is not only limited by the photon acollinearity after annihilation and the positron range but also by several instrumental parameters [1]. The most important instrumental influence on the spatial resolution is the limited cross-section d of the scintillator which leads to a positional uncertainty of the order of $d/\sqrt{12}$. Additional factors that may limit the resolution of a PET scanner are the readout strategy, the reconstruction algorithm, the parallax effect, and the width of the detector ring [1]. The total resolution of the PET is determined by the square root of the squared sum of the different contributions.

1.3 Calorimetry in high energy physics experiments

High-energy physics (HEP) is one of the driving forces in the development of new scintillating materials. This is due to the very challenging conditions in the inner regions of HEP experiments and the large volumes of scintillators that are involved. Every HEP experiment is based on the collision of a beam of accelerated particles with either a fixed target or the particles of a second beam. The energies of the particles that are produced during a collision are usually measured in calorimeters, where they lose their energy by producing a shower of secondary particles. Two different types of calorimeters can be distinguished. Sampling calorimeters consist of consecutive layers of a passive absorber material of high density, which acts as a converter of the particle energy, and an active medium that transforms the particle energy into a signal. In a homogeneous calorimeter, the active medium acts at the same time as absorber and no passive converter has to be used. Sampling calorimeters typically use plastic scintillators, silicon detectors, or gas detectors as active medium and iron or lead as absorber. As most of the energy is absorbed in the passive absorber plates, only a small fraction of the energy is actually measured. Homogeneous calorimeters, on the other hand, are made entirely of heavy inorganic scintillators, where a high percentage of the deposited energy is converted into a measurable signal.

Calorimeters can also be distinguished by their purpose, i.e. which particles they measure. Electromagnetic calorimeters are designed in a way that they allow for measuring the energy of electrons and photons that are produced during a collision. Likewise, hadronic calorimeters are optimised for the absorption

of particles that are made of quarks and therefore underly the strong nuclear force. Frequently, electromagnetic calorimeters are designed as homogeneous calorimeters whereas hadron calorimeters are almost always built as sampling calorimeters.

Calorimeter size

To ensure a precise measurement of the particle energy, any type of calorimeter is typically designed in a way that it contains $> 95\%$ of the electromagnetic or hadronic shower that is created by the incident particle. For electromagnetic calorimeters, a convenient parameter to determine the required calorimeter size is the radiation length X_0 , which is defined as the distance traveled by a high-energy electron until its energy has been reduced by a factor e due to radiation losses. An approximate expression of X_0 is

$$X_0 [\text{g} \cdot \text{cm}^{-2}] \approx 180 \cdot \frac{A}{Z^2} \quad (1.4)$$

where A and Z are the mole mass and the atomic number of the absorber, respectively.

Similarly, the size of hadronic calorimeters can be defined by the interaction length λ_i of hadronic reactions, which is given by

$$\lambda_i = \frac{A}{N_A \cdot \rho} \cdot \frac{1}{\sigma_{inelastic}} \quad (1.5)$$

where N_A is the Avogadro number, ρ the material density and σ_{inel} the cross section of inelastic interactions,

$$\sigma_{inel} = \sigma_{tot} - \sigma_{el} \quad (1.6)$$

In both cases, the longitudinal dimensions of calorimeters rise logarithmically with the particle energy.

Energy resolution

The energy resolution of calorimeters is usually expressed in terms of three parameters a , b and c in the following way [5]:

$$\frac{\sigma}{E} = \frac{a}{\sqrt{E}} \oplus \frac{b}{E} \oplus c \quad (1.7)$$

where \oplus stands for the quadratic sum. The first term in eq. 1.7 is called the stochastic or sampling term and includes the statistical fluctuations in the number of signal generating processes, as e.g. the conversion of light into photoelectrons. The second term is called the noise term and accounts mainly for the noise generated by the read out electronics. The constant third term contains quality imperfections in the construction of the calorimeter, intercalibration errors, the effect of dead detector parts, etc.

Typical values of σ/E for electromagnetic calorimeters are:

- $\frac{\sigma}{E} \approx \frac{2\%}{\sqrt{E[\text{GeV}]}} + 0.5\%$ for homogeneous calorimeters
- $\frac{\sigma}{E} \approx \frac{10\%}{\sqrt{E[\text{GeV}]}} + 1\%$ for sampling calorimeters

Clearly, the energy resolution of homogeneous calorimeters is several times better than that of sampling calorimeters.

1.3.1 HEP experiments at CERN

The LHC project

The Large Hadron Collider (LHC) project [6] was approved by the CERN council in December 1994 and is scheduled for start-up in 2008. This accelerator will provide proton-proton collisions with energies of 7-on-7 TeV and a luminosity of up to $10^{34} \text{ cm}^{-2}\text{s}^{-1}$. In addition to $p-p$ operation, the LHC will also be able to collide heavy nuclei up to lead with an ion centre-of-mass energy of 11 548 TeV and a luminosity of $10^{27} \text{ cm}^{-2}\text{s}^{-1}$. An outline of the LHC is given in Fig. 1.5.

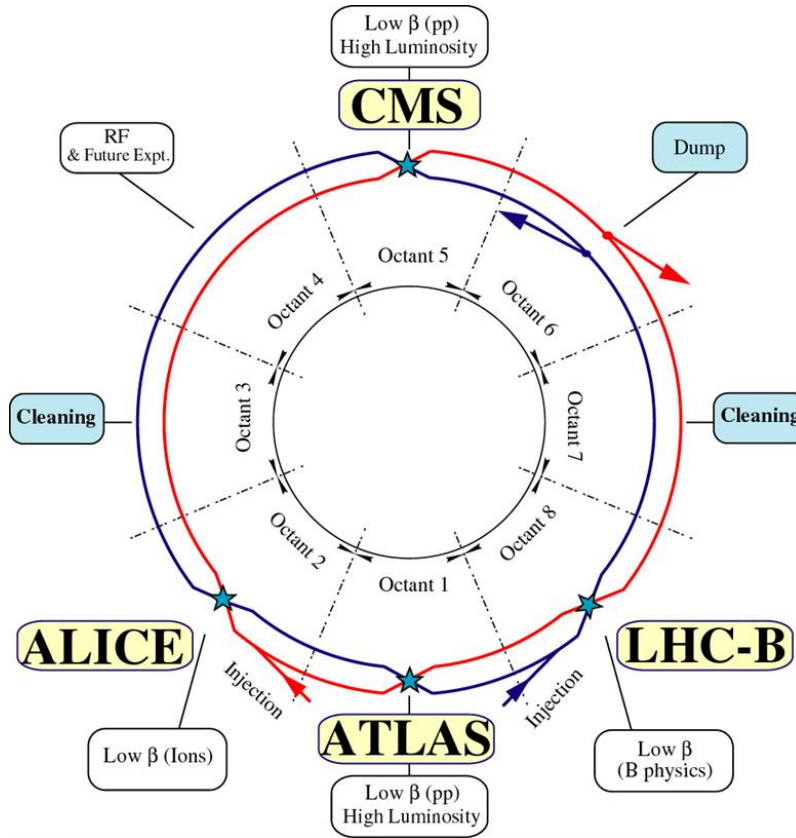


Figure 1.5: Outline of the LHC.

Associated with the LHC are the four experiments CMS, ALICE, ATLAS and LHCb which aim to study different aspects of particle physics at unprece-

dented energies. A short summary of CMS and ALICE is given in the following paragraphs.

The Compact Muon Solenoid (CMS)

The CMS experiment is, together with ATLAS, the largest detector at CERN. It consists of a rotational-symmetric cylindrical barrel of 21 m length and 16 m diameter flanked by two endcaps. The total weight of the detector is about 12500 tons, which is almost double the mass of the Eiffel tower in Paris. With the ATLAS experiment it shares also its purpose which is to discover the Higgs boson and to look for further evidence of physics beyond the standard model, such as supersymmetry, or extra dimensions, as predicted by string theory.

A general 3D view of the CMS detector is shown in Fig. 1.6. Outwards from

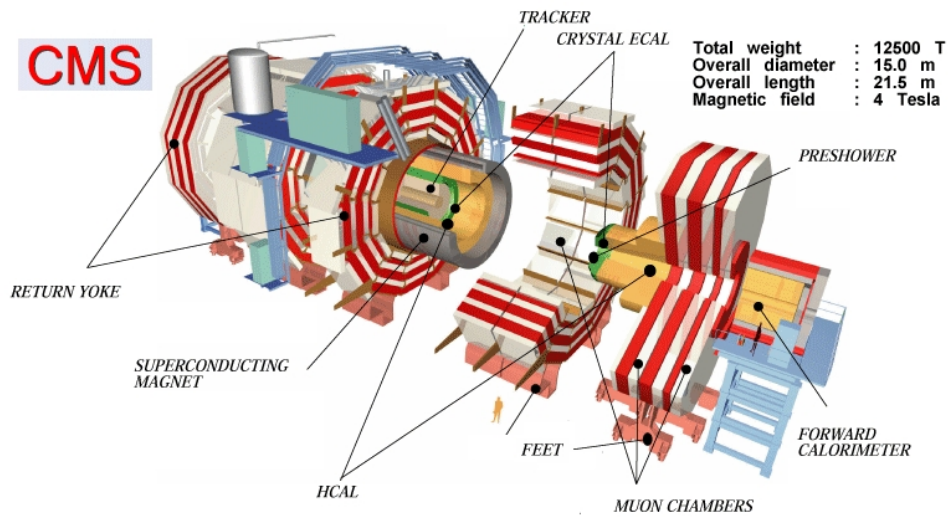


Figure 1.6: Outline of the CMS detector at CERN.

the interaction point, the detector consists of the following subsystems:

- The inner tracker system, consisting of several layers of silicon pixel and microstrip detectors
- The electromagnetic calorimeter (see below)
- The hadronic calorimeter, a sampling calorimeter with plastic scintillators as active medium and brass layers as absorber
- A superconducting solenoid generating a field of 4 T
- The muon system, consisting of four muon chambers in the barrel and each endcap integrated in the iron return yoke of the magnet

The electromagnetic calorimeter of CMS (ECAL) is a homogeneous calorimeter. It consists of a total of 75 848 tapered lead tungstate crystals (PbWO_4 , PWO, Fig. 1.7), of which 61 200 are located in the barrel and 7 324 in each endcap. Its main purpose is the measurement of the two-photon decay mode

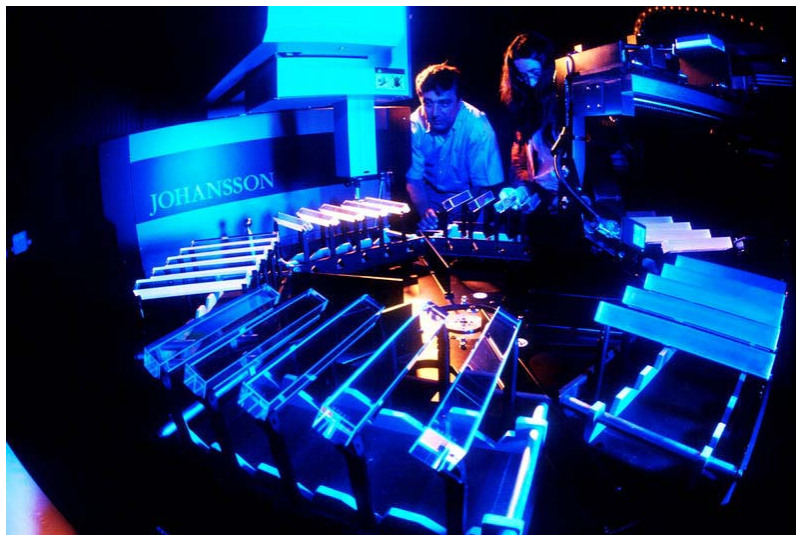


Figure 1.7: PWO crystals.

of the Higgs boson and the electrons and positrons from the decay of W and Z particles originating from $H \Rightarrow ZZ^*$ and $H \Rightarrow WW^*$ decay chains. In the following, several key parameters of the ECAL are listed:

- excellent energy resolution with $a \leq 3\%$ and $c \leq 0.5\%$
- fine granularity (crystal cross-section $\approx 2 \times 2$ cm), ensuring a high positional resolution
- fast response (< 25 ns)
- high radiation hardness

PWO crystals located in the barrel are read out by two APDs with a surface of 5×5 mm² each and a quantum efficiency of $\approx 80\%$ for PWO. For the endcap crystals, vacuum phototriodes (VPTs) are used as photo detectors instead of the less radiation hard APDs. In both cases, the photo detectors are glued onto the larger end faces to extract more light from the crystals.

A Large Ion Collider Experiment (ALICE)

The ALICE Experiment at CERN (Fig. 1.8) is designed to study the strong interaction of matter at extreme densities and temperatures. Of special interest is the phase transition from ordinary hadronic matter to the Quark Gluon Plasma (QGP), in which the quarks and gluons can exist for a very short time

unbounded to any other particle and can move freely inside the whole, high density system. In the ALICE experiment, the production of the QGP is achieved

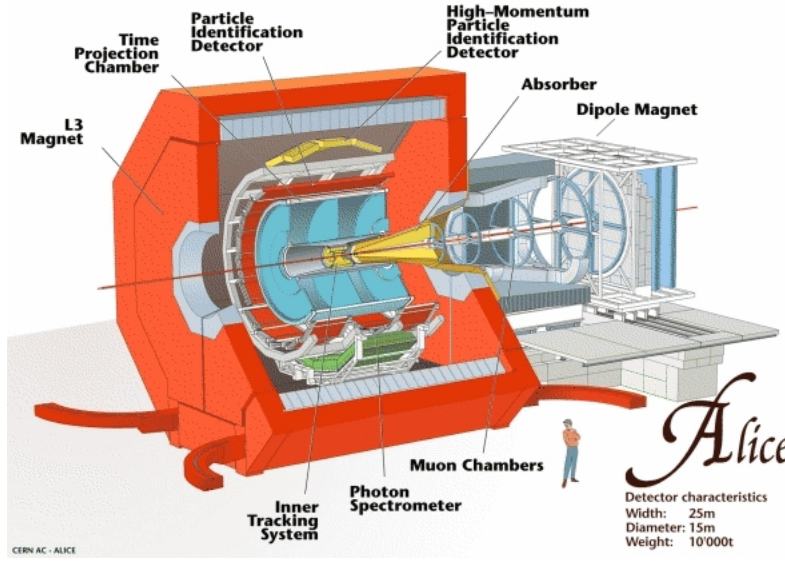


Figure 1.8: Outline of the ALICE detector at CERN.

by Pb-Pb collisions with a total energy in the PeV range. An interesting probe to investigate these collisions are high energy photons as they can provide unperturbed information on their creation conditions. Consequently, ALICE contains an electromagnetic calorimeter (PHOS, PHOTon Spectrometer); this detector is designed as a homogeneous detector and consists of five modules of which each contains 56×64 cuboid PWO crystals (size: $22 \times 22 \times 180 \text{ mm}^3$). The crystals are read out by APDs of $5 \times 5 \text{ mm}^2$ active surface that are coupled to a low-noise preamplifier. Its specifications allow for identifying and measuring with high accuracy photons, electrons, and π^0 and η mesons over a broad energy range (0.5 GeV - 100 GeV). The energy resolution of the PHOS detector ranges from 5% at 0.5 GeV to 1% at 120 GeV. These excellent numbers are achieved by operating the detector at a temperature of -25°C , which reduces the electronic noise and increases the light yield of PWO by a factor of three relative to operation at room temperature. Another important subdetector is the main tracker, which is the world's largest time projection chamber (TPC). This TPC is also used to determine the dE/dx of the particles.

Other important subsystems of the ALICE experiment include:

- An inner tracking system consisting of 6 layers of silicon detectors
- A Time Projection Chamber and a high granularity Transition Radiation Detector (TRD) for particle tracking
- Several subsystems for particle identification (TRD, Time Of Flight detector, Cherenkov detector)

- A conventional solenoidal magnet with a magnetic field of 0.5 T
- A forward muon spectrometer including a dipole magnet (0.7 T)

1.4 The Crystal Clear Collaboration (CCC)

The Crystal Clear Collaboration (CCC) is an interdisciplinary academic network of experts involved in different aspects of material science (as e.g. solid state physics, crystallography, and luminescence), high energy physics instrumentation, and medical imaging. Set up in 1990, its aims have been the development and characterization of new scintillating materials suitable for the extremely demanding environment at the LHC [7]. In addition to CERN, a total of 15 institutes and research laboratories from eight countries are currently members of the collaboration: The Institute of Physical Research, Ashtarak, Armenia; the Institute for Nuclear Problems, Minsk, Belarus; the Universiteit Gent and the Vrije Iniversiteit Brussel, Belgium; CPPM, Marseille, UCB Lyon I, Lyon, and CNRS, France; the Forschungszentrum Jülich and the German Cancer Research Center (DKFZ), Heidelberg, Germany; LIP-Lisboa, Portugal; CIEMAT, Madrid, Spain; UPM, Ancona, Italy; and the Sungkyunkwan University, Seoul, South Korea. The CCC works closely together with the Technology Transfer department at CERN which helps protecting the intellectual property, submitting patents, and establishing contacts with private companies.

The most notable achievements of the CCC in scintillator research are summarized in the following:

- a thorough understanding of the mechanisms that drive scintillation and radiation damage processes in PWO [8, 9, 10];
- establishing Cerium Fluoride (CeF_3) as an interesting candidate for HEP experiments [11];
- the development of new heavy scintillators based on fluoride glasses [12];
- the development of Lutetium- and Yttrium Aluminate Perovskite crystals ($\text{Lu}_{1-x}\text{Y}_x\text{AlO}_3$, LuYAP) with very promising scintillating properties and physical characteristics [13, 14, 15, 16, 17, 18, 19].

With the decision for using PWO in the CMS electromagnetic calorimeter in 1995, the main focus of the CCC was shifted from HEP towards the development of imaging systems in biomedical research. Two of these systems are presented in the following paragraphs.

1.4.1 Small animal imaging: the ClearPET

Small animal PET scanners are important tools in many fields of research. They are used by the pharmaceutical industry in the development of new drugs for a range of deadly diseases (as cancer or Alzheimer) and in molecular biology for

the imaging of the gene expression. Such studies require a high spatial resolution and therefore cannot be performed with conventional whole-body or brain PET scanners, whose resolution is low compared to the dimensions of the laboratory animals. Moreover, performing animal studies on clinical scanners is usually impractical and expensive. For these reasons, much effort has been devoted to the development of dedicated PET imaging devices that meet the requirements of the research fields mentioned above.

An example of such a device is the ClearPETTM, a high-resolution small animal PET scanner developed by the CCC [20, 21] (Fig. 1.9). The system consists of

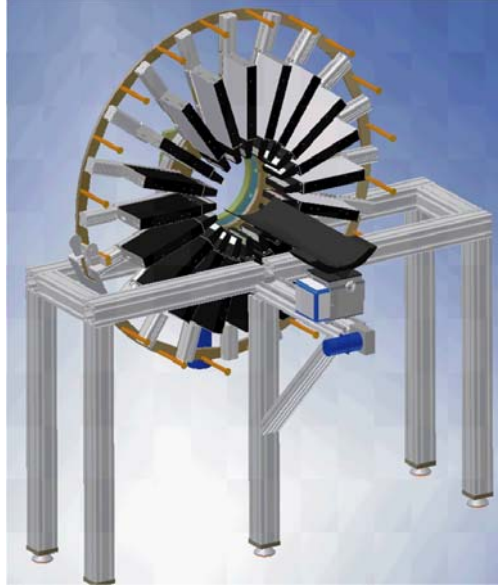


Figure 1.9: The ClearPETTM scanner.

a total of 10 240 LSO and LuYAP crystals that are assembled in 8×8 dual layer phoswich matrices [22] and coupled to a multi-anode PMT to form a detector head. Each crystal has a cross-section of 2×2 mm and a length of either 8 or 10 mm. The crystals are optically separated from their neighbors by a layer of BaSO_4 which serves also as a diffusing reflector. Four detector heads together build a detector module. Four of these detector modules plus their readout electronics are assembled in one of the 20 radially orientated cassettes. The gantry measures 120 cm in diameter and can rotate freely in 360° . Free running ADCs are used to sample the signal from each PMT continuously [23]. Detected events are then stored in List Mode Format (LMF) [24]; sorting of the events into coincidences is done off-line.

In total, four prototypes of the ClearPETTM device have been built, each of which is optimised in its specific field of study:

- the ClearPETTM Neuro for brain studies on non-human primates under physiological conditions [25];
- the ClearPETTM Rodent, a rodent version;
- PlanTIS, a machine for imaging plants; and
- one research prototype with a limited number of detector modules (see e.g. [26])

The ClearPETTM has now been commercialised by the German company Raytest GmbH, Straubenhardt, Germany. Key parameters of the Raytest system are [27]: a maximum sensitivity of 3.8% at the centre of the FOV; a spatial resolution of 1.25 mm FWHM along the central FOV axis and 2 mm at a point 3 cm distant from the axis; and a timing resolution of 5.7 ns FWHM. A unique feature of the system is that the FOV diameter is adjustable between 135 mm and 285 mm, which makes the scanner suitable for small and medium size animal PET studies. This is achieved by attaching the detector cassettes on moving parts that allow changing their radial position.

1.4.2 Mammography: The ClearPEM

Breast cancer is the second leading cause of cancer death for women. Especially at later stages of cancer development, the curing rate is very low and an early detection of breast cancer is therefore important. Unfortunately, the detection efficiency of standard X-ray mammography is insufficient for detecting breast cancer in early stages, especially in cases where the density of the tumor is not significantly different from the density of the surrounding tissue. In particular, this technique provides poor results for women with dense breast tissue or with breast implants. Normal whole-body PET scanners do not have these restrictions but suffer from poor spatial resolution and sensitivity, which are both important requirements to precisely localize a small tumor. Dedicated PET systems for breast imaging are expected to overcome this problem by a finer detector pixelisation, higher sensitivity and a shorter acquisition time. Finally, a dedicated PET will always be more cost-effective and more compact than a whole-body PET.

The ClearPEM [28] is a dedicated PET scanner for breast imaging developed and currently built by the CCC. Fig. 1.10 shows a view of the prototype of the model. The patient is positioned on an examination table with the face looking downwards. This table contains an opening through which the breast is passed. The two detector plates (surface each $17 \times 15 \text{ cm}^2$) are mounted on a robotic system that allows the rotation of the detector heads around the breast. The configuration of this system can be changed so that the lymphatic glands in the axilia region can also be examined (Fig. 1.10b). Each detector plate consists of 96 detector modules and allows a rotational movement around the breast for 3D image reconstruction. The detector modules are based on slightly depolished $2 \times 2 \times 20 \text{ mm}^3$ LYSO:Ce crystals that are arranged in 4×8 crystal matrices and

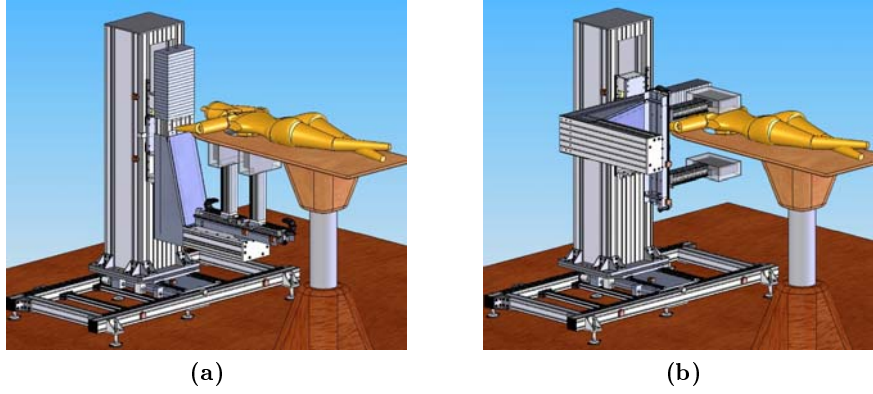


Figure 1.10: The ClearPEM scanner. (a) examination of the breast; (b) examination of the axillary region.

read out at both ends by APD arrays for depth-on-interaction determination. A fast low-noise electronic system for APD readout and a dedicated digital trigger and data acquisition system for on-line selection of coincidence events complete the system [29]. A short summary of the key parameters of the system is given below:

- sensitivity: 10% at the centre of the FOV (for a plate separation of 10 cm)
- spatial resolution: $< 2\text{mm}$
- 6 144 LYSO:Ce crystals ($2 \times 2 \times 20 \text{ mm}^3$)
- 12 288 APD channels (2 per crystal)
- low noise electronics: $< 1000 \text{ e}^- \text{ rms}$
- low power dissipation: $< 2 \text{ mW}$ per channel
- event rate: singles 10 Mhz, coincidences 1 Mhz
- data rate: 200 MB/s
- time resolution: 1 ns
- dead time: $\leq 100 \text{ ns}$

The aim of the ClearPEM project is to reach a spatial resolution and sensitivity that allows for detecting tumors with sizes down to 2 – 3 mm in the breast and axilla region.

1.4.3 Multimodality: the ClearPEM Sonic

A new trend in medical imaging is the combination of two different imaging techniques into one system (Fig. 1.11). Examples are combinations of PET with computer tomography (PET-CT), magnetic resonant imaging (PET-MRI),

ultrasound (PET-US) and single photon emission computed tomography (PET-SPECT). The idea behind these combinations is to obtain functional and morphological images during the same examination under identical conditions, i.e. with the patient still in the same position. Such an approach reduces costs and examination time and facilitates the fusion of the images generated by the subsystems.

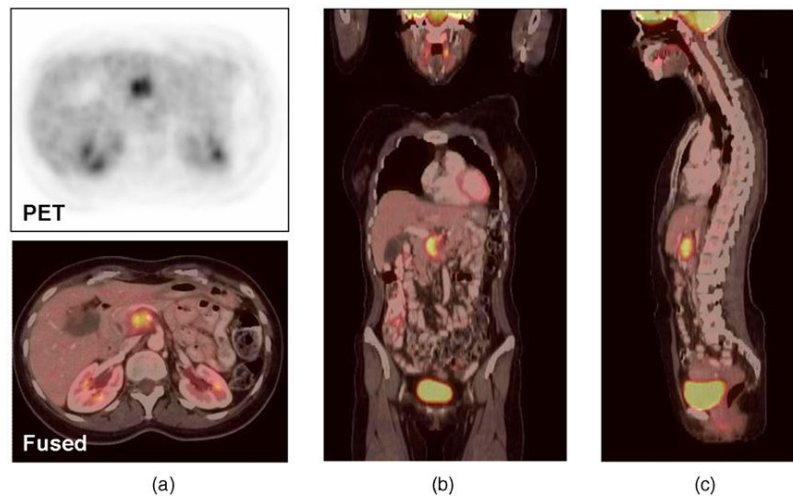


Figure 1.11: PET-CT image of a 50-year-old female with pancreatic cancer [30].

One such multimodal system is the ClearPEM Sonic, a PET-US system currently under development by CCC. Based on the ClearPEM system described in Sect. 1.4.2, it combines the metabolic information from the PET with the structural information from ultrasonography. Due to the high sensitivity of the mammography PET system and the high spatial resolution of the ultrasound (US) device of ≈ 0.5 mm, the combination of these two systems will produce results far superior to those of conventional x-ray mammography.

The PET detector system used in the ClearPEM Sonic is identical to that of the ClearPEM and consists of two detector plates that can be moved freely in all directions. However, unlike the ClearPEM the breast is fixed in two breast contention plates that consist of a radiolucent and sonolucent material (Fig. 1.12). This is necessary to avoid movement of the breast between the PET scan and the US examination [31]. Fusion of the PET and US images is achieved by reference points detected by both modalities (e.g. small β^+ -sources).

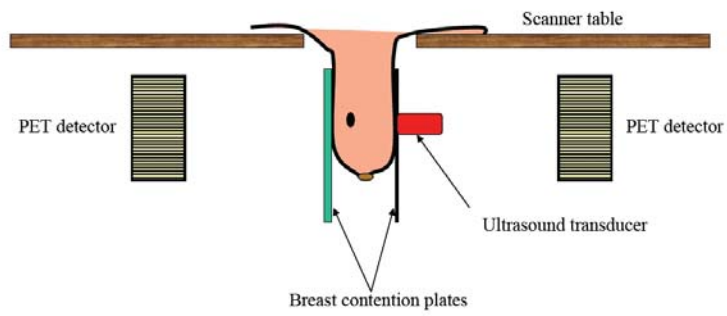


Figure 1.12: Examination of a breast with the ClearPEM-Sonic [31].

Bibliography

- [1] T. F. Budinger, K. M. Brennan, W. W. Moses, and S. E. Derenzo, Advances in Positron Tomography for Oncology. Nucl. Med. Biol. 23, 659 (1996)
- [2] W. W. Moses, S. E. Derenzo, T. F. Budinger, PET detector modules based on novel detector technologies. Nucl. Instr. Meth. A 353, 189 (1994)
- [3] M. Schmand, L. Eriksson, M. E. Casey, K. Wienhard, G. Flugge, R. Nutt, Advantages using pulse shape discrimination to assign the depth of interaction information (DOI) from a multi layer phoswich detector. IEEE Trans. Nucl. Sci. 46, 985 (1999)
- [4] A. Braem, M. Chamizo, E. Chesi, N. Colonna, F. Cusanno, R. De Leo, F. Garibaldi, C. Joram, S. Marrone, S. Mathot, E. Nappi, F. Schoenahl, J. Seguinot, P. Weilhammer and H. Zaidi, Novel design of a parallax free Compton enhanced PET scanner. Nucl. Instr. Meth. A 525, 268 (2004)
- [5] The CMS electromagnetic calorimeter project : Technical Design Report. CERN-LHCC-97-033
- [6] The LHC Study Group, The Large Hadron Collider, Conceptual Design. CERN/AC/95-05
- [7] R&D proposal for the study of new fast and radiation hard scintillators for calorimetry at LHC. Crystal Clear Collaboration, project RD 18, CERN / DRDC / P27 / 91-15 (1991)
- [8] P. Lecoq, I. Dafinei, E. Auffray, M. Schneegans, M. V. Korzhik, O. V. Mishevitch, V. B. Pavlenko, A. A. Fedorov, A. N. Annenkov, V. L. Kostylev, V. D. Ligun, Lead tungstate (PbWO_4) scintillators for LHC EM calorimetry. Nucl. Instr. Meth. A 365, 291 (1995)
- [9] A. A. Annenkov, M. V. Korzhik, P. Lecoq, Lead tungstate scintillation material. Nucl. Instr. Meth. A 490, 30 (2002)
- [10] G. Drobychev, E. Auffray, V. Dormenev, M. V. Korzhik, P. Lecoq, A. Lopatic, P. Nedelec, J.-P. Peigneux, D. Sillou, PWO crystals for CMS electromagnetic calorimeter: studies of the radiation damage kinetics. arXiv:physics/0504120v1

- [11] E. Auffray, D. Bouttet, I. Dafinei, J. Fay, P. Lecoq, J. A. Mares, M. Martini, G. Mazé, F. Meinardi, B. Moine, M. Nikl, C. Pedrini, M. Poulain, M. Schneegans, S. Tavernier, A. Vedda, Cerium doped heavy metal fluoride glasses, a possible alternative for electromagnetic calorimetry. Nucl. Instr. Meth. A 380, 524 (1996)
- [12] M. A. Schneegans, Cerium fluoride crystals for calorimetry at LHC. Nucl. Instr. Meth. A 344, 47 (1994)
- [13] A. G. Petrosyan, K. L. Ovanesyan, G. O. Shirinyan, M. V. Derzyan, T. I. Butaeva, C. Dujardin, N. Garnier, C. Pedrini, Growth of LuAP/LuYAP single crystals for PET applications. Radiat. Eff. Sol. 157, 943 (2002)
- [14] A. G. Petrosyan, G. O. Shirinyan, K. L. Ovanesyan, C. Pedrini, C. Dujardin, N. Garnier, S. Sowinski, P. Lecoq, A. Belsky, Potential of existing growth methods of LuAP and related scintillators. Nucl. Instr. Meth. A 486, 74 (2002)
- [15] C. Kuntner, E. Auffray, P. Lecoq, C. Pizzolotto, M. Schneegans, Intrinsic energy resolution and light output of the $\text{Lu}_{0.7}\text{Y}_{0.3}\text{AP}:\text{Ce}$ scintillator. Nucl. Instr. Meth. A 493, 131 (2002)
- [16] A. G. Petrosyan, K. L. Ovanesyan, G. O. Shirinyan, T. I. Butaeva, M. V. Derzyan, C. Pedrini, N. Garnier, C. Dujardin, L. A. Kamenskikh, LuAP/LuYAP single crystals for PET scanners: effects of composition and growth history. Opt. Mat. 24, 259 (2003)
- [17] C. Kuntner, E. Auffray, D. Bellotto, C. Dujardin, N. Grumbach, I. A. Kamenskikh, P. Lecoq, H. Mojzisoa, C. Pedrini, M. Schneegans, Advances in the scintillation performance of LuYAP:Ce single crystals. Nucl. Instr. Meth. A 537, 295 (2005)
- [18] J. Trummer, E. Auffray, P. Lecoq, A. Petrosyan, P. Sempere-Roldan, Comparison of LuAP and LuYAP crystal properties from statistically significant batches produced with two different growth methods. Nucl. Instr. Meth. A 551, 339 (2005)
- [19] A. G. Petrosyan, M. Derdzyan, K. Ovanesyan, P. Lecoq, E. Auffray, J. Trummer, M. Kronberger, C. Pedrini, C. Dujardin, P. Anfre, Properties of LuAP:Ce scintillator containing intentional impurities. Nucl. Instr. Meth. A 571, 325 (2007)
- [20] E. Auffray, P. Bruyndonckx, O. Devroede, A. Fedorov, U. Heinrichs, M. Korjik, M. Krieguer, C. Kuntner, C. Lartizien, P. Lecoq, S. Leonard, Ch. Morel, J. B. Mosset, Ch. Pedrini, A. Petrosyan, U. Pietrzyk, M. Rey, S. Saladino, D. Sappey-Marinier, L. Simon, M. Streun, S. Tavernier, J. M. Vieira, K. Ziemons, The ClearPET project. Nucl. Instr. Meth. A 527, 171 (2004)

-
- [21] K. Ziemons, E. Auffray, R. Barbier, G. Brandenburg, P. Bruyndonckx, Y. Choi, D. Christ, N. Costes, Y. Declais, O. Devroede, C. Dujardin, A. Fedorov, U. Heinrichs, M. Korjik, M. Krieguer, C. Kuntner, G. Largeron, C. Lartizien, H. Larue, P. Lecoq, S. Leonard, J. Marteau, Ch. Morel, J. B. Mosset, Ch. Parl, Ch. Pedrini, A. G. Petrosyan, U. Pietrzyk, M. Rey, S. Saladino, D. Sappey-Marini r, L. Simon, M. Streun, S. Tavernier, J. M. Vieira, The ClearPETTM project : development of a 2nd generation high-performance small animal PET scanner. Nucl. Instr. Meth. A 537, 307 (2005)
- [22] J.-B. Mosset, O. Devroede, M. Krieguer, M. Rey, J.-M. Vieira, J. H. Jung, C. Kuntner, M. Streun, K. Ziemons, E. Auffray, P. Sempere-Roldan, P. Lecoq, P. Bruyndonckx, J.-F. Loude, S. Tavernier, C. Morel, Development of an optimised LSO/LuYAP phoswich detector head for the ClearPET camera. IEEE Nucl. Sci. Sym. Conf. Rec. 4, 2439 (2004)
- [23] M. Streun, G. Brandenburg, H. Larue, E. Zimmermann, K. Ziemons, H. Halling, A PET system with free running ADCs. Nucl. Inst. Meth. A 486, 18 (2002)
- [24] P. Musmann, U. Pietrzyk, N. Schramm, S. Weber, List-Mode image reconstruction for the High Resolution ClearPET Neuro system. 2005 IEEE NSS-MIC Conference Record, 23.-29. Oct 2005
- [25] K. Ziemons, R. Achten, E. Auffray, A. Bauer, G. Brandenburg, P. Bruyndonckx, Y. Choi, J. Daemen, M. Dehnhardt, O. Devroede, M. Fleischer, L. Fuss, U. Heinrichs, A. Hollendung, M. Holschbach, M. Khodaverdi, P. Kirchner, H. Kleines, M. Krieguer, H. Larue, P. Lecoq, M. Leyendecker, R. Moeller, C. Morel, J.-B. Mosset, C. Parl, U. Pietrzyk, J. Schmitz, M. Streun, S. Tavernier, M. Veggian, E. Zimmermann, H. H. Coenen, H. Halling, R. Sievering, K. Zilles, The ClearPETTM neuro scanner: a dedicated LSO/LuYAP phoswich small animal PET scanner. IEEE Nucl. Sci. Sym. Conf. Rec. 4, 2430 (2004)
- [26] M. Rey, J.-M. Vieira, J.-B. Mosset, M. Moulin Sallanon, P. Millet, J.-F. Loude, C. Morel, Measured and simulated specifications of Lausanne ClearPET scanner demonstrator. IEEE Nucl. Sci. Sym. Conf. Rec. 4, 2070 (2005)
- [27] P. Sempere Roldan, E. Chereul, O. Dietzel, L. Magnier, C. Pautrot, L. Rbah, D. Sappey-Marini r, A. Wagner, L. Zimmer, M. Janier, V. Tarazona, G. Dietzel, Raytest ClearPETTM, a new generation small animal PET scanner. Nucl. Instr. Meth. A 571, 498 (2007)
- [28] P. Lecoq, J. Varela, Clear-PEM, a dedicated PET camera for mammography. Nucl. Instr. Meth. A 486, 1 (2002)
- [29] M. C. Abreu, D. Aguiar, E. Albuquerque, F. G. Almeida, P. Almeida, and 35 co-authors, Clear-PEM: A PET imaging system dedicated to breast cancer diagnostics. Nucl. Instr. Meth. A 571, 81 (2007)
- [30] D. W. Townsend, Multimodality imaging of structure and function. Phys. Med. Biol. 53, R1 (2008)

- [31] B. Frisch, ClearPEM-Sonic activities at CERN. Presentation, CCC meeting, Heidelberg, Germany; March 26th/27th 2008

Chapter 2

Scintillators

A scintillator is a substance that converts the energy deposited by an incoming electromagnetic wave or particle into a light pulse. The wavelength of the photons that are emitted during this process is usually in the visible range of the spectrum or in the near UV. A very useful property of scintillators is the dependence of the number of generated photons on the deposited energy: this permits a determination of the energy deposited by an incoming particle by measuring the light output of the scintillator. Conversion of the light pulse into an electronic signal is usually achieved by a PMT or APD. The following chapter provides a short review of the properties of inorganic solid scintillators and reviews the physical background of the scintillation process.

2.1 Inorganic scintillators

Scintillating materials can be inorganic or organic materials. According to their state of aggregation, they can be divided into three different groups:

- solids (crystals, glasses, powder, ...)
- liquids
- gases

The most important group of scintillators are inorganic solid scintillators. Due to their favorable properties, such as high stopping power and detection efficiency, they are widely used in high-energy physics and astrophysics, in dosimetry, and in medical applications to detect x-ray and γ -photons as well as high energy particles from radioactive sources, accelerators, or cosmic radiation. Many of these materials also have a high light output and reasonably short decay times what makes them appropriate materials for the use in applications which require good time resolution and photo statistics.

All known inorganic scintillating crystals can be categorized by their chemical composition (halides, oxides, chalcogenides) and their crystal structure (perovskites, glasses, ceramics, ...). A further distinction can be drawn by their

Table 2.1: Selected inorganic scintillators in medical imaging and high energy physics and their essential properties at room temperature. The light output is given relative to BGO.

Scintillator	Density [g/cm ³]	Light output [% BGO]	Peak emission λ [nm]	Decay time τ [ns]	Ref
NaI:Tl	3.67	390	415	230	[1]
CsI:Tl	4.51	700	560	1000	[2]
Bi ₄ Ge ₃ O ₁₂ (BGO)	7.13	100	505	300	[3]
PbWO ₄ (PWO)	8.28	4.4	420	15	[4, 5]
Lu ₂ SiO ₅ :Ce (LSO)	7.4	335	420	40	[2]
Lu _{2-x} Y _x SiO ₅ :Ce (LYSO)	7.1	390	420	40	[6, 7]
LuAlO ₃ :Ce (LuAP)	8.34	135	365	17 + 120	[2, 8]
Lu _{1-x} Y _x AlO ₃ :Ce (LuYAP)	7.1-7.4	180	365	20 + 250	[8]
CeF ₃	6.16	55	330	30	[4, 9]
LaBr ₃ :Ce	5.29	740	356 + 387	30	[10]

luminescence properties, i.e. if the luminescence is intrinsic or extrinsic. Table 2.1 provides a list of several inorganic scintillators commonly used in medical imaging and calorimetry.

2.1.1 Luminescence process

The scintillation process is based on the presence of luminescence centres in the crystal lattice. Such centres can originate either from the ions or molecules of the crystal lattice itself (intrinsic luminescence), or from defects or wanted and unwanted impurities in the lattice (extrinsic luminescence). Common to all these types of luminescent centres is that they introduce additional energy levels in the crystal which can be filled with electrons or holes.

A convenient model to describe the scintillation process is the collective electron or band theory introduced by Felix Bloch in 1928. It is based on the solution of the Schroedinger equation for an electron in a periodic potential. While the electrons of a single atom have discrete energy levels, the energy levels of a bound atom are significantly broadened due to perturbations induced by the interaction of the atom with its neighbors. This induces a continuous series of energy bands.

In ionic crystals, the band structure of the energy levels leads to the formation of an energy gap between the last occupied states, the valence band, and the first empty level, the conduction band (Fig. 2.1a). The width of this band gap depends on the composition of the crystal and its crystal structure, but is usually in the range of several eV. If an energy that is larger than the band gap energy is transmitted to one of the electrons in the valence band, it can move to the conduction band. Together with the empty position in the valence band, it forms an electron-hole pair. If the band gap is free of any additional energy levels, the electrons and holes start to interact with phonons and recombine in the valence band. This however changes if the band gap contains intrinsic or extrinsic energy levels (Fig. 2.1b): If these levels are unoccupied, they may be

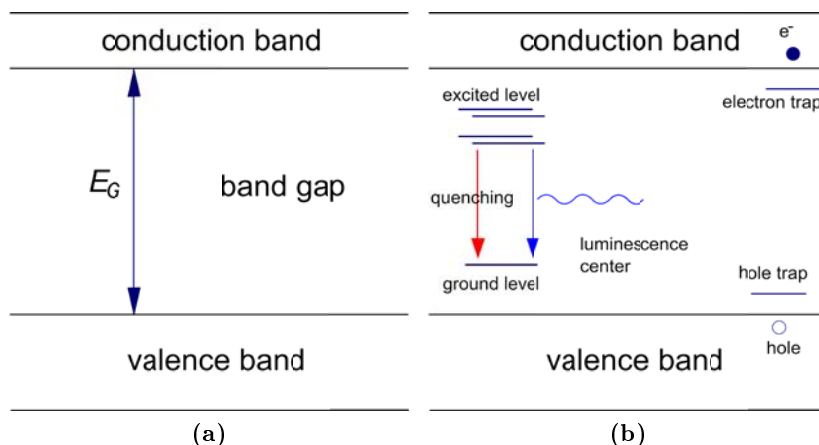


Figure 2.1: Energy band model of a crystal (a) without energy levels in the band gap (b) with energy levels in the band gap.

entered by electrons, holes, or excitons (i.e. bound states of electrons and holes).

Types of energy levels

Three different types of energy levels have to be distinguished: Luminescence centres, Quenching centres, and traps.

Luminescence centres are a prerequisite for most ionic crystals to exhibit scintillation. The transition from an excited state to the ground state occurs with the emission of a photon. The properties of the scintillator are defined by the nature of the luminescence centres. Depending on whether the luminescence centres are intrinsic or extrinsic, the luminescence process is called *intrinsic scintillation* or *extrinsic scintillation*. A middle course between these two types of scintillation is held by so-called *self-activated crystals*.

Quenching centres share several similarities with luminescence centres, however the transition from the energy level within the band gap to the valence band takes place non-radiatively through the emission of a phonon.

Traps are metastable levels within the band gap, i.e. centres with a very long lifetime compared to that of other types of centres. From these levels, trapped electrons can escape either to the conduction band by acquiring extra energy or fall back into the valence band without emitting a photon. For this reason, charge carriers that are trapped in deep traps are lost for the scintillation process. However, the effects of traps are not limited to the light output alone: while deep traps act mainly as passive sinks for mobile carriers, shallower traps may become active participants in the kinetic processes that govern the production of scintillation photons.

2.1.2 Energy absorption

An ionizing particle that interacts with a material loses energy by different fundamental processes that depend on the particle type and its energy. A measure of the strength of the interaction is the total energy loss per unit of length, $-(dE/dx)_{tot}$. This parameter can be determined by summing up the contributions of all mechanisms that are involved in the absorption process.

In the case of γ -radiation, $-(dE/dx)_{tot}$ is determined by

$$-\left(\frac{dE}{dx}\right)_{tot} = -\left(\frac{dE}{dx}\right)_{pheff} - \left(\frac{dE}{dx}\right)_{Compton} - \left(\frac{dE}{dx}\right)_{pair} - \left(\frac{dE}{dx}\right)_{phnucl}, \quad (2.1)$$

where $-(dE/dx)_{pheff}$, $-(dE/dx)_{Compton}$, $-(dE/dx)_{pair}$ and $-(dE/dx)_{phnucl}$ denote the energy loss by the photo effect, the Compton effect, pair production, and the emission of photonucleons, respectively. Which of these interaction processes dominates depends on the energy of the photon and the composition of the material.

The ability of a material to absorb an incoming γ -photon is often quantified by the attenuation coefficient μ of the material which is derived from the cross sections of all interaction processes. Using μ , the attenuation of a beam of γ -particles with initial intensity I_0 can be described by an exponential law of the form:

$$I(x) = I_0 e^{-\mu x} \quad (2.2)$$

An alternative expression of eq. 2.2 is

$$I(x) = I_0 e^{-\mu_m \rho x}, \quad (2.3)$$

where μ_m is the mass attenuation coefficient, $\mu_m = \mu/\rho$ and ρ the density of the material. At low and medium energies, μ and μ_m are mainly determined by photo absorption and Compton scattering, while at high energies they are dominated by pair production.

2.1.3 Generation of scintillation light

After the energy of the incident particle has been transferred to the material, several processes evolve that distribute the energy of the primary electrons and holes to other charge carriers and finally lead to the emission of scintillation light. In fact, it is possible to distinguish four essential phases of the scintillation process:

1. *Energy conversion*: relaxation of primary electrons and holes by the generation of secondary electrons and holes, photons, plasmons and other electronic excitations.
2. *Thermalization of the secondary electrons*: formation of electron-hole (e-h) pairs with an energy approximately equal to the band gap.

3. *Transfer to luminescence centres*: Energy transfer from the e-h pairs to the luminescence centres, formation of excitonic states and groups of excited luminescence centres.
4. *Photon emission*: radiative relaxation of excited luminescence centres.

Fig. 2.2 illustrates the elementary processes that take place in a scintillating crystal between the interaction of a primary or secondary particle with the electrons of the material and the emission of scintillation light. An incoming photon produces a primary electron together with a primary hole. The electron relaxes by producing a cascade of additional free electrons and holes, and by coupling on lattice vibration modes (phonons). In addition, it can interact with electrons in the valence band, producing collective oscillations of the electron continuum (plasmons) which in turn decay into electron-hole (e-h) pairs. The atom from which the primary electron has been released can itself relax by a sequence of nonradiative or radiative transitions, i.e. by the emission of Auger electrons or X-ray photons with characteristic shell energy. Both the photon and the Auger electron release their energy by creating more free electrons and holes. This avalanche process continues until the energy of the particles falls below the ionization threshold.

At the beginning of the thermalization stage, the cooled down electrons and holes begin to interact with phonons in the lattice. As the electrons lose energy during this process, they move down towards the lower boundary of the conduction band; likewise, the holes move up until they reach the top of the valence band. The e-h pair energy becomes then equal to the band-gap energy E_G of the crystal. As the total number of e-h pairs, N_{eh} , remains constant during this process, it can be assumed that

$$N_{eh} = \frac{E_\gamma}{bE_G} \quad (2.4)$$

where E_γ is the absorbed energy of the incident γ -photon and bE_G the energy that is required to create a thermalized e-h pair. b is a specific parameter that depends on the crystal structure and the type of chemical bonds in the material. For ionic crystals, $b \approx 1.5 - 2$, while for crystals with covalent bonding (as e.g. semiconductors), $b \approx 3 - 4$. This difference is a consequence of the less effective energy conversion in covalently bonded materials due to the greater likelihood of phonon emission.

The last two stages of the scintillation process include migration and localization of the electron, the energy transfer to the luminescence centres, and recombination. Electrons and holes that are produced at the end of the thermalization stage can be involved in the scintillation process in several ways. In the following, e and h denote electrons and holes, respectively, A an activator ion, ex an exciton, and $h\nu$ a photon:

1. $e + h \Rightarrow h\nu$

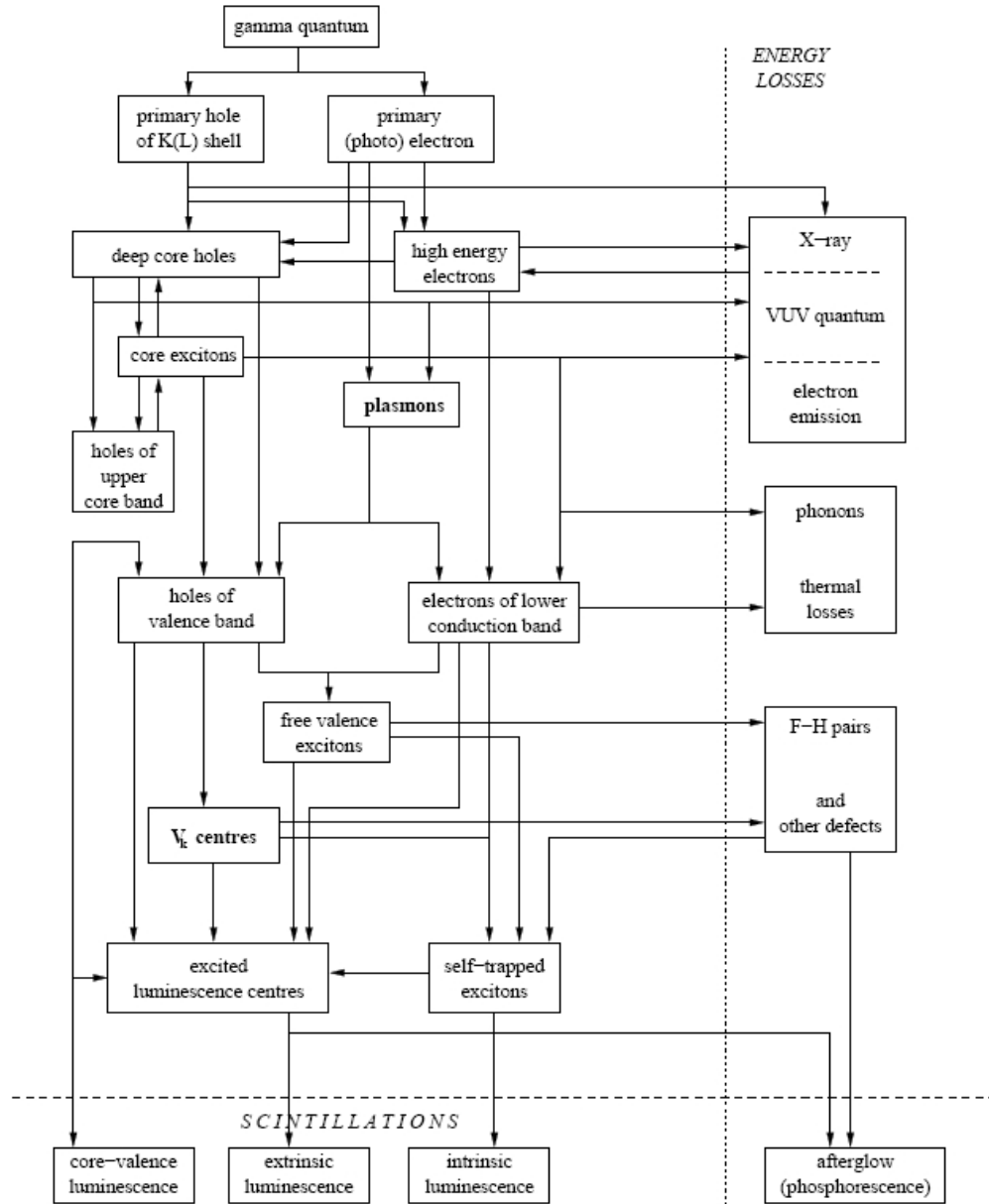


Figure 2.2: Elementary processes taking place in a scintillator [15].

2. $e + h \Rightarrow ex \Rightarrow h\nu$
3. $e + h + A \Rightarrow ex + A \Rightarrow A^* \Rightarrow A + h\nu$
4. $e + h + A \Rightarrow A^{1+} + e \Rightarrow A^* \Rightarrow A + h\nu$
5. $e + h + A \Rightarrow (A^{1-})^* + h \Rightarrow A + h\nu$
6. $A \Rightarrow A^* \Rightarrow A + h\nu$

The simplest emission process (1) results from the direct radiative recombination of free thermalized electrons in the conduction band with holes from the valence band or, from deeper electronic shells. Usually, this process takes place when the energies of the electron and the hole have sufficiently decreased so that they bind to each other and form an exciton. However, in materials as e.g. BaF₂, the electron can combine directly with a deep hole and a fast UV scintillation is observed. This latter kind of radiating recombination is also called *cross-luminescence*. The second process describes a radiative recombination where the thermalized carriers become bound in the lattice, e.g. by a specific atom or a structural defect, to form an autolocalized exciton which can then decay radiatively. This type of luminescence has so far only been observed in simple oxides. In process (3), the exciton luminescence becomes quenched by an activator ion A. After the energy of the exciton has been transferred to the activator ion, it can return to the ground state by photon emission. Two competing processes are the direct capture of free thermalized electrons (4) or holes (5) by the activator ion A, which in turn results in the subsequent formation of an excited state A*. The final process (6) denotes the direct excitation of activator ions by ionizing radiation. This process is especially important in heavily doped or self-activated crystals, as e.g. CeF₃, BGO or PWO.

Cerium-activated crystals

Rare-earth (RE) ions are the most frequently used activators in modern scintillators. This is mainly due to the parity-allowed 5d - 4f transition of several RE ions that is responsible for the fast decay time of many RE-doped compounds. The peak emission of this transition is usually in the UV or blue part of the spectrum [11]. Frequently used RE-ions are the divalent Eu²⁺ and the trivalent Nd³⁺, Pr³⁺ and Ce³⁺. As the experiments presented in this study were performed with the Cerium-activated oxides Lu_{1-x}Y_xAlO₃:Ce (LuYAP:Ce) and Lu_{2-x}Y_xSiO₅:Ce (LYSO:Ce), the emphasis in the following paragraphs is on the activation with Ce³⁺.

Cerium is, after Lanthanum, the RE element with the second lowest atomic number. The electron configuration of the ground state is [Xe].4f¹.5d¹.6s². Depending on the synthesis conditions, Ce can be localized in di-, tri- or tetravalent state. However, only the trivalent state (Ce³⁺) gives rise to bright luminescence, whereas Ce²⁺ and Ce⁴⁺ states lead to the creation of quenching centers. Clearly, the positioning of Ce ions in a trivalent site is preferred [12].

The energy level structure of the *free* Ce^{3+} ion is shown in Fig. 2.3. In this

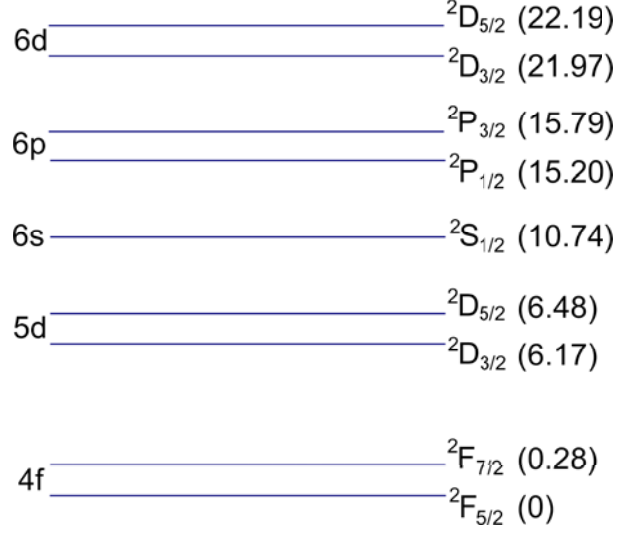


Figure 2.3: Energy-level structure of the free Ce^{3+} ion. Energy levels are in eV.

configuration, the Ce ion has a single electron in the $4f(^2F_J)$ state, and the excited states are $5d(^2D_J)$ and $6s(^2S_{1/2})$. The energy gap between the 4f ground state and the excited 5d states of the *bound* Ce^{3+} ion is lowered by the host material, but is usually in the range of a few eV. Due to spin-orbit interaction, the 2F_J ground and 2D_J excited states are split into two pairs of levels: $^2F_{7/2}$ and $^2F_{5/2}$ and $^2D_{5/2}$ and $^2D_{3/2}$, respectively. The separation between the levels is 2250 cm^{-1} for the F and 2500 cm^{-1} for D levels, what corresponds to respective energies of 0.28 eV and 0.31 eV. In crystals as LuAP with a low point symmetry at the Ce^{3+} sites, the excited 5d level is split into 5 Stark components by the crystal field and five 4f - 5d absorption bands are observed [13]. The stronger the crystal field is and the lower the symmetry, the splitting grows stronger, causing the lowest 5d level to be pushed towards the 4f ground state, which in turn lowers the wavelength of the luminescence. In crystals with higher local symmetry of Ce^{3+} , as LSO, only three Stark levels are present. Usually, not all these energy levels can be resolved at room temperature [14].

The accepted mechanism of scintillation in Ce-doped crystals is radiative recombination: the Ce^{3+} ion first captures a hole to become Ce^{4+} , which upon subsequent capture of an electron returns to an excited Ce^{3+} state. Return to the ground state is then achieved by emission of a photon which originates from transitions between the lowest 5d level and the $^2F_{7/2}$ and $^2F_{5/2}$ levels of the 4f ground state. The main non-radiative processes that compete with this transition are recombinations of e-h pairs via deep centers and trapping. As the outer 5s and 5d shells shield the 4f electron, the splitting between the two 2F_J states of the Ce^{3+} ion is only small and typically in the range of a few hundredth of an eV.

In addition to the Ce^{3+} ions, Ce^{4+} ions can be present in the crystal. Ce^{4+}

has no electron in the 4f shell but can be excited through a charge transfer process after capture of a valence electron. The resulting charge transfer state can be described as a Ce^{3+} ion with a hole in the valence band ($\text{Ce}^{3+} + h\nu$), which will nonradiatively relax to the ground state. Because this is a competing process to the radiative de-excitation of Ce^{3+} , the presence of Ce^{4+} nonradiative centers has to be avoided in Ce-doped crystals.

The efficiency of Ce^{3+} as an activator is mainly governed by the width of the band gap of the host material. In crystals with a wide band gap, such as LuAP, the excited levels of the Ce^{3+} ions fall into the band gap and the scintillation can be very efficient. If, on the other hand, the band gap of the scintillator is relatively narrow, the excited levels of the Ce^{3+} ions can fall into the conduction band and quench the Ce^{3+} luminescence. An exception of this rule is LSO: this material exhibits a fast and efficient scintillation although the band gap is rather narrow and the excited 5d levels are not well separated from the conduction band [15]. Other parameters that determine the quantum efficiency of Ce-doped crystals are the Cerium-anion bond type, the relation between ionizing potentials of Cerium and host cations, and the structural properties of the host crystal.

2.1.4 Light loss mechanisms

As eq. 2.4 indicates, only a fraction of the energy deposited by an incoming particle in the scintillator will be converted into thermalized e-h pairs. As a consequence, the number of photons generated during a particle event will always be smaller than expected alone from the energy transferred to the scintillator. Additional losses that further reduce the number of generated photons are the capture of free electrons and holes in traps and the non-radiative relaxation of the luminescence centres by the emission of phonons. After photon emission, the number of scintillation photons is further reduced by absorption processes in the crystal bulk. In the following, the most important loss mechanisms are shortly reviewed.

Thermal quenching

The term quenching describes the effect of the de-excitation of a luminescence centre without photon emission. The physical processes that lead to quenching can be understood by a configuration coordinate diagram in which the potential energies of the ground and excited states of a luminescence center are plotted vs. a configuration coordinate Q , where Q is the mean distance between the luminescence center and the neighboring ions in the crystal lattice. Fig. 2.4 shows such a diagram for the simple model of a harmonic oscillator. The potential energies of ground and excited state of the ion are represented as parabolic curves and the horizontal lines correspond to vibration levels of the nearby ions or phonons. The arrows indicate the optical transitions with maximum probability.

In general, the equilibrium positions of the ground and excited states (i.e.

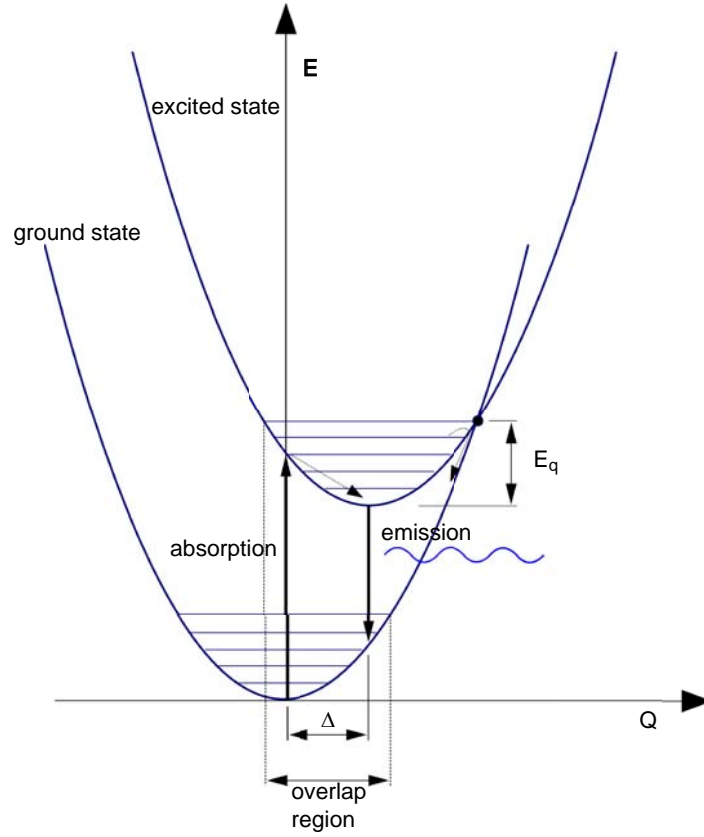


Figure 2.4: Configuration coordinate diagram for a luminescence center. The ground and excited states are represented by overlapping potential curves.

the minima of the curves) will be separated along the Q axis by an amount Δ which depends on the electron-phonon coupling in the crystal. As a consequence, there is a shift observed between the emission and absorption bands of the center. This shift is also called *Stokes shift*. If an excited electron acquires a thermal energy E_q (which corresponds to the energy difference between the curve minimum and the crossing point of the two parabolas), the electron can de-excite by creating a cascade of phonons and thermal quenching takes place.

For a given temperature T , the quantum efficiency q of a luminescence center can be expressed by the radiative and non-radiative transition probabilities p_r and p_{nr} . As only p_{nr} is temperature-dependent, $q(T)$ can be written as

$$q(T) = \frac{p_r}{p_r + p_{nr}} = \frac{1}{1 + C \cdot e^{-\frac{E_q}{k_B T}}}, \quad (2.5)$$

where k_B is the Boltzmann constant, $k_B = 1.38 \cdot 10^{-23} \text{ J} \cdot \text{K}^{-1}$, and C a quenching constant.

Eq. 2.5 implies that non-radiative transitions become increasingly important with increasing temperature. This can be observed by a decrease of the light yield and the decay time of the luminescence center with rising temperature. The temperature dependence of the light yield can be described by a parameter τ , which is given as the ratio

$$\tau = \frac{q(T)}{q(T_0)} = \frac{1 + C \cdot e^{-\frac{E_q}{k_B T_0}}}{1 + C \cdot e^{-\frac{E_q}{k_B T}}}. \quad (2.6)$$

$q(T_0)$ corresponds to the quantum efficiency of the luminescence center at a reference temperature T_0 . As follows from Fig. 2.4, crystals with a large Stokes shift have an increased probability of large thermal quenching at room temperature. Two examples for such behavior are the scintillators BGO and PWO which show a decrease in light yield of 1.5%/°C and 2%/°C, respectively [15, 16].

Concentration quenching

The probability of an interaction between individual luminescence centres increases with the dopant concentration in the lattice. Energy can be transferred from centre to centre until it is lost in a quenching centre. This type of quenching becomes relevant at a concentration above a few atomic percent of dopant ions in the crystal.

Absorption

In an ideal scintillator, the scintillation photons can propagate through the crystal without being absorbed by the host material. However, a real crystal always contains impurities or defects which can absorb these photons. How large this background absorption is depends on the impurity concentration of the material. Background absorption can be reduced by careful control of the crystal growth environment, by using raw materials of high purity and an appropriate crucible material, and a stable temperature.

Besides background absorption, also re-absorption by the luminescence centres themselves can take place. This effect does not decrease the light yield significantly as the major part of the re-absorbed photons becomes re-emitted again; however it leads to an increase of the decay time of the crystals. As can be seen from Fig. 2.4, this type of absorption is connected with the overlap between the ground and excited states and therefore, with Δ . As a consequence, it becomes less important with increasing displacement from the equilibrium position as the overlap between the absorption and emission bands is then smaller.

Radiation damage

Ionizing radiation can create various types of defects that change the optical and fluorescent properties of the material. The deterioration of the material properties results mainly from a degradation of the optical transmission which

is related to the production of colour centers. Such colour centers are created by the trapping of electric charges by crystal defects. Their formation is, in turn, correlated with the presence of inhomogeneities in the crystal, as structural defects and impurities [17]. Other radiation-induced effects involve [15]: quenching of luminescence centers due to valence changes or compensatory ion diffusion, reduction of the energy transfer efficiency, the emergence of afterglow due to the creation of shallow traps, and induced radioactivity.

The resistivity of scintillators against radiation can be improved by increasing the purity of the raw materials or by the addition of isovalent and isomorphous dopants to the melt. Radiation damage can also be partially healed; while some crystals exhibit a slow recovery rate already at room temperature, others can be annealed either by thermal bleaching at $200 - 350^\circ$, or by irradiation with UV or visible light. With the latter two methods, almost full recovery can be achieved for many materials.

2.2 General characteristics of inorganic scintillators

2.2.1 Conversion efficiency and absolute light yield

The *intrinsic* or *absolute light yield* of a scintillator is dependent on the band gap energy E_G and on the efficiency by which the energy of an incident gamma photon is converted into scintillation photons. According to [18], the conversion efficiency η of the scintillation process can be expressed by the following relation:

$$\eta = \beta S Q, \quad 0 \leq \eta, \beta, S, Q \leq 1 \quad (2.7)$$

The three parameters β , S , and Q characterize the three consecutive steps in which, as mentioned in Sect. 2.1.3, the scintillation process can be conveniently divided: energy conversion, energy transfer, and luminescence.

Using eqs. 2.4, the energy conversion efficiency β is found to be:

$$\beta = \frac{1}{b} = \frac{N_{eh}}{N_{eh,max}} \quad (2.8)$$

$N_{eh,max}$ is the number of electron-hole pairs that would be generated in absence of any losses to phonons (i.e. for $b = 1$) and is given by E_γ/E_G .

The second parameter in eq. 2.7, S , specifies the efficiency of the energy transfer from the e-h pairs to the luminescence centres. The third parameter, Q , is called the luminescence efficiency or quantum efficiency of the luminescence center, i.e. the probability that de-excitation takes place by the emission of a photon. The number of photons generated by a single γ -particle N_{ph} will then be:

$$N_{ph} = N_{eh,max} \cdot \eta = \frac{E_\gamma}{bE_G} \cdot S Q \quad (2.9)$$

Using eq. 2.9, the *absolute light yield* LY_{abs} (i.e. the number of photons created per MeV) can finally be expressed as:

$$LY_{abs}[\text{ph/MeV}] = \frac{N_{ph}}{E_{\gamma}[\text{MeV}]} = \frac{SQ}{bE_G[\text{MeV}]} \quad (2.10)$$

Both E_G and Q can be assessed by direct measurements via optical spectroscopy. β can be derived from the energy loss ratio K , which relates the energy lost by the production of phonons to the energy lost by ionization [18] and can be assessed by Monte-Carlo simulations of the energy dissipation in crystals [19, 20]. The energy transfer efficiency S , which is the only parameter that cannot be determined directly, can be derived from eq. 2.10 if LY_{abs} and all other parameters are known.

Because Q is close to unity for the majority of materials, the parameters that determine LY_{abs} are mainly the conversion efficiency β and the transfer efficiency S . Although β may be low because of high energy losses due to the production of phonons, it is in most cases the factor S which significantly lowers the light yield [21]. This, in turn, means that for many materials the energy transfer from e-h pairs to the luminescence centres is a rather ineffective process.

From eq. 2.10, it follows that the absolute light yield should rise to large values for vanishing band gap energies E_G . However, this is impractical as the risk of photo-ionization of the activator increases if its ground or excited states are too close to the valence or conduction bands. The density of traps in the forbidden band will also increase what results in further quenching. Furthermore, crystals with narrow band gaps usually belong to the covalent type and have a relatively low β .

2.2.2 Light collection efficiency and measured light output

As mentioned before, the absolute number of photons that are produced per MeV in the crystal is given by eq. 2.10. However, the light output *measured* in an experiment will always be smaller than LY_{abs} . This signal loss is due to several processes. Some scintillation photons are absorbed in the host material before they can be detected. Other photons may escape from the crystal through one of the faces not connected to the photo detector. The latter process can be avoided by enveloping the crystal with reflective or diffusing materials, which however induce additional losses by absorption. Further losses arise from the fact that not all photons that arrive at the face coupled to the PMT will enter the PMT due to mismatch of the refractive indices of crystal, PMT and optical coupling. This is especially the case for heavy inorganic scintillators which often exhibit a high refractive index. In addition, only a fraction of the photons that arrive at the photo detector will be transformed into photoelectrons and produce a signal in the sensor.

It is convenient to express all factors that govern the transport of the scintillation photons to the photo detector by a single parameter η_L which is called

light collection efficiency. This includes the absorption properties of the crystal at the wavelength of emission, reflections and scattering from the surfaces and the enveloping material, the size and shape of the crystal, the efficiency of photon transportation from the scintillator to the photo detector, and the transmission and reflection properties of the photo detector itself. η_L is given by the ratio between the number of photons arriving at the sensitive medium of the photo detector $N_{ph,det}$ and the number of generated photons N_{ph} (eq. 2.9):

$$\eta_L = \frac{N_{ph,det}}{N_{ph}} \quad (2.11)$$

Using eqs. 2.10 and 2.11, the *light output* or *effective light yield* LY of the scintillator, i.e. the number of photons per MeV arriving at the sensitive surface, can be expressed as:

$$LY[\text{ph/MeV}] = \frac{N_{ph,det}}{E_\gamma[\text{MeV}]} = \eta_L \cdot \tau \cdot LY_{abs}, \quad (2.12)$$

where τ was defined in eq. 2.6.

To determine the number of photoelectrons or electron-hole pairs N_{pe} generated in the photodetector by the incoming photons, it is necessary to account for the efficiency of the transformation of photons into charge carriers. If this efficiency is expressed by the *quantum efficiency* q of the photo detector, N_{pe} can be expressed as:

$$N_{pe}[\text{pe/MeV}] = \epsilon \cdot q \cdot LY = q_{eff} \cdot LY \quad (2.13)$$

ϵ denotes the collection efficiency of the photo detector regarding the generated photoelectrons or electron-hole pairs and q_{eff} the effective quantum efficiency of the photodetector, $q_{eff} = \epsilon \cdot q$. Therefore, eq. 2.13 determines the number of photons that are converted into an electronic signal by the detector.

2.2.3 Non-proportionality of energy response

One basic assumption for all scintillation counters is that the light output is proportional to the energy absorbed by the crystal. However, some scintillating crystals exhibit a distinctly non-proportional behaviour in certain energy regions. Examples for this are LSO and NaI:Tl which both show a significant decrease of the relative light output at low energies [15, 22]. Other scintillators, as YAP or LuAP, exhibit only weak non-proportionality [15, 22, 23]. Following Dorenbos [11], the degree of non-proportionality can be parametrized by the standard deviation

$$\sigma_{np} = \sqrt{\frac{1}{N} \sum_{i=1}^N \left(\frac{LY(E_i)}{LY(662)} - 1 \right)^2} \quad (2.14)$$

where N corresponds to the number of energies that have been taken into account and $LY(E_i)$ and $LY(662)$ refer to the effective light yields (in photons/MeV) at energies E_i and 662 keV, respectively. Fig. 2.5 shows the values

of σ_{np} for several common scintillators.

The physical explanation for non-proportionality is the statistical nature of the processes that generate secondary particles. For example, discontinuities of the

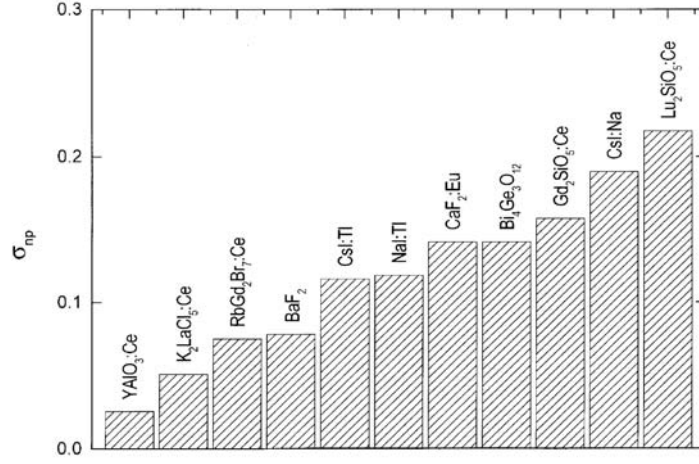


Figure 2.5: Degree of non-proportionality for several common scintillators [11].

relative light output are often observed near the K and L band energies of the scintillator atoms. Although different theories have been proposed and investigated [24, 25, 26], at present it is still impossible to predict the response function of any given material.

2.2.4 Energy Resolution

The energy resolution that can be achieved in any scintillation measurement is influenced by a number of contributions. According to Birks [27], the mean output pulse per photon of a PMT, $\overline{Q_0}$, is determined by the following equation:

$$\overline{Q_0} = \overline{N} \cdot \overline{p} \cdot \overline{M} \quad (2.15)$$

\overline{N} is the mean number of photons created in the scintillator, \overline{M} is the overall gain of the photo detector, and \overline{p} the mean photon transfer efficiency, i.e. the probability that a scintillation photon produces an electron at the first dynode:

$$\overline{p} = g_c \cdot C_{pe} \cdot G, \quad (2.16)$$

Where G is the fraction of N photons that impinge on the photocathode, C_{pe} the conversion efficiency of the photons into electrons, and g_c the collection efficiency of the electrons at the first dynode.

The energy resolution $R = (\Delta E/E)_{FWHM}$ is related to the fractional variance of Q_0 , $v(Q_0)$, by

$$R = \left(\frac{\Delta E}{E} \right)_{FWHM} = 2.36 \cdot \sqrt{v(Q_0)} \quad (2.17)$$

$v(Q_0)$ can be expressed as

$$v(Q_0) = v(p) + [1 + v(p)] \left[v(N) - \frac{1}{\bar{N}} \right] + \frac{1 + v(M)}{\bar{N}\bar{p}} \quad (2.18)$$

or, in first approximation,

$$v(Q_0) \approx \left[v(N) - \frac{1}{\bar{N}} \right] + v(p) + \frac{1 + v(M)}{\bar{N}\bar{p}} \quad (2.19)$$

The term in square brackets in eq. 2.19 represents the deviations of the number of photons from the Poisson statistics. $v(p)$ is the variance of the transfer process of the photons from the scintillator to the photomultiplier. The last term, $v(M)$, is the variance of the PMT gain.

By introducing the terms *intrinsic resolution* R_i , *transfer resolution* R_p , and *photomultiplier resolution* R_M , the energy resolution can be expressed as

$$R^2 = R_i^2 + R_p^2 + R_M^2 \quad (2.20)$$

As follows from eq. 2.17, the intrinsic resolution R_i is equal to 2.36 *times* the square root of the bracketed term in eq. 2.19. Accordingly, R_p and R_M can be derived in the same manner from the transfer and gain variances.

The intrinsic resolution R_i can be split into two main contributions. One is associated with the non-proportional response of the scintillator to secondary electrons of different energy and the second to inhomogeneities of the crystal causing different light yields at different interaction points of the crystal. Expressing these two contributions by the variables R_{se} and R_{inh} , the intrinsic resolution can be written as

$$R_i^2 = R_{se}^2 + R_{inh}^2 \quad (2.21)$$

The transfer resolution R_p is influenced by a number of factors, including the photon wavelength, the effective quantum efficiency of the PMT, the optical properties of the scintillator, the incidence angle of the photon on the photocathode, and the properties of the photocathode itself. For modern scintillation counters, it can be assumed that R_p is negligible compared to R_i and R_M . Thus, eq. 2.20 becomes

$$R^2 = R_i^2 + R_M^2 \quad (2.22)$$

where R_M can be expressed as

$$R_M = 2.36 \cdot \sqrt{\frac{1 + v(M)}{\bar{N}\bar{p}}} \quad (2.23)$$

The resolution of a scintillation counter depends therefore on the intrinsic resolution of the scintillator R_i , the number of photoelectrons $\bar{N} \cdot \bar{p}$ and the variance of the PMT gain, $v(M)$. In turn, eq. 2.23 expresses the fundamental limit of the energy resolution of a scintillation counter, i.e. the energy resolution

under the limit of a negligible intrinsic resolution R_i .

Fig. 2.6 shows the energy resolution of several common inorganic scintillators for $E_\gamma = 662$ keV. The black curve indicates the fundamental limit of the energy resolution for $v(M) = 0.1$ [11].

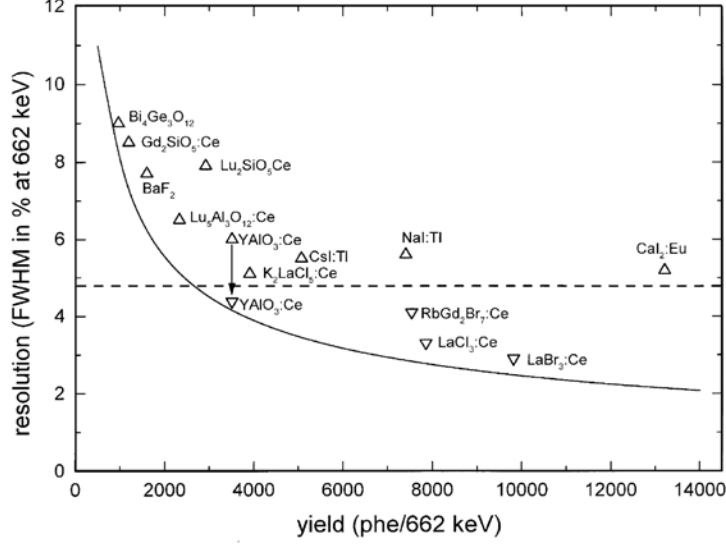


Figure 2.6: Energy resolution of several common scintillators [11].

2.2.5 Decay time

The decay time of a scintillator is defined as the time interval between the excitation of the crystal and the emission of the scintillation light. If only one type of luminescence center exists in the crystal, the decay is exponential with only one time constant, i.e. the intensity of the scintillation light at any moment $I(t)$ is given by (in photons/s):

$$I(t) = I(0)e^{-\frac{t}{\tau}} \quad (2.24)$$

τ is the decay time constant. Real scintillators usually exhibit a finite rise time and often more than one time constant. Such a behaviour is generally observed when secondary luminescence centres with delayed decay are present. The decay curve can then be described as the sum of the individual exponential decays with their individual time constants τ_i :

$$I(t) = \sum_i I_i(0) \cdot e^{-\frac{t}{\tau_i}} - I_1(0) \cdot e^{-\frac{t}{\tau_{rise}}} \quad (2.25)$$

τ_{rise} is the time constant of the rise time. The finite rise time is related to the fact that the excitation energy is first concentrated in traps and is transferred only after some delay to the luminescence centres. In reality, the situation is

very often even more complex and the time dependence of the light emission is strongly non-exponential.

The decay time constant τ is governed by the decay rate constants of radiative and non-radiative processes,

$$\tau^{-1} = \tau_R^{-1} + \tau_{NR}^{-1} \quad (2.26)$$

As these two processes act in sequence, the decay time of the luminescence will be mainly determined by the slower process. While the decay time of non-radiative processes does not exhibit any fundamental physical limit and can therefore be extremely rapid, the radiative decay time τ_R (and therefore the minimum achievable decay time τ) is limited by [18]:

$$\tau_R^{-1} = 1.5 \cdot 10^{-5} \cdot \frac{9\lambda^2}{f \cdot (n^2 + 2)^2 \cdot n} \quad (2.27)$$

λ is the transition wavelength, n the refractive index of the material, and f the oscillator strength of the transition from one quantum state to another.

Eq. 2.27 shows that the decay time decreases with decreasing λ and increasing n . For this reason, scintillators that emit in the violet or UV range of the spectrum are usually faster than scintillators that emit at larger wavelengths. By introducing non-radiative transitions, the decay time can even be decreased beyond this limit, although with the drawback of a degradation of the light output. An example for such behaviour is PWO whose fast decay is a consequence of the strong thermal quenching of the crystal light [28].

2.2.6 Afterglow

Many scintillators exhibit a long-time luminescence that lasts up to several microseconds and more. The origin of this delayed emission is phosphorescence which is due to the thermal release of charge carriers from traps. These traps are formed by impurities and defects introduced during crystal fabrication or by irradiation. The afterglow itself is defined as the amplitude of this phosphorescence at a fixed point of time after irradiation, e.g. $10 \cdot \tau_{rad}$. A prominent example of a crystal that exhibits considerable afterglow at room temperature is LSO.

2.2.7 Time resolution

The time resolution of a scintillator is defined as the smallest possible time span for which two consecutive scintillation pulses can be resolved. It is directly proportional to the square root of the decay time constant τ and indirectly proportional to the square root of the effective light yield:

$$\Delta t \propto \sqrt{\frac{\tau}{N_{ph}}} \quad (2.28)$$

Other factors that affect the time resolution of a scintillation detector are the geometry and shape of the crystal and the rise time. In the case of very fast scintillators, the time resolution of the readout electronics also needs to be taken into account.

2.2.8 Refractive index and transmission

The main optical characteristics of a scintillator are its transmission and its index of refraction. For an isotropic crystal, the *refractive index* N is a complex number depending only on the wavelength λ ,

$$N(\lambda) = n(\lambda) - ik(\lambda) \quad (2.29)$$

The imaginary part of the refractive index k is also called *extinction coefficient*. Using k , the *absorption coefficient* α_{abs} can be defined as

$$\alpha_{abs} = \frac{4\pi k}{\lambda} = \frac{1}{\lambda_{abs}}, \quad (2.30)$$

where λ_{abs} is also termed *absorption length*. In an anisotropic medium, the refractive index depends on the orientation of the electric field \vec{E} relative to the optical axis of the crystal. In a uniaxial birefringent medium, N can be represented by an index ellipsoid where two of the three principal axes are identical. The identical axes correspond to the ordinary refractive index N_{ord} while the third axis corresponds to the extraordinary refractive indices N_{ext} (Fig. 2.7). Assuming a plane wave that enters the medium at an angle β relative

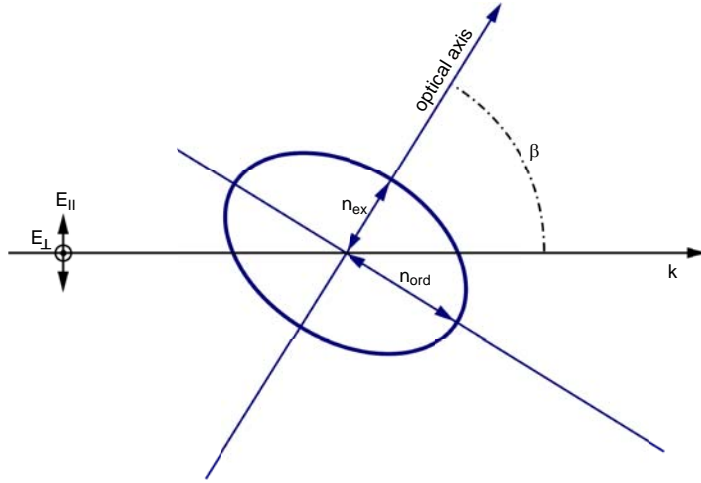


Figure 2.7: Ordinary and extraordinary refractive index in an uniaxial birefringent medium.

to the optical axis, the component of \vec{E} that lies in the plane containing the optical axis (\vec{E}_{\parallel}) will experience a mixed refractive index given by

$$N_{mix} = N_{ord} \cdot \sqrt{\sin^2 \left(\frac{\pi}{2} - \beta \right) + \frac{N_{ext}^2}{N_{ord}^2} \cos^2 \left(\frac{\pi}{2} - \beta \right)} \quad (2.31)$$

while the orthogonal component \vec{E}_\perp will experience only a refractive index N_{ord} . Accordingly, \vec{E}_\parallel is called *extraordinary ray* and \vec{E}_\perp *ordinary ray*.

In a medium that is biaxial birefringent, all three principal axes of the index ellipsoid are of different length. In this case, the notation N_α , N_β and N_γ is used for the three refractive indices.

In a transparent optical medium with $k \ll n$, the wavelength dependence of n can be described by the Sellmeier formula

$$n^2(\lambda) = 1 + \sum_j \frac{B_j \lambda^2}{\lambda^2 - C_j} \quad (2.32)$$

The Sellmeier coefficients B_j and C_j are determined empirically from dispersion curves of the medium. Typically, an abbreviated version of eq. 2.32 is used:

$$n^2(\lambda) = 1 + \frac{B_1 \lambda^2}{\lambda^2 - C_1} + \frac{B_2 \lambda^2}{\lambda^2 - C_2} + \frac{B_3 \lambda^2}{\lambda^2 - C_3} \quad (2.33)$$

The transmission of a medium is determined by n and the *attenuation coefficient* α_{att} , which is given by the sum of the absorption coefficient α_{abs} and the *scattering coefficient* α_{scat} of the material:

$$\alpha_{att} = \alpha_{abs} + \alpha_{scat} \quad (2.34)$$

In the following, an isotropic medium with refractive index n_2 and extinction coefficient $k_2 \ll n_2$ is assumed to be embedded in a second medium with refractive index n_1 and $k_1 = 0$. A plane wave that falls onto the boundary between the two media at normal incidence is split into a transmitted wave and a reflected wave. The transmittance and the reflectance of the plane wave are determined by n_1 and n_2 and given by

$$t = 1 - r \quad r = \left| \frac{n_1 - n_2}{n_1 + n_2} \right|^2 \quad (2.35)$$

Equivalent expressions are obtained if one or both media are uniaxial or biaxial birefringent. The transmitted wave now moves through medium 2 until it reaches the second interface. Due to the non-zero absorption coefficient of medium 2, the intensity of the wave is thereby reduced by a factor $\exp(-\alpha_{att}d)$, where d denotes the distance between the entry and exit faces. As both t and r are independent on the direction of wave propagation, i.e. whether the wave arrives from medium 2 and enters medium 1 or vice versa, the fraction of light that is reflected and transmitted at the exit face is again given by eq. 2.35. While the transmitted wave leaves medium 2 (and eventually hits a photo detector), the reflected wave travels back to the entry face and is again split into a transmitted and a reflected wave, and so forth (Fig. 2.8). The overall transmittance T is determined by the sum of all contributions [29],

$$\begin{aligned} T &= t^2 \cdot e^{-\alpha_{att}d} + t^2 \cdot r^2 \cdot e^{-3\alpha_{att}d} + t^2 \cdot r^4 \cdot e^{-5\alpha_{att}d} \\ &= t^2 \cdot e^{-\alpha_{att}d} \sum_k r^{2k} \cdot e^{-2k\alpha_{att}d} = \frac{t^2 \cdot e^{-\alpha_{att}d}}{1 - r^2 \cdot e^{-2\alpha_{att}d}} \end{aligned} \quad (2.36)$$

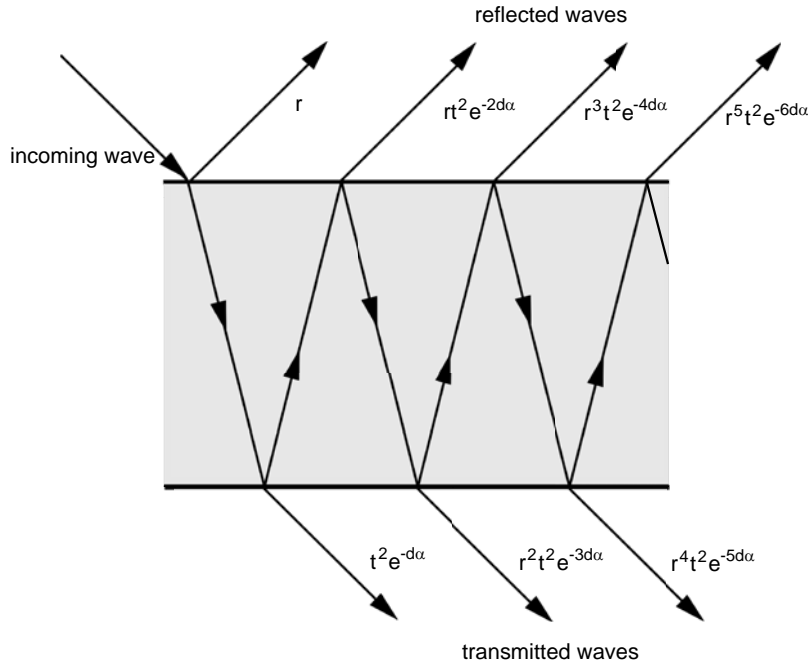


Figure 2.8: Contributions to T and R at quasi-normal incidence.

Correspondingly, the reflectance R is given as

$$R = r + \frac{r \cdot t^2 \cdot e^{-\alpha_{att}d}}{1 - r^2 \cdot e^{-2\alpha_{att}d}} \quad (2.37)$$

As eqs. 2.36 and 2.37 indicate, the reflectance and transmittance of a material are functions of the refractive index of the material, its attenuation length, and the sample dimensions. Performing transmittance measurements on two differently sized blocks of the same material makes it therefore possible to determine both the refractive index and the attenuation coefficient of the material.

An important parameter of any transmission curve is the cut-off wavelength λ_c which is defined as the turning point of the rising edge of the transmission curve. In the case of crystals free of impurities, λ_c is related to the band gap energy E_G by

$$E_G = \frac{hc}{\lambda_c} \quad (2.38)$$

In the case of doped crystals, as e.g. LuAP and LSO, the cut-off of the transmission curve originates from the dopant itself and eq. 2.38 is no longer valid.

2.3 Requirements for scintillators in high energy physics and PET

As mentioned at the beginning of this chapter, scintillators are used in a wide variety of industrial and scientific applications. It is therefore not surprising that the requirements which the scintillator has to fulfill differ considerably from application to application. Following [15], the most important parameters that determine the properties of a scintillator and possible fields of application are:

- effective light yield and energy resolution;
- decay time and afterglow;
- density and stopping power;
- scintillation wavelength;
- transparency for its own light and index of refraction;
- hardness, ruggedness and cleavage;
- radiation hardness.

Other important properties that have to be considered include hygroscopicity, the amount of non-proportionality and thermal quenching, homogeneity and uniform distribution of dopants and other impurities, and costs of raw materials and fabrication process. Clearly, there is no material that meets all criteria for an application and a compromise between the individual requirements has to be found.

2.3.1 High energy physics

Density

The most important requirement for a HEP calorimeter is that it allows for the distinction between electrons and pions. This requires the ratio between the radiation length X_0 (eq. 1.4) and the interaction length for hadronic interactions λ_a to be as small as possible. As $X_0 \propto A/Z^2$ and $\lambda_a \propto A/Z$, a small ratio X_0/λ_a is achieved for materials with a large effective Z . Since in addition, X_0 is approximately inversely proportional to the crystal density ρ , a scintillator with high ρ and large Z_{eff} makes the construction of compact and efficient calorimeters possible. A material with high density also exhibits a reduced lateral shower size, which is given by the Moliere radius $R_M \approx X_0 \cdot (Z_{eff} + 1.2)/37.74$. An small lateral shower size, in turn, limits the contamination of the energy measurement by other particles from the same or other events, increases the positional resolution of the detector and improves the rejection of particles that add to the background of unwanted events. Moreover, a compact material will reduce the lateral spread of the shower in a high-magnetic environment.

Decay time and effective light yield

An important criterium for a scintillator to be used in a HEP application at LHC is a short decay time < 30 ns to allow for large bunch-crossing time rates. On the other hand, a high effective light yield is not necessary as the energy deposited in the crystals (and therefore the number of produced photons) is in general very high. Regarding materials, intrinsic scintillators are preferred as it is easier to control the light yield uniformity in such crystals. Materials that exhibit considerable afterglow or a strong temperature dependence of the light output should in general be avoided. Moreover, the crystals must show a linear energy response over a large dynamic range.

Radiation hardness

Two additional important criteria in LHC HEP applications are the radiation hardness and the cost effectiveness of the scintillator. The high nominal luminosity of the LHC displays challenging demands on the materials used in the particle detectors. As an example, the crystals and electronics used for the electromagnetic calorimeters in the CMS and ALICE detectors have to endure a dose rate of 1-2 kGy/year. A good radiation resistance is therefore necessary to ensure transparency of the scintillators during the expected lifetime of the experiments.

Cost effectiveness

The large volumes of calorimeters restrict the selection to candidate materials that can be produced for a reasonable price. Important factors are the cost of the raw materials (materials and elements used, purity) and the cost of the production itself (growing technique, crucible material, energy consumption).

2.3.2 PET

Density and atomic number

As in HEP applications, crystals utilized for PET detectors should have a high density to ensure a high stopping power. A large Z_{eff} is also here preferred, as it guarantees that the photoelectric fraction ($\propto Z_{eff}^4$) at the maximum photon energy of 511 keV is increased relative to the Compton scattering fraction ($\propto Z_{eff}$). This is important as Compton scattered quanta can leave the crystal and induce a signal in neighboring crystals, which deteriorates the position resolution of the detector [30]. Crystals with high ρ and large Z_{eff} are therefore appropriate materials for compact, highly segmented scanners with a high spatial resolution.

Decay time

As in HEP applications, the response of scintillators used in PET imaging should be fast in order to minimize dead time. A short dead time reduces the examination time, and therefore, the costs of the examination and the patient dose as it

makes the use of positron emitters with very short half-lives possible. Moreover, a short decay time allows for using a shorter coincidence time window, which in turn reduces the background of random coincidences.

Effective light yield and energy resolution

Scintillators in PET applications are required to have a high effective light yield. This allows for a good timing and energy resolution. For a fixed decay time, a light yield increase by a factor of two leads to an improvement of time and energy resolution by 30%. This improvement can be used to reduce the background of Compton-scattered photons in the patient.

2.4 An ideal scintillator for PET imaging

In the preceding section, general aspects of scintillators used in PET imaging have been presented. In the following, the properties of an ideal scintillator for PET imaging are reviewed.

As noted in Sect. 2.3.2, a scintillator for PET imaging should have a high ρ and a large photoelectric fraction to ensure a high stopping power. For an energy $E_\gamma = 511$ keV and $Z_{eff} \approx 40$, the photo absorption coefficient σ_p amounts to only 10% of the Compton scattering coefficient σ_C . The photoelectric fraction increases with Z_{eff} and σ_p dominates over σ_C for $Z_{eff} \geq 79$. Consequently, Z_{eff} of the scintillator should be as large as possible.

An ideal PET scintillator should also exhibit a very good time resolution Δt . This requires a short decay time τ and a high effective light yield N_{ph} . Following eq. 2.27, a short radiative decay time τ_R requires a small emission wavelength λ and a high refractive index n . On the other hand, a high effective light yield can only be achieved for a small band gap energy E_G , a conversion efficiency $\eta \approx 1$, and a refractive index n similar to that of the entry window of the photo detector to ensure that most of the produced photons reach the photocathode. The latter point requires also an absorption coefficient of the scintillator $\alpha_{abs} \approx 0$ in the wavelength range of emission. Certainly, a compromise figure has to be found for n and λ to ensure an optimised time resolution. In addition, the requirement of a high light yield also excludes scintillators where a short τ is due to strong quenching of the crystal light. Afterglow or slow decay time components should also be absent to avoid a pile-up of the detector signal, especially at high count rates.

A high light output is also required to ensure good energy resolution R of the scintillation detector. Moreover, an ideal scintillator for PET should exhibit an intrinsic energy resolution R_i that is small relative to the photoelectron statistics. In addition, the scintillator should exhibit a linear energy response ($\sigma_{np} \approx 0$) at least in the energy range $300 \text{ keV} < E_\gamma < 600 \text{ keV}$. The light yield should exhibit only a negligible temperature dependence at least at room

Table 2.2: Selected inorganic scintillators for PET.

Scintillator	ρ [g/cm ³]	Z_{eff}	X_0 [cm ⁻¹]	σ_p/σ_C	Light output [ph/MeV]	Decay time τ [ns]	Ref
NaI:Tl	3.67	50.8	2.56	0.22	32 000	230	[1]
BGO	7.13	75.2	1.12	0.65	8 200	300	[3]
LSO	7.4	66	1.15	0.52	27 000	40	[2]
LYSO	7.1	63.5	1.2	0.49	32 000	40	[6, 7]
LuAP	8.34	65	1.1	0.47	11 000	17 + 120	[2, 8]
LuYAP	7.1-7.4	57-60	1.2-1.25	0.37-0.42	15 000	20 + 250	[8]
Lu ₂ Si ₂ O ₇ :Ce	6.2	64.4	1.39	0.45	30 000	24	[33]
LaBr ₃ :Ce	5.29	46.9	1.64	0.16	52 000	30	[10]
LuI ₃ :Ce	5.6	60.4	1.35	0.40	50 000	31, 400, 3000	[34]
K ₂ LaI ₅ :Ce	4.4	52.5	1.91	0.25	57 000	24	[35]

temperature to ensure that the scintillator signal becomes independent of fluctuations of the environmental temperature. Finally, the scintillator should be non-hygroscopic, stable, easy to fabricate, and cost-effective in the production.

Table 2.2 lists several materials that are commonly used in PET applications together with some of their properties. This table contains also a number of bright and fast scintillation crystals that have been developed and extensively studied during the past few years. The values for ρ , Z_{eff} and X_0 were taken from [31]. The ratio σ_p/σ_C was calculated from data from [32].

2.5 The Ce-doped compounds L(Y)SO and Lu(Y)AP

Crystals that contain the trivalent elements Lu³⁺, Gd³⁺, Y³⁺ or Sc³⁺ have found widespread use as scintillators in the past years. This is a consequence of the easy substitution of these rare-earth ions by Ce³⁺ ions that then act as scintillation centres. Two of the most prominent scintillators of this group are the two compounds Lutetium Yttrium Oxyorthosilicate Lu_{2-x}Y_xSiO₅:Ce (L(Y)SO) and Lutetium Yttrium Aluminum Perovskite Lu_{1-x}Y_xAlO₃:Ce (Lu(Y)AP), with which the measurements presented in this thesis were performed. These two materials are presented in the following and their most important properties are discussed.

2.5.1 LSO and LYSO

LSO was first described as a scintillator in 1992 by C. L. Melcher and J. S. Schweitzer [36]. Due to its favorable properties of a very high light yield, a short decay time, and a high density, it has found widespread use since then as a scintillator for PET detectors and calorimeters. Due to the high costs of the raw materials and the very high melting point of LSO (2150°C), it is now common to use Lu_{2-x}Y_xSiO₅:Ce (LYSO) which exhibits very similar properties as LSO but is easier to grow [6].

Scintillation process and spectral characteristics

The monoclinic crystal structure of LSO and LYSO (space group C2/c) contains two sites for Lu ions with 6 or 7 oxygen ligands [37]. Correspondingly, two activator centers (denoted Ce₁ and Ce₂) have been recognized. Of these two centers, only the Ce₁ center is dominant in the scintillation process at room temperature and exhibits bands at 263, 296 and 356 nm in the excitation spectrum. The emission spectrum reveals at low temperature two peaks at 393 and 427 nm that merge to one broad single peak at room temperature. The second center, Ce₂, is strongly quenched at room temperature and causes the low-energy tail of the LSO emission spectrum. Non-radiative processes into which the Ce₂ centres are involved are also responsible for the relatively low conversion efficiency of the deposited energy that is exhibited by this scintillator [7].

Light yield and energy resolution

LSO and LYSO both show a very high light yield of up to $\approx 25\,000 - 30\,000$ ph/MeV [6, 38]. In contrast to this, the intrinsic energy resolution R_i is only $\approx 7\%$, and therefore relatively poor [39]. This is by part due to the strong non-proportional response of this material that is especially evident at energies below 100 keV [24]. This non-linearity of the energy response is also expressed by a large σ_{np} of 0.176 (cf. eq. 2.14) [22].

Decay time and afterglow

LSO exhibits a decay time of about 35 ns (LYSO: 40 ns [38]) which is due to Ce₁ site emission. Shorter decay time components that are sometimes observed in the decay time spectrum originate from the quenched emission of the Ce₂ centers [7]. Unlike other Lutetium silicates, LSO exhibits a significant afterglow with a time constant of several tens of minutes at room temperature that is a consequence of the thermal release of charge carriers from shallow traps [33, 38, 40]. The time resolution of LSO at 1 MeV is 160 ps [33].

Optical properties

Transmission spectra of LSO and LYSO exhibit a high transparency near the theoretical limit at wavelengths above 400 nm. In spectra obtained for thin samples, another peak at 325 nm is observed which coincides with a dip in the excitation spectrum.

Stopping power

LSO and LYSO exhibit a very high density of $\approx 7.1 - 7.4$ g·cm³ [36, 38] and a high Z_{eff} of 66 (LYSO: $Z_{eff} = 63.5$). This implies a very good stopping power for γ -particles: For LSO, the photo absorption coefficient $\alpha = 0.28$ cm⁻¹ and $X_0 = 1.15$ cm for 511 keV photons; for LYSO, $\alpha = 0.25$ cm⁻¹ and $X_0 = 1.2$ cm [32].

2.5.2 LuAP and LuYAP

Lutetium Aluminium Perovskite doped with Cerium was first announced as a promising scintillator by Lempicki et al. [41] and soon identified as an interesting candidate for applications in medicine and HEP. Unfortunately, pure LuAP is very difficult to grow as the Perovskite phase occupies only very limited space in the phase diagram and a contamination with the garnet phase (LuAG, $\text{Lu}_3\text{Al}_5\text{O}_{12}$) changes the scintillation properties of the material significantly [42, 43]. As in the case of LSO, the addition of certain amounts of Yttrium (up to 35%) changes the properties of the crystal only slightly but makes the crystal growth and phase stability easier [43]. The development of LuYAP was to a good part achieved by the CCC which also established it as a cost-effective alternative to LuAP for the use in medical imaging devices [8, 22, 39].

Scintillation properties and spectral characteristics

In contrast to LSO, the orthorhombic crystal structure of LuAP features only one Ce site which attributes to the scintillation. The emission spectra of LuAP and LuYAP usually exhibit a peak around 365 – 370 nm that splits into two peaks at low temperature. Excitation spectra exhibit a broad band between 250 and 350 nm which is likely of Ce^{3+} $4f - 5d$ origin [41].

In emission spectra taken at room temperature, two major kinds of emission have been identified: a Ce^{3+} $5d - 4f$ band centered at about 365 nm and a wide, asymmetrical band peaking at 285 nm which dominates the emission of undoped LuAP samples and is due to host emission. The large Stokes shift of this 285 nm luminescence (3.3 eV) suggests that the emission is due to defect- or self-trapped excitons. Studies of the excitation of LuAP indicate that the presence of Ce prevents the formation of excitons from free charge carriers due to the efficient recombination of e-h pairs through Ce^{3+} ions, and consequently quenches this host emission [44].

Light yield and energy resolution

Despite of the fact that the band gap of LuAP is only slightly larger than that of LSO (LuAP: 7.65 eV [15]; LSO: 6.3 eV [40]), the light yield of LuAP:Ce is considerably smaller and amounts to only about 50% that of LSO. The light yield of LuYAP is slightly higher than that of pure LuAP but still significantly lower than expected from the band gap properties alone. The reason for this degradation of the scintillation light is a Ce-independent parasitic absorption which is well-revealed in excitation spectra as an underlying absorption slope. This slope extends up to 400 nm and intercepts some of the crystal emission [45]. The parasitic absorption may be related to electron trapping by neutral defects as interstitial atomic oxygen and can be quenched by adding tetravalent impurities (as e.g. Hf or Zr) to the melt [46]; however, unintentional impurities or Ce^{4+} centers may also play a role [43, 47]. Unlike LSO and LYSO, the light yield response of LuAP and LuYAP exhibits a good linearity, with a σ_{np}

of only 0.054. Consequently, the intrinsic energy resolution R_i is with $< 4\%$ significantly better than that of LSO [22].

Decay time and afterglow

The radiative lifetime of the excited Ce^{3+} ion is only about 17 ns, which makes it one of the shortest scintillation decay times in currently known Ce-activated scintillator materials. This is by a part a consequence of the relatively short wavelength of the scintillation emission [7]. The same accounts also to LuYAP, which exhibits a slightly slower fast component of 20 ns [8]. In both cases, an additional slow component of $\approx 100 - 200$ ns time constant has been noted by several authors; this component is less important for LuAP (20% of total emission) but significant for LuYAP (50% of total emission) [8]. The stronger slow component in LuYAP is likely a consequence of the modulation of the electronic structure by the presence of two dominant different ions in the rare-earth sites [43]. The time resolution at 1 MeV is 160 ps [48], which is somewhat worse than the time resolution of 110 ps calculated by the theory of Hyman [49]. The discrepancy between calculated and measured time resolution is due to the finite rise time of the decay time curve (time constant 600 ps) and a broadening of the light pulse around its maximum [50]. Unlike LSO, no significant afterglow has been observed in LuAP and LuYAP.

Optical properties

The overlap between emission and absorption areas is higher than for LSO and LYSO. The cut-off observed in the transmission curves is due to Ce^{3+} and usually in the range between 330 and 350 nm [8]. Typically, the transparency of LuAP is slightly better than that of LuYAP; on the other hand, the cut-off of the transmission curve is bluer for LuYAP than for LuAP for identical Ce concentrations.

Stopping Power

LuAP has a very high density of typically $\approx 8.3 \text{ g}\cdot\text{cm}^{-3}$ [44] and a Z_{eff} of 65. The density of LuYAP is slightly smaller and reaches values between 7.1 to 7.5, depending on the amount of Yttrium and the production process. Z_{eff} of LuYAP depends also on the Yttrium concentration but is typically between 57 and 60. At 511 keV, the photo absorption coefficient α of LuAP is 0.29 cm^{-1} (LuYAP: $0.20 - 0.22 \text{ cm}^{-1}$) and $X_0 = 1.1 \text{ cm}$ (LuYAP: $1.2 - 1.25 \text{ cm}$) [32].

Bibliography

- [1] E. Sakai, Recent measurements on scintillator-photodetector systems. IEEE Trans. Nucl. Sci. 34, 418 (1987)
- [2] M. Moszynski, M. Kapusta, M. Mayhugh, D. Wolski, S. O. Flyckt, Absolute light output of scintillators. IEEE Trans. Nucl. Sci. 44, 1052 (1997)
- [3] I. Holl, E. Lorenz, G. Mageras, A measurement of light yield of common inorganic scintillators. IEEE Trans. Nucl. Sci. 35, 105 (1988)
- [4] E. Auffray, Etudes des mecanismes de scintillation et des modifications sous irradiation des proprietes du fluorure de cerium en vus de son utilisation en calorimetrie electromagnetique de haute resolution. Doctoral thesis, Univ. Paris VI, Paris, France (1998)
- [5] E. Auffray, F. Cavallari, P. Lecoq, P. Semere, M. Schneegans, Status of the PWO crystal production from Russia for CMS-ECAL. Nucl. Instr. Meth. A 486, 111 (2002)
- [6] D. W. Cooke, K. J. McClellan, B. L. Bennett, J. M. Roper, M. T. Whittaker, R. E. Muenchausen, R. C. Sze, Crystal growth and optical characterization of cerium-doped $\text{Lu}_{1.8}\text{Y}_{0.2}\text{SiO}_5$. J. Appl. Phys. 88, 7360 (2000)
- [7] A. J. Wojtowicz, W. Drozdowski, D. Wisniewski, J. L. Lefaucheur, Z. Galazka, Z. Gou, T. Lukasiewicz, J. Kisielewski, Scintillation properties of selected oxide monocrystals activated with Ce and Pr. Opt. Mat. 28, 85 (2006)
- [8] J. Trummer, E. Auffray, P. Lecoq, A. Petrosyan, P. Sempere-Roldan, Comparison of LuAP and LuYAP crystal properties from statistically significant batches produced with two different growth methods. Nucl. Instr. Meth. A 551, 339 (2005)
- [9] A. J. Wojtowicz, M. Balerzyk, E. Berman, et al., Optical spectroscopy and scintillation mechanisms of $\text{Ce}_x\text{La}_{1-x}\text{F}_3$. Phys. Rev. B 49, 14880 (1994)
- [10] E. V. D. van Loef, P. Dorenbos, C. W. E. van Eijk, K. W. Krämer, H. U. Güdel, Scintillation properties of $\text{LaBr}_3\text{:Ce}^{3+}$ crystals: fast, efficient and high-energy-resolution scintillators. Nucl. Instr. Meth. A 486, 254 (2002)
- [11] P. Dorenbos, Light output and energy resolution of Ce^{3+} -doped scintillators. Nucl. Instr. Meth. A 486, 208 (2002)

- [12] M. Korzhik, P. Lecoq, Search of new scintillation materials for nuclear medicine applications. *IEEE Trans. Nucl. Sci.* 48, 628 (2001)
- [13] C. Dujardin, C. Pedrini, P. Meunier-Beillard, B. Moine, J. C. Gacon, A. Petrosyan, Recent results on the optical properties of $\text{LuAlO}_3\text{:Ce}$ scintillator crystals. *J. Lumin.* 72-74, 759 (1997)
- [14] J. D. Naud, T. A. Tombrello, C. L. Melcher, J. S. Schweitzer, The role of Cerium sites in the scintillation mechanism of LSO. *IEEE Trans. Nucl. Sci.* 43, 1324 (1996)
- [15] P. A. Rodnyi, *Physical Processes in Inorganic Scintillators*. New York, CRC Press (1997)
- [16] P. Lecoq, I. Dafinei, E. Auffray, M. Schneegans, M. V. Korzhik, O. V. Missevitch, V. B. Pavlenko, A. A. Fedorov, A. N. Annenkov, V. L. Kostylev, V. D. Ligun, Lead Tungstate (PbWO_4) scintillators for LHC EM calorimetry. *Nucl. Instr. Meth. A* 365, 291 (1995)
- [17] P. Lecoq, M. Schussler, M. Schneegans, Progress and prospects in the development of new scintillators for future high energy physics experiments. *Nucl. Instr. Meth. A* 315, 337 (1992)
- [18] A. Lempicki, A. J. Wojtowicz, E. Berman, Fundamental limits of scintillator performance. *Nucl. Instr. Meth. A* 333, 304 (1993)
- [19] D. J. Robbins, On predicting the maximum efficiency of phosphor systems excited by ionizing radiation. *J. Electrochem. Soc.* 127, 2694 (1980)
- [20] W. van Roosbroeck, Theory of the yield and Fano factor of electron-hole pairs generated in semiconductors by high-energy particles. *Phys. Rev.* 139, 1702 (1965)
- [21] R. H. Bartram, A. Lempicki, Efficiency of electron-hole pair production in scintillators. *J. Lumin.* 68, 225 (1996)
- [22] C. Kuntner, E. Auffray, P. Lecoq, C. Pizzolotto, M. Schneegans, Intrinsic energy resolution and light output of the $\text{Lu}_{0.7}\text{Y}_{0.3}\text{AP:Ce}$ scintillator. *Nucl. Instr. Meth. A* 493, 131 (2002)
- [23] J. A. Mares, M. Nikl, N. Solovieva, C. D'Ambrosio, F. de Notaristefani, K. Blazek, P. Maly, K. Nejezchleb, P. Fabeni, G. P. Pazzi, J. T. M. de Haas, C. W. E. van Eijk, P. Dorenbos, Scintillation and spectroscopic properties of Ce^{3+} -doped YAlO_3 and $\text{Lu}_x(\text{RE})_{1-x}\text{AlO}_3$ ($\text{RE} = \text{Y}^{3+}$ and Gd^{3+}) scintillators. *Nucl. Instr. Meth. A* 498, 312 (2003)
- [24] P. Dorenbos, J. T. M. De Haas, C. W. E. van Eijk, Non-proportionality in the scintillation response and the energy resolution obtainable with scintillation crystals. *IEEE Trans. Nucl. Sci.* 42, 2190 (1995)
- [25] R. B. Murray, A. Meyer, Scintillation response of activated inorganic crystals to various charged particles. *Phys. Rev.* 122, 815 (1961)

-
- [26] G. C. Meggit, The effect of the crystal surface on the derived electron scintillation response in NaI(Tl). Nucl Instr. Meth. 83, 313 (1970)
- [27] J. B. Birks, The theory and practice of scintillation counting. Pergamin Press, Oxford (1964)
- [28] M. Itoh, T. Sakurai, Time-resolved luminescence from Jahn-Teller split states of self-trapped excitons in PbWO₄. Phys. Rev. B 73, 235106 (2006)
- [29] S. Baccaro, L. M. Barone, B. Borgia, F. Castelli, F. Cavallari, F. de Notaristefani, M. Diemoz, R. Faccini, A. Festinesi, E. Leonardi, E. Longo, M. Mattioli, M. Montecchi, G. Organtini, S. Paoletti, E. Valente, Optical properties of lead tungstate (PbWO₄) crystal for LHC em-calorimetry. CMS TN/95-152
- [30] C. W. E. van Eijk, Inorganic scintillators in medical imaging detectors. Nucl. Instr. Meth. A 509, 17 (2003)
- [31] P. Lecoq, A. Annenkov, A. Getkin, M. Korzhik, C. Pedrini, Inorganic Scintillators for Detector Systems. Springer, Berlin, Heidelberg (2006)
- [32] NIST XCOM: Photon Cross Sections Database. <http://physics.nist.gov/PhysRefData/Xcom/Text/XCOM.html>
- [33] L. Pidol, A. Kahn-Harari, B. Viana, B. Ferrand, P. Dorenbos, J. T. M. de Haas, C. W. E. van Eijk, E. Virey, Scintillation properties of Lu₂Si₂O₇:Ce³⁺, a fast and efficient scintillator crystal. J. Phys. Condens. Matter 15, 2091 (2003)
- [34] K. S. Shah, J. Glodo, M. Klugerman, W. Higgins, T. Gupta, P. Wong, W. W. Moses, S. E. Derenzo, M. J. Weber, P. Dorenbos, LuI₃:Ce - A New Scintillator for Gamma Ray Spectroscopy. IEEE Trans. Nucl. Sci. 51, 2302 (2004)
- [35] E. V. D. van Loef, P. Dorenbos, C. W. E. van Eijk, K. W. Krämer, H. U. Güdel, Scintillation properties of K₂LaX₅:Ce³⁺ (X=Cl, Br, I). Nucl. Instr. Meth. A 537, 232 (2005)
- [36] C. L. Melcher, J. S. Schweitzer, Cerium-doped Lutetium Oxyorthosilicate: A fast, efficient new scintillator. IEEE Trans. Nucl. Sci. 39, 502 (1992)
- [37] H. Suzuki, T. A. Tombrello, C. L. Melcher, J. S. Schweitzer, UV and gamma-ray excited luminescence of cerium-doped rare-earth oxyorthosilicates. Nucl. Instr. Meth. A 320, 263 (1992)
- [38] P. Dorenbos, C. W. E. Van Eijk, A. J. J. Bos, C. L. Melcher, Scintillation and thermoluminescence properties of Lu₂SiO₅:Ce fast scintillation crystals. J. Lumin. 60&61, 979 (1994)
- [39] C. Kuntner, Evaluation of New Inorganic Scintillators for Application in a Prototype Small Animal PET scanner. Dissertation, TU Wien, Austria (2003)

- [40] N. V. Znamenskii, E. A. Manykin, E. A. Petrenko, T. G. Yukina, Y. V. Malyukin, P. N. Zhmurin, B. V. Grinev, A. A. Masalov, A. P. Shpak, The nature and mechanism of charging of electron traps in $\text{Lu}_2\text{SiO}_5\text{:Ce}^{3+}$ crystals. *J. Exp. Theor. Phys.* 99, 386 (2004)
- [41] A. Lempicki, M. H. Randles, D. Wisniewski, M. Balcerzyk, C. Brecher, A. J. Wojtowicz, $\text{LuAlO}_3\text{:Ce}$ and other aluminate scintillators. *IEEE Trans. Nucl. Sci.* 42, 280 (1995)
- [42] W. W. Moses, S. E. Derenzo, A. Fyodorov, M. Korzhik, A. Getkin, N. Minkov, V. Aslanov, $\text{LuAlO}_3\text{:Ce}$ - A high density, high speed scintillator for gamma detection. *IEEE Trans. Nucl. Sci.* 42, 275 (1995)
- [43] A. G. Petrosyan, K. L. Ovanesyan, G. O. Shirinyan, T. I. Butaeva, M. V. Derzyan, C. Pedrini, N. Garnier, C. Dujardin, L. A. Kamenskikh, LuAP/LuYAP single crystals for PET scanners: effects of composition and growth history. *Opt. Mat.* 24, 259 (2003)
- [44] D. Wisniewski, A. J. Wojtowicz, A. Lempicki, Spectroscopy and scintillation mechanism in $\text{LuAlO}_3\text{:Ce}$. *J. Lumin.* 72-74, 789 (1997)
- [45] A. Lempicki, J. Glodo, Ce-doped scintillators: LSO and LuAP. *Nucl. Instr. Meth. A* 416, 333 (1998)
- [46] A. G. Petrosyan, M. Derdzian, K. Ovanesyan, P. Lecoq, E. Auffray, J. Trummer, M. Kronberger, C. Pedrini, C. Dujardin, P. Anfre, Properties of LuAP:Ce scintillator containing intentional impurities. *Nucl. Instr. Meth. A* 571, 325 (2007)
- [47] R. H. Bartram, D. S. Hamilton, L. A. Kappers, A. Lempicki, Electron traps and transfer efficiency of cerium-doped aluminate scintillators. *J. Lumin.* 75, 183 (1997)
- [48] M. Moszynski, D. Wolski, T. Ludziejewski, A. Lempicki, C. Brecher, D. Wisniewski, A. J. Wojtowicz, LuAP, a new fast scintillator. *Proc. Int. Conf. on Inorganic Scintillators and their Applications, SCINT95*, 348 (1996)
- [49] L. G. Hyman, Time resolution of photomultiplier systems. *Rev. Sci. Instr.* 36, 193 (1965)
- [50] M. Moszynski, D. Wolski, T. Ludziejewski, M. Kapusta, A. Lempicki, C. Brecher, D. Wisniewski, A. J. Wojtowicz, Properties of the new LuAP:Ce scintillator. *Nucl. Instr. Meth. A* 385, 123 (1997)

Chapter 3

Experimental techniques

This chapter provides a description of the experimental techniques that have been used for the experiments discussed in the following chapters.

3.1 Light output and energy resolution

As indicated in Sect. 2.2.2, the light output measured in an experiment depends not only on the absolute light yield of the crystal but also on several instrumental and physical factors, e.g.

- the collection efficiency of the charge carriers in the photo detector
- the quantum efficiency of the photo detector
- the contrast of the refractive indices of PMT entrance window, crystal and the material used as optical coupling
- the surface state of the crystal faces
- the reflectivity of the enveloping material
- the temperature dependence of the scintillator light output

While some of these parameters can be determined by a simple measurement, others are much more difficult to assess. Therefore, an accurate determination of the absolute light yield is not straightforward but a relatively complex and difficult task. As will be shown later, sufficiently precise results can only be assessed by combining experimental methods and Monte-Carlo simulations (see also Chapter 4).

An approach commonly found in literature is the expression of the light output of a scintillator by the number of photo electrons N_{pe} for a specified setup, photodetector type, and photo detector sensitivity. Such measurements are generally accurate in the sense that the used method is independent of any assumptions concerning light collection efficiency and therefore simple and easy to reproduce.

3.1.1 Determination of the scintillator light yield

The number of photo electrons N_{pe} can be calculated by comparing the position of the full-energy peak in the light yield spectrum (Fig 3.1) with the position of the signal produced by a single photon. Assuming a linear response of the

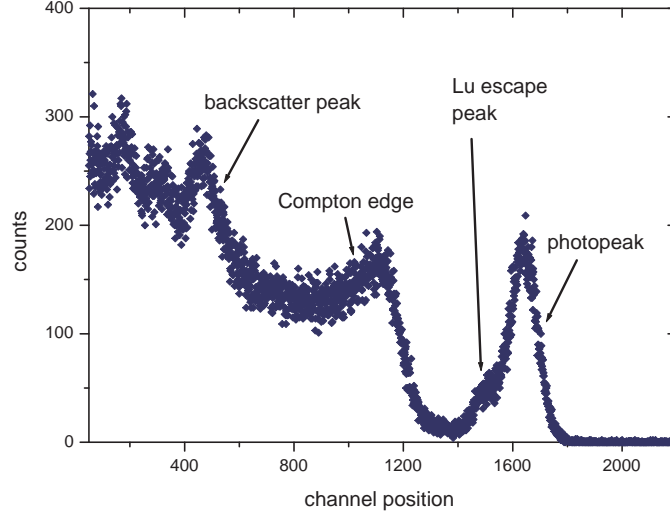


Figure 3.1: Light yield spectrum recorded of a LuYAP crystal.

read-out chain, the number of photo electrons per MeV of the incident γ -particle can be determined by

$$N_{pe}/\text{MeV} = \frac{\text{position of full-energy peak} - \text{pedestal}}{\text{position of single photo electron peak} - \text{pedestal}} \cdot \frac{A_1}{A_2} \cdot \frac{1}{E_\gamma} \quad (3.1)$$

Where E_γ is the energy of the incident γ -quantum in MeV. The factors A_1 and A_2 account for the attenuation of the PMT signal during the measurement of the full-energy and single photon electron peak,

$$A_i = e^{\frac{B_i}{20}} \quad i = 1, 2 \quad (3.2)$$

with the attenuation B_i in dB. To determine the number of photons emitted per MeV, eq. 3.1 has to be corrected for the effective quantum efficiency q_{eff} of the PMT:

$$N_{ph}/\text{MeV} = \frac{N_{pe}}{q_{eff}} \quad (3.3)$$

The exact position of the full energy peak and the energy resolution are determined from the light yield spectrum by fitting the region of the full energy peak with the sum of a Gaussian and a Fermi distribution:

$$y(x) = \frac{p}{e^{\frac{x-c}{\tau}} + 1} + a \cdot e^{-\frac{(x-\mu)^2}{2\sigma^2}}, \quad (3.4)$$

Table 3.1: Description of peaks visible in the light yield spectrum and their origin. $\alpha = E/m_0c^2$, $m_0c^2 = 0.511$ MeV; $E_{K_{\alpha,Lu}} = 63$ keV.

Name	Energy of peak in spectrum	E for ^{137}Cs source [keV]	Origin
Photopeak	E	662	Photoelectric effect and multiple absorption processes
Compton edge	$E_C = \frac{2\alpha \cdot E}{1+2\alpha}$	478	Compton 180° scattering
Single Compton distribution	E_C to 0	< 478	Single Compton scattering
Multiple Compton distribution	E to 0	< 662	Multiple Compton scattering
Lutetium escape peak	$E - E_{K_{\alpha,Lu}}$	599	Escape of Lutetium K_{α} x-rays
Backscatter peak	$\frac{E}{1+2\alpha}$	184	External Compton scattering

where p , c and $1/r$ correspond to height, position, and slope of the Compton edge; a is the height of the photo peak with position μ and FWHM width $2.36 \cdot \sigma$. With the position of the full energy peak determined by eq. 3.4, the light output of the crystal can be calculated by eqs. 3.1 and 3.3.

Apart from the full energy peak, the spectrum shown in Fig. 3.1 also exhibits several satellite peaks that originate either from the escape of characteristic Lutetium K_{α} photons from the crystal or from scattering processes. Table 3.1 provides a list of all processes that contribute to the shape of the pulse height spectrum for the case of a ^{137}Cs source ($E_{\gamma} = 662$ keV). If a source with an energy > 1.022 MeV is used, two additional peaks appear in the pulse height spectrum which are due to the escape of one or two annihilation photons originating from a preceding pair production process.

3.1.2 Experimental setup

The setup used for the measurements of the scintillator light output is shown in Fig. 3.2. In each measurement, the crystal was placed on top of a Philips XP2020Q photomultiplier. The fused silica entry window of this PMT ensures a high transparency in the blue and violet wavelength regime. The average quantum efficiency \bar{q}_{eff} of the PMT was determined by convoluting the spectral response of the PMT (Fig. 3.3) with the emission spectra of the scintillators. For LYSO and LuYAP, \bar{q}_{eff} was found to be 0.22 and 0.25, respectively. The scintillation of the crystal was stimulated by γ -rays originating from a ^{137}Cs source ($E_{\gamma} = 662$ keV) with an activity of ≈ 200 kBq which was placed at a distance of a few mm above the crystal. Shielding against background light was ensured by a light-tight black box surrounding the PMT and an aluminum cap with blackened inner walls covering PMT entry window and crystal. After the photo electrons were collected at the anode of the PMT, the signal was attenuated, shaped, and finally stored by the DAQ software.

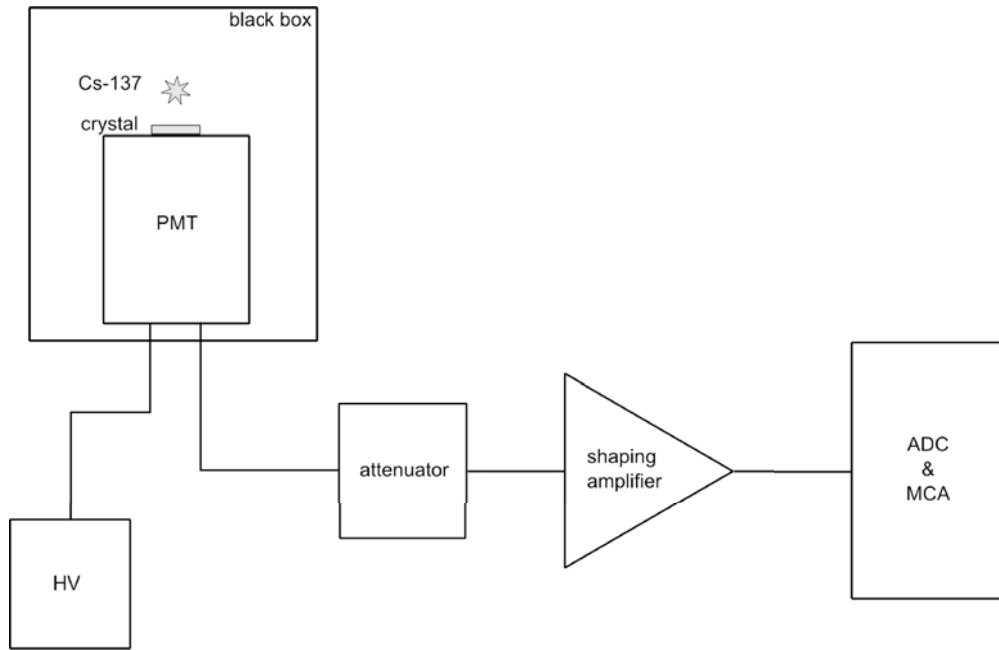


Figure 3.2: Schematic drawing of the light yield bench.

The signal produced by a single photo electron and the position of the pedestal were determined by recording the unattenuated PMT signal with the DAQ software. An example spectrum retrieved by this method is shown in Fig. 3.4. Although the single photo electron peak is well visible in the spectrum, the precise determination of its position has been complicated by the significant background noise apparent in the immediate area of the pedestal peak. This background noise is due to charge carriers thermally generated in the electronics, and electrons released in one of the dynodes by γ -photons from the ^{137}Cs source. To reduce the influence of the background on the determination of the single electron peak position, two separate measurements with and without crystal were performed and the spectra recorded during the measurements subtracted from each other. As the background component is widely reduced in the resulting difference spectrum, the position of the single photo electron peak can then be determined by means of a simple Gaussian fit.

3.1.3 Setup configurations

The setup configurations that were used in the measurements are summarized in Table 3.2. In all cases, the measurements were performed at least three times and the mean was taken for discussion. To correct for long-term variations of the PMT gain and quantum efficiency, the measured light yield was normalized to the light yield of a reference crystal with well known light output (LuYAP CCC 1098) that was recorded during the same measurement run.

Measurements with wrapping:

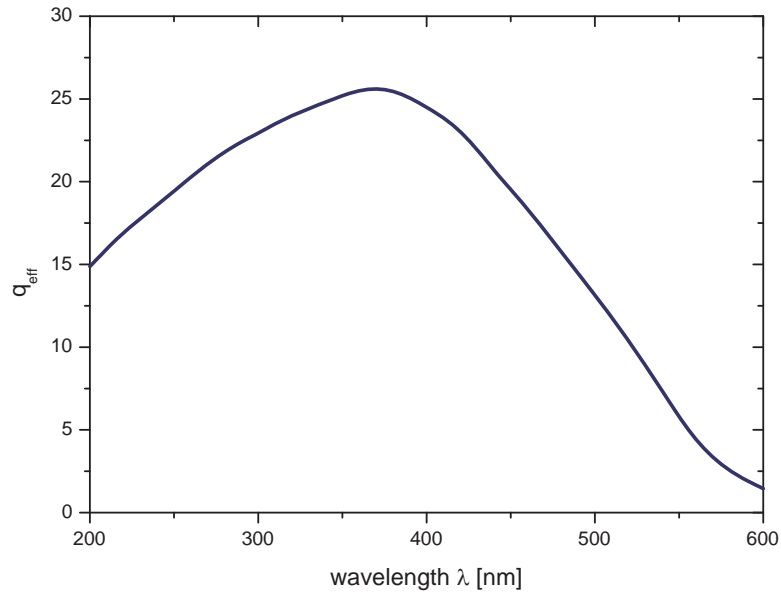


Figure 3.3: q_{eff} of the Philips XP2020Q photomultiplier.

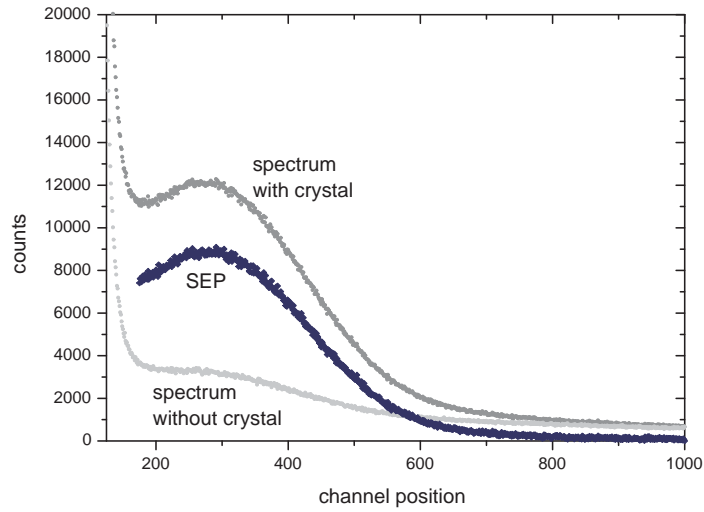


Figure 3.4: Single electron spectra measured with and without crystal and difference spectrum (SEP = single electron peak).

Table 3.2: Setup configurations used in the light yield measurements.

Crystal orientation	Wrapping	Optical coupling
horizontal	yes	grease
horizontal	no	grease / no grease
vertical	yes	grease / no grease
vertical	no	grease / no grease

Measurements in horizontal setup were performed by optically coupling the crystal to the PMT entry window by means of silicon grease (Rhodorsil Silicones pate 4) and covering it with several layers of Teflon tape. In vertical geometry, the crystal was wrapped with several layers of Teflon tape and then tucked into a Teflon tube with a hole of appropriate size. In addition, it was ensured in each measurement that the coupling face of the crystal was clear of Teflon tape to avoid light losses by a reduced aperture of the exit surface.

Measurements without wrapping:

In the measurements without wrapping, special care was taken that neither background light nor any reflected scintillation light could enter the PMT. This was achieved by covering the PMT entry window with a mask with an appropriate opening for the crystal and the crystal itself with an additional black shielding. This shielding served also as source holder.

3.2 Transmission

As noted in Sect. 2.2.8, the transmission of a crystal at a given wavelength provides information on the optical properties of the crystal at this wavelength. In particular, it permits a determination of the intrinsic attenuation of the crystal if the refractive index of the material is known. Such measurements are especially important in the assessment of the scintillator performance as these materials require a high optical quality in the wavelength range of emission.

The transmission measurements described in this thesis were performed by means of a custom made spectrophotometer. The principle of this machine is sketched in Fig. 3.5. The main elements that compose this spectrophotometer are [1]:

- a 150 W Xenon lamp covering the wavelength range between 200 nm and 700 nm.
- a monochromator (Jobin Yvon H20UV) with a grating to select a specific wavelength. The grating is coupled to a step motor that allows for an automated scan of a defined wavelength range.
- several UV lenses for focusing the light into a monochromator and collimating it at its exit.

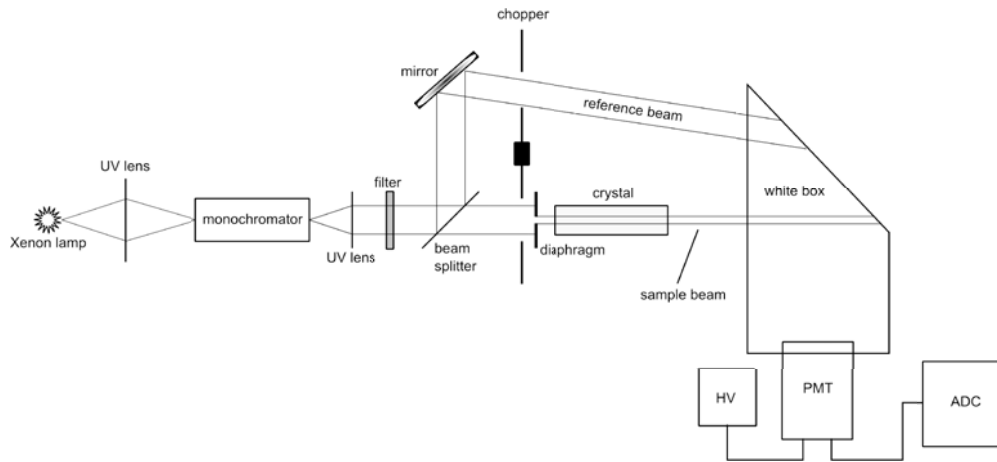


Figure 3.5: Schematic drawing of the spectrophotometer.

- a set of filters to eliminate upper order diffractions originating from the monochromator. These filters are driven by a step motor that changes them automatically with the monochromator wavelength.
- a chopper, which splits the beam coming from the monochromator into two beams that alternate with a frequency of 50 Hz: an indirect one, which serves as a reference beam, and a direct one, which is used for measuring the transmission of a sample.
- a PMT with a large spectral band width (Philips XP2254B). This PMT is placed in a white box that diffuses the light coming from the reference or the sample beam to ensure a uniform irradiation of the photocathode.
- a movable table driven by a step motor for positioning the sample transverse to the beam.
- a DAQ system which records the beam intensities and calculates the transmission of the crystal.

The simultaneous measurement of the intensities of two beams with only one PMT has the advantage that the measurement becomes independent on fluctuations of the intensity of the light source and the gain of the PMT.

The settings of the spectrophotometer, as well as the parameters important for data acquisition and analysis, are automatically operated by a LabVIEW program. This program allows the wavelength range of the transmission measurement, the step width of the monochromator, the spectral width of the beam, and the position of the table to be set. Before starting the measurements, a separate reference measurement without sample has to be performed during which the mean intensities $\langle I_{ref}(\lambda) \rangle$ and $\langle I_{sample}(\lambda) \rangle$ of the reference and sample beams are recorded and the ratio $R_{ref}(\lambda) = \langle I_{sample}(\lambda) \rangle / \langle I_{ref}(\lambda) \rangle$ is calculated. The

transmission of the crystal $T(\lambda)$ is then calculated by

$$T(\lambda) = \frac{R(\lambda)}{R_{ref}(\lambda)} \quad (3.5)$$

where $R(\lambda)$ denotes the ratio of the two beam intensities in the transmission measurement. Finally, the recorded transmission spectrum is fitted with the equation [2]

$$\ln T(\lambda) = A + e^{-\frac{\lambda - \lambda_c}{s}} \quad (3.6)$$

where λ_c is the cut-off wavelength (see Sect. 2.2.8) and $1/s$ is proportional to the slope of the curve at λ_c .

3.3 Emission and excitation spectra

Measurements of the emission and excitation spectra of the crystals were performed with a Perkin Elmer LS 55 fluorescence spectrometer. The principle of this machine is outlined in the sketch shown in Fig. 3.6. The light emitted by a high energy Xenon lamp passes through a monochromator with a slit width of a few nm, a polarizer, and a slit which focuses the beam onto the sample. The light emitted by the crystal is again sent through a polarizer and a monochromator before it is recorded by a photo detector. Several filters with various cut-off wavelengths can be used to suppress second-order diffraction peaks originating from the first monochromator. In addition, the machine contains holders on each side of the sample in which neutral filters with transmissions ranging from 8% to 33% can be manually inserted; this allows for reducing the intensity of the beams that arrive at or leave the crystal.

The spectrofluorometer can be run in two different operation modes. In the emission mode, the emission spectrum of the sample is recorded at a fixed excitation wavelength. Usually, an excitation wavelength is selected where the absorption of the luminescence centers - and therefore the efficiency of the conversion into scintillation light - is high. In the excitation mode, the recorded emission wavelength is kept fixed and the excitation wavelength is changed. The maxima in the recorded spectra indicate at which excitation wavelength the conversion efficiency is high and allow an identification of the excitation bands of the sample. This information can, in turn, be used to select an excitation wavelength for the emission mode.

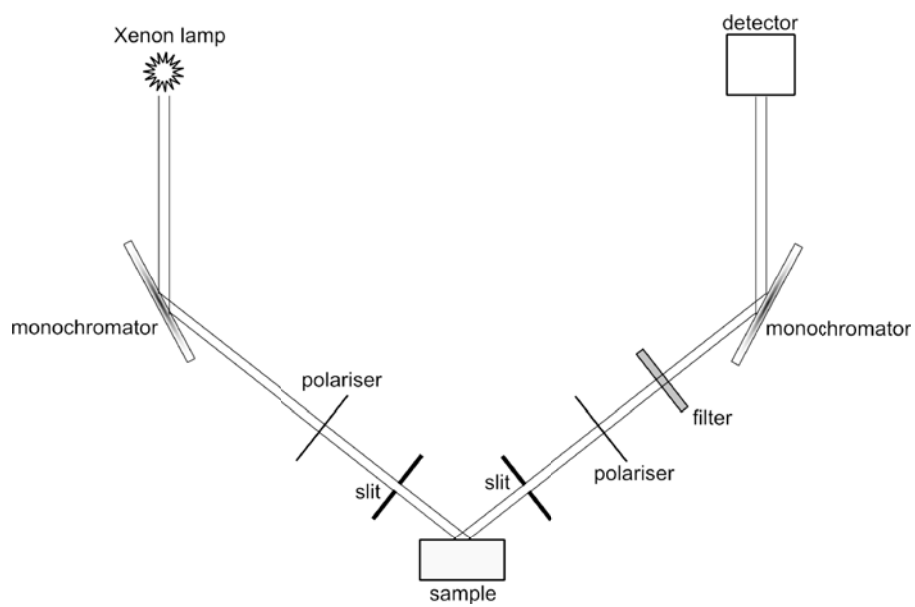


Figure 3.6: Schematic drawing of the spectrofluorimeter.

Bibliography

- [1] P. S. Roldan, Quality control and preparation of the PWO crystals for the electromagnetic calorimeter of CMS. Doctoral thesis, Universidad de Santiago de Compostela, Spain (2001)
- [2] J. Trummer, Study of a Positron Emission Tomograph. Doctoral thesis, TU Vienna, Austria (2007)

Chapter 4

Light propagation in inorganic scintillators

This chapter describes the results of simulations and experiments that were performed to understand qualitatively and quantitatively the main factors that influence the light propagation in inorganic scintillators. In combination with experimental data, these results are used to determine the light collection efficiencies and absolute light yields of the scintillators LYSO and LuYAP.

4.1 Light output and light collection efficiency

As noted in Sect. 2.2.2, the number of photoelectrons or electron-hole pairs measured in a LY experiment is determined by eqs. 2.13 and 2.12, which are repeated here in condensed form:

$$N_{pe} = q_{eff} \cdot LY = q_{eff} \cdot \tau \cdot \eta_L \cdot LY_{abs} \quad (4.1)$$

with the effective quantum efficiency q_{eff} of the photo detector, the temperature dependence of the scintillator light output τ , the light collection efficiency η_L , and the absolute light yield LY_{abs} .

While q_{eff} can be determined relatively easily by folding the emission spectrum of the crystal with the photo detector sensitivity, the determination of η_L is more problematic. Although the principal processes that govern the propagation of light in scintillating crystals and their effect on η_L are qualitatively known, it is not straightforward to develop a model that describes the light collecting properties of a given scintillator also in a quantitative way. Many factors that determine η_L , such as the absorption length, supplementary absorption effects, diffusion originating from surface and bulk defects, or the reflective properties of the enveloping material, cannot be assessed by a simple measurement and are therefore often only insufficiently known. It is therefore not surprising that absolute light yields determined by different methods often differ considerably from each other even for widely used scintillators. As an example, the values quoted in literature for the absolute light yield of LuAP:Ce scatter between 10 000 and 20 000 photons/MeV [1, 2, 3, 4].

Several approaches to determine the absolute light output of scintillators have been developed in the past years. A method widely used for characterising novel materials is to derive the absolute light yield of a crystal by comparing its light output with that of a reference crystal measured in parallel [2, 3, 5, 6, 7]. Although this method serves well in gaining a first insight into the principal quality of a scintillator, its reliability is reduced by uncertainties in the absolute light yield of the reference sample and mismatch of the geometrical and optical properties of the samples, such as refraction index, absorption length, and shape. Some authors [3, 7] propose the usage of thin crystal samples with polished top and bottom faces and ground side faces in combination with a reflector for measuring the total light output of scintillators. The grounding of the side faces, however, poses a problem because roughened surfaces usually exhibit a significantly reduced reflectivity [8, 9, 10]. For this reason, the absolute light yields derived by this method are likely too low. The same probably accounts also to the simple model of Wojtowicz et al. [11] who use a semi-empirical formula based on a loss parameter μ and the ratio $LY_{vertical}/LY_{horizontal}$ to determine LY_{abs} . Clearly, these relatively simple approaches serve well in assessing the principal performance of a scintillator but are not well suited for a precise determination of the absolute number of photons created by an incident particle.

A far more promising approach to determine light collection efficiencies and absolute light yields is to combine the experimental results with computer models that reproduce the experimental setup as closely as possible. Such methods have already been employed and highlight the importance of internal and external effects, e.g. light scattering in the crystal bulk and back-reflection of photons from the photosensitive layer of the PMT tube, on the light collection process [12, 13].

Several commercially available software packages and freewares exist with which the propagation of light in transparent media can be simulated. These packages all have in common that they contain routines that follow the scintillation photons from their origin to the recording photo detector. The probabilities that a photon is transmitted or reflected at an interface between two media are usually calculated on the basis of the laws of classical electromagnetism. An additional obligatory condition to allow the simulation of real systems is that the program takes into account the light absorption in the medium.

Light ray tracing programs that have been used for scintillator studies are e.g. Opticad [14], LIGHT [13], PHOTRACK [15] or Detect [8, 16, 17]. The simulations presented in this and the following chapter were performed with the freely available program LITRANI by F.-X. Gentit [18]. This Monte-Carlo program is presented in the following section.

4.2 LITRANI

LITRANI (*Light Ray Tracing in ANisotropic media*) is a ROOT-based general purpose Monte-Carlo program which allows for simulating the propagation of light in isotropic and anisotropic media [18]. Initially developed in the framework of the CMS experiment to simulate emission, collection and light detection for PWO, it has been widely used since then in the characterization of various other scintillator-based detectors [12, 19, 20, 21, 22]. The photon propagation in LITRANI is purely determined by the laws of classical optics, except for the handling of thin slices of material where interference is also taken into account. LITRANI is an open source program and can be downloaded freely at the LITRANI homepage of F. X. Gentit [23].

Geometry:

Any setup that is simulated in LITRANI consists of discrete entities (shapes) that define the various elements of the setup. As the LITRANI geometry is derived from the old ROOT geometry, only a few basic shapes (tubes, cylinders, trapezoids, cones, parallelepipeds, ...) are available. This makes it very complicated, if not impossible, to simulate very complex geometries or setups. Further restrictions originate from the fact that LITRANI only allows for additive construction, i.e. it is not possible to simulate a shape being fully or partly embedded in another shape.

Once the dimensions of the shape have been set, its global position is defined by affixing it to a node which defines the position and orientation of the shape. If a shape is in partial or total contact with another shape, it is necessary to declare this contact so that an exchange of photons can take place.

Materials:

Each shape of the setup has to be defined as being made of a certain material. Every material is defined by the following properties:

- optical type
- magnetic permeability μ
- absorption length λ_{abs}
- scattering length λ_{scat}
- photon sensitivity, i.e. if a material is a detector or not

The optical type of a material indicates, if it is isotropic, uniaxial birefringent, or biaxial birefringent. In isotropic materials, a photon will experience the same refractive index in any propagation direction, while in all other cases the refractive index is direction dependent. If the material is supposed to be birefringent, a dielectric tensor ϵ_{ijk} and the directions of the optical axes have

to be defined. In the case of an isotropic material, it is sufficient only to set the refractive index n . Both the components of ϵ_{ijk} and the refractive index can be defined as being wavelength dependent.

The absorption length λ_{abs} of a material can be defined either as isotropic or as anisotropic and can be constant or wavelength dependent.

Scattering is described by LITRANI by 3 different kinds of processes: Simple (elastic) scattering, inelastic scattering, and Rayleigh scattering. These processes are not exclusive of one another but can be implemented at the same time for a given material. In the case of simple scattering, the photon is absorbed and re-emitted at the same place with the same wavelength but with a different k-vector randomly generated in 4π . Inelastic scattering is described in an equivalent manner, except that the photon is re-emitted at a larger wavelength. Rayleigh scattering refers to the process of light scattering at particles that are much smaller than the wavelength of the photons, such as molecules or atoms. It differs from other scattering processes in that the photons do not scatter isotropically but have a preference for scatter in the forward and backward directions. Rayleigh scattering at atoms is an intrinsic property of all materials. However, in the majority of cases the corresponding scattering length is very large compared to the scattering lengths of other processes and therefore, can be neglected. All three types of scattering require the definition of a specific scattering length λ_{scat} that can be either wavelength dependent or constant. Unlike absorption, the scattering lengths have to be isotropic.

If a material in the setup should be able to emit light, it has to be defined as being fluorescent. This is done by definition of the fluorescence characteristics of the material, i.e. the wavelength of the emission bands and their band width, the lifetime of the luminescence centres, and the emission intensity. This permits the simulation of most spectra as long as the composing bands and their (relative) intensities are known.

Simulating the energy deposition of an electromagnetic shower or an incoming high energy particle requires the definition of the radiation length X_0 , the Moliere radius R_M , the critical energy of the material and its dE/dx . In addition, the damage introduced in the material by a shower or by radiation can be simulated.

If the radiation source emits low-energy gamma particles with energies of 1 MeV or less, Z_{eff} , mole mass A and the density ρ of the material have to be given to simulate photo effect and Compton scattering. As the intrinsic light yield of real scintillators often depends on the energy of the incoming particle (especially at energies $E_\gamma < 100$ keV), the light yield response of the material can be defined as non-proportional.

Polishing and depolishing of faces:

Any face of any shape can be described as being polished or depolished. Exceptions are faces that are either in contact with the face of another shape or enveloped by a wrapping: such faces can only be simulated as polished.

While the definition of a polished face is straightforward and shall not be discussed here, the definition of a depolished or roughened surface is more problematic. The simple model, which describes scattering corresponding to a diffusing surface by the Lambert Law, is certainly not correct [8, 17]. LITRANI solves the problem of depolishing by using an approach introduced in [9] where the roughened surface is described by a facet model. Although this model is clearly superior to any description of the roughening by the Lambert Law and describes the positional dependence of the light yield rather well, it still fails to provide results that are also quantitatively correct [9]. Certainly, the mechanical treatment of a surface leads to additional effects (e.g. additional absorption, ...) that change its reflection and transmission properties. In general, it should be pointed out that the optical properties of any non-ideal surface state (depolished, oxidized or thinly painted) are only poorly known and very difficult to model by a general approach; the results of any simulation involving such components therefore always has to be taken with a pinch of salt.

Reflector materials:

Each face of a shape can be simulated as being enveloped by a wrapping which reflects back light that escapes through that face. The approach for defining a wrapping is thereby similar as for defining a material. However, unlike a material the optical properties of the wrapping are uniquely defined by a complex dielectric tensor which determines its reflection and absorption properties. The reason for this difference is that LITRANI treats a wrapping not like a material in the sense of photon propagation but rather like a *surface*: a photon that hits the wrapping is either recovered by reflection or lost by absorption, but the propagation of a non-reflected photon *into* the wrapping itself is not simulated. For this reason, it is also not possible to simulate any material outside the wrapping with LITRANI.

The simulation of a diffusing reflector is carried out by defining the proportion of photons that are not specularly reflected back from the wrapping. If diffusion takes place for a photon, it is re-directed using a distribution $D(\theta, \phi)$ of the form

$$D(\theta, \phi) = \cos(\theta)\sin(\theta)d\theta d\phi \quad (4.2)$$

as generally observed for diffusing surfaces, such as a granular metallic surface.

Any wrapping can be simulated as being separated from the enveloped shape by a thin slice of a material (Fig. 4.1). This thin slice can consist of air or any other material, depending on whether the wrapping is only loosely wrapped around

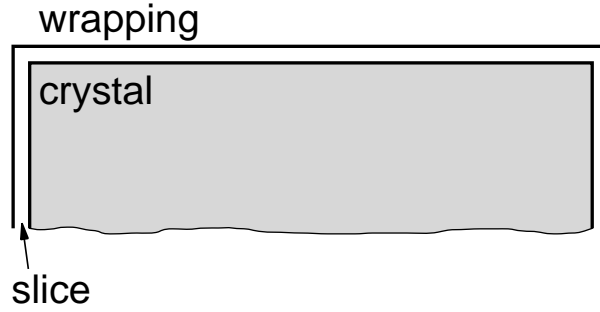


Figure 4.1: Sketch of the slice of material between crystal and wrapping.

the shape or directly connected with the shape by glueing or self-adhesive effects. Reflective paintings, such as BaSO_4 , are directly painted onto the crystal face and no slice of material is to be defined in the simulations.

Modelling the optical properties of realistic reflectors (e.g. metal + oxidized layer or wrappings contaminated by dust particles) is partly achieved by assigning a supplementary absorption component to the wrapping. This supplementary absorption eliminates a defined fraction of the photons that would otherwise be reflected. As in the case of ground surfaces, a realistic modeling of a reflector is nevertheless a complex task and a satisfactory agreement with experimental data is very difficult to achieve.

Light sources:

Litrani allows for simulating different types of light sources:

1. point sources
2. optical fibres
3. beams of high energy particles
4. electromagnetic showers
5. gamma photons with energies < 1 MeV

The angular distribution of the light that is emitted by point sources or optical fibres can be modeled such that it corresponds to the experimental case. Spontaneous sources generating photons isotropically in all directions are convenient tools to investigate e.g. the positional dependence of η_L .

In cases (3)-(5), the photons are generated by the deposition of energy from incoming particles. In LITRANI, photon creation by such a process is always modeled by a series of point-like isotropic generations. These discrete photon sources are generated by simulating the energy deposition mechanisms of the

respective processes. In the case of electromagnetic showers and high energy particles, the individual photon sources are created by modeling the energy distribution in the material. A notable exception is the emission of Cherenkov light, which has a characteristic angular distribution relative to the incoming particle.

For low energy gammas, energy can be deposited by the photoelectric or Compton effects. Energy deposition by the photoelectric effect is determined by the path length L of the radiation in the crystal,

$$L = \frac{1}{\sigma \cdot \rho}, \quad (4.3)$$

where ρ is the density of the material and σ the photoelectric cross section. While the density of the material is usually known for scintillating materials, the photoelectric cross sections can be calculated using values of the NIST database [29] and are implemented in the program in form of a fit (Fig. 4.2). The simu-

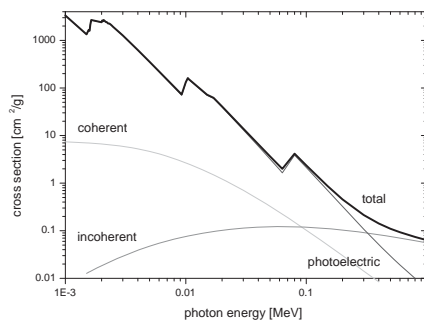


Figure 4.2: Photoelectric, coherent, and incoherent cross-sections of LuYAP.

lation of Compton scattering is based on an algorithm introduced by [24].

Detectors:

LITRANI permits the simulation of different detector types. Any detector is simulated as a material with bulk absorption (volume detector) or with an absorbing surface (surface detector). Any photon stopping at the surface or in the volume is registered so that it can be counted and the total number of photons can be retrieved. Each detector type needs to have a quantum efficiency defined which can also be wavelength dependent. An example for a surface detector is a phototube; examples for volume detectors are APDs and PIN diodes.

4.3 Experimental determination of crystal parameters

To ensure good agreement between the experimental and simulated crystal properties, the parameters used in the simulation describing the optical and fluorescent properties of the crystals were derived from one LYSO:Ce and one LuYAP:Ce crystal from PML. The basic properties of the crystals (i.e. size, weight, and density) are given in Table 4.1. These crystals were also used in the experiments described later in this chapter. The Cerium contents of both crystals were not precisely known but are expected to be in the range of 0.03% – 0.07% for the LYSO crystal and 0.1% – 0.3% for the LuYAP crystal [30].

Table 4.1: Crystals used for determination of crystal parameters for LITRANI.

crystal	material	size [mm ³]	weight [g]	ρ [g/cm ³]
CCC 1943	LuYAP	$1.98 \times 1.97 \times 8.06$	0.2317	7.37
CCC 1946	LYSO	$1.98 \times 1.95 \times 7.92$	0.2248	7.35

4.3.1 Emission and excitation spectra

LuYAP

The emission and excitation spectra of the LuYAP crystal were recorded following the procedure described in Sect. 3.3 and are shown in Fig. 4.3. The

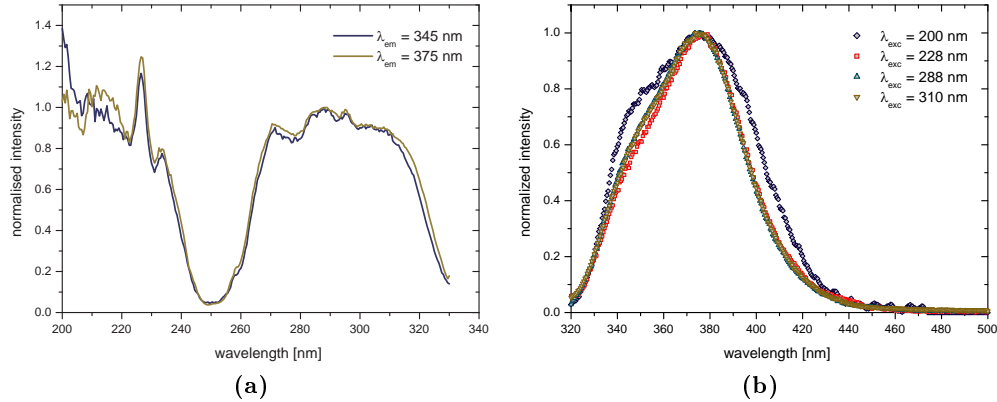


Figure 4.3: (a) Excitation and (b) emission spectra of LuYAP 1943.

excitation spectra were recorded at emission wavelengths of 345 nm and 375 nm, corresponding to the maxima of the two emission peaks that are observed in LuAP and LuYAP at low temperatures [25] and correspond to the $5d(^2D_{5/2})-4f(^2F_{7/2})$ and $5d(^2D_{3/2})-4f(^2F_{5/2})$ transitions of Ce^{3+} . Both curves share the most prominent features and exhibit several excitation bands between 250 nm

and 340 nm and below 240 nm.

The emission spectra recorded at 4 different excitation wavelengths (310 nm, 288 nm, 220 nm and 200 nm) all peak at about 375 nm and exhibit a distinct asymmetry which is due to the presence of the lower wavelength peak. The asymmetry (and therefore the strength of the peak) increases with decreasing excitation wavelength; still, the overall intensity of the $\lambda_{max} = 345$ nm peak is much lower than for the LuYAP samples studied in [25]. As Fig. 4.4 indicates, the emission spectra can be fitted with a sum of two Gaussians.

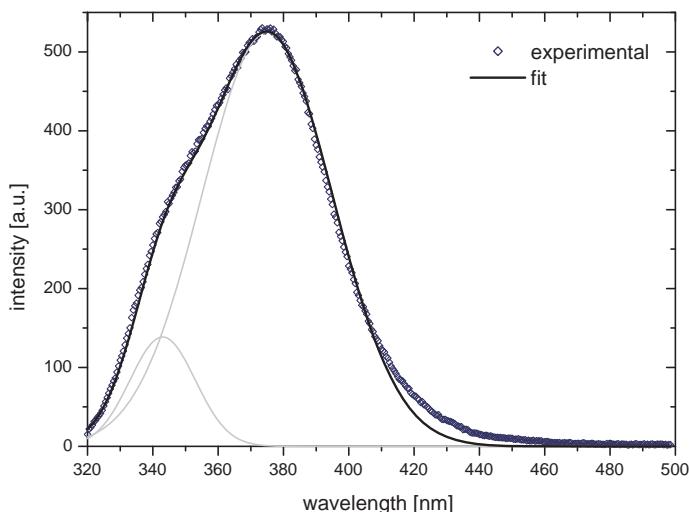


Figure 4.4: Fitted emission spectrum of LuYAP.

LYSO

Excitation spectra of LYSO taken at $\lambda_{em} = 390$ nm, 420 nm, and 500 nm are shown in Fig. 4.5. These spectra exhibit some interesting differences: While the excitation spectra at $\lambda_{em} = 390$ and 420 nm resemble each other very closely in showing three groups of peaks between 250 and 380 nm, the spectrum taken at 500 nm is clearly different in that these peaks are much less pronounced. Moreover, the $\lambda_{em} = 500$ nm curve exhibits a maximum at 325 nm whose position coincides to the dip observed in the two other spectra. This emission is possibly due to the quenched Ce_2 site of LYSO which has less symmetry and therefore a larger Stokes shift [25].

The presence of the Ce_2 site is also reflected in the UV-excited emission spectra of LYSO. Clearly, the emission peak is highly asymmetric due to a distinct tail at longer wavelengths which is more pronounced for shorter λ_{exc} . As the

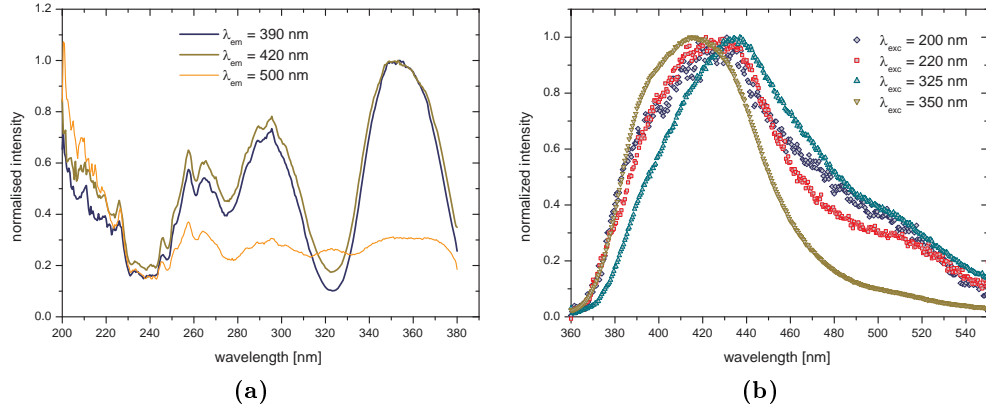


Figure 4.5: (a) Excitation and (b) emission spectra of LYSO 1946.

fit presented in Fig. 4.6 shows, all four emission bands are well resolved in the spectrum. However, there is a shift of the peak maximum observed for different λ_{exc} which cannot be explained alone by these four emission bands; this shift is especially evident in the $\lambda_{exc} = 325$ nm spectrum where it amounts to ≈ 10 nm. The reason for this shift is unclear but it is possibly due to emission from disturbed Ce_1 sites emitting at slightly larger wavelengths than the undisturbed sites.

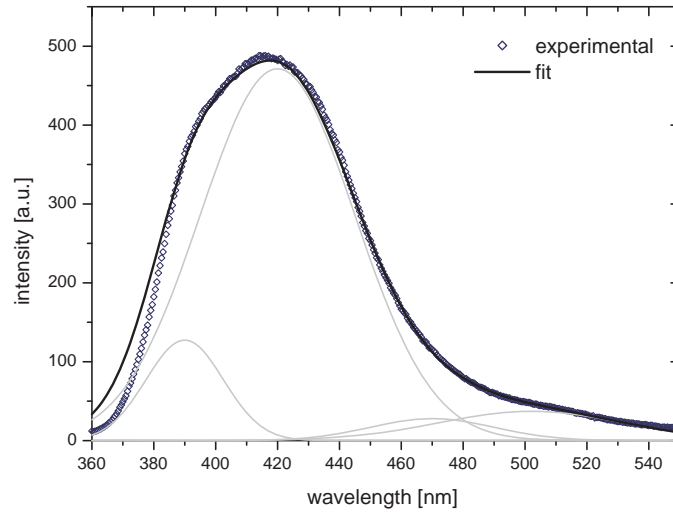


Figure 4.6: Fitted emission spectrum of LYSO.

4.3.2 Transmission spectra

The transmission spectra of LuYAP 1943 and LYSO 1946 are shown in Fig. 4.7. Each plot contains the transmission of the crystals along the shorter (2 mm)

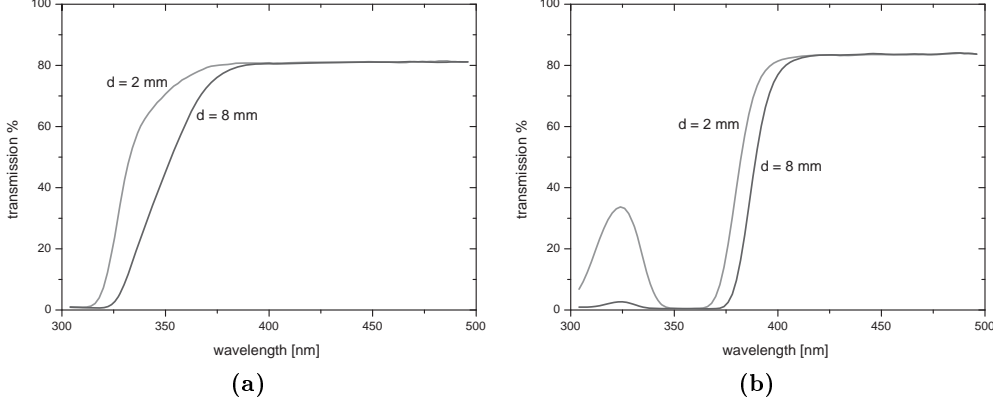


Figure 4.7: Transmission spectra of (a) LuYAP 1943 and (b) LYSO 1946 crystals along the shorter and longer axes.

and longer (8 mm) axes.

The transmission spectra reveal that the $5d(^2D_{5/2})$ - $4f(^2F_{7/2})$ peaks of both materials are situated at the falling edge of the transmission spectrum and are therefore significantly suppressed in the emission spectrum due to self absorption. This effect can be seen clearly for crystals of different size, where the intensity of this peak increases with decreasing sample thickness [5].

As indicated in Sect. 2.2.8, the difference in transmission along the shorter and longer axis can be used to determine the refractive index of the material and its attenuation length. Following eq. 2.36, the overall transmittance T_1 of a crystal with refractive index n , attenuation coefficient α_{att} and length l is given by

$$T_1 = \frac{t^2 \cdot e^{-\alpha_{att} \cdot l}}{1 - r^2 \cdot e^{-2\alpha_{att} \cdot l}} \quad (4.4)$$

The transmittance t and reflectance r are given by eq. 2.35. If this measurement is repeated for a crystal with identical n and α_{att} but length s , we will get two expressions for α_{att} [26]:

$$\begin{aligned} \alpha_{att} &= -\ln \left(\frac{-t^2 + \sqrt{t^4 + 4r^2 \cdot T_1^2}}{2r^2 \cdot T_1} \right) / l \\ \alpha_{att} &= -\ln \left(\frac{-t^2 + \sqrt{t^4 + 4r^2 \cdot T_2^2}}{2r^2 \cdot T_2} \right) / s \end{aligned} \quad (4.5)$$

Setting both equations identical and removing the logarithm yields

$$\left(\frac{-t^2 + \sqrt{t^4 + 4r^2 \cdot T_1^2}}{2r^2 \cdot T_1} \right)^{\frac{1}{l}} = \left(\frac{-t^2 + \sqrt{t^4 + 4r^2 \cdot T_2^2}}{2r^2 \cdot T_2} \right)^{\frac{1}{s}} \quad (4.6)$$

Setting $x = 4T_{1,2}^2 r^2 / t^4$ and omitting all elements of the Taylor series for $\sqrt{1+x}$ except the first two (since $t^4 \gg 4T_{1,2}^2 \cdot r^2$),

$$\sqrt{1+x} = \sum_n \frac{(-1)^n}{4^n} \frac{(2n)!}{(1-2n)n!^2} \cdot x^n, \quad |x| < 1 \quad (4.7)$$

yields

$$\left(\frac{T_1}{t^2} \right)^s \cdot \left[1 - \frac{T_1^2 \cdot r^2}{t^4} \right]^s = \left(\frac{T_2}{t^2} \right)^l \cdot \left[1 - \frac{T_2^2 \cdot r^2}{t^4} \right]^l \quad (4.8)$$

An approximate expression for n can be derived by eliminating the bracketed expressions in eq. 4.8 and re-ordering the equation:

$$\frac{T_1^s}{T_2^l} = t^{2(s-l)} \quad (4.9)$$

Eq. 4.9 can be reformulated to

$$t = \left(\frac{T_1^s}{T_2^l} \right)^{\frac{1}{2(s-l)}} \quad (4.10)$$

Using the expressions for the transmittance t and reflectance r in eq. 2.35 finally yields the following expression for the refractive index n of the material:

$$n = \frac{1 + \sqrt{1-t}}{1 - \sqrt{1-t}} \quad (4.11)$$

The attenuation coefficient α_{att} of the crystal or its inverse, the attenuation length λ_{att} , can then determined by one of the two eqs. 4.5.

The refractive indices and attenuation lengths of the LuYAP and LYSO crystals measured with this method are shown in Figs. 4.8 and 4.9. The transmission of each crystal was measured several times across its longer and shorter axes and the mean value for each wavelength was taken. In each measurement, it was assured that the crystal was aligned perpendicular to the beam. Further improvement was achieved by considering the bracketed expressions in eq. 4.8 in an iterative procedure. The standard deviations σ of the data points of n and λ_{att} was determined from the experimental errors.

Despite this, there is still considerable scatter of the measurement points visible in the plots. This can partly be accounted for the fact that the method presented above yields precise results only for the ideal case of crystals with perfectly parallel and polished faces and uniform, i.e position-independent bulk absorption. However, a major source of influence is the finite width of the spectral window

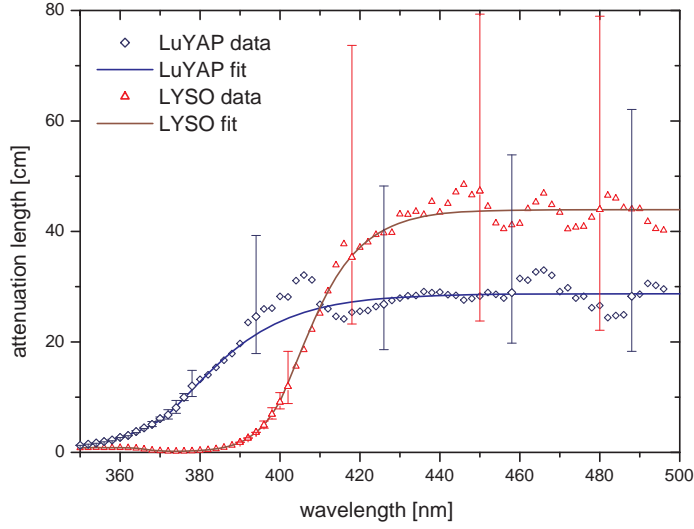


Figure 4.8: Absorption lengths of (a) LuYAP 1943 and (b) LYSO 1946. For reasons of clarity, error bars are only shown for selected values.

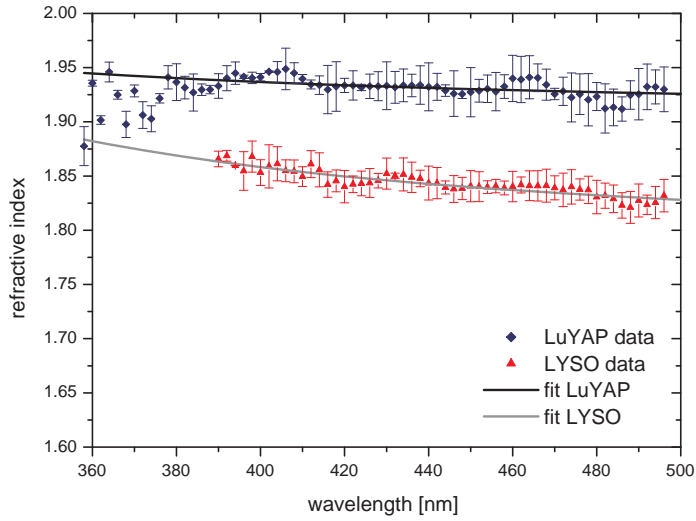


Figure 4.9: Refractive indices of (a) LuYAP 1943 and (b) LYSO 1946.

of the transmission bench, which measures ≈ 2.5 nm per measurement point. This is especially a problem at wavelengths where the second derivative of the transmission curve is significantly different from zero and leads to an overestimation of n and α_{att} or vice versa. Due to the small dimensions of the crystals, attenuation lengths $\lambda_{att} > 10$ cm exhibited very large errors; measurements of crystals with larger longitudinal dimensions would certainly provide a more precise result.

By restricting the measurements to points where the second derivative of both transmission curves is near zero, a fit of the data points can be applied by a single Sellmeier law approximation, where

$$n^2(\lambda) = A + \frac{B \cdot \lambda^2}{\lambda^2 - C} \quad (4.12)$$

The values of the Sellmeier coefficients for LuYAP and LYSO are given in Table 4.2. Because the wavelength range which was used for the fit ($360 \text{ nm} \leq \lambda \leq 500 \text{ nm}$) is relatively short, these values are probably only approximate ones. However, they still serve well to describe the wavelength dependence of the refractive indices of LYSO and LuYAP in the range of emission.

Table 4.2: Sellmeier coefficients of LuYAP 1943 and LYSO 1946.

crystal	A	B	C [nm ²]
LuYAP 1943	3.0665	0.57891	24 662
LYSO 1946	2.464	0.73098	41 756

4.4 Simulation of light propagation in LuYAP and LYSO

4.4.1 Simulated setups

The setup simulated with LITRANI is sketched in Fig. 4.10 and contains the following elements: a phototube (PMT), with a window of plain surface finish made of fused silica and a photo sensitive layer on the backside, a cuboid crystal of size $2 \times 2 \times 8 \text{ mm}^3$ with optical properties corresponding to that of LuYAP and LYSO, and a $50 \text{ }\mu\text{m}$ thin layer of material between PMT and crystal to account for the optical grease used in the experiment. The faces of the crystal cuboid were assumed to be perfectly polished and either unwrapped or enveloped by various reflector materials. When simulating unwrapped crystals, air cuboids were placed on top and at the sides of the crystal. Both vertically and horizontally aligned crystals were simulated. In the simulations, the scintillation light was either generated by gamma photons from a source 0.5 cm distant from the upper crystal face ($E_\gamma = 0.662 \text{ MeV}$), or by a point source placed at a fixed position within the crystal.

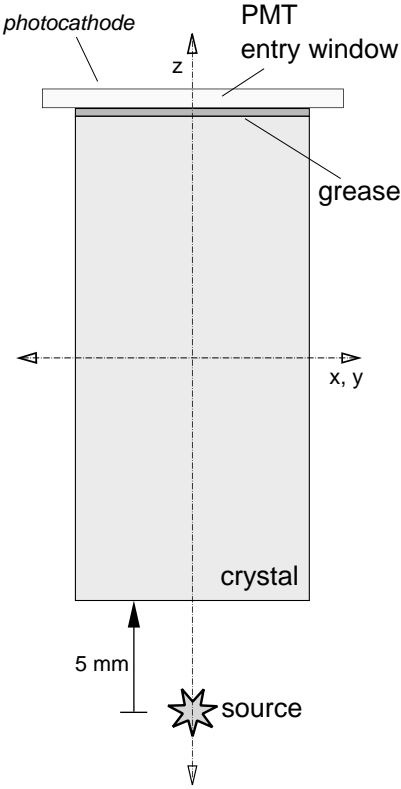


Figure 4.10: Setup simulated with LITRANI for crystals with plain exit surface.

4.4.2 Optical properties of setup materials

LuYAP and LYSO crystals

The emission spectra of LuYAP and LYSO were approximated by the sum of two Gaussian peaks. The maximum wavelengths λ_{max} , half-widths σ , and relative peak intensities are given in Table 4.3. For the line intensities, it was taken

Table 4.3: Emission properties of simulated LuYAP and LYSO crystals.

crystal	λ_{max} [nm]	σ [nm]	rel. intensity
LuYAP 1943	345	20	0.25
	375	40	0.75
LYSO 1946	390	25	0.30
	420	50	0.70

into account that the relative intensity of the lower wavelength emission band is smaller for UV induced emission than for emission induced by high energy radiation. From prior measurements of UV and x-ray excited spectra of LuYAP and LYSO in the CCC database, this correction factor was found to be near three for both crystal types. The Ce_2 components in the emission spectrum of LYSO were not taken into account due to their very low intensity exhibited

under x-ray excitation.

The attenuation lengths of both crystals were derived from Fig. 4.8. For the refractive indices, the Sellmeier coefficients from Table 4.2 were used. As the absolute light yield was unknown for both LuYAP and LYSO, its value was fixed to 10 000 ph/MeV in both cases. However, this was not a problem as the relevant parameter determined by the simulations was not the *number of photons* collected in a particle event but the *light collection efficiency* η_L , i.e. the ratio between collected and produced photons (see also eq. 2.11).

Optical coupling and PMT entry window

The refractive index n_{grease} of the slice between crystal and PMT was set to different values depending on whether an optical coupling by means of grease was simulated or not. In the case of a setup with grease, n_{grease} was set to 1.41. This value corresponds to the refractive index of the experimentally used grease [39]. If the case of no grease, n_{grease} was set to 1 to account for the small air gap between crystal and PMT. In both cases, the slice was simulated as highly transparent ($\lambda_{abs} = 1000$ cm). Refractive index and absorption length of the fused silica entry window of the PMT were taken from [27].

Reflector materials

The reflector materials used in the simulations are given in Table 4.4. The reflection properties of Teflon were modelled by adjusting the refraction index and extinction coefficient of the material so that the reflectivity met the results from experimental measurements [28]. The reflectivity of the material was assumed to

Table 4.4: Reflector materials used in the simulations of LuYAP and LYSO crystals.

material	type	reflectivity
Teflon	95% diffuse, 5% specular	wavelength dependent
Tyvek	99.8% diffuse, 0.02% specular	wavelength dependent
Aluminium	100% specular	wavelength dependent
Reflector (fictive)	100% specular	fixed 98%
Diffusor (fictive)	95% diffuse, 5% specular	fixed 98%

be 95% diffusing and 5% specular. Refractive indices and extinction coefficients for aluminium and Tyvek were taken from the LITRANI database. In addition, two reflector materials with 98% reflectivity were simulated: a diffusing one with diffusion characteristics equal to Teflon, and a purely specular reflector.

For testing the validity of different reflector models, the Teflon wrapping was simulated with and without gap between crystal and wrapping. In the case of a gap, the gap material was either simulated with $n_{gap} = 1$ or with $n_{gap} = 1.35$, depending on whether the diffusing layer was separated from the crystal by a

slice of air or, by a transparent Teflon layer. This latter case was simulated as the Teflon band used for the crystal wrappings in the experiments is very sticky and becomes partly transparent when gently squeezed onto the crystal.

4.4.3 Results of simulations

Position of source in gamma-irradiated crystals

Fig. 4.11 shows the number of generated photons per position in z for LuYAP in the presence of a ^{137}Cs γ -source. Clearly, the majority of photons is generated

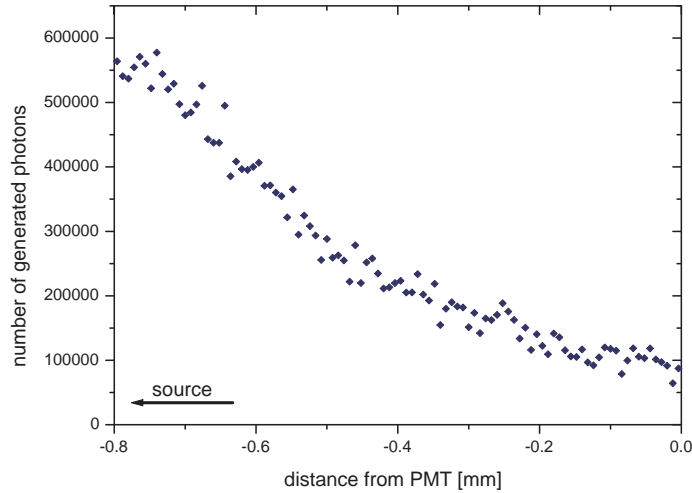


Figure 4.11: Number of photons generated in LuYAP per position in z .

near the source. The slope of the curve is steeper than would be expected from the attenuation length of the crystal alone, which is 1.6 cm for ^{137}Cs and $\text{Lu}_{0.7}\text{Y}_{0.3}\text{AlO}_3\text{:Ce}$ [29]. This is partly a consequence of the smaller solid angle of the lower crystal regions relative to the upper parts, as seen from the source; however, Compton-scattered γ -photons that leave the crystal before depositing all their energy also add to this effect.

Influence of scattering on the light collection process

As noted in Section 2.2.8, the attenuation of a beam observed in a transmission measurement is not only due to absorption of the incoming light but also caused by scattering of the light at atoms and internal defects. Accordingly, a transmission measurement only gives information on the combined effect of absorption and scattering; an independent experimental determination of either the absorption length or the scattering length is, however, not possible [12].

What is the effect of light scattering on η_L ? In a crystal without scattering, the destiny of a photon is fixed at the moment of generation: photons that are emitted at an angle larger than the angle of total reflection will remain trapped within the crystal and will never induce a signal in the PMT. On the other hand, in a crystal with scattering, the propagation direction of photons outside the extraction cone may be modified so that they become un-trapped [31]. As a consequence, η_L will be dependent on the scattering coefficient α_{scat} .

As the sum of α_{abs} and α_{scat} is always determined by α_{att} (eq. 2.34), the problem of fixing α_{abs} and α_{scat} in the simulations can be reduced to fixing any one of these two. This is done by introducing a variable B , which is given as the ratio of α_{scat} to α_{abs} [13]:

$$B = \frac{\alpha_{scat}}{\alpha_{abs}} = \frac{\lambda_{abs}}{\lambda_{scat}} \quad (4.13)$$

Using B , the probabilities that a photon undergoes scattering or absorption can be expressed by

$$\begin{aligned} P_{scat} &= \frac{B}{1+B} \\ P_{abs} &= \frac{1}{1+B} \end{aligned} \quad (4.14)$$

The importance of scattering on the process of light collection is well seen in Fig. 4.12 which illustrates the correlation between B and η_L for a LuYAP crystal for different configurations (with/without Teflon wrapping, with/without grease). As the plot shows, η_L is strongly dependent on B , with differences of

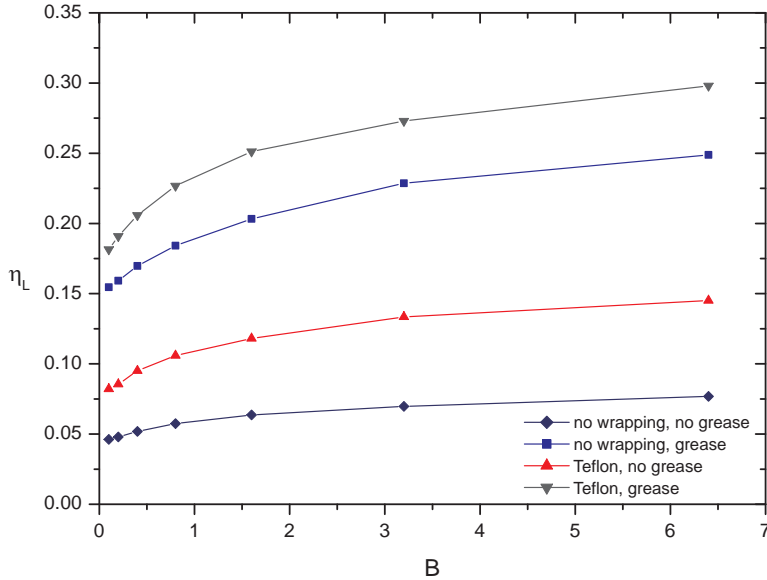


Figure 4.12: Dependence of η_L on B for LuYAP.

up to 70% between η_L at $B = 0.1$ and $B = 6.4$ (unwrapped crystal, grease).

The dependence of η_L on the scattering coefficient has an important consequence: if for a given scintillator the amount of scattering in the crystal bulk can be increased without changing the absorption properties, the scintillator will exhibit a higher light yield relative to the situation before. Increasing the scattering coefficient is therefore an efficient way to improve the light collection efficiency (and therefore the light output) of a scintillator.

Influence of n_{grease}

The dependence of η_L of LuYAP and LYSO crystals on n_{grease} is shown in Fig. 4.13. In both cases, the crystals were simulated with Teflon wrapping plus

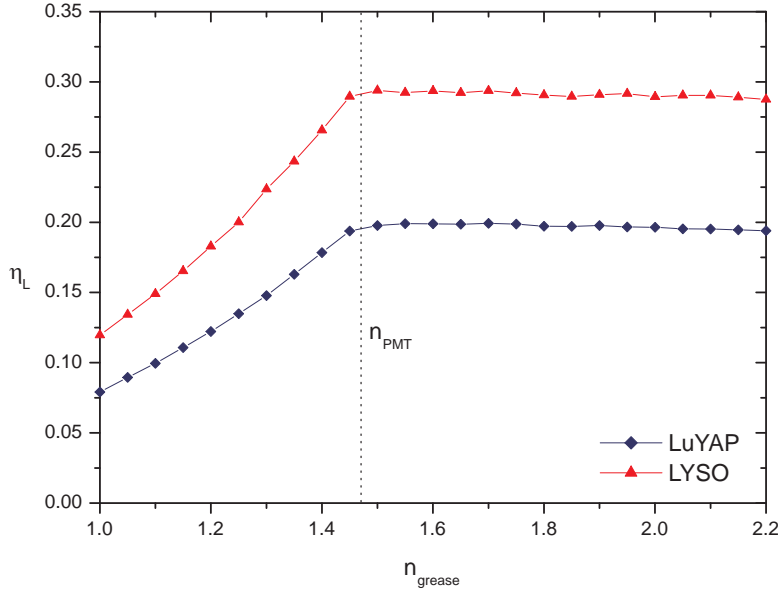


Figure 4.13: Dependence of η_L on n_{grease} .

air gap.

The curves for LuYAP and LYSO exhibit a very similar behaviour: a steep rise of η_L for $n_{grease} < n_{PMT}$ and an almost constant η_L for $n_{grease} > n_{PMT}$ (there is, in fact, a slight decrease in η_L apparent); n_{PMT} signifies the refractive index of the PMT entry window. On the other hand, this means that η_L is almost independent of n_{grease} , as long as n_{grease} is equal or larger than the refractive index of the entry window of the PMT [33].

This behavior is surprising at first glance, but becomes clear when the situation at the two interfaces is considered by Snell's law. Assuming that $n_{grease} > n_{PMT}$, the angle of total reflection θ_{tot} of the interface grease-PMT is given by

the formula

$$\sin(\theta_{tot}) = \frac{n_{PMT}}{n_{grease}} \quad (4.15)$$

On the other hand, any wave that hits the interface PMT-grease at an angle θ_{tot} has been traveling through the crystal at an angle θ_c , which is given by

$$n_{crys} \cdot \sin(\theta_c) = n_{grease} \cdot \sin(\theta_{tot}) \quad (4.16)$$

Substituting $\sin(\theta_{tot})$ by eq. 4.15 yields

$$\sin(\theta_c) = \frac{n_{PMT}}{n_{crys}}, \quad (4.17)$$

which is nothing else than Snell's law for an interface between two media with refractive indices n_{PMT} and n_{crys} . An n_{grease} higher than the refractive index of the PMT expresses itself therefore only in an increasing reflection coefficient at the interface grease-PMT (cf. eq. 2.35). However, this effect is almost totally compensated by the high transparencies of the materials: almost every back-reflected photon will re-appear at the interface grease-PMT and eventually, become extracted.

Influence of source position

The dependence of η_L on the distance of the light source from the PMT is depicted in Fig. 4.14 for a vertically aligned LuYAP crystal. Simulations were

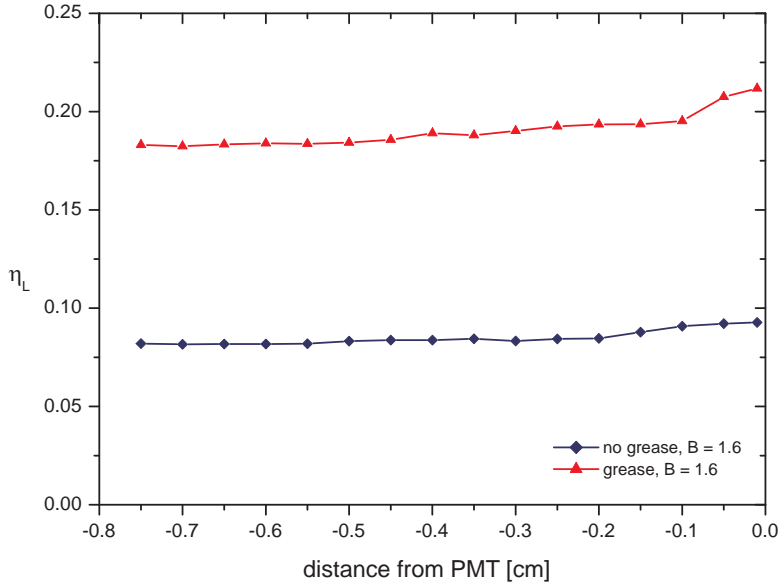


Figure 4.14: Dependence of η_L on the position of the light source. The light source is placed on the symmetry axis of the crystal.

performed for various values of B and with and without optical coupling to the

PMT.

Due to the high transparency of the materials, η_L is only weakly dependent on the source position. Only in proximity to the PMT, a slight increase is observed if optical coupling is present. This increase is a well-known feature in other heavy inorganic scintillators as PWO [32] and is due to the detection of scintillation photons with $\lambda \approx \lambda_c$ which otherwise suffer from the strong decrease of the absorption length around the falling edge of the transmission curve.

Influence of the wrapping

Figs. 4.15a and 4.15b compare η_L of LuYAP and LYSO for different wrapping types. In each case, the value of η_L for $B = 1.6$ is shown.

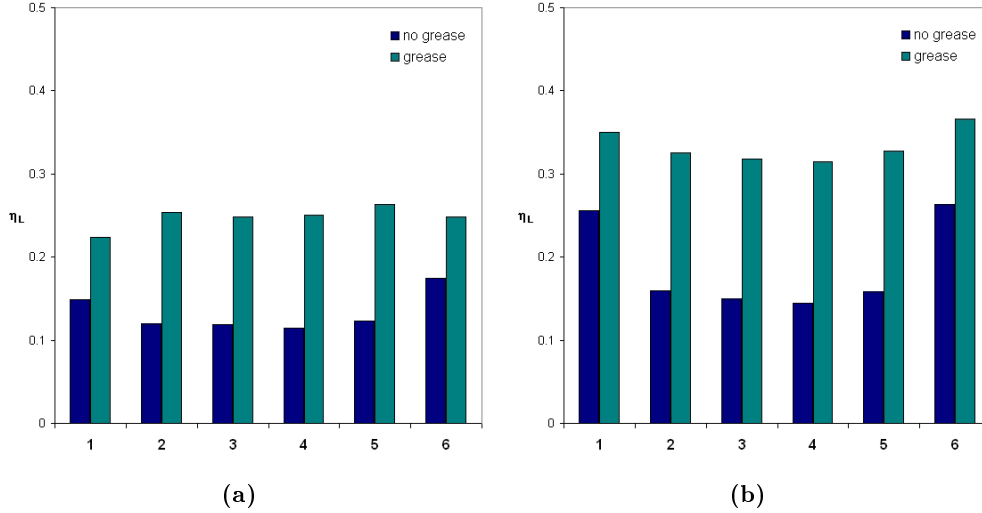


Figure 4.15: Dependence of η_L of (a) LuYAP and (b) LYSO on the wrapping type and for $B = 1.6$. (1) Teflon, $n_{gap} = 1.35$; (2) Teflon, $n_{gap} = 1$; (3) Tyvek, $n_{gap} = 1$; (4) Aluminium, $n_{gap} = 1$; (5) 98% Reflector, $n_{gap} = 1$; (6) 98% Diffusor, $n_{gap} = 1.35$.

It is apparent from the plots that if no optical coupling is used, the diffusing reflectors with $n_{gap} = 1.35$ perform considerably better than all other wrappings. This is a consequence of the fact that more photons arrive within the extraction cone as the higher n_{gap} allows an exchange of photons between the wrappings on perpendicular faces. In other words, the diffusion of the photons by the wrapping 'assists' the light scattering processes in the bulk in terms of changing the propagation direction of the photons so that they can be extracted. This effect is significantly reduced if an optical coupling is used: in this case, the majority of the detected photons are transported to the exit surface by total internal reflection at the side faces and the exchange of photons between perpendicular faces has much less influence on η_L .

Angular distribution of photons that arrive at the exit surface

In order to evaluate the potential of any method to increase η_L of a scintillator, it is necessary to know *how many* of the photons that are produced by an incident particle actually reach the coupling face of the scintillator. These photons comprise the 'pool' of photons that could be extracted from the crystal under ideal conditions.

In total, there are three possibilities how a photon can get lost before it arrives at the exit surface of the crystal:

1. escape from the bulk through side faces or back face;
2. absorption in the bulk; and
3. absorption by the wrapping.

Each of these processes eliminates photons from the pool of extractable photons and therefore reduces the value of η_L that is achievable *at best*, i.e. when all photons arriving at the exit surface are extracted.

However, the number of photons which finally arrive at the exit surface depends not only on the absorption length of the bulk and the reflectivity of the wrapping but also on whether the wrapping is a specular or a diffusing reflector. This can be seen in Fig. 4.16 which compares, for a LuYAP crystal with $B = 1.6$

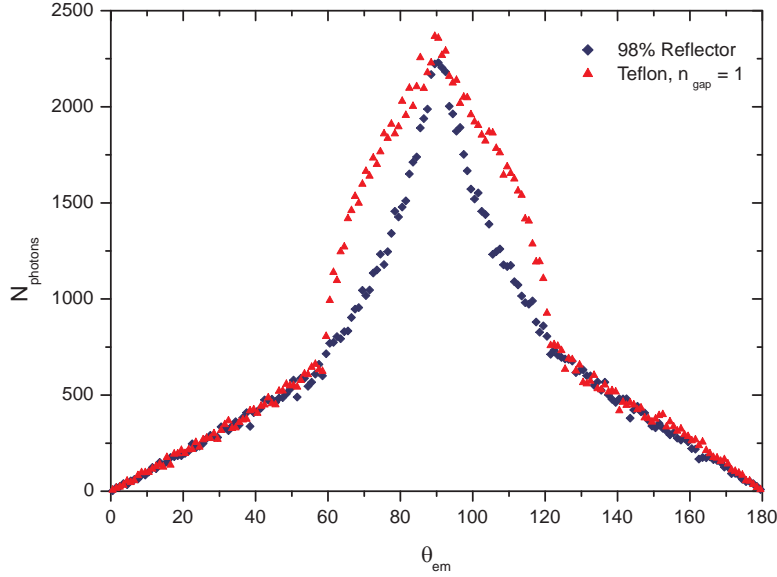


Figure 4.16: Angular distribution of photons which never reach the exit surface for LuYAP.

the angular distribution of the lost photons (i.e. photons that never arrive at

the exit surface) for two wrappings (Teflon, 98% reflector). θ_{em} indicates the angle of the photon relative to the z -axis at the moment of emission; the PMT is positioned in positive z direction (Fig. 4.17).

Clearly, the Teflon wrapping is less efficient in transporting photons to the exit surface than the 98% reflector. This is especially evident for $\theta_{em} > 60^\circ$ where a

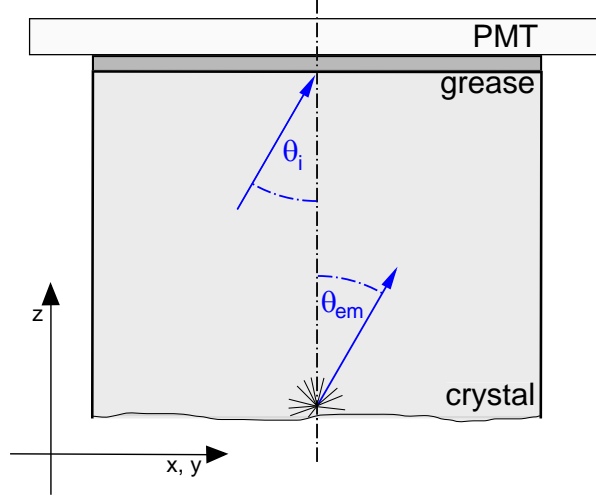


Figure 4.17: Definition of θ_{em} and θ_i .

sudden increase of the number of lost photons can be observed. This behaviour is not seen for the reflective wrapping.

Although surprising at first glance, the curve shape observed in the case of Teflon wrapping can be understood when the propagation of a photon through the crystal is more closely examined. In the case of a reflective wrapping, any reflection at a crystal face or at the wrapping will be specular, and the only possibility for a photon to change its propagation angle relative to the z axis is to undergo scattering. For this reason, the angular distribution of the arriving photons will be primarily determined by the absorption characteristics of the bulk and the wrapping.

This is different in the case of a diffusing wrapping: While photons where $90^\circ - \theta$ is larger than θ_{tot} of the side face will be efficiently transported towards the coupling face by means of total reflection, photons with an $90^\circ - \theta < \theta_{tot,side}$ will change their propagation direction each time they hit the wrapping. Since θ will be randomly changed only between $90^\circ - \theta_{tot,side}$ and $90^\circ + \theta_{tot,side}$ after each hit, the majority of these photons will end up bouncing between two opposing crystal faces until they eventually become absorbed in the bulk or by the wrapping.

It is interesting to compare, for different wrappings, the angular distribution of

photons at the moment they hit the exit surface for the first time $D_{hit}(\theta)$ with the angular distribution of the extracted photons $D_{ex}(\theta)$. $D_{hit}(\theta)$ is shown in Figs. 4.18a and 4.18b for LuYAP and LYSO with $B = 1.6$, respectively. As can be seen from the plots, the number of arriving photons as well as $D_{hit}(\theta)$ depend largely on the wrapping type. While the diffusing wrappings with $n_{gap} = 1.35$ show a pronounced deficit of photons with angles $> 50^\circ$, the number of photons is still large for the reflective wrapping at $\theta = 75^\circ$; in other words, the pool of 'extractable' photons is much larger for the reflective wrapping than for the diffusing ones.

Interestingly, the effect of the different wrappings on the actual number of extracted photons is only small. This is a consequence of the fact that only photons arriving within the extraction cone (i.e. $\theta < \theta_{tot}$) can be extracted; in this angular regime, the arriving photons are transported towards the exit surface by total internal reflection at the side faces and wrapping-dependent effects play only a secondary role. On the other hand, this means that for every wrapping, a significant fraction of the photons arriving at the exit surface remains trapped in the crystal due to total internal reflection. This is illustrated in Figs. 4.19a and 4.19b, where the angular distributions of arriving and extracted photons are compared for LuYAP and LYSO in the case of the 98% reflector. The slightly larger numbers of extracted photons at angles $< \theta_{tot}$ is due to photons that are scattered into the extraction cone after their first arrival at the exit surface.

The influence of the simulated wrappings on the numbers of arriving and extracted photons are summarized in Table 4.5. Clearly, the losses due to total internal reflection at the exit surface are significant in all cases; the highest losses are observed for the fictive 98% reflector where they amount to $\approx 60\%$ of the arriving photons in the case of grease and to almost 80% in the case of no grease.

Table 4.5: Arriving (ph_{arr}) and extracted (ph_{ext}) photons for different wrappings ($B = 1.6$) relative to the number of generated photons from simulations of LuYAP and LYSO.

crystal	wrapping	ph_{arr} [%]	ph_{ext} no grease [%]	ph_{ext} grease
LuYAP	Teflon, $n_{gap} = 1.35$	35.8	14.9	22.4
	Teflon, $n_{gap} = 1$	50.5	12.0	25.4
	Tyvek	49.5	11.9	24.8
	Aluminium	52.8	11.4	25.0
	98% reflector	59.1	12.3	26.3
	98% diffusor	42.6	17.5	24.9
LYSO	Teflon, $n_{gap} = 1.35$	48.1	25.5	35.0
	Teflon, $n_{gap} = 1$	60.1	15.9	32.5
	Tyvek	55.1	15.0	31.8
	Aluminium	60.3	14.4	31.5
	98% reflector	69.3	15.8	32.8
	98% diffusor	50.6	26.3	36.6

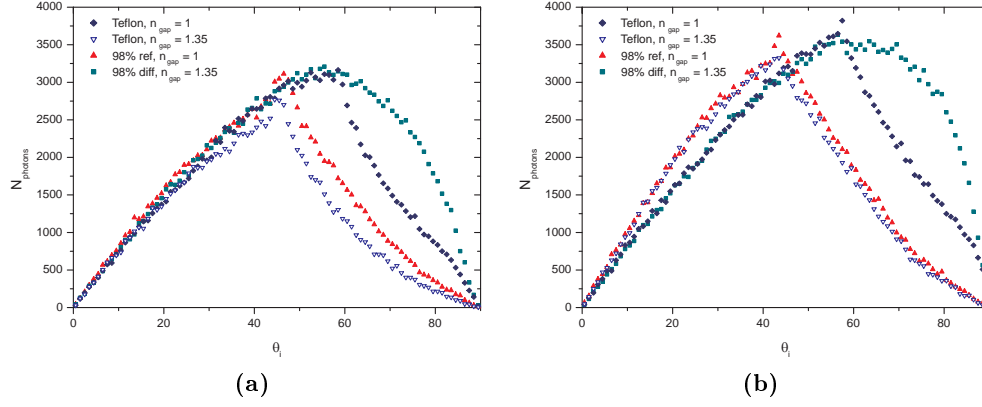


Figure 4.18: Angular distribution of the photons arriving at the exit surface ($B = 1.6$). (a): LuYAP (b) LYSO.

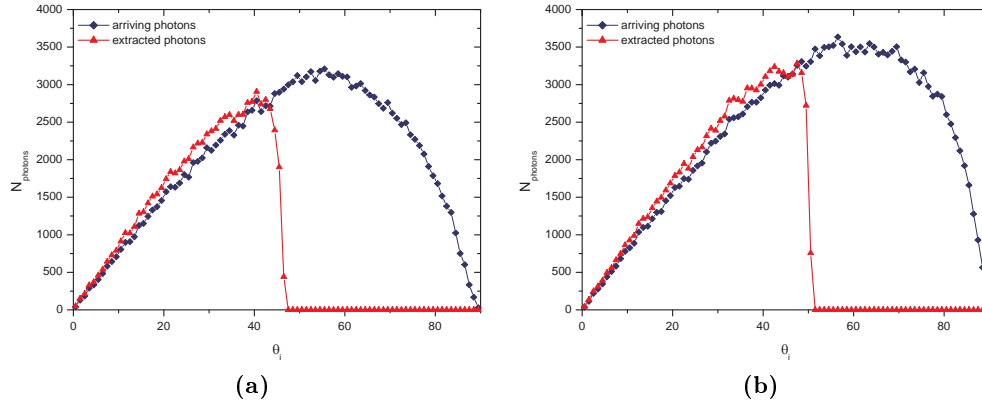


Figure 4.19: Comparison between arriving and extracted photons for (a) LuYAP and (b) LYSO wrapped with the fictive 98% reflector ($B = 1.6$).

4.5 Measurements of LuYAP and LYSO samples

The simulations performed with LITRANI presented in the last section have given an insight into the propagation of the scintillation photons inside the scintillators and the influence of various parameters, as the scattering length, the refractive index of the optical coupling, and the wrapping. In addition, it was shown that only a fraction of the photons arriving at the exit surface are extracted due to losses induced by total internal reflection at the coupling face. However, the impact of the simulated results critically depends on whether they can be reproduced under experimental conditions. In order to validate the simulated results of these simulations, they are compared in the following with results of measurements of LuYAP and LYSO.

4.5.1 Light output measurements

The results of measurements of the light output performed for the $2 \times 2 \times 8$ mm³ LuYAP and LYSO crystals are outlined in Table 4.6. In each case, the light output was determined by folding the number of collected photoelectrons with the quantum efficiency of the PMT shown in Fig. 3.3. The table nicely

Table 4.6: Results of measurements for the $2 \times 2 \times 8$ mm³ LuYAP and LYSO crystals.

crystal	alignment	no wrapping		Teflon wrapping	
		no grease [ph/MeV]	grease [ph/MeV]	no grease [ph/MeV]	grease [ph/MeV]
LuYAP	vertical	629 ± 27	$2\,472 \pm 141$	$2\,159 \pm 10$	$3\,836 \pm 17$
	horizontal	$1\,320 \pm 20$	$3\,782 \pm 141$		
LYSO	vertical	$3\,397 \pm 392$	$10\,882 \pm 701$	$13\,132 \pm 450$	$19\,417 \pm 543$
	horizontal	$5\,598 \pm 277$	$14\,048 \pm 317$		

reveals the effect of the grease and the wrapping on the extraction of light from the crystals: while the light output is very low for measurements without wrapping and without grease, it is higher if any of these two is used and highest if both are used. In addition, it is apparent that the light output measured in horizontal position is significantly higher than in vertical position. This is mostly a consequence of the shorter average distance between photon emission point and PMT due to which less photons are absorbed before arriving at the exit surface. This is also supported by the fact that the effect is more pronounced for the LuYAP crystal whose absorption length is significantly smaller than that of LYSO.

4.5.2 Comparison with simulated data

Light yield spectra

Simulated and measured light yield spectra are compared in Figs. 4.20a and 4.20b for a Teflon wrapped LuYAP crystal with and without grease. To make the com-

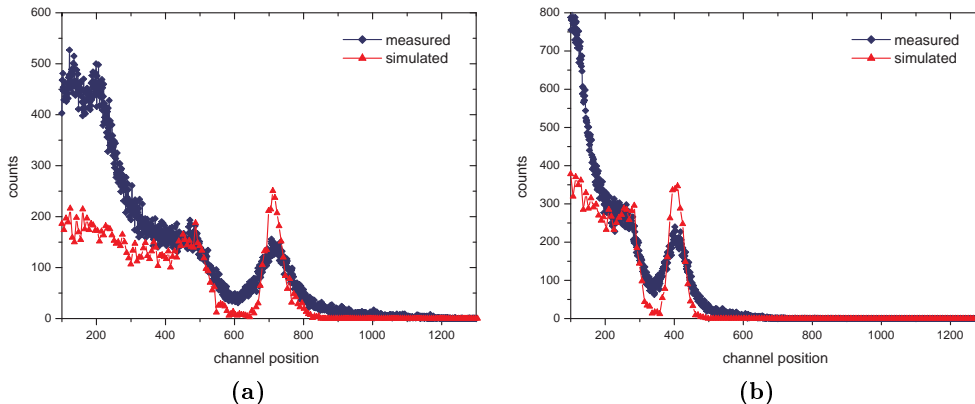


Figure 4.20: Comparison between simulated and measured light yield spectra for LuYAP. (a) grease; (b) no grease.

parison possible, the simulated spectrum was scaled on the position of the photo peak and its height was normalized to that of the Compton edge of the measured light yield spectrum.

Clearly, the general shape of the curve and the relative positions of Compton edge and photopeak are well reproduced by the simulations; the different appearance of the simulated and measured spectra at lower channel positions is a consequence of the fact that backscatter of γ -photons could not be simulated. The better energy resolution of the simulated photopeak is a consequence of the fact that in the simulations, neither the intrinsic energy resolution R_i of the scintillator (which amounts to $\approx 4\%$ FWHM in the case of LuYAP) nor any PMT-dependent resolution parameters have been taken into account.

Light yield and η_L of crystals without wrapping

The experimental light yield values obtained for LuYAP and LYSO crystals without wrapping are compared with the values of the simulations in Table 4.7. In all cases, the given experimental values are average values of several ($= 3-5$) individual measurements obtained for each crystal in different configurations (horizontal/vertical, with/without grease). Simulation values are derived from the values of η_L calculated by LITRANI and given for $B = 0.1$ and $B = 1.6$. Both experimental and simulated values are normalized to the light yield or the value of η_L obtained for the case of a vertical crystal coupled with grease to the PMT.

It is apparent that the simulations reflect the response of the measured light yield on different setups and environmental conditions very well. With one exception (LuYAP - vertical - without grease), the simulated and experimental values are usually within 10% of the simulated values. This means that even

Table 4.7: Comparison of measured and simulated light yields: crystals without wrapping.

crystal	alignment	grease	LY measured	LY simulated	
				$B = 0.1$	$B = 1.6$
LuYAP	vertical	no	25 ± 2	30 ± 1	31 ± 1
	vertical	yes	100	100	100
	horizontal	no	53 ± 3	54 ± 1	53 ± 1
	horizontal	yes	153 ± 10	149 ± 2	139 ± 1
LYSO	vertical	no	31 ± 4	28 ± 1	30 ± 1
	vertical	yes	100	100	100
	horizontal	no	51 ± 4	47 ± 1	48 ± 1
	horizontal	yes	129 ± 9	132 ± 1	128 ± 1

though the quality of the shape and the face polishing of the scintillators have not been tested and likely cannot be assumed to be perfect, the simulation still describes the experimental system reasonably well.

As the differences between η_L for the studied setup configurations are only small for different values of B , a precise determination of the diffusion coefficient, as in [12], was not possible. However, there is a tendency detectable that the values measured for LuYAP fit better with the $B = 0.1$ simulations while the LYSO data agree better with the $B = 1.6$ simulations. This indicates that scattering may play a more dominant role for LYSO than for LuYAP in the photon propagation.

Light yield and η_L of crystals with wrapping

As mentioned in Sect. 4.2, the simulation of a crystal enveloped by a reflecting or diffusing material is not straightforward. This is due to the fact that it is often very difficult to model the optical properties of the wrapping in a precise way; typically, the relevant optical parameters are often unknown or changed in an unknown manner by the interplay between crystal and wrapping. Additional effects that influence the performance of a wrapping under experimental conditions come from its surface state and uniformity, i.e. if the surface is oxidized or contains dusty spots, if it fits flatly to the crystal or exhibits wrinkles, etc. In addition, any imperfection of shape and/or surface finishing of the crystal will influence the measured light yield stronger than for a crystal without wrapping since the mean path length of the photons will be significantly larger in the wrapped crystal.

The results of the simulations with wrapping are shown in Table 4.8 for LuYAP and LYSO. As before, the measured and simulated light yields were normalized to the value obtained for the respective values for unwrapped crystals with optical coupling. Clearly, none of the simulated systems reflect the behavior under experimental conditions reasonably well; without exception, the measured light yields are much higher compared to the unwrapped case as predicted by the simulations. In the case of LuYAP, the best agreement is found for the setup where

the Teflon layer is separated from the crystal by the $n_{gap} = 1.35$ gap, while the largest discrepancies are found for the model where the diffusing Teflon layer is directly attached to the crystal surface. In the case of LYSO both models agree reasonably well, very likely due to the very high reflectivity ($> 95\%$) of Teflon in the LYSO emission range. Despite this, it is apparent that additional effects play a major role in the light collection process when a wrapping is used in the experimental system.

When comparing the values of LY and η_L determined for the reference setup (unwrapped, vertical, grease) with the values obtained for wrapped crystals given in Table 4.8, it is also apparent that the effect of the wrapping on the light yield of the crystals is more pronounced in the case of LYSO. As before, this is probably a consequence of the higher reflectivity of Teflon in the emission wavelength range of LYSO compared to that of LuYAP.

Table 4.8: Comparison of measured and simulated light yields: crystals with Teflon wrapping. The last column indicates the refractive index of the slice of material between crystal and wrapping.

crystal	alignment	grease	LY measured	LY simulated		n_{gap}
				$B = 0.1$	$B = 1.6$	
LuYAP	vertical	no	87 ± 5	53 ± 1	58 ± 1	1 (air)
				72 ± 1	76 ± 1	1.35
				50 ± 1	49 ± 1	no gap
	vertical	yes	155 ± 9	117 ± 1	124 ± 1	1 (air)
				113 ± 1	110 ± 1	1.35
				81 ± 1	79 ± 1	no gap
LYSO	vertical	no	121 ± 9	55 ± 1	61 ± 1	1 (air)
				98 ± 1	97 ± 1	1.35
				97 ± 1	96 ± 1	no gap
	vertical	yes	178 ± 13	121 ± 1	123 ± 1	1 (air)
				136 ± 1	133 ± 1	1.35
				144 ± 2	138 ± 1	no gap

Comparison with $2 \times 2 \times 10 \text{ mm}^3$ LuYAP and LYSO crystals

An additional test of the results obtained for the $2 \times 2 \times 8 \text{ mm}^3$ crystals was performed with four $2 \times 2 \times 10 \text{ mm}^3$ LuYAP and LYSO crystals measured in parallel (CCC 1997 - 2000; see also Section 5.3.1). The results are summarized in Tables 4.9 and 4.10. As before, the light yield under different setup configurations is well reproduced by the simulations if the crystals are unwrapped while the simulated light yields are significantly too low in the case where a wrapping is apparent.

4.6 The absolute light yield of LuYAP and LYSO

In the preceding section, the results of light yield measurements on LuYAP and LYSO crystals were presented and compared with the values that would be expected from simulations. However, the knowledge of the light yields and η_L for

Table 4.9: Comparison of measured and simulated light yields for $2 \times 2 \times 10$ mm³ LuYAP crystals. All measurements were performed with the crystals in vertical alignment.

wrapping	grease	CCC 1999	CCC 2000	LY simulated $B = 0.1$	LY simulated $B = 1.6$	n_{gap}
no	no	24 ± 1	30 ± 2	31 ± 1	31 ± 1	
	yes	100	100	100	100	
yes	no	79 ± 9	86 ± 6	53 ± 1	58 ± 1	1 (air)
				71 ± 1	72 ± 1	1.35
	yes	136 ± 6	156 ± 8	119 ± 1	123 ± 1	1 (air)
				114 ± 9	109 ± 1	1.35

Table 4.10: Comparison of measured and simulated light yields for $2 \times 2 \times 10$ mm³ LYSO crystals. All measurements were performed with the crystals in vertical alignment.

wrapping	grease	CCC 1997	CCC 1998	LY simulated $B = 0.1$	LY simulated $B = 1.6$	n_{gap}
no	no	29 ± 1	31	28 ± 1	29 ± 1	
	yes	100	100	100	100	
yes	no	112 ± 5	98	54 ± 1	60 ± 1	1 (air)
				93 ± 1	92 ± 1	1.35
	yes	170 ± 5	163	120 ± 1	122 ± 1	1 (air)
				130 ± 1	125 ± 1	1.35

the same setup configurations makes it also possible to determine the absolute light yield LY_{abs} of the crystals [12].

Following eq. 2.12, the light output of a scintillator is determined by

$$LY[\text{ph/MeV}] = \eta_L \cdot \tau \cdot LY_{abs} \quad (4.18)$$

Reformulating this expression for LY_{abs} and setting $\tau = 1$ yields

$$LY_{abs}[\text{ph/MeV}] = \frac{LY}{\eta_L} \quad (4.19)$$

The results are presented in graphical form in Fig. 4.21 and summarized in Table 4.11 for two values of B ($B = 0.1$ and $B = 1.6$). In each case, LY_{abs} was

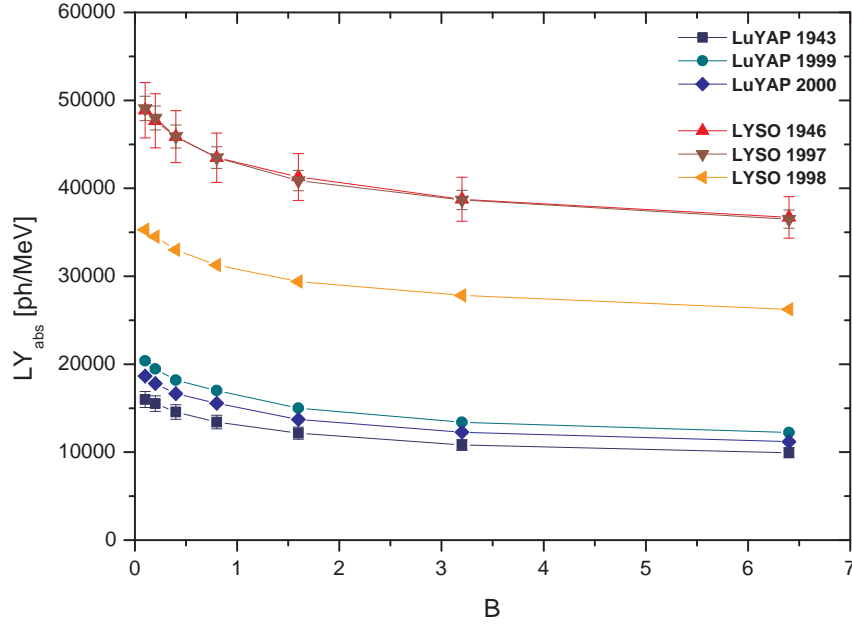


Figure 4.21: Absolute light yields of measured LuYAP and LYSO crystals vs. B .

determined from LY and η_L for the measurements and simulations in vertical orientation without wrapping and with optical coupling. The average value for LYSO given in Table 4.11 corresponds to the average of LYSO 1946 and 1997 only due to the significantly smaller light output of the crystal LYSO 1998. The errors correspond to statistical errors based on the measurements.

The new values of LY_{abs} permit a new estimation of the product $S \cdot Q$ according

Table 4.11: Absolute light yields of measured LuYAP and LYSO samples. The average value of LYSO is determined only by LYSO 1946 and 1997.

crystal		LY	η_L		LY_{abs} [ph/MeV]	
		[ph/MeV]	$B = 0.1$	$B = 1.6$	$B = 0.1$	$B = 1.6$
LuYAP	1943	2472 ± 141	0.1546	0.2032	15991 ± 1033	12164 ± 775
	1999	2941 ± 44	0.1443	0.1961	20385 ± 472	15001 ± 330
	2000	2690 ± 30	0.1443	0.1961	18646 ± 361	13721 ± 250
LYSO	1946	10882 ± 701	0.2226	0.2636	48879 ± 3455	41290 ± 2897
	1997	10660 ± 302	0.2172	0.2608	49079 ± 1715	40881 ± 1403
	1998	7665	0.2172	0.2608	35290	29394
Average LuYAP					18341 ± 1605	13629 ± 1084
Average LYSO					48979 ± 2798	41086 ± 2421

to eq. 2.10, which is repeated here for convenience reasons:

$$LY_{abs}[\text{ph/MeV}] = \frac{SQ}{N_{eh}} = \frac{SQ}{bE_G[\text{MeV}]} \quad (4.20)$$

$N_{eh} = 1/bE_G$ gives the number of e-h pairs created per MeV according to eq. 2.4. Reformulating eq. 4.20 yields

$$S \cdot Q = \frac{LY_{abs}}{N_{eh}} \quad (4.21)$$

The results are shown in Table 4.12 for $B = 0.1$ and $B = 1.6$. As before, only LuYSO 1946 and 1997 are considered in the average value for LYSO. The

Table 4.12: $S \cdot Q$ of LuYAP and LYSO.

crystal		N_{eh}	$S \cdot Q$	$S \cdot Q$
			$B = 0.1$	$B = 1.6$
LuYAP	1943	55 556	0.288 ± 0.019	0.219 ± 0.014
	1999		0.367 ± 0.008	0.270 ± 0.006
	2000		0.336 ± 0.006	0.247 ± 0.005
LYSO	1946	69 444	0.704 ± 0.050	0.595 ± 0.042
	1997		0.707 ± 0.025	0.589 ± 0.020
	1998		0.508	0.423
Average LuYAP			0.330 ± 0.029	0.245 ± 0.020
Average LYSO			0.705 ± 0.041	0.592 ± 0.035

estimated numbers of e-h pairs N_{eh} per MeV were taken from [34].

A comparison with previously published values of LY_{abs} (Table 4.13) shows that the absolute light yield of LuYAP and LYSO was by far underestimated in previous publications; this highlights the importance of Monte-Carlo simulations in the determination of LY_{abs} .

Table 4.13: Previously published values of LY_{abs} of LuYAP and LYSO.

crystal	LY_{abs} [ph/MeV]	reference
LuYAP	8 530	[38]
	7 400	[4]
LYSO	33 800	[35]
	< 30 000	[36]
	29 000	[37]

4.7 Conclusions

In this chapter, the basic properties of the propagation of light in scintillating crystals have been reviewed and their impact on LuYAP and LYSO crystals with small aspect ratio studied.

The fluorescent properties of the scintillators were determined by means of their emission and excitation spectra. The emission curves of LuYAP can be fitted by a sum of two Gaussians with $\lambda_{max} = 345$ nm and 375 nm, respectively. The LYSO emission spectrum appears to be composed of four emission peaks at $\lambda_{max} = 390$ nm, 425 nm, 470 nm, and 500 nm which are due to the radiation from the Ce₁ and Ce₂ sites. In addition, there was a peculiar shift of the maximum of the curve observed for different excitation wavelengths λ_{ex} which is possibly due to the presence of a disturbed Ce₁ site.

Attenuation lengths λ_{att} and refractive indices n of LuYAP and LYSO were derived from transmission measurements obtained along the longer and shorter axes of the scintillators. The results show that λ_{att} is larger for LYSO than for LuYAP in the wavelength range of emission. For n_{LuYAP} and n_{LYSO} , the wavelength dependence was fitted by a Sellmeier parametrization.

The simulations of LuYAP and LYSO crystals show that the light collection efficiency η_L increases strongly with the amount of scattering in the crystal bulk. This has an important consequence: if for a given scintillator the probability of photon scattering can be increased without deteriorating the absorption characteristics at the same time, the scintillator will exhibit a higher light output. This is observed e.g. for PWO, where a higher light output is observed for Chinese crystals despite of a significantly shorter λ_{att} relative to Russian crystals [40].

Other important factors that strongly influence η_L are the refractive index n_{grease} of the optical coupler between crystal and PMT entry window, and the wrapping. For the optical coupling, it is shown that η_L varies strongly with n_{grease} only for $n_{grease} < n_{PMT}$ while it remains almost constant for $n_{grease} \geq n_{PMT}$.

As depicted in Fig. 4.15, the dependence of η_L on the type of wrapping is

relatively small. Diffusing wrappings perform in general slightly better than specular reflectors, especially if the crystal is not optically coupled to the PMT and if the wrapping is connected to the crystal face by a transparent Teflon layer. A different behaviour, however, is observed if the angular distributions of the photons which arrive at least once at the exit surface are compared for different wrappings (Fig. 4.18). Here, it can be clearly seen that specular reflectors with a high reflectivity are much more efficient in transporting photons to the exit surface than diffusing wrappings. These plots also show that a significant fraction of photons which arrive at the exit surface cannot be extracted due to total internal reflection. Obviously, the light output could be significantly improved, if at least a fraction of these photons could be extracted.

A comparison of the simulated with experimental data shows that the experimental data are well represented by the simulations if no wrapping is used. However, in the case of wrapped crystals, the value of η_L predicted by the simulations is lower than observed in the measurements; apparently, there are additional effects, as e.g. a slight shape mismatch, that lead to an improvement of the light yield in the experimental system relative to the idealised model used in the simulations. A precise determination of the scattering-to-absorption ratio B is not possible; however, the experimental values indicate at least that B is relatively small for LuYAP and larger for LYSO.

By combining the measured light outputs with η_L , absolute light yields LY_{abs} for LYSO and LuYAP have been determined for different values of B . For LuYAP, LY_{abs} is found to be $18\,341 \pm 1\,605$ ph/MeV for $B = 0.1$ and $13\,629 \pm 1\,084$ for $B = 1.6$; for LYSO, $LY_{abs} = 48\,979 \pm 2\,798$ ph/MeV for $B = 0.1$ and $41\,086 \pm 2\,421$ for $B = 1.6$. A comparison with published values shows that LY_{abs} is significantly higher than previously reported. Accordingly, the values of $S \cdot Q$ are also higher than previously published: for LuYAP, $S \cdot Q = 0.330 \pm 0.029$ for $B = 0.1$ and 0.245 ± 0.020 for $B = 1.6$; for LYSO, $S \cdot Q = 0.705 \pm 0.041$ for $B = 0.1$ and 0.592 ± 0.035 for $B = 1.6$. Both results highlight the importance of Monte-Carlo simulations in the assessment of these values. As Q is usually ≈ 1 , it still shows that the efficiency of the transfer of the $e - h$ pairs to the luminescence centers is poor for LuYAP.

Bibliography

- [1] W. W. Moses, S. E. Derenzo, A. Fyodorov, M. Korzhik, A. Getkin, N. Minkov, V. Aslanov, $\text{LuAlO}_3\text{:Ce}$ - A high density, high speed scintillator for gamma detection. IEEE Trans. Nucl. Sci. 42, 275 (1995)
- [2] A. Lempicki, M. H. Randles, D. Wisniewski, M. Balcerzyk, C. Brecher, A. J. Wojtowicz, $\text{LuAlO}_3\text{:Ce}$ and other aluminate scintillators. IEEE Trans. Nucl. Sci. 42, 280 (1995)
- [3] M. Moszynski, M. Kapusta, M. Mayhugh, D. Wolski, S. O. Flyckt, Absolute light output of scintillators. IEEE Trans. Nucl. Sci. 44, 1052 (1997)
- [4] W. Drozdowski, A. J. Wojtowicz, T. Lukasiewicz, J. Kisielewski, Scintillation properties of LuAP and LuYAP crystals activated with Cerium and Molybdenum. Nucl. Instr. Meth. A 562, 254 (2006)
- [5] C. Dujardin, C. Pedrini, W. Blanc, J. C. Gacon, J. C. van't Spijker, O. W. V. Frijns, C. W. E. van Eijk, P. Dorenbos, R. Chen, A. Fremout, F. Tallouf, S. Tavernier, P. Bruyndonckx, A. G. Petrosyan, The study of small and large size $\text{LuAlO}_3\text{:Ce}^{3+}$. IEEE Nucl. Sci. Symp. 1997, 174 (1998)
- [6] E. Sysoeva, V. Tarasov, O. Zelenskaya, Comparison of the methods for determination of scintillation light yield. Nucl. Instr. Meth. A 486, 67 (2002)
- [7] J. A. Mares, M. Nikl, N. Solovieva, C. D'Ambrosio, F. de Notaristefani, K. Blazek, P. Maly, K. Nejezchleb, P. Fabeni, G. P. Pazzi, J. T. M. de Haas, C. W. E. van Eijk, P. Dorenbos, Scintillation and spectroscopic properties of Ce^{3+} -doped YAlO_3 and $\text{Lu}_x(\text{RE})_{1-x}\text{AlO}_3$ ($\text{RE} = \text{Y}^{3+}$ and Gd^{3+}) scintillators. Nucl. Instr. Meth. A 498, 312 (2003)
- [8] C. Moisan, A. Levin, H. Laman, Testing Scintillation Transport Models with Photoelectron Yields Measured under Different Surface Finishes. IEEE Nucl. Sci. Symp. 1, 824 (1997)
- [9] J. Bea, A. Gadea, L. M. Garcia-Raffi, J. Rico, B. Rubio, J. L. Tain, Simulation of light collection in scintillators with rough surfaces. Nucl. Instr. Meth. A 350, 184 (1994)
- [10] R. Chipaux, F.-X. Gentit, simulation of light collection in the CMS lead tungstate crystals with the program LITRANI: coating and surface effects. Nucl. Instr. Meth. A 486, 48 (2002)

- [11] A. J. Wojtowicz, W. Drozdowski, M. Ptaszyk, Z. Galazka, J.-L. Lefaucheur, Scintillation light yield of Ce-doped LuAP and LuYAP pixel crystals. *Proc. Int. Conf. on Inorganic Scintillators and their Applications, SCINT05*, 473 (2006)
- [12] D. Wahl, V. B. Mikhailik, H. Kraus, The Monte-Carlo refractive index matching technique for determining the input parameters for simulation of the light collection in scintillating crystals. *Nucl. Instr. Meth. A* 570, 529 (2007)
- [13] Y. A. Berdnikov, V. V. Grebenshchikov, V. F. Kosmach, I. E. Leonov, V. M. Samsonov, O. Y. Khrushcheva, A. P. Shishlo, Special features of light collection processes in heavy-crystal-based scintillation detectors. *Instr. Exp. Tech.* 44, 466 (2001)
- [14] Opticad Corporation, 511 Juniper Drive, Santa Fe, NM 87501 USA
- [15] N. Ghal-Eh, M. C. Scott, R. Koochi-Fayegh, M. F. Rahimi, A photon transport model code for use in scintillation detectors. *Nucl. Instr. Meth. A*, 516, 116 (2004)
- [16] H. Rothfuss, M. Casey, M. Conti, N. Doshi, L. Eriksson, M. Schmand, Monte Carlo simulation study of LSO crystals. *IEEE Trans. Nucl. Sci.* 51, 770 (2004)
- [17] A. Wirrwar, N. Schramm, H. Vosberg, H.-W. Müller-Gärtner, Influence of crystal geometry and wall reflectivity on scintillation photon yield and energy resolution. *IEEE Nucl. Sci. Conf. R.*, 3, 1443 (1999)
- [18] F. X. Gentit, Litrani: a general purpose Monte-Carlo program simulating light propagation in isotropic and anisotropic media. *CMS Note* 2001/044
- [19] M. Taiuti, A project for a high-efficiency direction-sensitive photo-detector to be used in underwater neutrino telescopes. *Nucl. Instr. Meth. A* 525, 137 (2004)
- [20] A. Braem, E. Chesi, F. Ciocia, R. de Leo, C. Joram, L. Lagamba, E. Nappi, J. Seguinot, I. Vilardi, P. Weilhammer, Scintillator studies for the HPD-PET concept. *Nucl. Instr. Meth. A* 571, 419 (2007)
- [21] P. Achenbach, C. Ayerbe Gayoso, J. Bernauer, R. Böhm, M. O. Distler, L. Doria, J. Friedrich, H. Merkel, U. Müller, L. Nungesser, J. Pochodzalla, S. Sanchez Majos, S. Schlimme, Th. Walcher, M. Weinriefer, Measurement of propagation time dispersion in a scintillator. *Nucl. Instr. Meth. A*, 578, 253 (2007)
- [22] I. Vilardi, A. Braem, E. Chesi, F. Ciocia, N. Colonna, and 14 coauthors, Optimization of the effective light attenuation length of YAP:Ce and LYSO:Ce crystals for a novel geometrical PET concept. *IEEE Nucl. Sci. Symp. Conf. Rec.* 5, 2859 (2004)

-
- [23] <http://gentit.home.cern.ch/gentit/litrani/>
- [24] F. Arqueros, G. D. Montesinos, A simple algorithm for the transport of gamma rays in a medium. *Am. J. Phys.* 71, 38 (2003)
- [25] C. Kuntner, Evaluation of new inorganic scintillators for application in a prototype small animal PET scanner. Dissertation, TU Wien (2003)
- [26] C. H. Huang, G. Zhang, Z. Q. Chen, X. J. Huang, H. Y. Shen, Calculation of the absorption coefficients of optical materials by measuring the transmissivities and refractive indices. *Opt. Las. Tech.* 34, 209 (2002)
- [27] E. D. Palik, E. J. Prucha, Handbook of optical constants of solids. Boston, Mass.: Boston Academic Press (1998)
- [28] U. Heinrichs, A. Blume, N. Bußmann, R. Engels, G. Kemmerling, S. Weber, K. Ziemons, Statistical studies on the light output and energy resolution of small LSO single crystals with different surface treatments combined with various reflector materials. *Nucl. Instr. Meth. A*, 486, 60 (2002)
- [29] NIST XCOM: Photon Cross Sections Database. <http://physics.nist.gov/PhysRefData/Xcom/Text/XCOM.html>
- [30] J.-L. LeFaucheur, Private communication (2008)
- [31] C. Carrier, R. Lecomte, Effect of geometrical modifications and crystal defects on light collection in ideal rectangular parallelepipedic BGO scintillators. *Nucl. Instr. Meth. A* 294, 355 (1990)
- [32] P. Sempere Roldan, Quality control and preparation of the PWO crystals for the electromagnetic calorimeter of CMS. Doctoral thesis, Univ. de Santiago de Compostela, Spain (2001)
- [33] M. Montecchi, Q. Ingram, Study of some optical glues for the Compact Muon Solenoid at the Large Hadron Collider of CERN. CMS Note 2001/030
- [34] A. Lempicki, J. Glodo, Ce-doped scintillators: LSO and LuAP. *Nucl. Instr. Meth. A* 416, 333 (1998)
- [35] L. Pidol, A. Kahn-Harari, B. Viana, E. Virey, B. Ferrand, P. Dorenbos, J. T. M. de Haas, C. W. E. van Eijk, High efficiency of Lutetium Silicate scintillator, Ce-doped LPS, and LYSO crystals. *IEEE Trans. Nucl. Sci.* 51, 1084 (2004)
- [36] I. G. Valais, I. S. Kandarakis, A. Konstantinidis, D. N. Nikolopoulos, I. Sianoudis, D. A. Cavouras, N. Dimitropoulos, C. D. Nomicos, G. S. Panayiotakis, Evaluation of the light emission efficiency of LYSO:Ce scintillator under X-ray excitation for possible applications in medical imaging. *Nucl. Instr. Meth. A* 569, 201 (2006)

- [37] H. Loudyi, Y. Guyot, J.-C. Gacon, C. Pedrini, M.-F. Joubert, Understanding the scintillation efficiency of cerium-doped LSO, LYSO, YSO and LPS crystals from microwave study of photoconductivity and trapping. *Opt. Mat.* 30, 26 (2007)
- [38] C. Kuntner, E. Auffray, P. Lecoq, C. Pizzolotto, M. Schneegans, Intrinsic energy resolution and light output of the $\text{Lu}_{0.7}\text{Y}_{0.3}\text{AP}:\text{Ce}$ scintillator. *Nucl. Instr. Meth. A* 493, 131 (2002)
- [39] Bluestar Silicones, Private communication (2007)
- [40] E. Auffray, Overview of the 63000 PWO barrel crystals for CMS_ECAL production. Accepted for publication in *IEEE Trans. Nucl. Sci.*

Chapter 5

Scintillators with macromachined exit surfaces

As the simulations presented in the previous chapter have shown, a large fraction of the scintillation photons that arrive at the coupling face between scintillator and photo detector is lost simply because they hit the surface under an angle outside the extraction cone. This, on the other hand, implies that the light output measured in a standard PET detector is only a fraction of the light output that could potentially be measured if all arriving photons could be extracted from the crystal.

An increased scintillator light output would have several benefits. One important implication would be an improvement of the time resolution Δt of the detector: as was discussed in Sect. 2.2.7,

$$\Delta t \propto \sqrt{\frac{1}{N_{pe}}}. \quad (5.1)$$

This implies that an increase of the light collection efficiency η_L and therefore, of the light output and the number of photo electrons N_{pe} , leads to an improvement of the timing properties of the detector. The improved Δt can be used, in turn, to narrow down the coincidence time window of a PET detector and therefore, can help in reducing the background of random coincidences. In addition, it may help to improve the positional resolution in a TOF PET.

A second important consequence of an increased η_L stems from the fact that also the energy resolution of the scintillation detector is a function of N_{pe} . As quoted in Sect. 2.2.4, the energy resolution R of the detector is defined by the equation

$$R^2 = R_i^2 + R_M^2 \quad (5.2)$$

where $R_M \propto \overline{N}_{pe}^{-1}$. An increased η_L will therefore also lead to an improvement of R . An improvement of R , in turn, allows for better discrimination between true and scattered coincidences, which again improves the quality of the reconstructed PET image.

As eq. 5.2 however implies, the improvement in R that can be achieved depends on whether the photomultiplier resolution R_M or the intrinsic resolution R_i is the dominant term; if $R_M \gg R_i$, a significant improvement of R can be expected, while for $R_M \ll R_i$, the improvement will be negligible. Increasing the light output is therefore especially interesting for scintillators with $R_M \gg R_i$, i.e. scintillators whose energy resolution is close to the fundamental limit given by the black curve in Fig. 2.6.

In order to improve η_L significantly, it is necessary to create conditions under which these lost photons can be recovered. However, neither of the possible solutions discussed in recent years, such as the use of diffusing wrappings or coatings or grounding of the side and end faces of the crystals [1, 2, 3, 4], has lead to a large improvement of η_L . Another possibility to reduce total internal reflection is the use of tapered crystals [3, 4] yet this option is often not appropriate due to restrictions imposed by the detector geometry and the readout technique. Clearly, other approaches are required to improve η_L for such cases.

In this chapter, a novel approach is presented which uses grooves machined into the exit surface of the crystals to break up total internal reflection. This approach has been tested in [5] in order to expand the FOV of large size NaI gamma cameras, but its potential on increasing η_L of scintillators with small aspect ratio has so far not been studied. The approach is tested by means of LITRANI simulations and the results compared with experimental data obtained for prototype samples.

5.1 Principle of method

As noted in Sect. 4.4.3, a large amount of scintillation photons reaches the exit surface of the scintillator under an angle that is larger than the angle of total internal reflection θ_{tot} . Although some of these photons are recovered by scattering in the crystal bulk, the majority will remain trapped and eventually, become absorbed (Fig. 5.1a).

What happens now if the shape of the exit surface is locally altered by introducing a groove? If a photon reaches the plain part of the exit surface, nothing changes; photons within the extraction cone are likely to be extracted while photons outside the extraction cone are reflected back into the crystal bulk.

However, the situation will be different for photons that hit one of the faces of the groove: a photon outside the extraction cone of the plain surface may fall inside the extraction cone of one of the groove faces and will exit; on the other hand, a photon arriving within the extraction cone of the plain surface might fall outside the extraction cone of the groove face and may be reflected back (Fig. 5.1b). In other words, by modifying the planarity of the exit surface by means of grooves, some of the trapped photons may exit the crystal, while

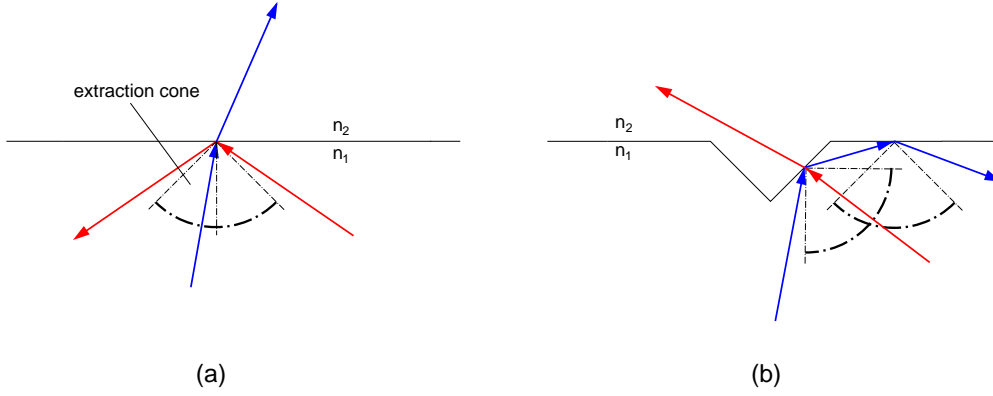


Figure 5.1: Extraction of photons for (a) a plain surface and (b) a surface with a groove.

some of the extractable photons may not be extracted any more. Clearly, the first effect increases η_L while the second effect leads to a decrease. The gain in η_L that can be achieved by surface structuration therefore depends on the relative contributions of these two mechanisms.

5.2 Simulations of crystals with macromachined exit surfaces

5.2.1 Simulated setup

The basic elements of a setup used to simulate a scintillator with a grooved exit surface are shown in Fig. 5.2a. In contrast to the setup used in the simulations of chapter 4, an additional layer consisting of several trapezoidal substructures was introduced between the crystal and grease shapes to simulate the grooved exit surface. Fig. 5.2c depicts the shape of a groove, as used in the simulations. Fig. 5.2b presents a top view of a crystal with one groove. Unless otherwise noted, a trapezoidal shape with $w_{low} = 0.1 \cdot w_{up}$ and $\alpha = 45^\circ$ was used. This ratio was found to approximate the groove shape obtained for the experimental samples reasonably well (see Sect. 5.3.1). Due to the restricted geometry of LITRANI, the rounded lower end of the groove could not be reproduced in the simulated system.

In simulations of crystals with a single groove or with two crossed grooves, the grooves were positioned in the crystal center. If more than one groove was simulated in each direction, the grooves were positioned equidistantly from each other and from the crystal edges.

5.2.2 Results of simulations

In the following, the results of the simulations are described and the impact of several parameters (groove size, opening angle, number of grooves, ...) on η_L is

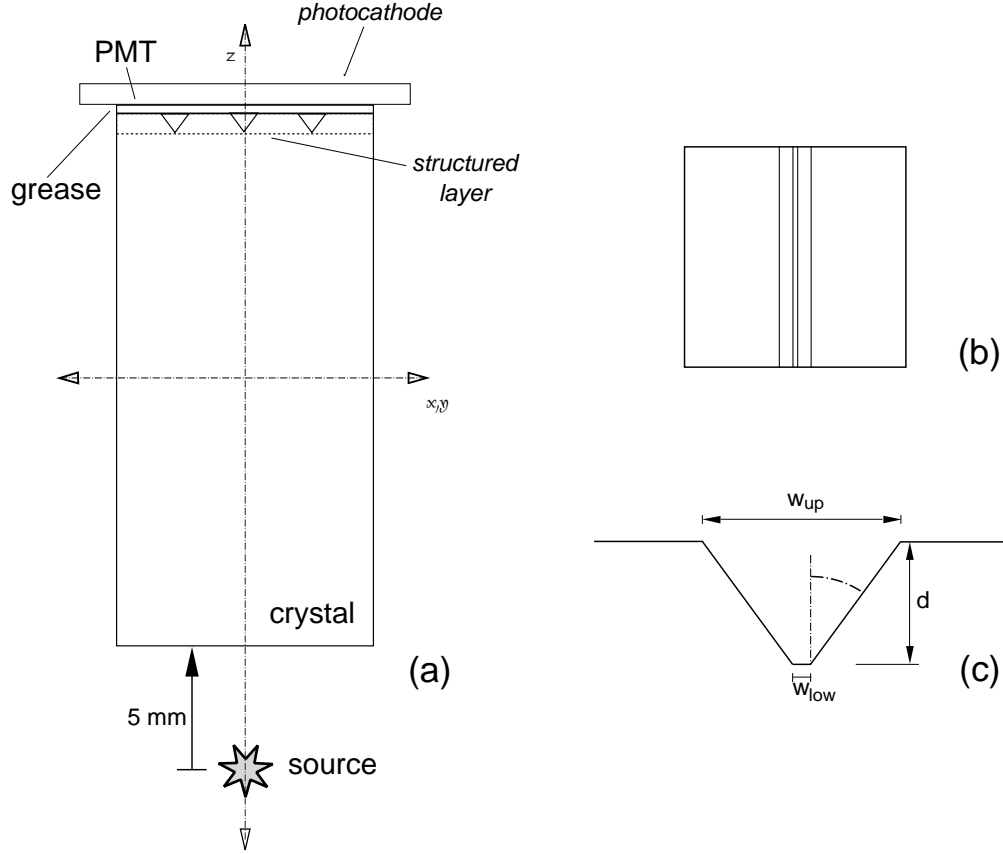


Figure 5.2: Simulated system in LITRANL. (a): Simulated system. (b): Top view of exit surface with one groove. (c): Sketch of a groove.

evaluated. Unless otherwise noted, the simulations were performed for Teflon wrapped $2 \times 2 \times 10 \text{ mm}^3$ LYSO and LuYAP crystals with $B = 0.1$ and $B = 1.6$. Simulated were grooves with depth $d = 0.3 \text{ mm}$ or 0.5 mm and opening angle $\alpha = 45^\circ$. The slice between crystal and PMT was either set to $n_{grease} = 1$ or to $n_{grease} = 1.41$ to account for the cases of an air gap between crystal and PMT and optical coupling by means of grease, respectively.

Light extraction

As noted in Sect. 5.1, the presence of the groove will change the light extraction properties of the exit surface relative to that of a plain exit surface. In particular, the presence of the groove leads to a decreased extraction efficiency at low θ_i due to reflection at the groove faces but to an increased extraction efficiency for angles outside the extraction cone.

This change of the light extraction properties induced by the groove can be easily assessed by comparing the angular distributions of the extracted photons

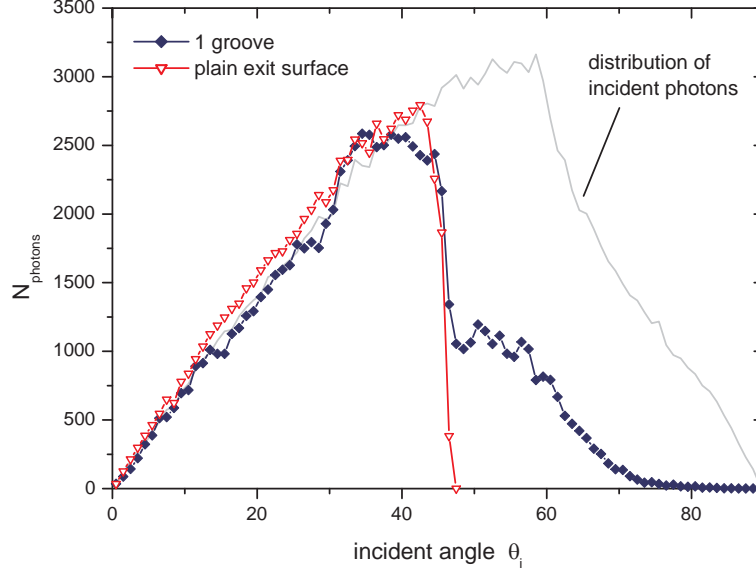


Figure 5.3: Comparison of angular distributions of extracted photons for LuYAP with standard Teflon wrapping in the case of a plain and a grooved exit surface.

for a plain and a grooved exit surface (Fig. 5.3). In both curves, the incidence angle θ_i corresponds to the angle of the photon *relative to z* at the moment of extraction; this is important to note as a definition of θ_i relative to the normal of the extracting surface would not make sense due to the non-perpendicularity of the groove faces relative to z .

As the plot shows, there are indeed minor losses observable at incident angles $< \theta_{tot}$ relative to the crystal with plain exit surface. However, these losses are more than compensated by the gain in light extraction at angles $> \theta_{tot}$; as a consequence, the crystal with grooved exit surface will exhibit an increased η_L relative to a crystal with the same general properties but with a plain exit surface.

Influence of groove size and shape

In order to optimize the groove parameters for an experimental system, it is necessary to evaluate the impact of the groove size and the opening angle of the groove on η_L . Fig. 5.4a shows the dependence of η_L on the groove size ($\alpha = 45^\circ$). Clearly, the presence of the groove leads to a significant increase of η_L compared to a crystal with plain exit surface (i.e. the case $d = 0$ mm). The maximum value of η_L is achieved for both LuYAP and LYSO for groove depths $d \approx 0.5 - 0.6$ mm. In addition, it is also apparent that the increase in η_L is more pronounced for LYSO, probably as a consequence of its higher transparency, as compared to LuYAP.

The dependence of η_L on the opening angle α of the groove is depicted in Fig. 5.4b for LYSO and LuYAP ($B = 1.6$) and two different groove depths d ($d = 0.3$ and $d = 0.5$ mm). The case $\alpha = 0^\circ$ corresponds to a groove with rectangular cross section. As can be seen, η_L reaches a maximum around $\alpha = 45^\circ$. In addition, it shows that the increase in η_L relative to $\alpha = 0^\circ$ is more pronounced for LYSO than for LuYAP.

Influence of the number of grooves

The results presented so far indicate that the presence of a groove can lead to a significant increase in η_L . Even better results can be obtained if a second groove is machined perpendicular to the first one into the exit surface. This is shown in Fig. 5.5 which compares η_L for LuYAP and LYSO crystals with plain exit surface, with one groove, and with crossed grooves. Clearly, the gain in η_L between the system with the crossed grooves and the system with just one groove is not as large as between the system with one groove and the system with plain exit surface. Nevertheless, the increase of η_L amounts to $\approx 10\%$ in all cases.

One could now believe that η_L can be further increased by machining additional grooves into the exit surface of the crystal; however, as Fig. 5.6 indicates, this is not the case. Indeed, the optimum value of η_L for LuYAP is found if only one groove is present, while for LYSO one or two grooves perform almost equally well. Every additional groove leads to a decreasing η_L , which for larger numbers of grooves can be even lower than the value obtained for the plain exit surface.

This behaviour seems surprising at first glance but becomes clear when one looks at the angular distribution of the photons that are extracted in each case (Fig. 5.7). Although a crystal with several parallel grooves extracts slightly more photons with angles $> 45^\circ$ than a crystal with only one groove, the effect is only weak and by far does not compensate for the losses at lower angles. The reason for this is clear: Although the number of extracted photons with large incident angles θ_i increases because of the higher amount of faces non-perpendicular to z , many photons with small θ_i that would normally be extracted through a face $\perp z$ cannot be extracted any more since the total area covered by these faces is small. Instead, these photons are reflected back into the crystal where they are eventually absorbed by the bulk or the wrapping. This explains also why the deterioration is less pronounced for LYSO: The transparency of LYSO is better than that of LuYAP and the back-reflected photons are therefore more likely to return to the exit surface and become extracted at second attempt.

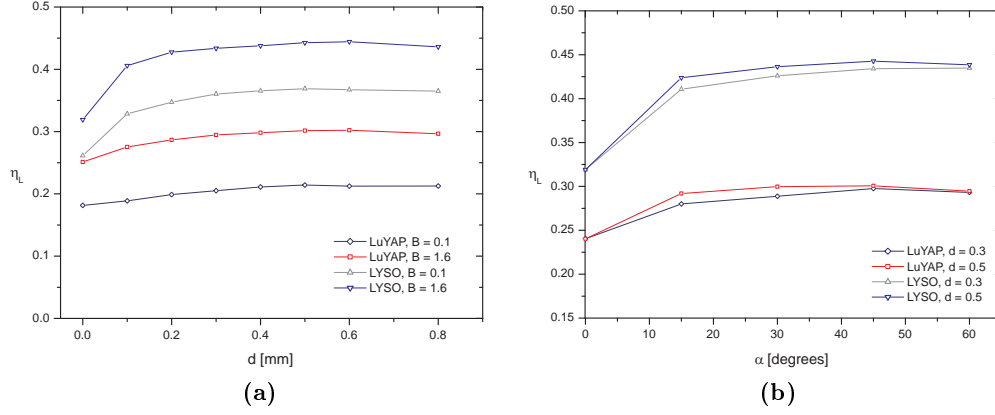


Figure 5.4: Dependence of η_L on (a) depth d and (b) opening angle α of the groove. The case $d = 0$ mm corresponds to a plain exit surface, the case $\alpha = 0^\circ$ to a groove with rectangular cross section.

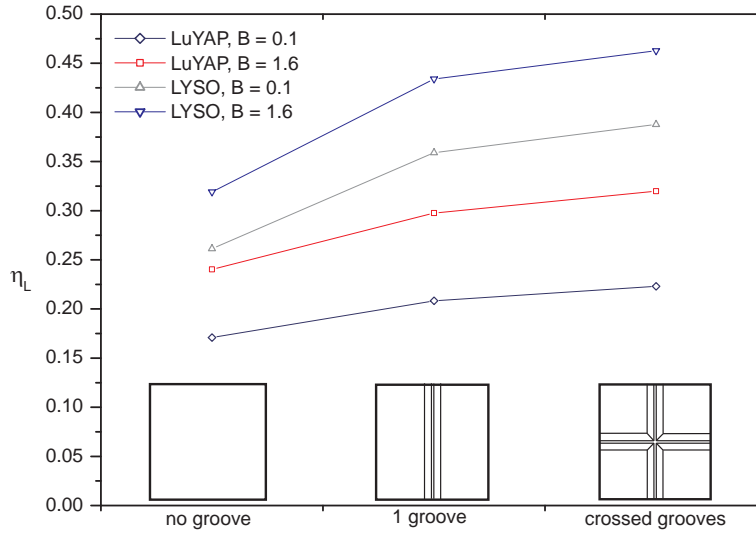


Figure 5.5: Comparison of η_L for crystals with plain exit surface, 1 groove in x , and 1 groove in x and y each.

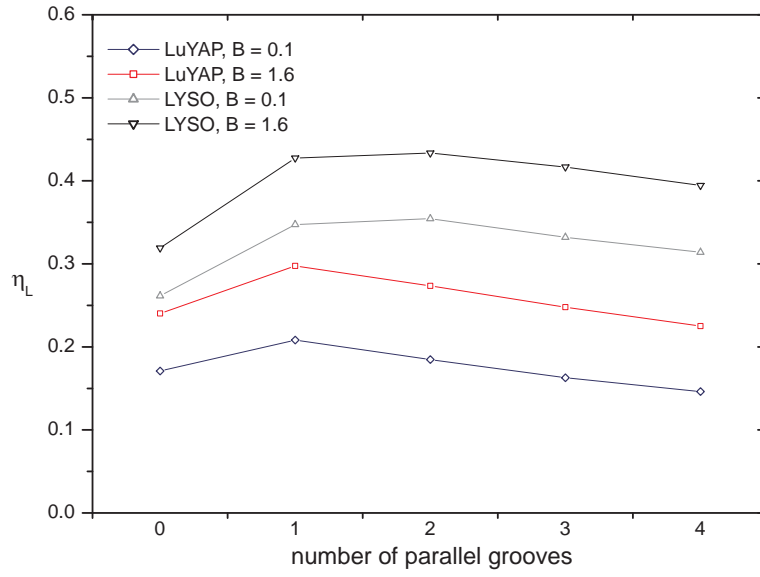


Figure 5.6: Comparison of η_L for the case of several parallel grooves.

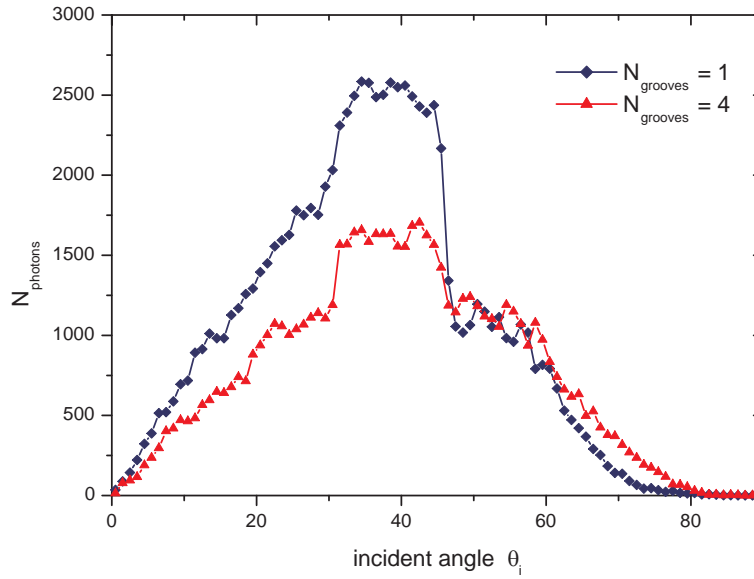


Figure 5.7: Comparison of the angular distributions of extracted photons for different numbers of grooves.

Influence of n_{crys} and n_{grease}

The dependence of the gain in η_L on n_{crys} is shown in Fig. 5.8 for a Teflon wrapped $2 \times 2 \times 8 \text{ mm}^3$ crystal with a 0.5 mm deep groove and an absorption length of 30 cm. The plot shows that the impact of the groove on η_L increases

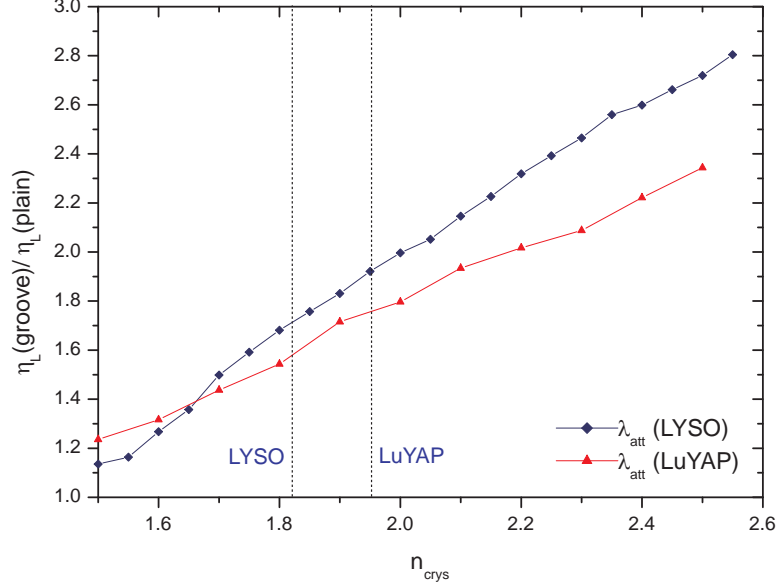


Figure 5.8: Dependence of η_L on n_{crys} .

approximately linearly with the refractive index of the scintillator for the studied range of n_{crys} . This makes its use especially attractive for scintillators with very high n_{crys} , as PWO and BGO.

As discussed in chapter 4, the amount of light that can be extracted from a crystal with plain exit surface also strongly depends on n_{grease} . This is also true if a groove is present in the exit surface; however, as Figs. 5.9a and 5.9b depict, a slightly different relationship between η_L and n_{grease} than in the case of a plain exit surface is observed. While η_L remains almost flat for $n_{grease} \geq n_{PMT}$ in the case of a plain exit surface, a pronounced maximum around $n_{grease} = 1.55 - 1.6$ is observed for the grooved crystals. An additional interesting feature visible in the curves of the grooved crystals is that η_L does not decrease continuously for higher values of n_{grease} but rises again for $n_{grease} \geq n_{crys}$.

Influence of the wrapping

As noted in Figs. 4.18a and 4.18b, the amount of photons arriving at the exit surface and their angular distribution depends strongly on the type of wrapping that is used as a reflector. In particular, the differences in the number of arriving photons are large for angles outside the extraction cone of the plain exit surface but only small for angles within the extraction cone; as a consequence, only a

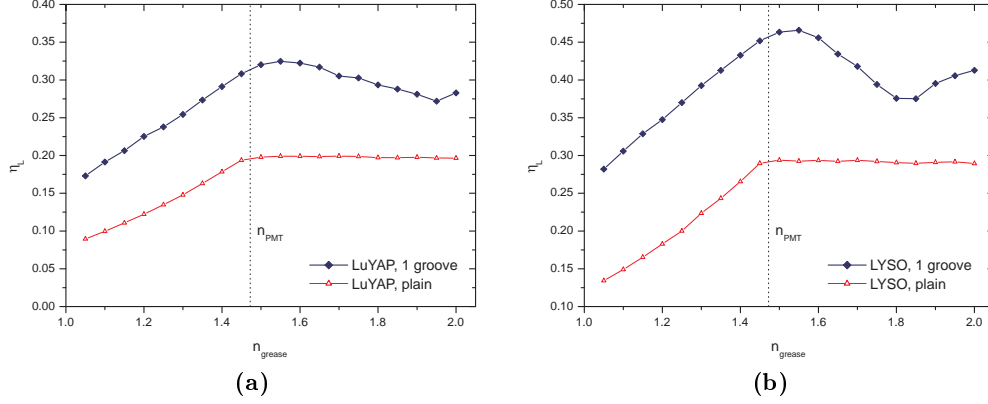


Figure 5.9: Dependence of η_L on n_{grease} . (a) LuYAP; (b) LYSO.

weak dependence of η_L on the wrapping type has been observed for crystals with a plain exit surface.

This is different for crystals with a grooved exit surface: In this case, photons arriving at angles outside the extraction cone of a plain exit surface become extractable by the introduction of the groove and differences in the numbers of these photons are expected to have significant impact on η_L . Indeed, as Fig. 5.10 indicates, this assumption is correct: wrappings that have been shown to be the most efficient in transporting photons to the exit surface are also more efficient in terms of light extraction if a groove is present at the exit surface. The specular reflector with 98% reflectivity performs especially well and exhibits the highest η_L of all four studied wrappings. On the other hand, the Teflon wrapping with $n_{gap} = 1.35$ and the 98% diffusor transport only a small fraction of the photons emitted at large θ to the exit surface and no significant increase in light yield relative to the case of a plain surface can be observed.

Dependence of η_L on the scattering length

Since scattering has been shown in Chapter 4 to influence η_L of crystals with a plain exit surface in a positive way, it is now interesting to see how scattering affects η_L for crystals with grooved exit surface.

As expected, a significant increase of η_L with the scattering-to-absorption ratio B is observed if a groove is apparent (Fig. 5.11). Moreover, the scattering-induced gain in η_L is more pronounced than for a plain exit surface. This means that although bulk scattering already helps with the extraction of otherwise trapped modes in crystals with a plain exit surface, its effect is even enhanced for crystals where the exit surface contains a groove.

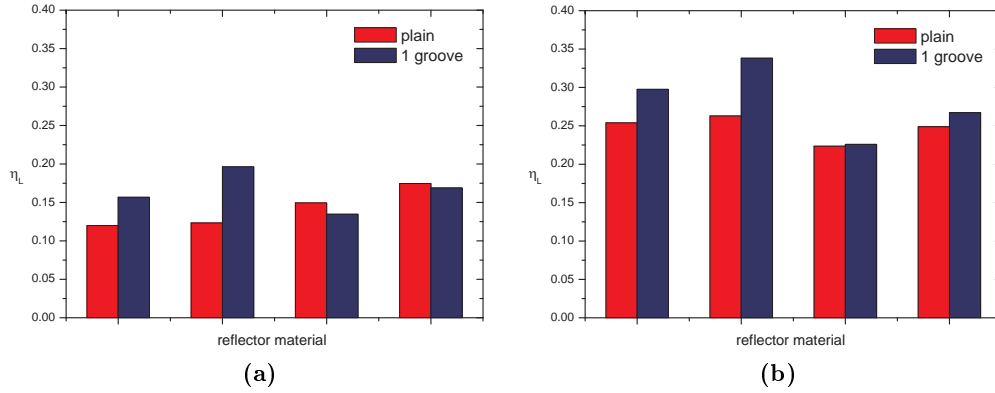


Figure 5.10: Dependence of η_L on the wrapping for LuYAP (a) without optical coupling to the PMT; (b) with optical coupling to the PMT. (1) Teflon, $n_{gap} = 1$; (2) 98% Reflector, $n_{gap} = 1$; (3) Teflon, $n_{gap} = 1.35$; (4) 98% Diffusor, $n_{gap} = 1.35$

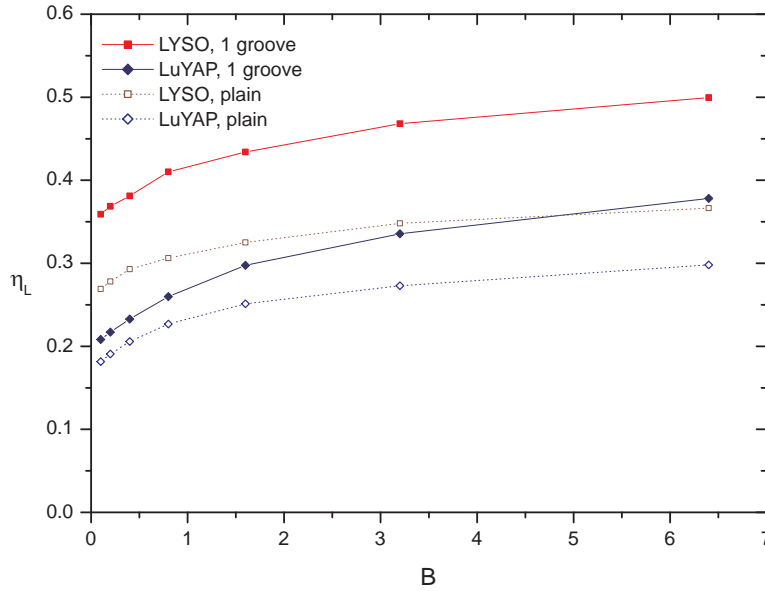


Figure 5.11: Dependence of η_L on B for grooved crystals and comparison with the case of a plain surface.

5.3 Measurements of LuYAP and LYSO samples

5.3.1 Fabrication of samples

The machining of the grooves was performed with a diamond disk mounted onto a custom designed machine based on the commercially available cutter LGB 5030. A sketch of the setup is shown in Fig. 5.12. The properties of diamond disk and the LGB 5030 are given in Table 5.1.

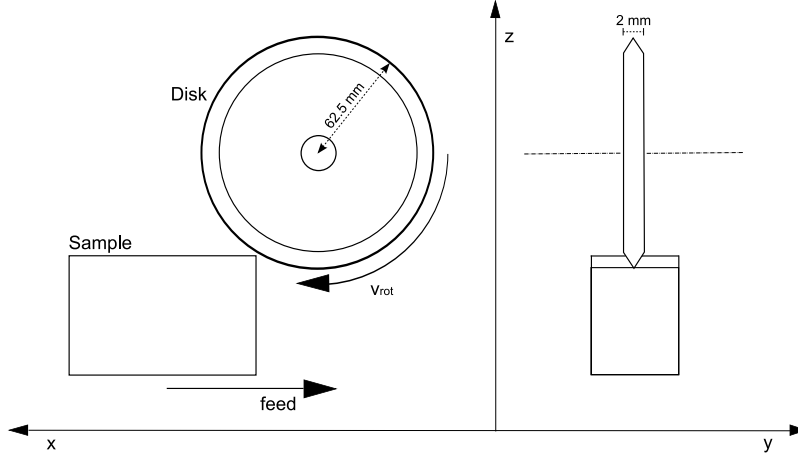


Figure 5.12: Setup used for groove cutting.

Table 5.1: Properties of the diamond disk and the LGB 5030 used for groove fabrication.

Diamond disk	
Producer	Wendt group
Material	bronze + natural diamond powder
Diameter	125 mm
Grain size	54 μm
Grain conc.	0.44 $\text{g}\cdot\text{cm}^{-3}$
Angle of bevels at disk edge:	45°
cutting edge radius:	$\approx 40 \mu\text{m}$
LGB 5030	
Rotational velocity v_{rot}	$0 \leq v_{rot} \leq 6000 \text{ rpm}$
Feed f	$0 \leq f \leq 100 \text{ mm}\cdot\text{min}^{-1}$
Positional reproducibility	$\leq 5 \mu\text{m}$

Cutting tests with glass samples

Before prototype production, a test series was performed on standard window pane float-type glass samples to optimize the groove cutting parameters for processing the scintillators. The quality of the grooves was assessed by visual inspection with a microscope at low magnification (50 \times). For two samples, additional roughness measurements were performed by means of laser interferometry.

Table 5.2 shows the results of the roughness measurements. The roughness R_a corresponds to the rms of the groove profile. Typically, R_a was found to be in the range of 1 - 2 μm . The relatively high value obtained for groove #2

Table 5.2: Roughness R_a of the test grooves.

Sample	Groove	Average roughness R_a [μm]	
		lateral	parallel
4	#1	1.465	0.595
	#2	2.31	1.13
	#3	0.80	1.135
5	#1	1.615	1.005
	#2	1.58	1.24
	#3	1.855	1.005

of sample 4 results from a deviation of the lateral groove profile from planarity which causes the upper ends of the groove to be 5 - 10 μm above the average value; the real roughness of the groove is therefore expected to be considerably smaller. As measurements of the groove depths and widths showed, the produced grooves are slightly larger than expected from the cutting parameters alone. This is mostly due to supplementary abrasion from small grains of sample material produced during the cutting process; however, vibrations and slight eccentricities of the disk and the mount may also play a role.

Fabrication of LuYAP and LYSO prototypes

The cutting of the LuYAP and LYSO prototypes was performed by glueing the samples onto a glass holder with one of the smaller surfaces pointing upwards. Based on the results from the test samples, a feed $f = 20$ mm/min and a rotational disk velocity $v_{rot} = 3000$ rpm was used in the cutting process. Table 5.3 lists basic data of several crystal batches for which grooves have machined into

Table 5.3: Properties of crystals for groove fabrication.

Batch	date of groove production	crystal	producer	size [mm ³]	d_{groove} [mm]	Number of grooves
1	Jun 07	LuYAP 1942	PML	$2 \times 2 \times 8$	0.5	1
		LYSO 1945	PML	$2 \times 2 \times 8$	0.5	1
2	Oct 07	LuYAP 1979	PML	$2 \times 2 \times 10$	0.3	1+1
		LuYAP 1980	PML	$2 \times 2 \times 10$	0.3	1+1
		LYSO 1981	PML	$2 \times 2 \times 10$	0.3	1+1
		LYSO 1982	PML	$2 \times 2 \times 10$	0.3	1+1
3	Dec 07	LuYAP 1999	PML	$2 \times 2 \times 10$	0.3	1
		LuYAP 2000	PML	$2 \times 2 \times 10$	0.3	1+1
		LYSO 1997	PML	$2 \times 2 \times 10$	0.3	1
		LYSO 1998	PML	$2 \times 2 \times 10$	0.3	1+1

the exit surfaces. The depths of the produced grooves vary between 0.3 and 0.5

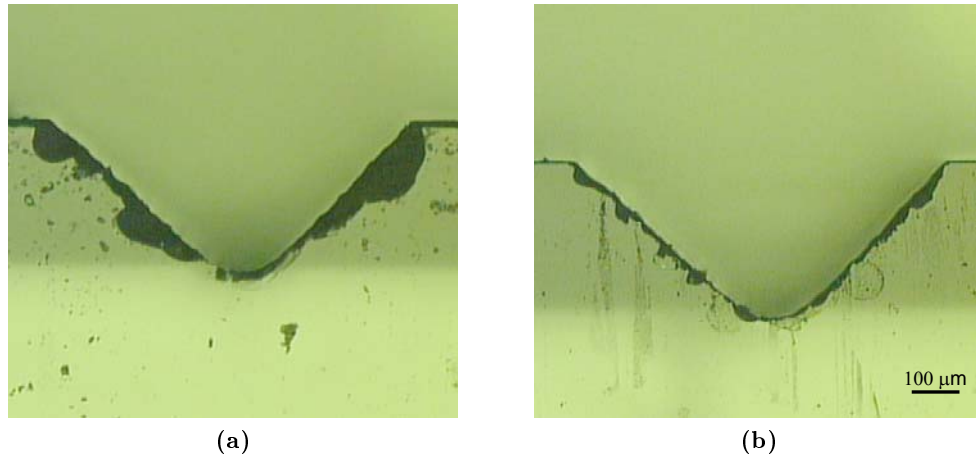


Figure 5.13: Microscopic images of grooves. (a): LuYAP 1980 (b): LYSO 1982.

mm.

Microscopic images of grooves of two crystals (LuYAP 1980 and LYSO 1982) are shown in Figs. 5.13a and 5.13b. These images show that despite the optimization of the cutting parameters, the groove edges are still relatively rough and exhibit significant chipping.

5.3.2 Results of measurements

The light yield (LY) measurements were performed in an analogue manner as the measurements described in Chapter 4. The LY of each sample was determined before and after cutting to assess the change in LY induced by the groove. In each case, the measurements were obtained under different setup configurations (grease / no grease, wrapping / no wrapping). To avoid systematic errors originating from fluctuations of the PMT sensitivity, the measured LY was normalised to the LY of one of the reference crystals (LuYAP 1943 and LuYAP 1098) measured in parallel. For crystals where a second groove was machined perpendicular to the first groove into the exit surface, measurements were performed after each production step to assess the effect of the second groove on the LY.

5.3.3 Discussion

Tables 5.4 and 5.5 compare the change in LY after each procedural step in percentage of the LY measured before the machining of the grooves. Clearly, an increase of the LY, as expected from the simulations, is indeed detectable for the majority of samples. This is especially evident for measurements without wrapping and optical coupling where an increase of several tens of percent can be observed after each processing step. In general, the increase in LY is more pronounced in configurations where no optical coupling is used; with optical coupling, the LY increase is either weak or even reversed. No significant differences can be seen between the $2 \times 2 \times 8 \text{ mm}^3$ crystals with 0.5 mm deep grooves

Table 5.4: LY of the crystals with macromachined exit surface relative to a plain exit surface. Case: no wrapping. The simulated values correspond to the case $B = 1.6$.

	Sample 1 groove [%]	no grease		grease	
		1+1 groove [%]	1 groove [%]	1+1 groove [%]	
simulation	LuYAP	172	238	122	134
	LYSO	202	326	128	139
experiment	LuYAP 1999	151 ± 5		97 ± 3	
	LuYAP 2000	136 ± 9	168 ± 19	107 ± 4	105 ± 2
	LYSO 1997	128 ± 5		96 ± 5	
	LYSO 1998	142 ± 7	165 ± 6	100 ± 6	118 ± 6
	Average LuYAP	143 ± 7	168 ± 19	102 ± 3	105 ± 2
	Average LYSO	135 ± 6	165 ± 6	98 ± 4	118 ± 6

Table 5.5: LY of the crystals with macromachined exit surface relative to a plain exit surface. case: Teflon wrapping. The simulated values correspond to the case $B = 1.6$.

	Sample 1 groove [%]	no grease		grease	
		1+1 groove [%]	1 groove [%]	1+1 groove [%]	
simulation	LuYAP	138	175	124	133
	LYSO	169	227	136	145
experiment	LuYAP 1942			106 ± 7	
	LuYAP 1979	100 ± 8	115 ± 3	103 ± 3	103 ± 3
	LuYAP 1980	111 ± 6	121 ± 6	110 ± 6	106 ± 6
	LuYAP 1999	111 ± 12		109 ± 5	
	LuYAP 2000	110 ± 8	107 ± 9	104 ± 7	100 ± 5
	LYSO 1945			105 ± 4	
	LYSO 1981	102 ± 11	105 ± 8	98 ± 3	94 ± 6
	LYSO 1982	108 ± 6	121 ± 6	110 ± 6	106 ± 6
	LYSO 1997	108 ± 10		101 ± 5	
	LYSO 1998	136 ± 5	139 ± 8	112 ± 7	117 ± 7
	Average LuYAP	108 ± 9	114 ± 6	107 ± 6	103 ± 5
	Average LYSO	114 ± 7	117 ± 7	104 ± 5	102 ± 6
	without LYSO 1998	106 ± 8	106 ± 7	102 ± 4	94 ± 5

and the $2 \times 2 \times 10 \text{ mm}^3$ crystals with 0.3 mm deep grooves. With wrapping, the addition of a second groove usually does not have a positive effect on the LY but leads to a deterioration in the majority of cases. A notable exception is the LYSO crystal CCC 1998 which shows a considerable increase of the LY both with and without optical coupling; however, this crystal was not found to be representative as its LY is much lower than that of the remaining LYSO samples.

Comparing these results with those presented in Sect. 5.2.2 for the simulations of crystals with grooved exit surface shows that in the produced prototypes much less light is extracted than predicted by the simulations. This is also clearly seen in Figs. 5.14 and 5.15 which compare the average LYs per crystal and setup configuration with simulation results of equivalent systems; apparently, the idealized model which is used in the simulations does not reflect well the real behaviour of the fabricated prototypes.

5.4 The 'absorbing layer' approach

As noted before, there is a significant discrepancy between the change in LY expected from the simulations and the experimental reality. However, it must be considered that the grooves of the scintillator prototypes were not polished after fabrication but still in the rough cut stage; for this reason, their effect on η_L is, as expected, significantly different from that of the idealized grooves in the simulations. This is partly due to the ground surface of the grooves and the large amount of chipping at the groove edges. However, a major influence comes from the fact that the cutting process not only affects the groove surface but also the layers in the immediately vicinity of the groove due to the forces applied during groove fabrication. As a consequence, the crystal lattice will be severely distorted in these areas and the scattering and absorption lengths are likely to be inferior compared to the rest of the bulk. In addition, there is still the unexplained excess in LY which is observed for wrapped crystals and which probably also accounts for the difference between simulation and experiment (cf. Section 4.5.2).

5.4.1 Simulation

The measurements of unwrapped LuYAP and LYSO samples presented in Table 5.4 offer a possibility to test a more advanced model that approximates the observed properties of the grooved crystals. This model resembles the idealised model (Fig. 5.2a) in its general outline but differs from it by the introduction of thin layers of crystalline material with much higher absorption and scattering rates between the grooves and the shapes defining the crystal bulk (Fig. 5.16). The thickness of the layers (d_{layer}) was assumed to be $50 \text{ }\mu\text{m}$. To account for the rough surface of the grooves in the experimentally tested samples, a scattering length $\lambda_{\text{scat,layer}} = d_{\text{layer}}$ was assumed. Absorption lengths between $10 \text{ }\mu\text{m}$ and 1 cm were simulated. In all cases, the scattering-to-absorption ratio B was set to 1.6.

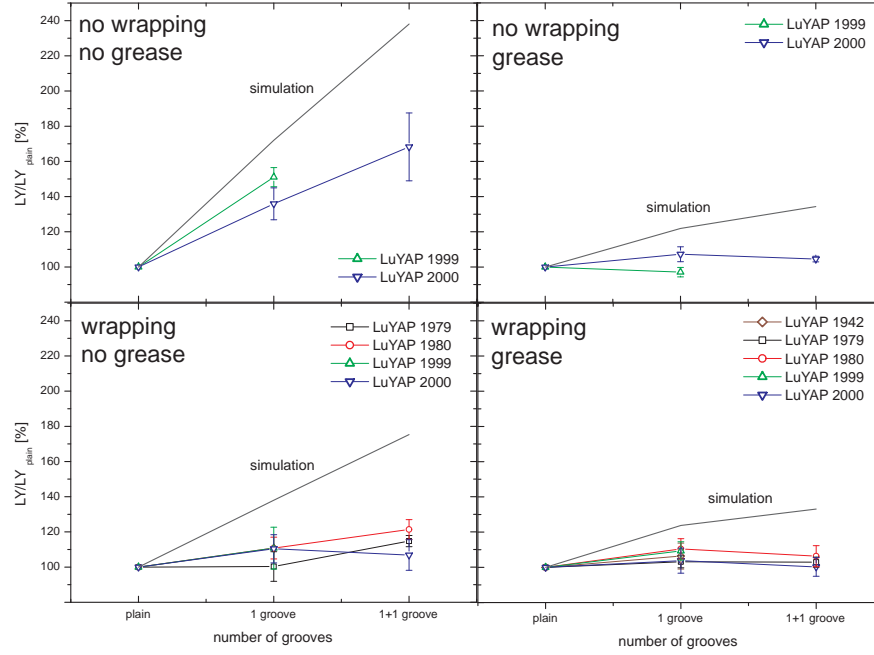


Figure 5.14: Comparison of experimental data with the simulation results of the idealized grooves for LuYAP.

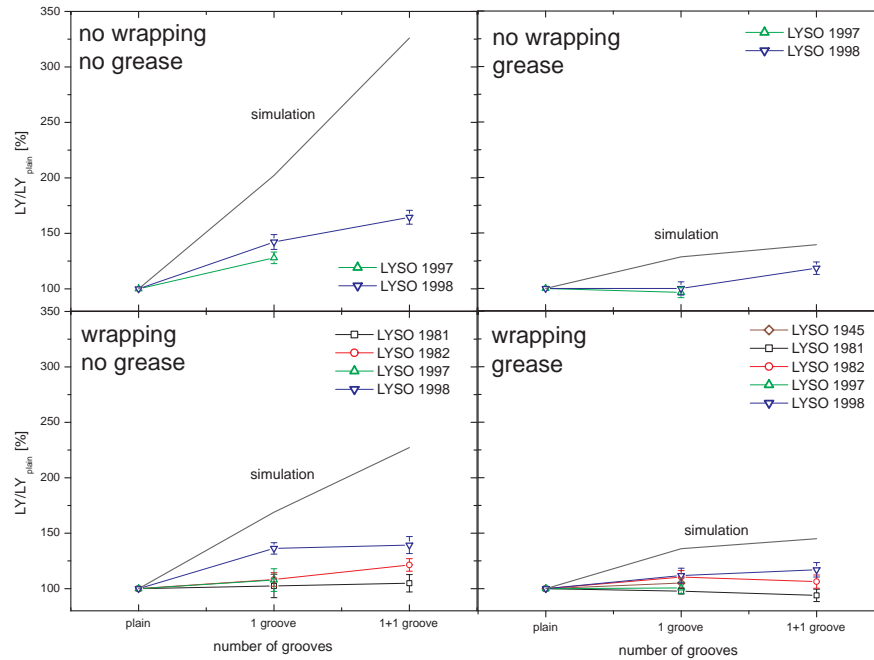


Figure 5.15: Comparison of experimental data with the simulation results of the idealized grooves for LYSO.

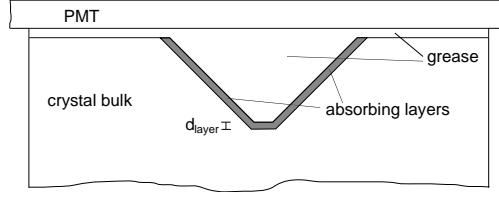


Figure 5.16: Sketch of LITRANI setup with absorbing layers.

5.4.2 Discussion of results

The results for unwrapped crystals are shown in Fig. 5.17. It is apparent from

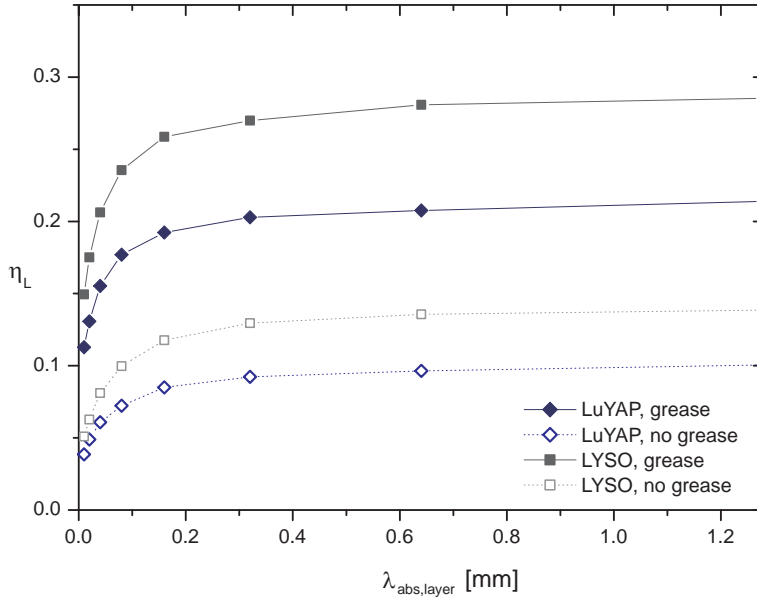


Figure 5.17: Dependence of η_L on $\lambda_{abs,layer}$ from the simulations.

the figure that the presence of the absorbing layer strongly reduces η_L of the LuYAP and LYSO crystals, especially for $\lambda_{scat,layer} < 800\mu\text{m}$.

By comparing the simulated and measured LY for plain and grooved exit surfaces it becomes possible to determine an approximate value of the absorption length of the layer. Figs. 5.18 and 5.19 indeed show that the model can describe the behaviour of the real crystals quite well. In particular, a reasonably good approximation of the experimental results can be found for $200\mu\text{m} \leq \lambda_{abs,layer} \leq 800\mu\text{m}$ for LuYAP 1999, LuYAP 2000 and LYSO 1997, and for $100\mu\text{m} \leq \lambda_{abs,layer} \leq 200\mu\text{m}$ for LYSO 1998.

The apparent presence of a thin, strongly absorbing layer just underneath the

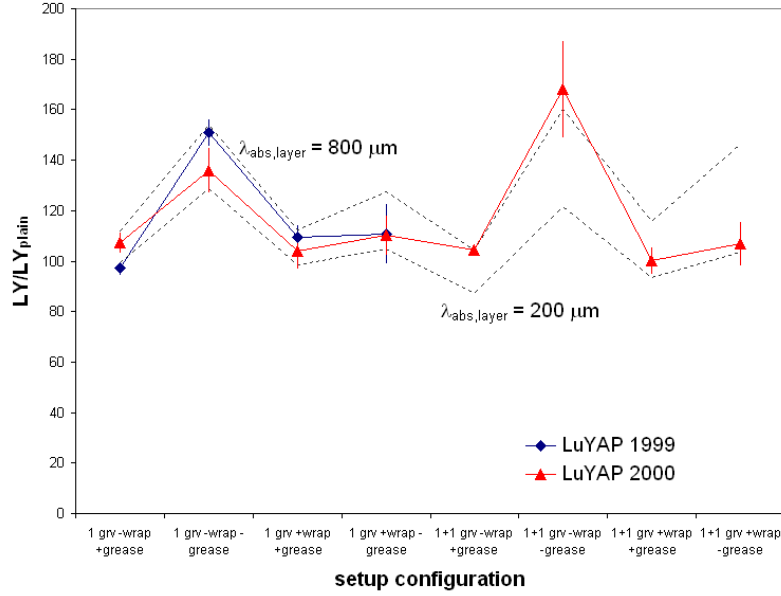


Figure 5.18: Comparison of experimental light yields with the results of the absorbing layer approach ($B = 1.6$). Results for LuYAP 1999 and LuYAP 2000.

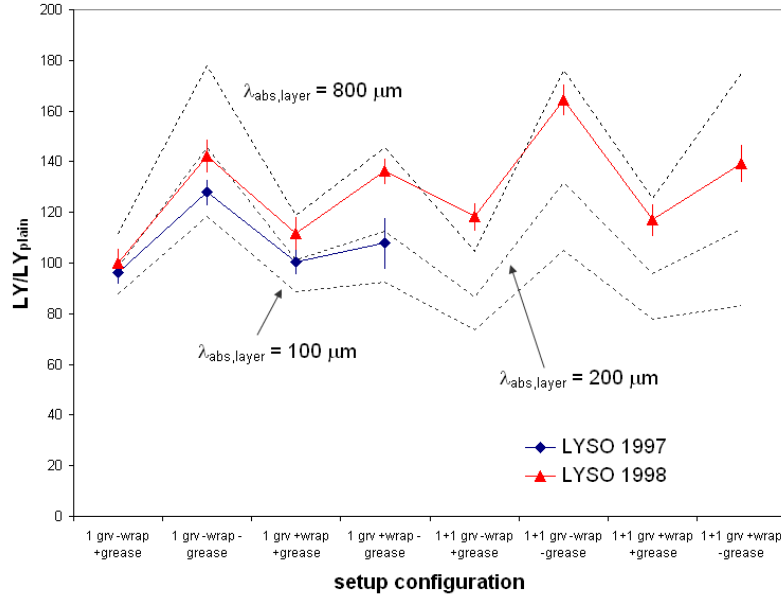


Figure 5.19: Comparison of experimental light yields with the results of the absorbing layer approach ($B = 1.6$). Results for LYSO 1997 and LYSO 1998.

groove surface indicates that an improvement of η_L can be possibly achieved by polishing the groove to such an extent that this absorbing layer disappears. Unfortunately, both LYSO and LuYAP are very brittle materials and therefore, only difficult to process mechanically. In fact, our attempts of mechanical polishing resulted in the partial or complete destruction of some of the samples. Possibly a different polishing technique or chemical treatment of the groove surfaces would yield better results here.

5.5 Conclusions

LITRANI simulations show that the light collection efficiency η_L of scintillators with small aspect ratio can be improved by machining grooves into the exit surface of the scintillators. The gain in η_L by these grooves depends on their shape, the refractive indices of bulk and grease, the scattering length, and the wrapping. An optimised performance for $2 \times 2 \times 8 \text{ mm}^3$ and $2 \times 2 \times 10 \text{ mm}^3$ LuYAP and LYSO pixels is found for grooves with depth $d \approx 0.5 - 0.6 \text{ mm}$ and opening angle $\alpha = 45^\circ$. Unlike plain exit surface crystals, η_L exhibits a pronounced maximum for $n_{grease} \approx 1.55 - 1.6$. Moreover, the gain in η_L induced by the groove rises almost linearly with n_{crys} . In addition, it is shown that η_L can be improved further if a second groove is machined perpendicularly to the first one; on the other hand, the presence of two or more parallel grooves often leads to a reduction of η_L .

Both bulk scattering and wrapping have more impact on η_L than in the case of a plain exit surface crystal. Especially the wrapping plays a significant role in the effectivity of the light extraction process: While specular reflectors with a high reflectivity allow for a high gain in η_L , diffusing wrappings perform less well, especially for cases where the wrapping is optically coupled to the crystal faces. This is a consequence of the reduced amount of incident photons at large angles which, in turn, is due to the randomization of the propagation direction in the diffusion process.

A comparison with experimental results shows that the idealised model of a perfectly polished groove does not reproduce the behaviour of the produced prototypes well. However, good agreement is achieved by a model that implements a strongly absorbing and diffusing layer just beneath the groove surface; for a layer thickness of $50 \text{ }\mu\text{m}$, the absorption length $\lambda_{abs,layer}$ of the layer is found to be between $200 \text{ }\mu\text{m}$ and $800 \text{ }\mu\text{m}$ for LuYAP 1999, LuYAP 2000 and LYSO 1997 and between $100 \text{ }\mu\text{m}$ and $200 \text{ }\mu\text{m}$ for LYSO 1998. This is an important result as it indicates that the performance of the grooved crystals can be improved by subsequent mechanical or chemical treatment which removes this absorbing layer and polishes the groove.

Bibliography

- [1] C. Carrier, R. Lecomte, Effect of geometrical modifications and crystal defects on light collection in ideal rectangular parallelepipedic BGO scintillators. Nucl. Instr. Meth. A 294, 355 (1990)
- [2] S. R. Cherry, Y. Shao, M. P. Tornai, S. Siegel, A. R. Ricci, M. E. Phelps, Collection of scintillation light from small BGO crystals. IEEE Trans. Nucl. Sci. 42, 1058 (1995)
- [3] Y. A. Berdnikov, V. V. Grebenshchikov, V. F. Kosmach, I. E. Leonov, V. M. Samsonov, O. Y. Khrushcheva, A. P. Shishlo, Special features of light collection processes in heavy-crystal-based scintillation detectors. Instr. Exp. Tech. 44, 466 (2001)
- [4] E. Auffray, F. Cavallari, M. Lebeau, P. Lecoq, M. Schneegans, P. Sempere-Roldan, Crystal conditioning for high-energy physics detectors. Nucl. Instr. Meth. A 48, 22 (2002)
- [5] V. L. Gayshan, A. V. Gektin, A. Boyarintsev, V. Pedash, Expanding of FOV of NaI(Tl) gamma camera detectors - Is it possible? Nucl. Instr. Meth. A 569, 159 (2006)
- [6] A. J. Wojtowicz, W. Drozdowski, M. Ptaszyk, Z. Galazka, J.-L. Lefaucheur, Scintillation light yield of Ce-doped LuAP and LuYAP pixel crystals. Proc. Int. Conf. on Inorganic Scintillators and their Applications, SCINT05, 473 (2006)

Chapter 6

Scintillators with nanostructured exit surfaces

Micro- and nanostructurization of materials has found widespread interest in the last years as a tool to overcome the problem of total internal reflection in media with high refractive index. Recent efforts in this regard include microtexturing of surfaces [1], the addition of diffusive layers [2] and nanoporous films [3], the usage of microspheres [4], microlenses [5, 6], or nanowires [7], surface plasmons [8], and Bragg gratings [9].

Currently, the most common technique is to improve light extraction from light-emitting and -transmitting media by means of photonic crystals (PhCs). This chapter reviews the properties of photonic crystals, evaluates their potential to improve the light extraction efficiency of inorganic scintillators, and presents possible realizations of a scintillator-PhC prototype.

6.1 Photonic crystals

Photonic crystals (PhCs) are media with a periodic modulation of the dielectric constant ϵ [10, 11]. This modulation is created by arranging two materials with different ϵ in one, two, or three dimensions such that they form a regular structure, analogous to the atomic lattice of a crystal (Fig. 6.1). A PhC is therefore not a 'crystal' in the common sense of the word; in fact, its name refers to the ability of the material to affect the propagation of electromagnetic waves much in the same way as the periodic potential of a crystal lattice affects electrons moving through the lattice. For this reason, the propagation of photons through a PhC lattice is described, as the propagation of electrons through an 'atomic' crystal, by the Bloch-Floquet theorem. In the following sections, the major implications of the theorem regarding the optical properties of PhCs are reviewed; a more rigorous mathematical description is given in Appendix A.1. Both in the text and in the appendix, vectors are denoted by **bold**-faced letters and matrices by *italic*-faced letters.

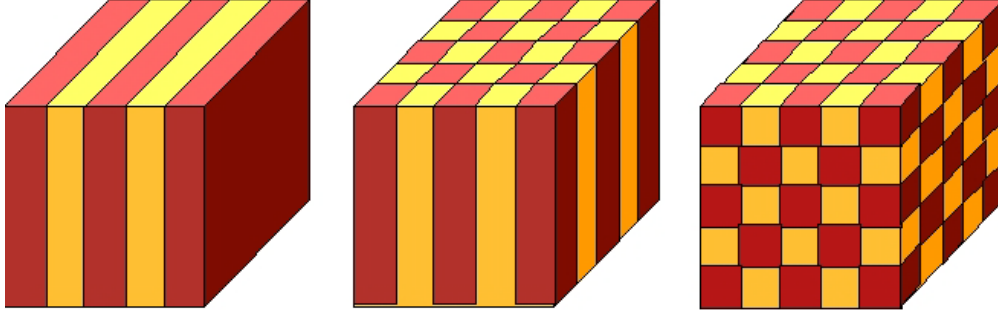


Figure 6.1: Principal outline of PhCs [12]. Left: 1D PhC. Middle: 2D PhC. Right: 3D PhC.

6.1.1 The Bloch-Floquet theorem

The Bloch-Floquet theorem states that the solution of the Hermitian eigenproblem of the magnetic field \mathbf{H} ,

$$\nabla \times \frac{1}{\epsilon} \nabla \times \mathbf{H} = \frac{\partial^2 \mathbf{H}}{\partial ct^2} \quad (6.1)$$

for a periodic dielectric $\epsilon = \epsilon(\mathbf{r})$ can be assumed to be of the form:

$$\mathbf{H} = \mathbf{H}_{\mathbf{k}} \cdot e^{i(\mathbf{k} \cdot \mathbf{r} - \omega t)}, \quad (6.2)$$

where ω denotes the eigenfrequency of the wave and \mathbf{k} the wavevector. The amplitude $\mathbf{H}_{\mathbf{k}}$ is a periodic function of the position \mathbf{r} . The application of the Bloch-Floquet theorem to PhCs has several important consequences: First, the eigenproblem is restricted to the unit cell of the periodicity and yields a discrete set of eigenvalues and eigenfrequencies $\omega_n(\mathbf{k})$ which are continuous functions of \mathbf{k} . Second, the PhC eigenmodes are not only periodic in \mathbf{r} but also periodic in \mathbf{k} . Assuming a PhC with a periodic modulation of ϵ in x -direction, \mathbf{k} will be periodic in x with the reciprocal wavevector $\hat{\mathbf{b}}$:

$$\hat{\mathbf{b}} = \frac{2\pi}{a} \hat{\mathbf{x}}, \quad (6.3)$$

where a is the period of the PhC lattice. Analogous to a regular 'atomic' crystal, $\hat{\mathbf{b}}$ is termed *primitive reciprocal lattice vector* and the region $-\pi/a < k_x < \pi/a$ *first Brillouin zone*. Additional symmetries that apply to the PhC, as e.g. time-reversal symmetry and rotational symmetry, further reduce the range of unique wavevectors to a region which is called the *irreducible Brillouin zone*. Accordingly, any eigenvalue problem for \mathbf{k} needs to be solved only for this region.

Scaling invariance

Another important property of PhCs originates from the absence of any fundamental length scale in the Maxwell equations. This means that for any solution found at one length scale, an equivalent solution can be found at another length scale. Because of this scale invariance, it is convenient to describe a PhC by

means of its periodicity a and all angular frequencies ω by a/λ . Similarly, if $\epsilon(\mathbf{r})$ is substituted by $s^2\epsilon'(\mathbf{r})$, the harmonic modes of the PhC remain unchanged except from their frequencies, which scale with a factor s : $\omega \rightarrow s \cdot \omega'$. Both are important properties of PhCs as they allow for testing a microscopic PhC by means of an equivalent macroscopic system.

6.1.2 Optical properties of photonic crystals

The periodic modulation of ϵ in PhCs is responsible for their unique optical properties. The most important one of these is the existence of a band gap, i.e. a wavelength range for which the PhC neither absorbs light nor allows light propagation (see also Appendix A.2). This band gap is the photonic analogue to the forbidden energy range between the valence and conduction bands, as observed in isolators and semiconductors (cf. Sect. 2.1.1)

The existence of the band gap is a consequence of two general properties of Hermitian eigenvalue problems. The first property is the orthogonality of the PhC eigenfunctions for any two eigenstates ($m \neq n$) at a given \mathbf{k} point,

$$\int \mathbf{H}_{\mathbf{k}}^{(m)*} \cdot \mathbf{H}_{\mathbf{k}}^{(n)} = 0 \quad (6.4)$$

In addition, every band has to solve a variational problem of the form

$$\omega_n(\mathbf{k})^2 = \min \frac{\int |(\nabla + i\mathbf{k}) \times \mathbf{H}_{\mathbf{k}}|^2 / \epsilon}{\int |\mathbf{H}_{\mathbf{k}}|^2} \cdot c^2 \quad (6.5)$$

where $\omega_n(\mathbf{k})$ denotes the eigenfrequency of the node. As a consequence, the electric field of the lowest band (i.e. the curl in eq. 6.5) should only oscillate slowly and should be concentrated in the high- ϵ regions of the PhC, while the second lowest band will either be concentrated in the lower ϵ regions or will exhibit a sign oscillation inside the high- ϵ regions to make the integral zero. Both options will lead to an increase in the band frequency, and therefore to the appearance of a gap in the photonic band structure [12]. If the dielectric contrast between the ϵ_{low} and ϵ_{high} regions is large enough, the gaps at all \mathbf{k} points can overlap in a certain frequency range and an omni-directional band gap occurs.

Fig. 6.2 illustrates the band structure of a two-dimensional PhC with a hexagonal pattern of air holes ($\epsilon_{hole} = 1$) in a bulk with $\epsilon_{bulk} = 2.5$ and a hole radius $R = 0.33 \cdot a$. The abbreviations TE (transversal electric) and TM (transversal magnetic) denote modes with different polarization states. For TE modes, the electric field extends in the x - y plane and the magnetic field in z direction; for TM modes, the magnetic field extends in x - y and the electric field points towards z . Clearly, the presented structure exhibits a large omni-directional band gap in TE polarisation around $a/\lambda \approx 0.35$ whereas no band gap is visible for the TM modes. When this is compared with the band structure of a homogeneous material (Fig 6.3), the periodic corrugation begins to affect the optical

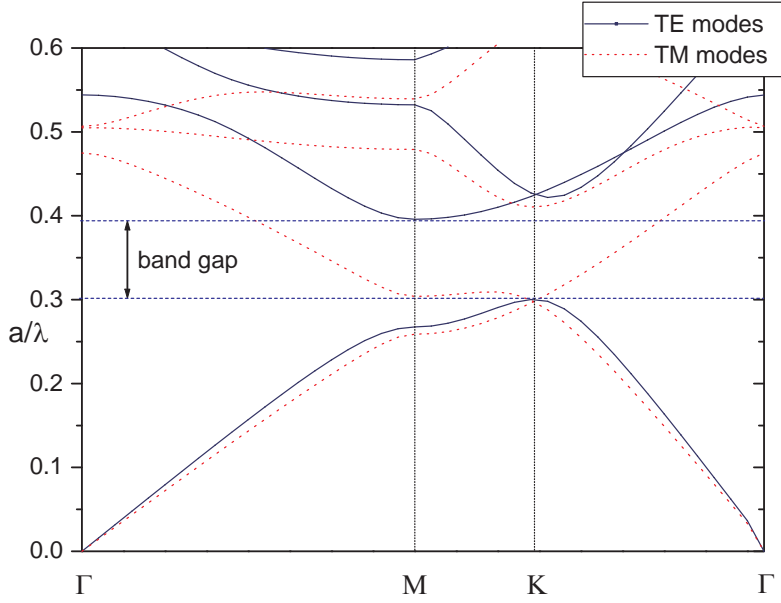


Figure 6.2: Band structure of a 2D PhC.

properties of the material only above a certain threshold of a/λ . This is a consequence of the fact that the photon cannot 'feel' the periodic modulation any more but sees it only as a homogeneous dielectric background if its wavelength λ is significantly larger than a . In the following, the interval of a/λ where the optical properties of the PhC are resembling those of a homogeneous slab is denoted *homogeneous regime* while the interval of a/λ where the optical properties are determined by the periodic modulation in ϵ is denoted *photonic regime*.

As Fig. 6.2 shows, the dispersion relations for TE and TM modes in the homogeneous regime are not congruent with each other but slightly different; this means that in the homogeneous regime, the PhC does not exhibit an isotropic ϵ but acts effectively like a birefringent medium.

The location and width of a band gap depends not only on the dielectric constants of PhC bulk and holes but also on the PhC structure and the fraction of the PhC surface occupied by the holes. This fraction is usually expressed by the filling factor f :

$$f = \frac{A_{hole}}{A_{hole} + A_{bulk}} \quad (6.6)$$

A_{hole} and A_{bulk} denote the areas (or volumes) of the holes and the bulk in a unit cell, respectively. In the case of a square or triangular PhC structure with

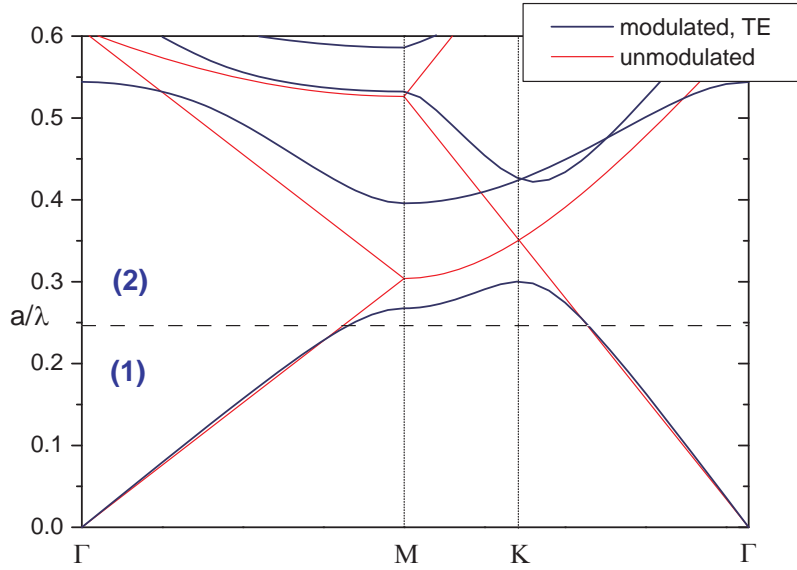


Figure 6.3: Comparison of the band structure of a homogeneous material and a PhC. (1): homogeneous regime; (2): photonic regime.

circular holes, f is related to the hole radius R by:

$$\begin{aligned} \text{Square : } f &= \frac{\pi R^2}{a^2} \\ \text{Triangular : } f &= \frac{2\pi R^2}{\sqrt{3}a^2} \end{aligned} \quad (6.7)$$

The dielectric contrast η is usually expressed by the quantity:

$$\eta = \frac{\epsilon_{bulk}}{\epsilon_{hole}} - 1 \quad (6.8)$$

In the presence of a band gap, several distinct optical phenomena, such as inhibition of spontaneous emission, threshold-less lasing [25, 26], omnidirectional reflection [27], and low-loss-waveguiding [28, 29], can be observed. Other phenomena of PhCs, as negative refractive index [13, 14, 15, 16, 17, 18, 19], superlensing [13, 15, 16, 20], superprism effects [21, 22], polarisation splitting [24], and Cherenkov cone inversion [23], are directly related to the band structure of the material.

6.1.3 Photonic crystal slabs

A photonic crystal slab is a dielectric structure analogous to a two-dimensional PhC but extending finitely into the direction perpendicular to the periodicity plane (Fig. 6.4). Similar to a regular 2D PhC, it may exhibit a frequency range in which wave propagation for all in-plane directions is forbidden due to Bragg

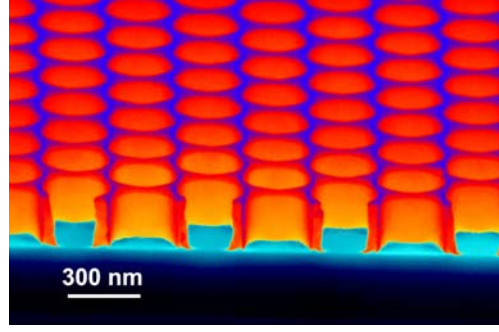


Figure 6.4: Image of a PhC slab [58].

interference; due to the finite height of a PhC slab, however, the band diagram differs from that of a 2D PhC by exhibiting a continuum of states that extend infinitely in the region outside the slab. This continuum destroys the gap of the purely two-dimensional structure. Due to its shape in the band diagram, the continuum region is called *light cone* (Fig. 6.5); its lower boundary is given by the equation

$$\omega = ck_{||}/\sqrt{\epsilon_m}, \quad (6.9)$$

with the in-plane wavevector $k_{||}$ and the dielectric constant ϵ_m of the medium that surrounds the PhC slab.

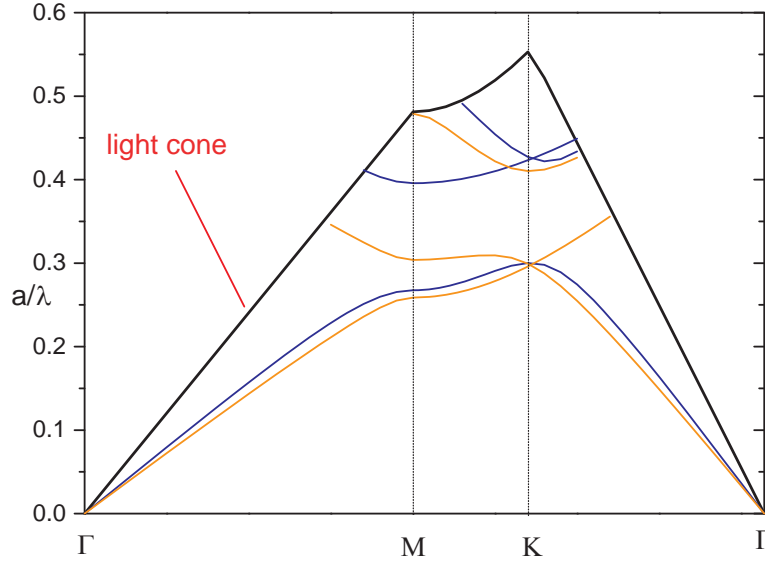


Figure 6.5: Band structure of a PhC slab.

Due to the presence of the light cone, guided modes can only exist in regions of the band diagram where $\omega < ck_{||}/\sqrt{\epsilon_m}$. These modes cannot couple with modes

in the bulk background, but instead extend infinitely within the periodicity plane and decay exponentially into the surrounding medium. Consequently, the band gap observed in a PhC slab is different to the band gap of a 2D PhC in that it indicates a range of frequencies in which *no guided modes* exists. However, it is not a true band gap as the light cone still contains radiation modes at such frequencies. Any light with such a frequency will thus not be able to travel within the PhC slab, but will couple to one of the radiation modes in the light cone; vice versa, modes above the light cone are guided into the PhC during a finite lifetime which depends on the coupling with free space modes. Such modes are called *pseudoguided* or *leaky* modes. Some of these modes, especially at the gamma point, cannot interact with the continuum for symmetry reasons and therefore, can be considered as true guided modes.

As in a real 2D PhC, it is possible to decompose the guided modes into two non-interacting classes. Due to the lack of translational symmetry, it is not possible to define purely TE or TM polarized states; instead, the guided bands can be classified according to whether they are even or odd in respect to reflections at a horizontal symmetry plane. These even and odd states have strong similarities with TE and TM polarized states but are not necessarily TE or TM-like. In addition, a classification into even and odd bands is only possible if the dielectric constant of the medium that is above the slab is equal to that of the medium below the slab; if this symmetry is lifted, the even and odd states are mixed and the PhC properties of the slab are lost. In such a case, a band gap is just possible if the guided modes are sufficiently localized within the slab and the wavefunctions can still be approximated as being even or odd [12].

6.1.4 Fabrication of PhCs

A number of techniques for PhC fabrication have been employed during the past 20 years. These methods involve classical UV and X-ray lithography [30], holographic methods [31], and mask-less methods such as self-assembly [32], selective area vapor epitaxy [33], or direct imprinting methods using a mold [34]. The most common approaches to produce PhCs are lithographic methods that use particle beams to expose a photo resistive mask. Two of these methods - electron-beam and ion-beam lithography - are shortly reviewed in the following.

Electron beam lithography (EBL)

In EBL, a layer of an electro sensitive resist is deposited on top of the sample and sensitized by a beam of accelerated electrons. The electron beam is produced in an analogous manner as in a scanning electron microscope. Electrons emitted by a heated filament are accelerated by an electric field of several kV. By a system of electromagnetic lenses and diaphragms, the beam is narrowed down to several nm and focused onto the structure into which the lithographic pattern is written. This is obtained by moving the beam in x and y direction by means of magnetic fields generated by several solenoids with variable voltage. The energy acquired by the electrons during the acceleration process is sufficient

for the electrons to fully travers the thin ($< 1 \mu\text{m}$) layer of electro sensible resist and sensibelize the resist locally by a physical transformation. After exposure, the sample is moved to a developer. Depending on the type of resist (positive / negative), this developer removes either the exposed or the non-exposed parts of the resist.

After developing the resist, the lithographic PhC structure is transferred to the sample by reactive ion etching (RIE). Reactive gazes are injected into a reactor with a pressure of $10^{-2} - 10^{-1}$ Pascal. Subsequently, the gas is ionized by a strong electromagnetic field with a frequency of several MHz. The ions are sent to the sample by means of a vertically oriented electric field. As soon as the ions reach the sample, they either react chemically with the materials on the sample surface, or sputter some sample material by kinetic energy transfer. The electric field ensures that the ions can propagate only in directions perpendicular to the sample surface; this ensures a purely vertical growth of the lithographic PhC pattern and therefore, vertical hole flanks.

The resolution of the EBL is determined by the diameter of the electron beam at the position of the sample, the distance between the sample and the last metallic element regulating the beam, the amount of electron backscattering in the resist, and the lateral diffusion of the electrons [36]. The highest resolutions achieved with EBL are in the range of 10 nm [35].

Ion beam lithography

Ion beam lithography works similar to electron beam lithography except that it uses a focused ion beam (FIB) instead of electrons. This beam scans across the surface of the substrate and exposes a sensitive coating, which is then removed in a subsequent development step. Alternatively, the sample can also be directly exposed, e.g. with a programmable aperture plate with a large number of apertures of micrometric dimension [37].

The resolution achievable with FIB lithography is comparably to that of EBL. The major advantage of FIB is that backscattering of particles poses much less problems than in the case of EBL.

6.2 Photonic crystals and light extraction

As was first discussed in [38], the unique optical properties of a thin PhC slab can be used to diffract, from a high refraction index substrate, light that would otherwise be trapped by total internal reflection.

If an electromagnetic wave with wave vector \mathbf{k} hits the interface between two media with $n_1 > n_2$ under an incident angle θ_i , the z component of the wave vector in the medium above the substrate will be imaginary if

$$\sin(\theta_i) \geq \sin(\theta_{tot}) = \frac{n_2}{n_1}. \quad (6.10)$$

In this case, no light will be transmitted through the interface (Fig. 6.6a). This changes if the interface is not flat but comprises a PhC slab (Fig. 6.6b): In this case, the incoming wave is split into different harmonics \mathbf{k}_p and the z component of the wave vector in medium 2, k_{z,n_2}^p , becomes

$$k_{z,n_2}^p = \sqrt{n_2^2 \cdot k^2 - (\mathbf{k}_{\parallel} + \mathbf{G}_p)^2} \quad (6.11)$$

where \mathbf{k}_{\parallel} is the in-plane component of \mathbf{k} and \mathbf{G}_p is a reciprocal lattice vector,

$$\mathbf{R}_m \cdot \mathbf{G}_p = 2\pi \cdot \delta_{m,p} \quad (6.12)$$

If k_{z,n_2}^p is real for one harmonic, this particular partial wave is diffracted out of the substrate and the transmission of the interface becomes larger than zero. This approach has already been successfully used to improve light extraction

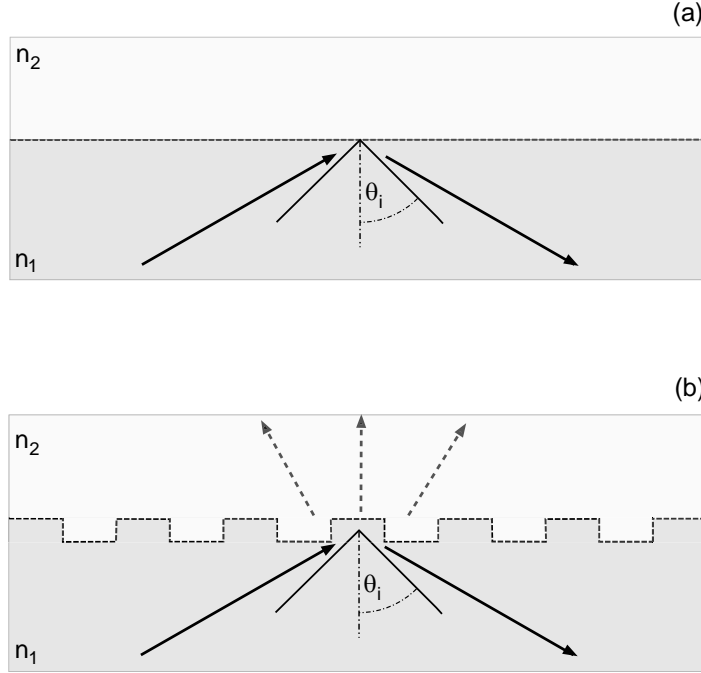


Figure 6.6: Situation at the interface between two materials ($n_1 > n_2$) for (a) plain geometry and (b) a periodic modulation of the interface.

from light-emitting diodes [39, 40, 41, 42, 43, 44, 45], whose light output traditionally suffers from the high refractive indices of the semiconducting materials that are typically used. Other examples where this effect has been employed are the collimation of light coming from and entering a waveguide [46], and the increase of the efficiency of solar cells [47].

6.3 Simulation of the nanopatterned exit surface

To evaluate the impact of a nanopatterned exit surface on η_L of scintillating materials with high refractive index, studies of the transmissive and reflective properties of the periodically modulated exit surface were performed and compared with the results for unmodulated scintillators presented in Chapter 4. This was necessary to do as the properties of the modulated surface need to be optimised on the angular distribution of the photons incident on this surface.

6.3.1 Simulation algorithm

In the past years, a multitude of algorithms has been developed that allow for simulating the in- and out-of-plane properties of 2D- and 3D PhCs [15, 49, 50, 51, 52, 53, 54, 55, 56]. The simulations presented in this chapter have been performed by adapting the scattering matrix method of Tikhodeev et al. [48] to the current problem. In the following, the basic principle of the method is reviewed; a detailed description of the principle of the method and the applied adaptations is given in Appendix A.3.

The Tikhodeev algorithm calculates the energy flow through a series of N interfaces by expanding the electric and magnetic fields of the incoming, transmitted, and reflected waves into a Fourier series. The amplitudes of the partial waves are then connected by a scattering matrix S :

$$\begin{pmatrix} \mathbf{A}_0 \\ \mathbf{B}_N \end{pmatrix} = S \cdot \begin{pmatrix} \mathbf{A}_N \\ \mathbf{B}_0 \end{pmatrix} \quad (6.13)$$

The vectors \mathbf{A}_0 , \mathbf{B}_N , \mathbf{A}_N and \mathbf{B}_0 contain the in-plane field components of the incoming waves in positive and negative z -direction, the field components

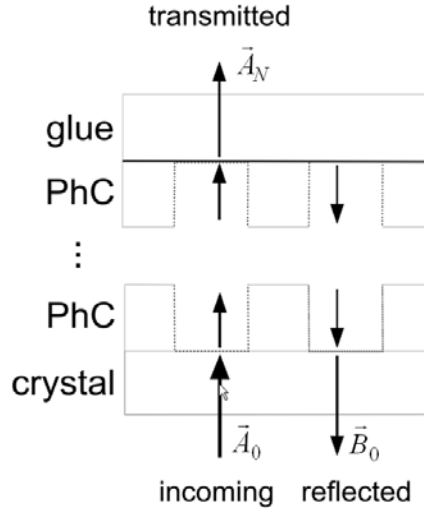


Figure 6.7: Principle of the Tikhodeev algorithm.

of the transmitted wave, and the field components of the reflected wave, respectively. Simulated were only cases with $\mathbf{B}_N = \mathbf{0}$, i.e. cases where the light was approaching the PhC slab only from the scintillator side (Fig. 6.7).

The model structure simulated with this method is sketched in Fig. 6.8. It

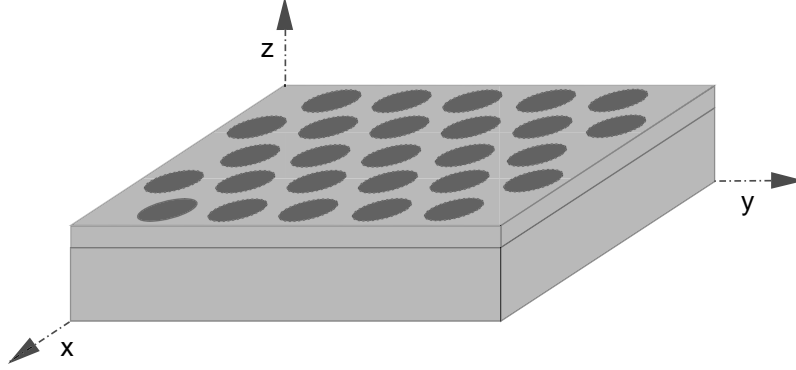


Figure 6.8: Outline of the simulated system. For reasons of clarity, the layer of grease on top of the PhC is not shown.

consists of an LYSO or LuYAP type substrate material, a PhC slab consisting of a regular pattern of air holes, and a layer of grease. The refractive index of the substrate and the grease was kept fixed, with $n_{grease} = 1.47$ and $n_{sub} = 1.82$ and 1.94 for LYSO and LuYAP, respectively. All materials were simulated as ideally transparent, i.e. with an extinction coefficient k equal to zero. The PhC slab was simulated as of square or triangular geometry with lattice constant a and filling factors f between 0.2 and 0.8. The refractive index of the PhC bulk, n_{bulk} , was varied between 1.82 and 4.8. Quasi-crystalline lattices with higher symmetry than the triangular lattice were not simulated but are expected to lead to a further improvement of η_L due to the increased number of directions into which diffraction could take place [40, 57].

In each run, between 85 and 151 plane waves were simulated. These numbers were found to be sufficient for assessing the principal optical properties of the material. Two different polarization states of the wave were considered: for S polarized waves, the electric field of the incident wave is oriented parallel to the x - y plane, whereas for P polarized waves, the magnetic field of the incident wave is parallel to the x - y plane. Transmissions were determined for incident angles θ_i between 0° (normal incidence) and 90° by averaging over all possible polar angles ϕ and polarization states (Fig. 6.9).

6.3.2 Results of simulations

As noted earlier, the transmission of a PhC slab depends not only on its overall structure but also on the hole shape, the filling factor f , the slab thickness d_{slab} , the dielectric contrast between holes and bulk, the wavelength of the incident photon λ , and the incident angle θ_i . In the following, the impact of some of

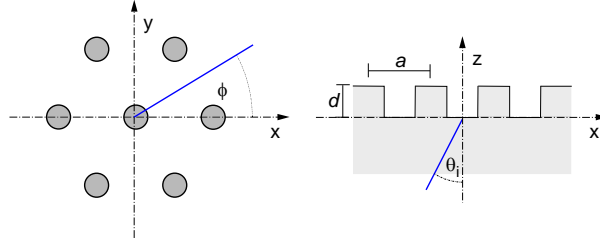


Figure 6.9: Definition of angles θ_i and ϕ .

these parameters on the transmission of the PhC slab is evaluated with the results of simulations performed with the Tikhodeev method. Unless otherwise noted, the presented plots regard PhCs with $f = 0.7$, $d_{slab} = 0.3$, $n_{bulk} = 3$ and $n_{hole} = 1$. The often diametrically opposed trends observed at high and low incident angles are assessed by plots for $\theta_i = 0^\circ$ and $\theta_i = 60^\circ$.

Dependence on a/λ

As discussed in Sect. 6.1.2, a photon propagating through a PhC slab feels the presence of the periodic modulation only above a certain threshold of a/λ . Below this threshold, the PhC slab behaves analogously to a homogeneous slab with effective dielectric constant $\epsilon_{eff} = f \cdot \epsilon_{hole} + (1-f) \cdot \epsilon_{bulk}$ (Fig. 6.3). Consequently, the transmission properties of the PhC slab should exhibit a transition region in which the optical properties of the slab change from the homogeneous regime to the photonic regime.

This transition is clearly seen in the left part of Fig. 6.10 which illustrates the dependence of the transmission of a PhC slab on a/λ . Clearly, the periodic modulation of the slab effectively influences photon propagation only for $a/\lambda > 0.3$, i.e. when the wavelength of the photon approaches the lattice period a . In addition, the plot shows that even in the photonic regime, the transmission does not remain constant but shows pronounced dips and maxima. This is a consequence of the contribution of different harmonics to the total transmission at different values of a/λ : the dips and maxima correspond to wavelengths where new harmonics are transmitted into the glue layer or reflected back into the substrate of the scintillator.

Influence of incident angle θ_i

Fig. 6.11 shows the dependence of the slab transmission on the incident angle θ_i of the photon. Clearly, the presence of the periodic modulation leads to a reduced slab transmission at angles within the extraction cone relative to an uncorrugated slab.

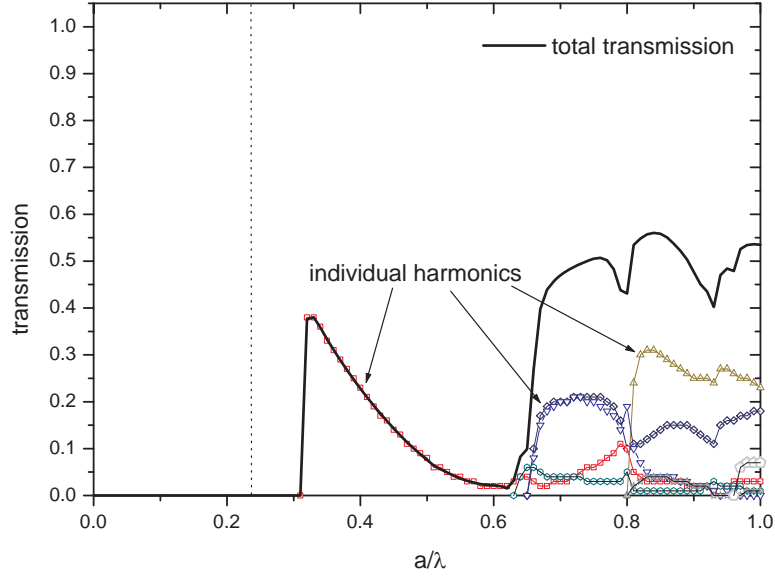


Figure 6.10: Dependence of the transmission of a PhC slab ($n_{bulk} = 1.95$; $f = 0.3$; $d_{slab} = 1$) on top of a LuYAP crystal ($\theta_i = 55^\circ$; $\phi_i = 0^\circ$).

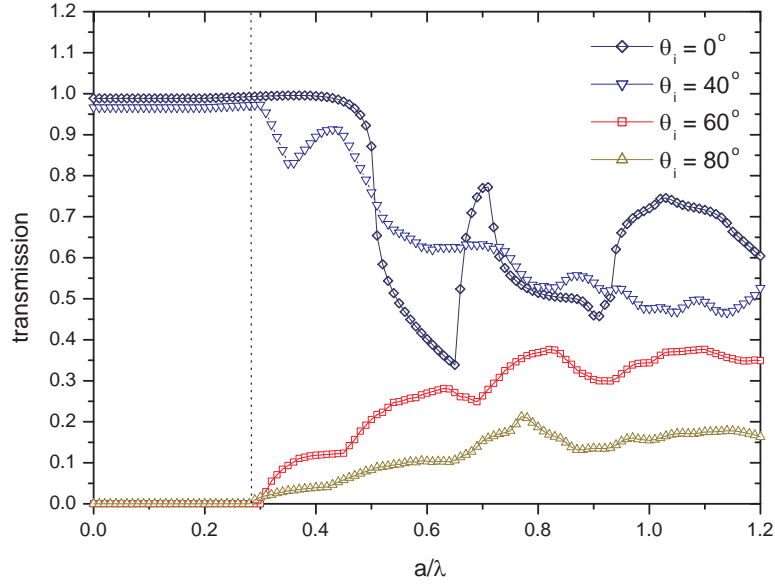


Figure 6.11: Dependence of the slab transmission on θ_i . PhC slab on LuYAP, $n_{bulk} = 3$, $f = 0.7$, $d_{slab} = 0.3$. Note that for an unmodulated slab, no transmission is possible for $\theta_i > 50^\circ$.

A different behaviour is observed when the photon is incident at the exit surface with an angle that is larger than the angle of total reflection θ_{tot} . In this case, the PhC slab helps in extracting some of the incident photons and the total internal reflection at the exit surface is lifted. As Fig. 6.11 indicates, the effect is not restricted to incident angles near θ_{tot} but is also apparent for large θ_i .

Dependence on structural parameters

Filling factor f

The dependence of the transmission on the filling factor f is depicted in Figs. 6.12a and 6.12b for incident angles $\theta_i = 0^\circ$ and $\theta_i = 60^\circ$, respectively. Clearly, a change of the filling factor f also affects the transmission properties of the slab. This is especially evident in the range $0.4 < a/\lambda < 0.65$ where the transmission at $\theta = 0^\circ$ varies considerably with f . At higher a/λ , the differences smooth out and the slabs exhibit similar transmission. From the plots it is also apparent that a PhC slab with f between 0.5 and 0.7 performs slightly less well at small θ_i but significantly better at large θ_i relative to the slab with $f = 0.8$.

Slab thickness

The effect of the slab thickness on the transmission is illustrated in Figs. 6.13a ($\theta_i = 0^\circ$) and 6.13b ($\theta_i = 60^\circ$). As both plots show, the slab thickness affects η_L mostly at small a/λ ; above $a/\lambda \approx 1$, the effect is smoothed out and the slabs show similar transmissions.

Dielectric contrast η

The dielectric contrast η (eq. 6.8) expresses the strength of the variation of ϵ in a PhC. Accordingly, a slab with larger η is expected to affect the photon propagation more strongly than a slab with smaller η .

This is seen in Figs. 6.14a and 6.14b which illustrate the impact of the dielectric contrast on the slab transmission. As n_{hole} was assumed to be 1 in each case, only n_{bulk} is given. Clearly, slabs with small n_{bulk} affect the photons much less than slabs with large n_{bulk} . On the other hand, the plots show that an increase of n_{bulk} does not automatically lead to an increase of the transmission at large θ_i (cf. Fig. 6.14b).

6.4 Determination of the extraction potential

As the results presented in the last section show, the transmission of a scintillator with modulated exit surface depends on the structural parameters of the PhC slab and the incident angle of the photon. However, the potential of a system crystal + PhC in terms of light extraction depends not only on the transmission of the PhC slab but also on the angular distribution of the photons incident at the PhC slab, as shown in Figs. 4.18a and 4.18b. This means that the PhC slab has to be optimised such that as many of the incident photons as possible become extracted.

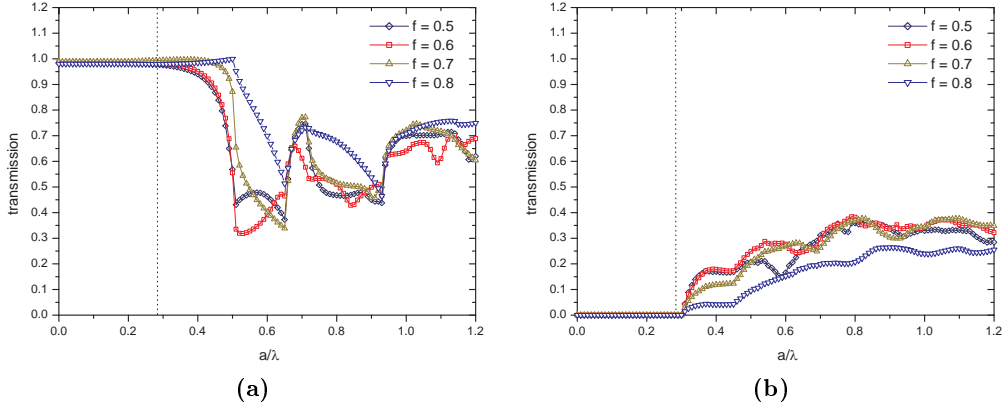


Figure 6.12: Dependence of the slab transmission on f . (a) $\theta_i = 0^\circ$. (b) $\theta_i = 60^\circ$. PhC slab on LuYAP, $n_{bulk} = 3$, $d_{slab} = 0.3$.

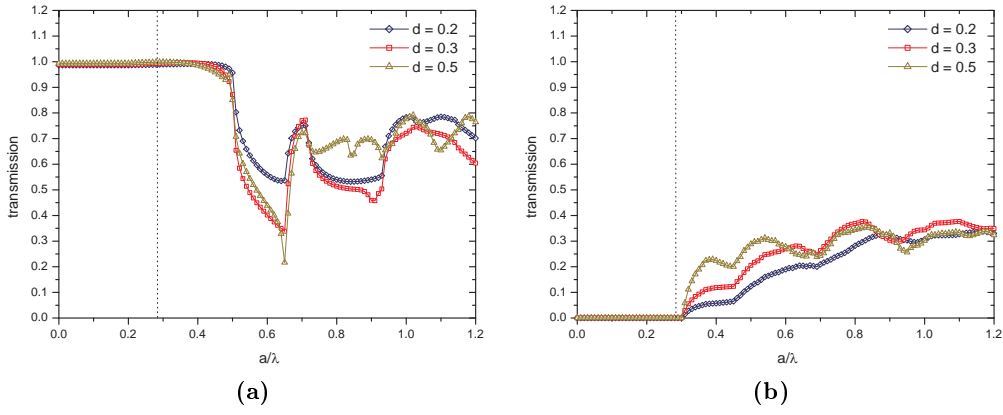


Figure 6.13: Dependence of the slab transmission on d_{slab} . (a) $\theta_i = 0^\circ$. (b) $\theta_i = 60^\circ$. PhC slab on LuYAP, $n_{bulk} = 3$, $f = 0.7$.

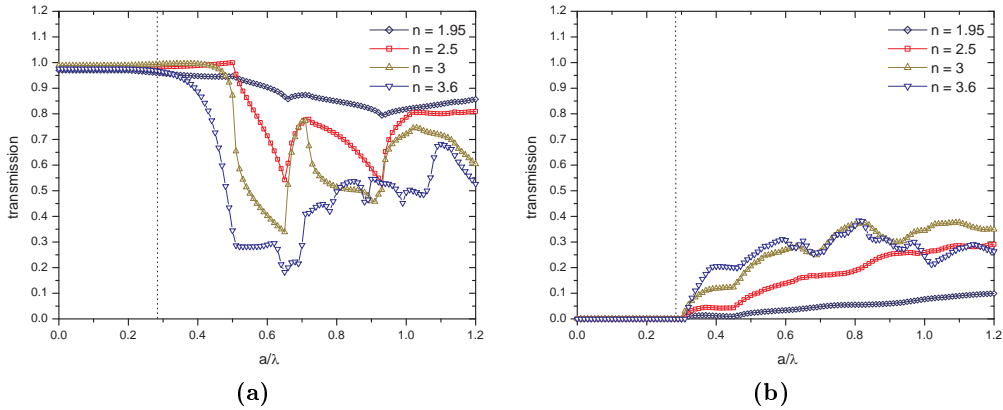


Figure 6.14: Dependence of the slab transmission on n_{bulk} . (a) $\theta_i = 0^\circ$. (b) $\theta_i = 60^\circ$. PhC slab on LuYAP, $d_{slab} = 0.3$, $f = 0.7$.

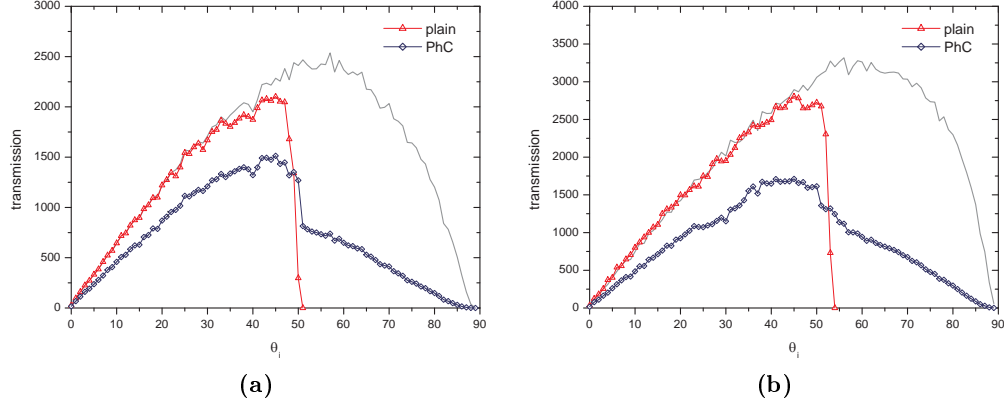


Figure 6.15: Angular distribution of photons extracted at first incidence on an exit surface with PhC slab for (a) LuYAP and (b) LYSO and $a/\lambda = 0.8$. The grey line indicates the angular distribution of all incident photons for a specular reflector with 98% reflectivity. The angular distribution of photons extracted for a plain exit surface is shown for comparison.

Fig. 6.15 compares, for $2 \times 2 \times 8 \text{ mm}^3$ LuYAP and LYSO crystals, the angular distribution of the photons that are extracted by the PhC *immediately*, i.e. at first incidence of the photon, with the angular distribution of the photons extracted by a crystal with plain exit surface. In both cases, a PhC slab with $n_{bulk} = 2.3$ was simulated with structural parameters $d = 0.3$ and $f = 0.5$ (LuYAP) and $d = 0.5$ and $f = 0.6$ (LYSO); a/λ was in both cases set to 0.8. The calculation of the number of extracted photons is based on the angular distribution of the incident photons in the case of a specular reflector with 98% reflectivity.

As already suggested by the results shown in Fig. 6.11, the nanopatterned exit surface has a reduced transmission at angles below the angle of total reflection θ_{tot} and the total number of photons transmitted in this angular region is clearly smaller than for a plain exit surface. However, the plots also show that this is at least partly compensated by photons with $\theta_i > \theta_{tot}$ which add to the transmission of the PhC slab.

These considerations concern only those photons which are transmitted at first incidence at the PhC slab. In evaluating the impact of the PhC slab on η_L , it is also necessary to account for the photons that are not transmitted but *reflected back* into the scintillator. These backreflected photons can be extracted during their next incidence onto the PhC slab, and therefore are likely to contribute significantly to η_L . Unfortunately, it is not straightforward to calculate the probability of recurrence, due to the splitting of the reflected waves into several harmonics by the PhC slab and the change of the propagation direction

by scattering in the crystal bulk and by diffusion at the wrapping. A precise determination of the light collection efficiency η_L of a scintillator with corrugated exit surface is therefore a complicated task and probably only achievable by a combination of a plane wave expansion method with a light ray tracing program such as LITRANI. In addition, such a program has to account for possible absorption in the PhC bulk material itself.

A relatively simple method to evaluate the impact of a PhC on η_L is it to calculate the number of extracted photons for a 'best-case' model. This model is based on the following assumptions:

1. α_{abs} of the crystal is independent on the wavelength λ .
2. no scattering in the crystal ($\alpha_{scat} = 0$)
3. a specularly reflecting wrapping with reflectivity $\approx 100\%$
4. a lossless PhC bulk material ($k = 0$)
5. the number of photons reflected into one direction, $N_r(\theta_i)$ is equal to the number of incident photons in this direction $N_i(\theta_i)$ minus the number of transmitted photons, i.e. $N_r(\theta_i) = (1 - t)N_i(\theta_i)$.

$t = t(\theta_i)$ denotes the transmission of the PhC slab at a given incident angle and depends on a/λ .

The assumptions quoted above have several consequences. Assumption (1) means that the absorption characteristics of the crystal are described by a single absorption coefficient α_{abs} . This is necessary as the model seeks to find an optimised value of a/λ of the PhC structure and any wavelength-dependent parameters have to be avoided. (2) and (3) imply that the path lengths l of the photons between reflection and recurrence depend only on the incident angle θ_i and the crystal height d . In this case, l is given by (Fig. 6.16)

$$l = \frac{2d}{\cos(\theta_i)} \quad (6.14)$$

In addition, the assumption of a perfect reflector ensures that photons can only be absorbed by the bulk, i.e. the probability $P_{re}(\theta_i)$ that a reflected photon recurs at the exit surface is only determined by l and the absorption length λ_{abs} via

$$P_{re}(\theta_i) = e^{-\frac{l}{\lambda_{abs}}} = e^{-\frac{2d}{\lambda_{abs} \cdot \cos(\theta_i)}} \quad (6.15)$$

Similarly, assumption (4) specifies that absorption in the PhC bulk can be neglected. Finally, assumption (5) means that the splitting of the reflected wave into several modes does not have an influence on the angular distribution of the reflected photons. This does not necessarily mean that the splitting itself is neglected but that the various harmonics produce an angular distribution that resembles that of the reflected waves at the moment of incidence.

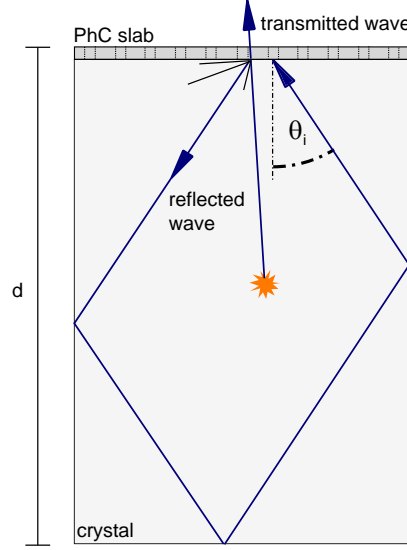


Figure 6.16: Definition of the path length l .

Under these assumptions, the *total transmission* per unit of angle $T(\theta_i)$ is determined by

$$\begin{aligned}
 T(\theta_i) &= t(\theta_i) + t(\theta_i) \cdot (1 - t(\theta_i)) \cdot e^{-\frac{2d}{\lambda \cdot \cos \theta_i}} + t(\theta_i) \cdot (1 - t(\theta_i))^2 \cdot e^{-\frac{4d}{\lambda \cdot \cos \theta_i}} + \dots \\
 &= t(\theta_i) \cdot \frac{1}{1 - (1 - t(\theta_i)) \cdot e^{-\frac{2d}{\lambda \cdot \cos \theta_i}}}
 \end{aligned} \tag{6.16}$$

As $t(\theta_i)$ depends on a/λ , $T(\theta_i)$ is also a function of a/λ . By folding $T(\theta_i)$ with the angular distribution of the photons incident on the exit surface, it is possible to determine the light collection efficiency η_L of the system.

Discussion

Figs. 6.17a and 6.17b depict the angular distribution of the extracted photons for the same two systems as in Fig 6.15. In the case of LuYAP, λ_{abs} was set to 10 cm while for LYSO, $\lambda_{abs} = 20$ cm. Clearly, the number of extracted photons, as determined by the model presented above, is significantly higher than that of the plain exit surface. In fact, the majority of the photons that arrive at the exit surface become extracted and η_L becomes close to the theoretical limit $\eta_{L,max}$ given by

$$\eta_{L,max} = \frac{N_{inc}}{N_{tot}} \tag{6.17}$$

where N_{inc} and N_{tot} denote the number of incident photons and the total number of produced photons, respectively.

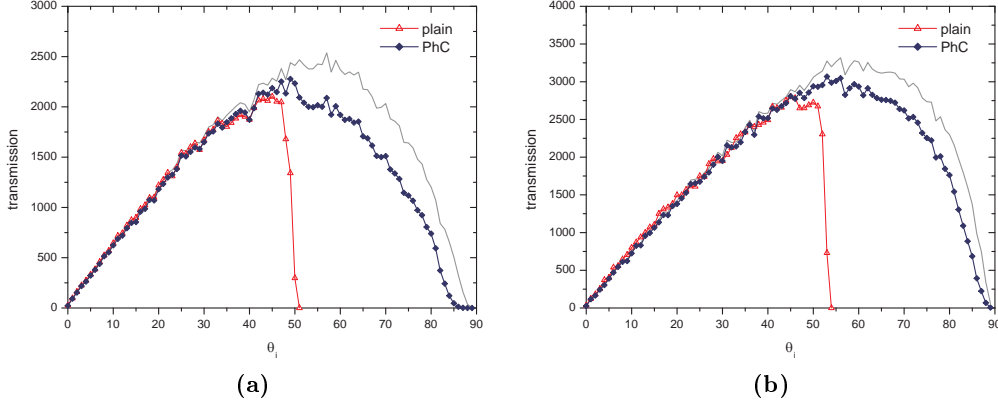


Figure 6.17: Angular distribution of all photons extracted from a scintillator + PhC exit surface for (a) LuYAP and (b) LYSO and $a/\lambda = 0.8$.

Figs. 6.18a and 6.18b illustrate the dependence of η_L on a/λ for $2 \times 2 \times 8$ mm³ LuYAP and LYSO crystals and several scintillator-PhC combinations.

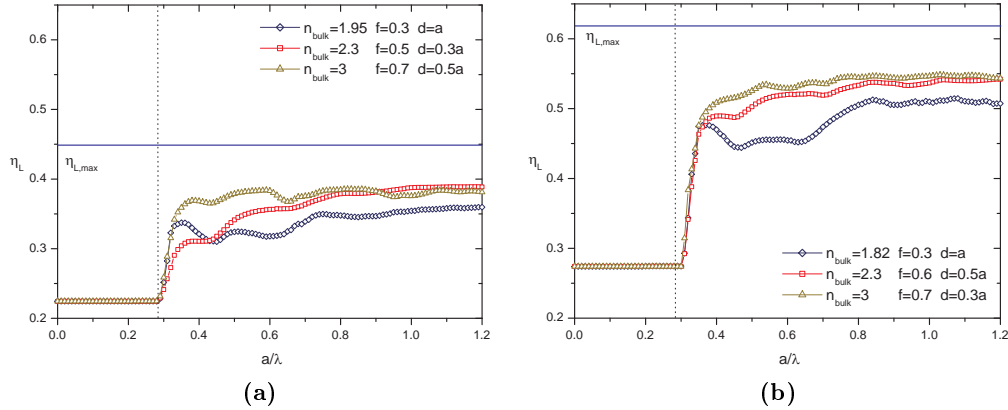


Figure 6.18: Dependence of η_L on a/λ for several PhC-scintillator combinations. (a) LuYAP; (b) LYSO. The theoretical limit $\eta_{L,max}$ is indicated in both plots.

The figures indicate that η_L exhibits a steep rise at the transition from the homogeneous to the photonic regime. In the photonic regime, η_L remains at a relatively constant high level and only small variations with a/λ are observed. This is mainly a consequence of the high reoccurrence rate of the photons which makes the number of extracted photons per unit of angle only weakly dependent on $t(a/\lambda)$. The gain in η_L observed at $a/\lambda = 0.8$ is significant and amounts to $\approx 50\%$ - 70% for LuYAP and 80% - 100% for LYSO relative to the homogeneous regime.

As noted before, the values determined by the idealized model should only be seen as what can be *possible* in terms of light extraction improvement, i.e. as an upper limit for η_L . This can also be seen by the results obtained for the homogeneous regime which are somewhat larger than the values obtained by the LITRANI simulations performed in Chapter 4. Nevertheless, it can be assumed that the model serves well in indicating which combinations of scintillators and PhC structures are promising in terms of light extraction and which not.

6.5 Experimental realisation of a PhC-scintillator system

As noted before, the curves of η_L vs. a/λ shown in Figs. 6.18a and 6.18b can be used to find combinations of structural parameters and a/λ for which the PhC exit surface extracts as much light as possible from the crystal. This information can be used, in turn, to design a scintillator with a nanostructured exit surface that is optimised on the fluorescent and optical properties of the scintillator.

Basically, a scintillator with nanostructured exit surface can be realised in two ways. One possibility is to imprint the PhC structure directly onto the crystal by means of electron- or ion beam lithography combined with RIE. This has the advantage of a reduced time consumption of the fabrication process as no additional layer has to be deposited; however, direct imprinting is problematic due to technological restrictions and does not yield the gain in η_L observed for a high- n bulk material. More promising therefore seem to be approaches where the PhC is contained in a layer of a high- n material that is deposited onto the exit surface of the crystal. Such layers are relatively easy to fabricate and the imprinting processes are well understood. However, it has to be noted that the selection of possible bulk materials is restricted to materials with $\alpha_{abs} \leq 10^3 - 10^4 \text{ cm}^{-1}$ in the wavelength range of emission as otherwise, too many photons are lost due to absorption in the PhC slab.

A promising material for PhC fabrication appears to be TiO_2 which exhibits high transmission at wavelengths $> 370 \text{ nm}$ and a refractive index that can be varied from ≈ 1.8 to 2.5 by suitable choice of the deposition parameters [59, 60]. An even higher refractive index material ($n > 3$) which could possibly also be used is GaP which however exhibits a strongly increasing α_{abs} for $\lambda < 400 \text{ nm}$ [61] and is therefore probably suited only for scintillators that emit at larger wavelengths, as e.g. LuAG. Other possible candidate materials include e.g. SiN, $\text{Al}_x\text{Ga}_{1-x}\text{N}$, and SiC [62, 63, 64].

In collaboration with the Institute de Nanotechnologie Lyon (INL), a prototype of a scintillator with PhC exit surface has been designed and is currently under fabrication. This prototype consists of a $2 \times 2 \times 10 \text{ mm}^3$ scintillator crystal (LuYAP or LYSO) with a triangular PhC etched into a layer of SiN. The structural parameters of the PhC structure have been selected according to the results of the simulations previously presented and are listed in Table 6.1.

To imprint the PhC structures onto the scintillator exit surface, the samples

Table 6.1: Structural parameters of the INL PhC samples.

	LuYAP	LYSO
layer thickness d [nm]	300	300
lattice constant a [nm]	300	340
hole diameter D [nm]	180	200

are packed in a mold made of PDMS (Polydimethylsiloxane). This is necessary to avoid problems with layer deposition and pattern production at the crystal edges; moreover, the polymer improves the handling of the samples. Subsequently, a 7 nm thin layer of $\text{In}_2\text{O}_3/\text{Sn}_2\text{O}_3$ (Indium tin oxide, ITO) is deposited by vapor deposition; this layer is used to improve the lithographic process by reducing electron backscatter but does not affect the optical properties of the whole structure due to its small thickness. The ITO layer is followed by a vapor deposited 300 nm thick layer of SiN. Finally, the structure is coated with PMMA which serves as resist. After creating the PhC pattern by means of EBL, the PhC structure is etched into the SiN layer by means of RIE. As of May 2008, this process is currently tested with LYSO samples; the production of the prototypes itself is expected to be started before summer 2008 .

6.6 Conclusions

In this chapter, the optical properties of photonic crystal (PhC) slabs and their impact on the light extraction from high- ϵ media have been discussed. Simulations with a scattering-matrix algorithm show that a periodic corrugation of the exit surface does indeed change the extraction properties of the scintillator; in particular, it allows to extract photons that hit the exit surface under an angle larger than the angle of total reflection of a plain surface. The influence of different structural parameters of the PhC slab, such as slab thickness d , dielectric contrast η , and filling factor f , on the light extraction efficiency η_L of LuYAP and LYSO have been evaluated.

Calculating the number of extracted photons for a simplified model shows that a scintillator with PhC exit surface has a higher η_L compared to a scintillator with plain exit surface. This increase becomes evident when the photon wavelength λ reaches the photonic regime of the PhC slab, i.e. when $\lambda \approx a$. By comparison of η_L determined for PhC slabs with different properties, it is shown that the gain in η_L depends on the ratio a/λ and the structural parameters of the PhC slab. In general, the gain in η_L is higher for PhC slabs with high- n bulk material; depending on a/λ , the gain can reach values up to 70% for LuYAP and up to 100% for LYSO. Finally, the possible outline of an experimental system has been reviewed and a short discussion has been given on prototype samples currently fabricated by INL Lyon.

Bibliography

- [1] R. Windisch, C. Rومان, S. Meinschmidt, P. Kiesel, D. Zipperer, G. H. Doehler, B. Dutta, M. Kujik, G. Broghs, P. Heremans, Impact of texture-enhanced transmission on high-efficiency surface-textured light-emitting diodes. *Appl. Phys. Lett.* **79**, 2315 (2001)
- [2] T. Nakamura, N. Tsutsumi, N. Juni, H. Fujii, Improvement of coupling-out efficiency in organic electroluminescent devices by addition of a diffusive layer. *J. Appl. Phys.* **96**, 6016 (2004)
- [3] H. J. Peng, Y. L. Ho, X. J. Yu, H. S. Kwok, Enhanced coupling of light from organic light emitting diodes using nanoporous films. *J. Appl. Phys.* **96**, 1649 (2004)
- [4] T. Yamasaki, K. Sumioka, T. Tsutsi, Organic light-emitting device with an ordered monolayer of silica microspheres as a scattering medium. *Appl. Phys. Lett.* **76**, 1243 (2000)
- [5] S. Moeller, S. R. Forrest, Improved light out-coupling in organic light emitting diodes employing ordered microlens arrays. *J. Appl. Phys.* **91**, 3324 (2002)
- [6] M. K. Wei, I. L. Su, Y. J. Chen, M. Chang, H. Y. Lin, T. C. Wu, The influence of a microlens array on planar organic light-emitting devices. *J. Micromech. Microeng.* **16**, 368 (2006)
- [7] S. Y. Hsu, M. C. Lee, K. L. Lee, P. K. Wei, Extraction enhancement in organic light emitting devices by using metallic nanowire arrays. *Appl. Phys. Lett.* **92**, 013303 (2008)
- [8] K. Okamoto, I. Niki, A. Shvartser, Y. Narukawa, T. Mukai, A. Scherer, Surface-plasmon-enhanced light emitters based on InGaN quantum wells. *Nature Mat.* **3**, 602 (2004)
- [9] M. Y. Su, R. P. Mirin, Enhanced light extraction from circular Bragg grating coupled microcavities. *Appl. Phys. Lett.* **89**, 033105 (2006)
- [10] E. Yablonovitch, Inhibited spontaneous emission in solid-state physics and electronics. *Phys. Rev. Lett.* **58**, 2059 (1987)
- [11] J. Sajeev, Strong localization of photons in certain disordered dielectric superlattices. *Phys. Rev. Lett.* **58**, 2486 (1987)

- [12] S. G. Johnson, J. D. Joannopoulos, Photonic crystals. The road from theory to practice. Kluwer Academic Publishers, Boston, USA (2002)
- [13] M. Notomi, Theory of light propagation in strongly modulated photonic crystals: Refractionlike behaviour in the vicinity of the photonic band gap. Phys. Rev. B 62, 10696 (2000)
- [14] B. Gralak, S. Enoch, G. Tayeb, Anomalous refractive properties of photonic crystals. J. Opt. Soc. Am. A 17, 1012 (2000)
- [15] C. Luo, S. G. Johnson, J. D. Joannopoulos, J. B. Pendry, All-angle negative refraction without negative effective index. Phys. Rev. B 65, 201104 (2002)
- [16] C. Luo, S. G. Johnson, J. D. Joannopoulos, All-angle negative refraction in a three-dimensionally periodic photonic crystal. Appl. Phys. Lett. 81, 2352 (2002)
- [17] D. R. Smith, J. B. Pendry, M. C. K. Wiltshire, Metamaterials and negative refractive index. Science 305, 788 (2004)
- [18] E. Cubukcu, K. Aydin, E. Ozbay, S. Foteinopoulou, C. M. Soukoulis, Negative refraction by photonic crystals. Nature 423, 604 (2003)
- [19] H. J. Lezec, J. A. Dionne, H. A. Atwater, Negative refraction at visible frequencies. Science 316, 430 (2007)
- [20] P. V. Parimi, W. T. Lu, P. Vodo, S. Sridhar, Imaging by flat lens using negative refraction. Nature 426, 404 (2003)
- [21] H. Kosaka, T. Kawashima, A. Tomita, M. Notomi, T. Tamamura, T. Sato, S. Kawakami, Superprism phenomena in photonic crystals. Phys. Rev. B 58, 10096 (1998)
- [22] A. Lupu, E. Cassan, S. Laval, L. El Melhaoui, P. Lyan, J. M. Fedeli, Experimental evidence for superprism phenomena in SOI photonic crystals. Opt. Expr. 12, 5690 (2004)
- [23] C. Luo, M. Ibanescu, S. G. Johnson, J. D. Joannopoulos, Cerenkov radiation in photonic crystals. Science 299, 368 (2003)
- [24] Y. Ohtera, T. Sato, T. Kawashima, T. Tamamura, S. Kawakami, Photonic crystal polarization splitters. Electron. Lett. 35, 1271 (1999)
- [25] X. Wu, A. Yamilov, X. Liu, S. Li, V. P. Dravid, R. P. H. Chang, H. Cao, Ultraviolet photonic crystal laser. Appl. Phys. Lett. 85, 3657 (2004)
- [26] L. M. Chang, C. H. Hou, Y. C. Ting, C. C. Chen, C. L. Hsu, J. Y. Chang, C. C. Lee, G. T. Chen, J. I. Chyi, Laser emission from GaN photonic crystals. Appl. Phys. Lett. 89, 071116 (2006)
- [27] H. Miyazaki, M. Hase, H. T. Miyazaki, Y. Kurokawa, N. Shinya, Photonic material for designing arbitrarily shaped mirrors and microcavities in two dimensions. J. Appl. Phys. 95, 4555 (2004)

-
- [28] B. Temelkuran, E. Ozbay, Experimental demonstration of photonic crystal based waveguides. *Appl. Phys. Lett.* 74, 486 (1999)
- [29] V. N. Astratov, I. S. Culshaw, R. M. Stevenson, D. M. Whittaker, M. S. Skolnick, T. F. Krauss, R. M. De La Rue, Resonant coupling of near-infrared radiation to photonic band structure waveguides. *J. Lightwave Tech.* 17, 2050 (1999)
- [30] C. Cuisin, Y. Chen, D. Decanini, A. Chelnokov, F. Carcenac, A. Madouri, J.-M. Lourtioz, H. Launois, Fabrication of three-dimensional microstructures by high resolution X-ray lithography. *J. Vac. Sci. Tech. B*, 17, 3444 (1999)
- [31] M. Campbell, D. N. Sharp, M. T. Harrison, R. G. Denning, A. J. Turberfield, Fabrication of photonic crystals for the visible spectrum by holographic lithography. *Nature*, 404, 53 (2000)
- [32] A.-P. Hynninen, J. H. J. Thijssen, E. C. M. Vermolen, M. Dijkstra, A. Van Blaaderen, Self-assembly route for photonic crystals with a bandgap in the visible region. *Nature Mat.* 6, 202 (2007)
- [33] L. Yang, J. Motohisa, J. Takeda, T. Fukui, Promising low-damage fabrication method for the photonic crystals with hexagonal or triangular air holes: selective area metal organic vapor phase epitaxy. *Opt. Expr.* 13, 10823 (2005)
- [34] S. Y. Chou, C. Keimel, J. Gu, Ultrafast and direct imprint of nanostructures in silicon. *Nature* 417, 835 (2002)
- [35] H. G. Craighead, R. E. Howard, L. D. Jackel, and P. M. Mankievich, 10-nm linewidth electron beam lithography on GaAs. *Appl. Phys. Lett.* 42, 38 (1983)
- [36] P. Pottier, Nanostructures a base de cristaux photoniques 1D et 2D pour circuits integres photoniques. Doctoral thesis, ECL Lyon, France (2001)
- [37] E. Platzgummer, H. Loeschner, G. Gross, Projection Mask-Less Patterning (PMLP) for the fabrication of leading-edge complex masks and nano-imprint templates. *SPIE Proc.* 6730, 673033 (2007)
- [38] S. Fan, P. R. Villeneuve, J. D. Joannopoulos, and E. F. Schubert, High Extraction Efficiency of Spontaneous Emission from Slabs of Photonic Crystals. *Phys. Rev. Lett.* 78, 3294 (1997)
- [39] A. David, T. Fujii, R. Sharma, and 6 coauthors, Photonic-crystal GaN light-emitting diodes with tailored guided modes distribution. *Appl. Phys. Lett.* 88, 061124 (2006)
- [40] A. David, T. Fujii, E. Matioli, and 5 coauthors, GaN light-emitting diodes with Archimedean lattice photonic crystals. *Appl. Phys. Lett.* 88, 073510 (2006)

- [41] A. A. Erchak, D. J. Ripin, S. Fan, and 5 coauthors, Enhanced coupling to vertical radiation using a two-dimensional photonic crystal in a semiconductor light-emitting diode. *Appl. Phys. Lett.* 78, 563 (2001)
- [42] H. Y. Ryu, Y. H. Lee, R. L. Sellin, and D. Bimberg, Over 30-fold enhancement of light extraction from free-standing photonic crystal slabs with InGaAs quantum dots at low temperature. *Appl. Phys. Lett.* 79, 3573 (2001)
- [43] M. Rattier, H. Benisty, R. P. Stanley, and 6 coauthors, Towards ultrahigh-efficiency Aluminium Oxide microcavity Light-Emitting Diodes: guided mode extraction by photonic crystals, *IEEE J. Quantum Electron.* 8, 238 (2002)
- [44] Y. J. Lee, S. H. Kim, J. Huh, and 5 coauthors, A high-extraction-efficiency nanopatterned organic light-emitting diode. *Appl. Phys. Lett.* 82, 3779 (2003)
- [45] M. Zelsmann, E. Picard, T. Charvolin, and 7 coauthors, Seventy-fold enhancement of light extraction from a defectless photonic crystal made on silicon-on-insulator. *Appl. Phys. Lett.* 83, 2542 (2003)
- [46] E. Moreno, F. J. Garcia-Vidal, L. Martin-Moreno, Enhanced transmission and beaming of light via photonic crystal surface modes. *Phys. Rev. B* 69, 121402 (2004)
- [47] L. Zeng, Y. Yi, C. Hong, J. Lui, N. Feng, X. Duan, L. C. Kimering, B. A. Alamariu, Efficiency enhancement in Si solar cells by textured photonic crystal back reflector. *Appl. Phys. Lett.* 89, 111111 (2006)
- [48] S. G. Tikhodeev, A. L. Yablonskii, E. A. Muljarov, N. A. Gippius, T. Ishihara, Quasiguidded modes and optical properties of photonic crystal slabs. *Phys. Rev. B* 66, 045102 (2002)
- [49] D. M. Whittaker, I. S. Culshaw, Scattering-matrix treatment of patterned multilayer photonic structures. *Phys. Rev. B* 60, 2610 (1999)
- [50] A. C. Marsh, J. C. Inkson, Scattering matrix theory of transport in heterostructures. *Semicon. Sci. Technol.* 1, 285 (1986)
- [51] L. C. Botten, T. P. White, A. A. Asatryan, T. N. Langtry, C. M. de Sterke, R. C. McPhedran, Bloch Mode scattering matrix methods for modeling extended photonic crystal structures. I. Theory. *Phys. Rev. E* 70, 056606 (2004)
- [52] L. M. Li, Z. Q. Zhang, Multiple-scattering approach to finite-sized photonic band-gap materials. *Phys. Rev. B* 58, 9587 (1998)
- [53] G. Gantzounis, N. Stefanou, V. Yannopapas, Optical properties of a periodic monolayer of metallic nanospheres on a dielectric waveguide. *J. Phys. Condens. Matter* 17, 1791 (2005)
- [54] K. Koshino, Analytic approach to the optical response of one-dimensional photonic crystal slabs. *Phys. Rev. B* 67, 165213 (2003)

-
- [55] X. Chen, W. Jiang, J. Chen, R. T. Chen, Theoretical study of light refraction in three-dimensional photonic crystals. *IEEE J. Lightwave Techn.* 25, 2469 (2007)
- [56] W. Jiang, R. T. Chen, X. Lu, Theory of light refraction at the surface of a photonic crystal. *Phys. Rev. B* 71, 245115 (2005)
- [57] A. David, H. Benisty, C. Weisbuch. Optimization of light-diffracting photonic-crystals for high extraction efficiency LEDs. *IEEE J. Disp. Tech.* 3, 133 (2007)
- [58] IBM Research, <http://domino.research.ibm.com>
- [59] F. Gracia, F. Yubero, J. P. Holgado, J. P. Espinos, A. R. Gonzalez-Elie, T. Girardeau, $\text{SiO}_2/\text{TiO}_2$ thin films with variable refractive index prepared by ion beam induced and plasma enhanced chemical vapor deposition. *Thin Solid Films* 500, 19 (2006)
- [60] H. J. Frenck, W. Kulisch, M. Kuhr, R. Kassing, Deposition of TiO_2 thin films by plasma-enhanced decomposition of Tetraisopropyltitanate. *Thin Solid Films* 201, 327 (1991)
- [61] D. E. Aspnes and A. A. Studna, Dielectric functions and optical parameters of Si, Ge, GaP, GaAs, GaSb, InP, InAs, and InSb from 1.5 to 6.0 eV. *Phys. Rev. B* 27, 985 (1983)
- [62] J. F. Muth, J. D. Brown, M. A. L. Johnson, Z. Yu, R. M. Kolbas, J. W. Cook, J. F. Schetzina, Absorption coefficient and refractive index of GaN, AlN and AlGaIn alloys. *MRS Internet J. Nitride Semicond. Res.* 4S1, G5.2 (1999)
- [63] R. Wolf, K. Wandel, B. Gruska, Low-temperature ICPECVD of silicon nitride in $\text{SiH}_4\text{-NH}_3\text{-Ar}$ discharges analyzed by spectroscopic ellipsometry and etch behaviour in KOH and BHF. *Surf. Coat. Tech.* 142, 786 (2001)
- [64] H. R. Philipp, E. A. Taft, Silicon Carbide - A High Temperature Semiconductor. Eds. J. R. O'Connor, J. Smiltens, Pergamon Press, Oxford, London, New York, Paris, 366 (1960)

Chapter 7

Summary and outlook

Inorganic scintillators are widely used as converter for high-energy radiation into an electronic signal. In particular, they are integral part of experiments in high-energy physics and in modern medical imaging modalities, as PET, SPECT, or CT. In high-energy physics, inorganic scintillators are used to measure, with high precision, the energy of particles which are created during the collisions of particle beams with each other or with a fixed target. In medical imaging, they allow to detect the X- or γ -rays that carry information about the morphology and/or the metabolism of the body. Their widespread use in these and other fields is a consequence of their favorable properties (high stopping power, high sensitivity) which makes it possible to construct relatively compact and finely pixelised systems with a high spatial resolution and good detection efficiency.

Although a number of new scintillators with properties favourable for PET imaging have been developed in recent years, their light output is still limited due to losses by total internal reflection at the surface that couples to the photo detector. This is especially a problem for scintillators with a high refractive index, as the extraction cone (i.e. the angular range within which photons can be extracted) of these materials covers only a relatively small solid angle and many scintillation photons are therefore reflected back into the bulk. The reduced light output of the scintillators causes an increase of the statistical fluctuations of the detector signal and therefore, a deterioration of the energy resolution of the scintillation detector. On the other hand, the energy resolution of the detector plays an important role in the detection of rare events in high-energy physics and in the image quality of a PET or CT camera. In the development of the next generation of particle physics experiments and medical imaging modalities, the optimisation of the energy resolution is therefore a key issue.

The present work aims to find possible ways to overcome the problem of total internal reflection at the coupling face of the scintillator. An introduction to high-energy physics and PET is given in chapter 1. This chapter also presents the past and present work of the Crystal Clear Collaboration and highlights its achievements in scintillator research and in the development of novel medical imaging modalities for small animal imaging and mammography. Chapter 2

describes the basic principles of the scintillation process and the main characteristics of scintillators and presents the scintillators $\text{Lu}_{1-x}\text{Y}_x\text{AlO}_3:\text{Ce}$ (LuYAP) and $\text{Lu}_{2-x}\text{Y}_x\text{SiO}_5:\text{Ce}$ (LYSO) which have been employed in this study. Chapter 3 provides a description of the experimental techniques used to characterise these materials. The remaining part of the thesis is dedicated to the presentation of experiments and simulations on these materials.

In chapter 4, the propagation of light in the scintillators is studied. Starting point are simulations performed with the light-ray tracing program LITRANI. The simulated setups were designed such that they resembled the standard experimental setups used to determine the light output of the scintillators as closely as possible. The fluorescent and optical properties of LuYAP and LYSO relevant for the simulation were determined from measurements performed on one LuYAP and one LYSO sample with sizes of $2 \times 2 \times 2 \text{ mm}^3$ each. The emission spectra were measured by means of a spectrofluorometer and fitted with 2 (LuYAP) or 4 (LYSO) Gaussians to determine the relative intensities and widths of the individual emission components. Attenuation lengths λ_{att} and refractive indices n were derived from transmission measurements obtained along the longer and shorter axis; in addition, the dependence of n_{LuYAP} and n_{LYSO} on λ was modelled by a Sellmeier parametrization.

The simulations of LuYAP and LYSO crystals show that the light collection efficiency η_L depends on several factors, as the refractive index n_{grease} of the optical coupler between crystal and PMT entry window, the wrapping used as reflector, and the amount of scattering in the crystal bulk. In general, the light collection efficiency is optimised for $n_{\text{grease}} \leq n_{\text{PMT}}$ and for diffusing wrappings which are optically coupled to the crystal face. Especially interesting is that the light collection efficiency increases strongly with the scattering-to-absorption ratio in the crystal bulk. This has the important consequence that a scintillator will exhibit a higher light yield if the probability of photon scattering within the bulk is increased without deteriorating the absorption characteristics at the same time; this is in agreement with recent observations on PWO crystals from different manufacturers. The simulations also reveal that a large fraction of the photons arriving at the exit surface is lost due to total internal reflection; for specular reflectors with high reflectivity, the losses amount to up to 60%. This shows that overcoming total internal reflection at the exit surface holds strong potential to increase the light yield of the scintillators.

A comparison of the simulated and experimental data shows that the experimental data agree well with the simulations if no wrapping is used, but differ significantly in the case of a wrapping due to additional effects, as e.g. slight shape mismatches, that are not included in the simulations. Combining the experimental data obtained without wrapping with the results from corresponding simulations makes it possible to determine the absolute light yields of LuYAP and LYSO, which amount to 10 000 – 20 000 ph/MeV for LuYAP and 35 000 – 50 000 ph/MeV for LYSO depending on the amount of scattering assumed in the crystals. These values are higher than those quoted in literature

and highlight the importance of Monte-Carlo simulations in the determination of the absolute light yield.

In chapter 5, it is shown by means of LITRANI simulations that η_L can be improved by several tens of percent by machining grooves into the exit surface of the scintillators. An optimised performance is found for grooves with depth $d \approx 0.5 - 0.6$ mm and opening angle $\alpha = 45^\circ$. η_L can be improved further if a second groove is machined perpendicular to the first one while additional grooves generally do not help in further improving η_L . Both bulk scattering and wrapping have much more impact on η_L than in the case of a plain exit surface crystal, with high-reflecting specular reflectors achieving the highest gain in η_L .

A comparison with light yield measurements of several prototype crystals shows that the idealised model of a perfectly polished groove does not reflect well the experimental behaviour. Instead, a good agreement is found for a model that contains a strongly absorbing and diffusing layer just beneath the groove surface. This is important as it indicates that the performance of the grooved crystals can be improved by mechanical or chemical treatment after cutting by which this absorbing layer is removed. As only a diffusing wrapping (Teflon) was used in the experiments, it would also be interesting to perform additional tests e.g. with specular reflectors to validate the implications from the simulations.

The final chapter reviews the optical properties of photonic crystal (PhC) slabs and their impact on the light extraction from media with high n . It is shown by means of simulations with a scattering-matrix algorithm that a periodic modulation of the exit surface allows for extracting photons outside the extraction cone of a plain surface. Consequently, a scintillator with PhC exit surface has a higher η_L compared to a scintillator with plain exit surface when the photon wavelength λ is of the range of the lattice constant a of the slab. The gain in η_L that can be achieved depends on the ratio a/λ and the structural parameters of the PhC slab but is in general higher for PhC slabs with high- n bulk material. Finally, the possible properties of an experimental system have been reviewed.

It is important to note that the potential of microstructurization for improving η_L has only been evaluated with simulations which rely on idealized materials and involve several simplifications. However, a first set of prototypes - consisting of LYSO crystals with a PhC slab etched into a layer of SiN - is currently under fabrication at the Institute de Nanotechnology in Lyon and is expected to be available before summer 2008. It is expected that the results from these measurement will provide more insight into this topic and help to find an optimised PhC-scintillator system for future applications.

The results of this thesis highlight that the light output of scintillator crystals can be improved by structurization of the coupling face of the crystals. This higher light output can be used to improve the timing properties of the scintillation detector and the energy resolution R ; the latter especially accounts to scintillators as LuYAP where the major contribution to R comes from the

photo statistics and not from the intrinsic term. Both, the improved time and energy resolution of such scintillators can be used in future PET detectors to produce images with better contrast and higher spatial resolution.

Appendix A

Bloch Theorem, band gaps, and Tikhodeev algorithm

A.1 The Bloch-Floquet theorem

The Maxwell equations in a medium that does not contain any free charges or currents (i.e. $\rho = 0$, $\mathbf{j} = \mathbf{0}$) are given by:

$$\begin{aligned}\nabla \cdot \mathbf{B} &= 0 & \nabla \times \mathbf{H} &= \frac{1}{c} \frac{\partial \mathbf{D}}{\partial t} \\ \nabla \cdot \mathbf{D} &= 0 & \nabla \times \mathbf{E} &= \frac{1}{c} \frac{\partial \mathbf{B}}{\partial t}\end{aligned}\tag{A.1}$$

The vector fields \mathbf{B} and \mathbf{H} and, respectively, \mathbf{D} and \mathbf{E} are related to each other by means of the equations

$$D_i = \sum_j \epsilon_{ij} \cdot E_j + \sum_{j,k} \chi_{ijk} \cdot E_j \cdot E_k + O(E^3)\tag{A.2}$$

$$B_i = \mu_i \cdot H_i\tag{A.3}$$

with the dielectric tensor ϵ_{ij} , the susceptibility tensor χ_{ijk} , and the magnetic permeability μ_i . For most dielectric materials, these equations can be simplified by employing the following standard assumptions:

- $\mu \approx 1 \Rightarrow \mathbf{B} = \mathbf{H}$
- small field strengths: $\Rightarrow D_i = \sum_j \epsilon_{ij} \cdot E_j$
- isotropic dielectric tensor $\Rightarrow \mathbf{D}(\mathbf{r}, \omega) = \epsilon(\mathbf{r}, \omega) \cdot \mathbf{E}(\mathbf{r}, \omega)$
- ϵ independent on frequency $\Rightarrow \epsilon(\mathbf{r}, \omega) = \epsilon(\mathbf{r})$
- low-loss dielectric media $\Rightarrow \epsilon(\mathbf{r}) = |\epsilon(\mathbf{r})|$

Applying these assumptions to the eqs. A.1-A.3 and eliminating the time dependence of the fields by $\mathbf{H}(\mathbf{r}, t) = \mathbf{H}(\mathbf{r})e^{-i\omega t}$ and $\mathbf{E}(\mathbf{r}, t) = \mathbf{E}(\mathbf{r})e^{-i\omega t}$ yields:

$$\begin{aligned}\nabla \cdot \mathbf{H} &= 0 & \nabla \times \mathbf{H} &= \frac{i\omega}{c} \cdot \epsilon \cdot \mathbf{E} \\ \nabla \cdot \mathbf{E} &= 0 & \nabla \times \mathbf{E} &= -\frac{i\omega}{c} \cdot \mathbf{B}\end{aligned}\tag{A.4}$$

where $\mathbf{H} = \mathbf{H}(\mathbf{r})$ and $\mathbf{E} = \mathbf{E}(\mathbf{r})$. Expressing $\mathbf{E}(\mathbf{r})$ from the first curl equation and inserting it into the second curl equation yields

$$\nabla \times \left(\frac{1}{\epsilon} \nabla \times \mathbf{H} \right) = \Theta \mathbf{H} = \left(\frac{\omega}{c} \right)^2 \cdot \mathbf{H}(\mathbf{r}) \quad (\text{A.5})$$

where $\Theta = \nabla \times \left(\frac{1}{\epsilon} \nabla \times \right)$ is a linear and Hermitian operator.

Assuming now a periodic modulation of the dielectric constant in x-direction, i.e. $\epsilon(\mathbf{r} + \mathbf{R}) = \epsilon(\mathbf{r})$, where $\mathbf{R} = l \cdot \hat{x}$ and $l \in \mathbb{N}$. If we now introduce a translational operator $T_{\mathbf{R}}$,

$$T_{\mathbf{R}} \cdot \mathbf{H}(\mathbf{r}) = \mathbf{H}(\mathbf{r} + \mathbf{R}) \quad (\text{A.6})$$

and assume that the mode has a functional form $e^{ik_x x}$, we get

$$T_{\mathbf{R}} \cdot e^{ik_x x} = e^{ik_x(x+la)} = \left(e^{ik_x la} \right) e^{ik_x x}. \quad (\text{A.7})$$

$e^{ik_x x}$ is therefore an eigenvector of the translational operator $T_{\mathbf{R}}$ with the eigenvalue $e^{ik_x la}$. Since

$$e^{i(k_x + 2\pi m/a)x} = e^{2\pi i \cdot m \cdot l} e^{ik_x la} = e^{ik_x la}, \quad (\text{A.8})$$

all modes with wave vector $k_x + 2\pi/a \cdot m$ have the same eigenvalue of $e^{ik_x la}$ under the symmetry operation $T_{\mathbf{R}}$. The vector $\hat{b} = 2\pi/a \cdot \hat{x}$ is termed *primitive reciprocal lattice vector* and the region $-\pi/a < k_x < \pi/a$ *Brillouin zone*.

As any linear combination of these eigenfunctions produces another eigenfunction with the same eigenvalue, we can write $\mathbf{H}_{k_x, \mathbf{k}_\rho}$ in the form

$$\begin{aligned} \mathbf{H}_{k_x, \mathbf{k}_\rho} &= e^{i\mathbf{k}_\rho \rho} \sum_m c_{k_x, m}(\rho) \cdot e^{i(k_x + mb)x} \\ &= e^{ik_x x} e^{i\mathbf{k}_\rho \rho} \sum_m c_{k_x, m}(\rho) \cdot e^{imbx} \\ &= e^{ik_x x} e^{i\mathbf{k}_\rho \rho} \cdot u_{k_x}(x, \rho), \end{aligned} \quad (\text{A.9})$$

with the expansion coefficient $c_{k_x, m}(\rho)$ and the wave modulation $u_{k_x}(x, \rho)$ which is, by construction, a periodic function in x. A discrete periodicity in x-direction leads therefore to an x-dependence of \mathbf{H} and the solution of eq. A.5 is a periodic function of the form

$$\mathbf{H}(\dots x \dots) \propto e^{ik_x x} \cdot u_{k_x}(x, \dots). \quad (\text{A.10})$$

A.2 Formation of the band gap

An important property of photonic crystals is the possible presence of a gap in its band structure, i.e. a frequency range in which no modes are allowed to travel through the photonic crystal. This band gap is a consequence of the

periodic variation in ϵ : Assuming a linear polarised electromagnetic wave that propagates through the material in x -direction, i.e. $\mathbf{k} = k\hat{z}$, the wave equation eq. A.5 transforms into

$$\frac{1}{\epsilon(x)} \cdot \frac{\partial^2 H(x)}{\partial x^2} = \frac{\omega^2}{c^2} \cdot H(x). \quad (\text{A.11})$$

If $\epsilon(x)$ is a periodic function, i.e. $\epsilon(x+a) = \epsilon(x)$, then the inverse $\epsilon^{-1}(x)$ is also periodic. This makes it possible to expand $\epsilon^{-1}(x)$ into a Fourier series:

$$\epsilon^{-1}(x) = \sum_{m=-\infty}^{\infty} \kappa_m \cdot e^{i\frac{2\pi m}{a}x}, \quad (\text{A.12})$$

with the Fourier coefficients κ_m ,

$$\kappa_m = \frac{1}{2a} \int_{-a}^a dx \cdot \epsilon^{-1}(x) \cdot e^{-i\frac{2\pi m}{a}x}. \quad (\text{A.13})$$

As ϵ , the eigenfunctions of the electromagnetic wave can also be expanded into a Fourier series. In the 1-dimensional case, this corresponds to

$$H(x) = H_k(x) = \sum_{m=-\infty}^{\infty} H_m \cdot e^{i(k+\frac{2\pi m}{a})x}. \quad (\text{A.14})$$

If it is assumed that only the components with $|m| \leq 1$ are dominant in the expansion of $\epsilon^{-1}(x)$, we get from eq. A.12

$$\epsilon^{-1}(x) = \kappa_0 + \kappa_1 \cdot e^{i\frac{2\pi}{a}x} + \kappa_{-1} \cdot e^{-i\frac{2\pi}{a}x} \quad (\text{A.15})$$

By inserting eqs. A.14 and A.15 into the wave equation eq. A.11, a recursive expression is derived:

$$\begin{aligned} \kappa_1 \cdot \left[k + \frac{2\pi(m-1)}{a} \right]^2 \cdot H_{m-1} + \kappa_{-1} \cdot \left[k + \frac{2\pi(m+1)}{a} \right]^2 \cdot H_{m+1} \approx \\ \approx \left[\frac{\omega^2}{c^2} - \kappa_0 \left(k + \frac{2\pi m}{a} \right)^2 \right] \cdot H_m \end{aligned} \quad (\text{A.16})$$

With the constraints that k is approximately equal to the size of the Brillouin zone,

$$|k| \approx \frac{\pi}{a}, \quad (\text{A.17})$$

and that κ_0 dominates $\epsilon^{-1}(x)$,

$$\omega^2 = \omega_k^2 = \frac{c^2 k^2}{\epsilon(x)} \approx \kappa_0 c^2 k^2, \quad (\text{A.18})$$

we find that only the two components of H_m with $m = 0$ and $m = -1$ are dominant in eq. A.16. This yields the following system of equations:

$$\begin{aligned} (\omega_k^2 - \kappa_0 c^2 k^2) \cdot H_0 - \kappa_1 \left[k - \frac{2\pi}{a} \right]^2 \cdot H_{-1} &= 0 \\ -\kappa_{-1} c^2 k^2 \cdot H_0 + \left[\omega_k^2 - \kappa_0 c^2 \cdot \left(k - \frac{2\pi}{a} \right)^2 \right] \cdot H_{-1} &= 0 \end{aligned} \quad (\text{A.19})$$

A non-trivial solution of this system is just possible when the determinant of the coefficients vanishes; this leads to

$$\omega_{\pm} \approx \frac{\pi c}{a} \cdot \sqrt{\kappa_0 \pm |\kappa_1|} \pm \frac{ac}{\pi |\kappa_1|} \cdot \left(\kappa_0^2 - \frac{|\kappa_1^2|}{2} \right) \cdot \left(k - \frac{\pi}{a} \right)^2 \quad (\text{A.20})$$

Taking $(k - \frac{\pi}{a}) \ll \frac{\pi}{a}$ into account, it follows that under the constraints given above, no mode exists in the interval

$$\frac{\pi c}{a} \cdot \sqrt{\kappa_0 - |\kappa_1|} < \omega_k < \frac{\pi c}{a} \cdot \sqrt{\kappa_0 + |\kappa_1|} \quad (\text{A.21})$$

Eq. A.21 indicates that the presence of a periodically varying ϵ opens a band gap in which no modes can exist. This has important implications: as no purely real wave vector exists for any mode of that frequency, any electromagnetic wave with a frequency within the photonic band gap that strikes the surface of the crystal from outside cannot propagate in the crystal. Instead, the wave vector is complex and the amplitude of the wave decays exponentially into the material.

A.3 The Tikhodeev algorithm

The Tikhodeev algorithm calculates off-plane transmission and reflection of a PhC slab by solving the Maxwell equations by a set of plane waves and connecting the incoming and outgoing fields by a scattering matrix. The following notations are taken from [1].

The algorithm starts from the Maxwell equation resolved for the electric field:

$$-\Delta \mathbf{E} + \nabla \cdot (\nabla \cdot \mathbf{E}) = \frac{\omega^2}{c^2} \quad (\text{A.22})$$

Assumed a 2D periodic slab analogous to Fig. 6.8 couples with an incident photon of frequency ω and wave vector $\mathbf{k} = (k_x, k_y, k_z)$,

$$\begin{aligned} k_x &= \frac{\omega}{c} \sin(\theta) \cos(\phi), \\ k_y &= \frac{\omega}{c} \sin(\theta) \sin(\phi), \\ k_z &= \frac{\omega}{c} \cos(\theta), \end{aligned} \quad (\text{A.23})$$

Due to the periodic modulation of the slab, the wave splits into several harmonics with wave vectors

$$\mathbf{k}_{\mathbf{G},i}^{\pm} = (k_x, \mathbf{G}, k_y, \mathbf{G}, \pm k_z, \mathbf{G}, i) \quad (\text{A.24})$$

under reflection into the substrate ($i = s$) or transmission into the layer of grease ($i = g$). The components of $\mathbf{k}_{\mathbf{G},i}^{\pm}$ are given by

$$\begin{aligned} k_{x,\mathbf{G}} &= k_x + G_x, \\ k_{y,\mathbf{G}} &= k_y + G_y, \\ k_{z,\mathbf{G},i} &= \sqrt{\frac{\omega^2 \epsilon_i}{c^2} - (k_x + G_x)^2 - (k_y + G_y)^2}, \end{aligned} \quad (\text{A.25})$$

G_x and G_y are the x and y components of the reciprocal lattice vector \mathbf{G} which is given by

$$\mathbf{G} = \frac{2\pi}{a} (n, q, 0), \quad n, q = 0, \pm 1, \pm 2, \dots, N \quad (\text{A.26})$$

for a rectangular PhC lattice and by

$$\mathbf{G} = \frac{2\pi}{a} \left(n, \frac{2n-q}{\sqrt{3}}, 0 \right) \quad (\text{A.27})$$

for a triangular PhC lattice.

The solution of eq. A.22 can then be Fourier decomposed into a sum of plane waves of the type

$$\begin{aligned} \mathbf{E}(\mathbf{r}, t) &= \mathbf{E}_{\mathbf{G}} \cdot e^{i(k_x \mathbf{G}x + k_y \mathbf{G}y)} \cdot e^{i(Kz - \omega t)} \\ \mathbf{D}(\mathbf{r}, t) &= \mathbf{D}_{\mathbf{G}} \cdot e^{i(k_x \mathbf{G}x + k_y \mathbf{G}y)} \cdot e^{i(Kz - \omega t)} \\ \mathbf{H}(\mathbf{r}, t) &= \mathbf{H}_{\mathbf{G}} \cdot e^{i(k_x \mathbf{G}x + k_y \mathbf{G}y)} \cdot e^{i(Kz - \omega t)} \end{aligned} \quad (\text{A.28})$$

where K are the (to be determined) eigenvalues of the z projection of the wave number \mathbf{k} of the mode and the $\mathbf{D}_{\mathbf{G}}$ are given by

$$\mathbf{D}_{\mathbf{G}} = \sum_{\mathbf{G}'} \epsilon_{\mathbf{G}, \mathbf{G}'} \mathbf{E}_{\mathbf{G}'} \quad (\text{A.29})$$

where $\epsilon_{\mathbf{G}, \mathbf{G}'}$ is the Fourier transform of $\epsilon(\mathbf{r})$:

$$\epsilon_{\mathbf{G}, \mathbf{G}'} = \frac{1}{S} \int \epsilon(\mathbf{r}) e^{i(\mathbf{G}' - \mathbf{G})\mathbf{r}} dxdy \quad (\text{A.30})$$

S denotes the area of the unit cell. For better convergence, it is often useful to expand the inverse of the dielectric constant $\epsilon^{-1}(\mathbf{r})$ instead of $\epsilon(\mathbf{r})$, as shown in eq. A.12.

Using these definitions, the solution of eq. A.22 can be written in form of an eigenproblem

$$N^{-1} M E_{\parallel} = E_{\parallel} K^2 \quad (\text{A.31})$$

where M and N are $2N \times 2N$ -dimensional matrices given by

$$M = \begin{pmatrix} M_{11} & M_{12} \\ M_{21} & M_{22} \end{pmatrix}, \quad N = \begin{pmatrix} N_{11} & N_{12} \\ N_{21} & N_{22} \end{pmatrix}, \quad (\text{A.32})$$

and composed of $N \times N$ matrices

$$\begin{aligned} M_{11} &= \frac{\omega^2}{c^2} \epsilon_{\mathbf{G}, \mathbf{G}'} - (k_y + G_y)^2 \delta_{\mathbf{G}, \mathbf{G}'}, \\ M_{22} &= \frac{\omega^2}{c^2} \epsilon_{\mathbf{G}, \mathbf{G}'} - (k_x + G_x)^2 \delta_{\mathbf{G}, \mathbf{G}'}, \\ M_{12} &= M_{21} = (k_x + G_x)(k_y + G_y) \delta_{\mathbf{G}, \mathbf{G}'}, \\ N_{11} &= \delta_{\mathbf{G}, \mathbf{G}'} - (k_x + G_x) Z_{\mathbf{G}, \mathbf{G}'}^{-1} (k_x + G'_x), \\ N_{22} &= \delta_{\mathbf{G}, \mathbf{G}'} - (k_y + G_y) Z_{\mathbf{G}, \mathbf{G}'}^{-1} (k_y + G'_y), \\ N_{12} &= N_{21}^T = -(k_x + G_x) Z_{\mathbf{G}, \mathbf{G}'}^{-1} (k_y + G'_y), \end{aligned} \quad (\text{A.33})$$

where

$$Z_{\mathbf{G},\mathbf{G}'} = [(k_x + G_x)^2 + (k_y + G_y)^2] \delta_{\mathbf{G},\mathbf{G}'} - \frac{\omega^2}{c^2} \epsilon_{\mathbf{G},\mathbf{G}'} \quad (\text{A.34})$$

K is a $2N \times 2N$ -dimensional diagonal matrix that contains the eigenvalues K_1, K_2, \dots, K_{2N} of $N^{-1}M$ and E_{\parallel} is a $2N \times 2N$ -dimensional matrix whose columns are the corresponding $2N$ -dimensional eigenvectors.

If the simulated structure consists of a combination of several slabs (as in our case), it is necessary to connect the amplitudes of the partial waves in each plane with each other. This is done by defining $4N$ -dimensional amplitude vectors $\vec{A}(z)$ and $\vec{B}(z)$ that contain the amplitudes of the plane waves going into the structure and leaving the structure on each side,

$$\vec{A}(z) = \begin{pmatrix} \mathbf{A}_s^+(\mathbf{z}) \\ \mathbf{A}_g^-(\mathbf{z}) \end{pmatrix}, \quad \vec{B}(z) = \begin{pmatrix} \mathbf{B}_g^+(\mathbf{z}) \\ \mathbf{B}_s^-(\mathbf{z}) \end{pmatrix}, \quad (\text{A.35})$$

$\mathbf{A}_s^+(\mathbf{z})$ and $\mathbf{B}_s^-(\mathbf{z})$ correspond to the waves coming from and being reflected back into the substrate and $\mathbf{B}_g^+(\mathbf{z})$ and $\mathbf{A}_g^-(\mathbf{z})$ correspond to the transmitted waves and the waves incident from the grease side.

Adaptation of the original method

In the original publication of the method [1], the incoming and outgoing fields are connected by a $4N \times 4N$ -dimensional *scattering matrix* $S_{s,g}$,

$$\vec{B} = S_{s,g} \vec{A}, \quad (\text{A.36})$$

which is calculated iteratively by starting from the layer from which the photon is incident, which corresponds to the substrate in our system. However, as no photons arrive at the PhC slab from the opposite side (i.e. the grease), $\mathbf{A}_g^-(\mathbf{z})$ can be set to $\mathbf{0}$; this makes it possible to apply several simplifications to the original scattering matrix formalism.

Assuming a system as shown in Fig. A.1 with \mathbf{A}_0 the amplitude vector of the incident plane waves and \mathbf{A}_3 the amplitude vector of the transmitted plane waves. Let us define an *interface matrix* $T_{P,G}$ which connects the amplitudes on the left and right side of the interface $P - G$:

$$\begin{pmatrix} \mathbf{A}_2 \\ \mathbf{B}_2 \end{pmatrix} = T_{P,G} \begin{pmatrix} \mathbf{A}_3 \\ \mathbf{0} \end{pmatrix} \quad (\text{A.37})$$

$T_{P,G}$ is calculated from the *material matrices* F of slab P and slab G by

$$T_{P,G} = \begin{pmatrix} T_{PG,11} & T_{PG,12} \\ T_{PG,21} & T_{PG,22} \end{pmatrix} = F_P^{-1} F_G \quad (\text{A.38})$$

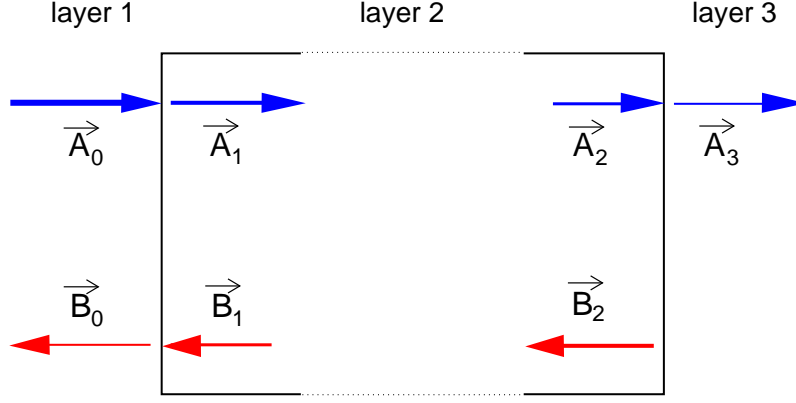


Figure A.1: Amplitude vectors at the interfaces.

Each material matrix F is given by

$$F = \begin{pmatrix} E_{\parallel} & E_{\parallel} \\ \frac{c}{\omega} C E_{\parallel} K & -\frac{c}{\omega} C E_{\parallel} K \end{pmatrix} \quad (\text{A.39})$$

and the $2N \times 2N$ matrices C are defined by

$$C = \begin{pmatrix} -N_{21} & -N_{22} \\ N_{11} & N_{12} \end{pmatrix}. \quad (\text{A.40})$$

As only the outgoing plane waves in layer G have non-zero amplitude vectors, eq. A.37 can be simplified to

$$\begin{aligned} \mathbf{A}_2 &= T_{PG,11} \cdot \mathbf{A}_3 \\ \mathbf{B}_2 &= T_{PG,21} \cdot \mathbf{A}_3 \end{aligned} \quad (\text{A.41})$$

which can be reformulated to

$$\begin{aligned} \mathbf{A}_3 &= T_{PG,11}^{-1} \cdot \mathbf{A}_2 = R_{PG,11} \cdot \mathbf{A}_2 \\ \mathbf{B}_2 &= T_{PG,21} T_{PG,11}^{-1} \cdot \mathbf{A}_2 = R_{PG,21} \cdot \mathbf{A}_2 \end{aligned} \quad (\text{A.42})$$

where $R_{PG,11}$ and $R_{PG,21}$ are the scattering sub-matrices. The amplitudes \mathbf{A}_2 and \mathbf{B}_2 are connected to the amplitudes \mathbf{A}_1 and \mathbf{B}_1 by a *transfer matrix* T_L which is given as

$$T_L = e^{-iKL} \quad (\text{A.43})$$

where L denotes the thickness of slab P . The amplitudes \mathbf{A}_1 and \mathbf{B}_1 are given by

$$\begin{aligned} \mathbf{A}_1 &= T_L \cdot \mathbf{A}_2 \\ \mathbf{B}_1 &= T_L^{-1} \cdot \mathbf{B}_2 \end{aligned} \quad (\text{A.44})$$

what yields

$$\begin{aligned} \mathbf{A}_3 &= R_{PG,11} \cdot T_L^{-1} \cdot \mathbf{A}_1 = R_{PP,11} \cdot \mathbf{A}_1 \\ \mathbf{B}_1 &= T_L \cdot R_{PG,21} \cdot T_L^{-1} \cdot \mathbf{A}_1 = R_{PP,21} \cdot \mathbf{A}_1 \end{aligned} \quad (\text{A.45})$$

Finally, the interface matrix $T_{S,P}$ of the interface $S - P$ is calculated analogously to eq. A.38 and used to connect the amplitudes on both sides of the interface with each other. This yields the total scattering sub-matrices R_{11} and R_{21} of the system:

$$\begin{aligned}\mathbf{A}_3 &= R_{PP,11} \cdot D \cdot \mathbf{A}_0 = R_{11} \cdot \mathbf{A}_0 \\ \mathbf{B}_0 &= E \cdot D \cdot \mathbf{A}_0 = R_{21} \cdot \mathbf{A}_0\end{aligned}\tag{A.46}$$

The matrices D and E are given by

$$\begin{aligned}D &= (T_{SP,11} + T_{SP,12} \cdot R_{PP,21})^{-1} \\ E &= T_{SP,21} + T_{SP,22} \cdot R_{PP,21}\end{aligned}\tag{A.47}$$

Subsequently, reflection, absorption, and transmission coefficients are calculated according to the formulae given in [1].

Bibliography

- [1] S. G. Tikhodeev, A. L. Yablonskii, E. A. Muljarov, N. A. Gippius, T. Ishihara, Quasiguided modes and optical properties of photonic crystal slabs. Phys. Rev. B 66, 045102 (2002)

List of Figures

1.1	Principle of a PET scanner.	3
1.2	Principle of a PET scan.	4
1.3	Coincidence types.	6
1.4	Origin of the parallax error in a PET scanner [2].	8
1.5	Outline of the LHC.	11
1.6	Outline of the CMS detector at CERN.	12
1.7	PWO crystals.	13
1.8	Outline of the ALICE detector at CERN.	14
1.9	The ClearPET TM scanner.	16
1.10	The ClearPEM scanner. (a) examination of the breast; (b) examination of the axillary region.	18
1.11	PET-CT image of a 50-year-old female with pancreatic cancer [30].	19
1.12	Examination of a breast with the ClearPEM-Sonic [31].	20
2.1	Energy band model of a crystal (a) without energy levels in the band gap (b) with energy levels in the band gap.	27
2.2	Elementary processes taking place in a scintillator [15].	30
2.3	Energy-level structure of the free Ce ³⁺ ion. Energy levels are in eV.	32
2.4	Configuration coordinate diagram for a luminescence center. The ground and excited states are represented by overlapping potential curves.	34
2.5	Degree of non-proportionality for several common scintillators [11].	39
2.6	Energy resolution of several common scintillators [11].	41
2.7	Ordinary and extraordinary refractive index in an uniaxial birefringent medium.	43
2.8	Contributions to T and R at quasi-normal incidence.	45
3.1	Light yield spectrum recorded of a LuYAP crystal.	58
3.2	Schematic drawing of the light yield bench.	60
3.3	q_{eff} of the Philips XP2020Q photomultiplier.	61
3.4	Single electron spectra measured with and without crystal and difference spectrum (SEP = single electron peak).	61
3.5	Schematic drawing of the spectrophotometer.	63
3.6	Schematic drawing of the spectrofluorimeter.	65
4.1	Sketch of the slice of material between crystal and wrapping. . .	74

4.2	Photoelectric, coherent, and incoherent cross-sections of LuYAP.	75
4.3	(a) Excitation and (b) emission spectra of LuYAP 1943.	76
4.4	Fitted emission spectrum of LuYAP.	77
4.5	(a) Excitation and (b) emission spectra of LYSO 1946.	78
4.6	Fitted emission spectrum of LYSO.	78
4.7	Transmission spectra of (a) LuYAP 1943 and (b) LYSO 1946 crystals along the shorter and longer axes.	79
4.8	Absorption lengths of (a) LuYAP 1943 and (b) LYSO 1946. For reasons of clarity, error bars are only shown for selected values. . .	81
4.9	Refractive indices of (a) LuYAP 1943 and (b) LYSO 1946.	81
4.10	Setup simulated with LITRANI for crystals with plain exit surface.	83
4.11	Number of photons generated in LuYAP per position in z	85
4.12	Dependence of η_L on B for LuYAP.	86
4.13	Dependence of η_L on n_{grease}	87
4.14	Dependence of η_L on the position of the light source. The light source is placed on the symmetry axis of the crystal.	88
4.15	Dependence of η_L of (a) LuYAP and (b) LYSO on the wrapping type and for $B = 1.6$. (1) Teflon, $n_{gap} = 1.35$; (2) Teflon, n_{gap} $= 1$; (3) Tyvek, $n_{gap} = 1$; (4) Aluminium, $n_{gap} = 1$; (5) 98% Reflector, $n_{gap} = 1$; (6) 98% Diffusor, $n_{gap} = 1.35$	89
4.16	Angular distribution of photons which never reach the exit surface for LuYAP.	90
4.17	Definition of θ_{em} and θ_i	91
4.18	Angular distribution of the photons arriving at the exit surface ($B = 1.6$). (a): LuYAP (b) LYSO.	93
4.19	Comparison between arriving and extracted photons for (a) LuYAP and (b) LYSO wrapped with the fictive 98% reflector ($B = 1.6$). . .	93
4.20	Comparison between simulated and measured light yield spectra for LuYAP. (a) grease; (b) no grease.	95
4.21	Absolute light yields of measured LuYAP and LYSO crystals vs. B	99
5.1	Extraction of photons for (a) a plain surface and (b) a surface with a groove.	109
5.2	Simulated system in LITRANI. (a): Simulated system. (b): Top view of exit surface with one groove. (c): Sketch of a groove. . .	110
5.3	Comparison of angular distributions of extracted photons for LuYAP with standard Teflon wrapping in the case of a plain and a grooved exit surface.	111
5.4	Dependence of η_L on (a) depth d and (b) opening angle α of the groove. The case $d = 0$ mm corresponds to a plain exit surface, the case $\alpha = 0^\circ$ to a groove with rectangular cross section.	113
5.5	Comparison of η_L for crystals with plain exit surface, 1 groove in x , and 1 groove in x and y each.	113
5.6	Comparison of η_L for the case of several parallel grooves.	114
5.7	Comparison of the angular distributions of extracted photons for different numbers of grooves.	114

5.8	Dependence of η_L on n_{crys}	115
5.9	Dependence of η_L on n_{grease} . (a) LuYAP; (b) LYSO.	116
5.10	Dependence of η_L on the wrapping for LuYAP (a) without optical coupling to the PMT; (b) with optical coupling to the PMT. (1) Teflon, $n_{gap} = 1$; (2) 98% Reflector, $n_{gap} = 1$; (3) Teflon, $n_{gap} = 1.35$; (4) 98% Diffusor, $n_{gap} = 1.35$	117
5.11	Dependence of η_L on B for grooved crystals and comparison with the case of a plain surface.	117
5.12	Setup used for groove cutting.	118
5.13	Microscopic images of grooves. (a): LuYAP 1980 (b): LYSO 1982.	120
5.14	Comparison of experimental data with the simulation results of the idealized grooves for LuYAP.	123
5.15	Comparison of experimental data with the simulation results of the idealized grooves for LYSO.	123
5.16	Sketch of LITRANI setup with absorbing layers.	124
5.17	Dependence of η_L on $\lambda_{abs,layer}$ from the simulations.	124
5.18	Comparison of experimental light yields with the results of the absorbing layer approach ($B = 1.6$). Results for LuYAP 1999 and LuYAP 2000.	125
5.19	Comparison of experimental light yields with the results of the absorbing layer approach ($B = 1.6$). Results for LYSO 1997 and LYSO 1998.	125
6.1	Principal outline of PhCs [12]. Left: 1D PhC. Middle: 2D PhC. Right: 3D PhC.	130
6.2	Band structure of a 2D PhC.	132
6.3	Comparison of the band structure of a homogeneous material and a PhC. (1): homogeneous regime; (2): photonic regime.	133
6.4	Image of a PhC slab [58].	134
6.5	Band structure of a PhC slab.	134
6.6	Situation at the interface between two materials ($n_1 > n_2$) for (a) plain geometry and (b) a periodic modulation of the interface.	137
6.7	Principle of the Tikhodeev algorithm.	138
6.8	Outline of the simulated system. For reasons of clarity, the layer of grease on top of the PhC is not shown.	139
6.9	Definition of angles θ_i and ϕ	140
6.10	Dependence of the transmission of a PhC slab ($n_{bulk} = 1.95$; $f = 0.3$; $d_{slab} = 1$) on top of a LuYAP crystal ($\theta_i = 55^\circ$; $\phi_i = 0^\circ$).	141
6.11	Dependence of the slab transmission on θ_i . PhC slab on LuYAP, $n_{bulk} = 3$, $f = 0.7$, $d_{slab} = 0.3$. Note that for an unmodulated slab, no transmission is possible for $\theta_i > 50^\circ$	141
6.12	Dependence of the slab transmission on f . (a) $\theta_i = 0^\circ$. (b) $\theta_i = 60^\circ$. PhC slab on LuYAP, $n_{bulk} = 3$, $d_{slab} = 0.3$	143
6.13	Dependence of the slab transmission on d_{slab} . (a) $\theta_i = 0^\circ$. (b) $\theta_i = 60^\circ$. PhC slab on LuYAP, $n_{bulk} = 3$, $f = 0.7$	143
6.14	Dependence of the slab transmission on n_{bulk} . (a) $\theta_i = 0^\circ$. (b) $\theta_i = 60^\circ$. PhC slab on LuYAP, $d_{slab} = 0.3$, $f = 0.7$	143

6.15	Angular distribution of photons extracted at first incidence on an exit surface with PhC slab for (a) LuYAP and (b) LYSO and $a/\lambda = 0.8$. The grey line indicates the angular distribution of all incident photons for a specular reflector with 98% reflectivity. The angular distribution of photons extracted for a plain exit surface is shown for comparison.	144
6.16	Definition of the path length l	146
6.17	Angular distribution of all photons extracted from a scintillator + PhC exit surface for (a) LuYAP and (b) LYSO and $a/\lambda = 0.8$	147
6.18	Dependence of η_L on a/λ for several PhC-scintillator combinations. (a) LuYAP; (b) LYSO. The theoretical limit $\eta_{L,max}$ is indicated in both plots.	147
A.1	Amplitude vectors at the interfaces.	167

List of Tables

1.1	Properties and selected fields of application of frequently used PET isotopes.	5
2.1	Selected inorganic scintillators in medical imaging and high energy physics and their essential properties at room temperature. The light output is given relative to BGO.	26
2.2	Selected inorganic scintillators for PET.	49
3.1	Description of peaks visible in the light yield spectrum and their origin. $\alpha = E/m_0c^2$, $m_0c^2 = 0.511$ MeV; $E_{K_{\alpha,Lu}} = 63$ keV.	59
3.2	Setup configurations used in the light yield measurements.	62
4.1	Crystals used for determination of crystal parameters for LITRANI.	76
4.2	Sellmeier coefficients of LuYAP 1943 and LYSO 1946.	82
4.3	Emission properties of simulated LuYAP and LYSO crystals.	83
4.4	Reflector materials used in the simulations of LuYAP and LYSO crystals.	84
4.5	Arriving (ph_{arr}) and extracted (ph_{ext}) photons for different wrappings ($B = 1.6$) relative to the number of generated photons from simulations of LuYAP and LYSO.	92
4.6	Results of measurements for the $2 \times 2 \times 8$ mm ³ LuYAP and LYSO crystals.	94
4.7	Comparison of measured and simulated light yields: crystals without wrapping.	96
4.8	Comparison of measured and simulated light yields: crystals with Teflon wrapping. The last column indicates the refractive index of the slice of material between crystal and wrapping.	97
4.9	Comparison of measured and simulated light yields for $2 \times 2 \times 10$ mm ³ LuYAP crystals. All measurements were performed with the crystals in vertical alignment.	98
4.10	Comparison of measured and simulated light yields for $2 \times 2 \times 10$ mm ³ LYSO crystals. All measurements were performed with the crystals in vertical alignment.	98
4.11	Absolute light yields of measured LuYAP and LYSO samples. The average value of LYSO is determined only by LYSO 1946 and 1997.	100
4.12	$S \cdot Q$ of LuYAP and LYSO.	100

4.13	Previously published values of LY_{abs} of LuYAP and LYSO. . . .	101
5.1	Properties of the diamond disk and the LGB 5030 used for groove fabrication.	118
5.2	Roughness R_a of the test grooves.	119
5.3	Properties of crystals for groove fabrication.	119
5.4	LY of the crystals with macromachined exit surface relative to a plain exit surface. Case: no wrapping. The simulated values correspond to the case $B = 1.6$	121
5.5	LY of the crystals with macromachined exit surface relative to a plain exit surface. case: Teflon wrapping. The simulated values correspond to the case $B = 1.6$	121
6.1	Structural parameters or the INL PhC samples.	149